

2005

Sources and magnitude of fluid venting from the Mariana forearc serpentine mud volcanos

Samuel M. Hulme
San Jose State University

Follow this and additional works at: https://scholarworks.sjsu.edu/etd_theses

Recommended Citation

Hulme, Samuel M., "Sources and magnitude of fluid venting from the Mariana forearc serpentine mud volcanos" (2005). *Master's Theses*. 2834.

DOI: <https://doi.org/10.31979/etd.nax5-2v32>

https://scholarworks.sjsu.edu/etd_theses/2834

This Thesis is brought to you for free and open access by the Master's Theses and Graduate Research at SJSU ScholarWorks. It has been accepted for inclusion in Master's Theses by an authorized administrator of SJSU ScholarWorks. For more information, please contact scholarworks@sjsu.edu.

NOTE TO USERS

This reproduction is the best copy available.

UMI[®]

SOURCES AND MAGNITUDE OF FLUID VENTING FROM
THE MARIANA FOREARC SERPENTINE MUD VOLCANOS

A Thesis

Presented to

The Faculty of Moss Landing Marine Laboratories

San Jose State University

In Partial Fulfillment

of the Requirements for the Degree

Master of Science

by

Samuel M. Hulme

December 2005

UMI Number: 1432452

INFORMATION TO USERS

The quality of this reproduction is dependent upon the quality of the copy submitted. Broken or indistinct print, colored or poor quality illustrations and photographs, print bleed-through, substandard margins, and improper alignment can adversely affect reproduction.

In the unlikely event that the author did not send a complete manuscript and there are missing pages, these will be noted. Also, if unauthorized copyright material had to be removed, a note will indicate the deletion.

UMI[®]

UMI Microform 1432452

Copyright 2006 by ProQuest Information and Learning Company.

All rights reserved. This microform edition is protected against unauthorized copying under Title 17, United States Code.

ProQuest Information and Learning Company
300 North Zeeb Road
P.O. Box 1346
Ann Arbor, MI 48106-1346

© 2005


Samuel M. Hulme

ALL RIGHTS RESERVED

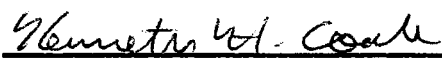
APPROVED FOR MOSS LANDING MARINE LABORATORIES



Dr. H. Gary Greene




Dr. C. Geoffrey Wheat, University of Alaska Fairbanks



Dr. Kenneth H. Coale

APPROVED FOR THE UNIVERSITY

 12/05/05

ABSTRACT

SOURCES AND MAGNITUDE OF FLUID VENTING FROM THE MARIANA FOREARC SERPENTINE MUD VOLCANOS

by Samuel M. Hulme

This thesis examines the geologic phenomenon of serpentine mud volcanism. In the Mariana Forearc, dehydration of the subducting Pacific Plate releases fluids that react with the overlying mantle to produce serpentine. This serpentine is extruded through the tectonically-fractured Philippine Plate and, over time, forms large seamounts up to 50 km wide and nearly 3 km tall. Fluid continuously rises along paths of serpentine expulsion, creating cold springs of exotic chemical compositions.

A research expedition to the Mariana Forearc conducted sonar surveys which pinpointed the location of actively-venting serpentine mud volcanos. This guided remote operated vehicle (ROV) dives and core-sampling along a transect of the Mariana Forearc. Geochemical profiles of sedimentary-serpentine pore fluids were used to determine fluid flow rates and dehydration fluid compositions at depth. Elemental compositions varied systematically with increasing fluid-source depths. These chemical patterns added constraints upon existing thermal and mass-transfer models of subduction zones.

Table of Contents

	Page
I. Introduction	1
1. The Significance of Subduction Zones	1
2. A Comparison of Three Convergent Margins	5
2.1. The Nankai Trough	5
2.2. The Costa Rica Margin	8
2.3. The Mariana Forearc	12
2.4. Summary	15
3. A Geological Description of the Mariana Forearc	17
3.1. Tectonics of the Mariana Forearc	17
3.2. Mechanisms for Serpentine Mud Volcanism	17
3.3. Fluid Flow in the Mariana Forearc	22
4. Pore Fluid Chemistry of Serpentine Seamounts	26
II. Methods	32
1. Cruise Overview	32
2. Swath Mapping Survey Methods	32
2.1. Multibeam Sonar Details	32
2.2. Sidescan Sonar Details	35
3. Sampling Procedures	36
3.1. Shipboard Coring Methods	36
3.2. ROV Surveys	40

	Page
4. Chemical Analysis	43
4.1. Shipboard Chemical Analysis	43
4.2. ICP-AES Analysis	44
4.3. Dilution HR-ICP-MS Analysis	45
4.4. Standard Addition HR-ICP-MS Analysis	51
4.5. Extraction HR-ICP-MS Analysis	54
III. Results	63
1. Geophysical data	63
2. ROV Exploration	72
3. Pore Fluid Chemistry	77
IV. Discussion	93
1. Tectonics and Geomorphology	
of Serpentine Mud Volcanism	93
1.1. Tectonics of the Mariana Forearc	93
1.2. Serpentine Seamount Distribution	
and Geomorphology	100
1.3. Model of Slab Depth	107
2. Geochemistry	111
2.1. Modeling Flow Rates of Upwelling Fluids	111
2.2. Chemical alteration of upwelling fluids	121
2.2.1. Major elements	121
2.2.2 Trace elements	130
2.2.3. Rare Earth Elements	138

	Page
3. Source of the Fluids	140
3.1. Major element end-members	140
3.2. Minor and trace element end-members	144
3.3. Transition metals	150
3.4. Rare earth element end-members	152
V. Conclusions	158
Citations	168
Appendix A. Push Core Extruder Design	178
Appendix B. Push Core Descriptions	182
Appendix C. Detailed ICP-MS Methods	191
Appendix D. 8-HQ Extraction Apparatus	197
Appendix E. Maps of Multibeam and Bathymetry	202
Appendix F. Complete Chemical Analysis Results	218

List of Figures	Page
Figure 1. Shaded relief map of the Nankai Trough region produced from the Hydrographic Department of Japan's topographic data set	6
Figure 2. Interpretation of a seismic profile transecting the sites drilled in ODP Legs 190 and 196	7
Figure 3. Map of the Costa Rica Margin	9
Figure 4a. Depth-corrected multichannel seismic profile of the Costa Rica Margin interpreted from the results of ODP Leg 170	11
Figure 4b. Schematic cross section of the Costa Rica Margin depicting the proposed fluid pathways within the subducting ocean lithosphere and overlying forearc wedge	11
Figure 5. Overview of the Mariana Subduction Zone from the trench to the back-arc basin	13
Figure 6. Schematic illustration of the basement beneath the Mariana Forearc	14
Figure 7. Diagram of the major tectonic features west of the northwestern Pacific Plate boundary	18
Figure 8. Bathymetry of the Mariana Forearc from combined ETOPO 1 and multibeam sonar surveys gridded at 10 arc second resolution	21

	Page
Figure 9a-d. Frame grabs of ROV Jason2 (a-c and e) and Submersible Shinkai 6500 (9d) dives on serpentine seamounts in the Mariana Forearc	23
Figure 10. Seismic reflection profile of Big Blue Seamount, an active serpentine mud volcano	25
Figure 11. Results of HR-ICP-MS dilution analysis of varying U content and dilution factor	47
Figure 12. Sunshaded bathymetry of the northern serpentine seamounts in the Mariana Forearc combining Em300 and Hydrosweep surveys with Geoware 1 minute data	64
Figure 13. Sunshaded bathymetry of the central serpentine seamounts in the Mariana Forearc combining Em300 and Hydrosweep surveys with Geoware 1 minute data	69
Figure 14. Sunshaded bathymetry of the southernmost serpentine seamounts in the Mariana Forearc combining Em300 and Hydrosweep surveys	71
Figure 15. Location of sampling that occurred during the 2003 Mariana Forearc expedition	78
Figure 16. Results of major and minor elemental pore fluid chemistry from selected gravity and piston cores that represent the greatest variation down-section	80
Figure 17. Results of minor and trace elemental pore fluid chemistry from selected gravity and piston cores that represent the greatest variation down-section	82

	Page
Figure 18. Depth profiles of redox sensitive elements and K at Big Blue Seamount	86
Figure 19. Depth profiles of redox sensitive elements and K at Cerulean Springs, Pacman Seamount	87
Figure 20. Results of HR-ICP-MS analysis of serpentine seamount pore fluids at Big Blue Seamount from two push cores (J36-2 and J36-4) and a gravity core (GC19)	89
Figure 21. Results of HR-ICP-MS analysis of serpentine seamount pore fluids from the deeper core sections	91
Figure 22. Sunshaded bathymetry of region D from Figure 1, Geoware 1 minute data, 250 m contours	95
Figure 23. Rose diagrams showing orientations of apparent fault strikes across the Mariana Forearc	97
Figure 24. Model of distance to Mariana Trench Axis	108
Figure 25. Pore fluid diffusion/advection flow models used to calculate flow rates at Big Blue Seamount and Cerulean Springs, Pacman Seamount	115
Figure 26. Location of transect conducted across Big Blue Seamount summit	117
Figure 27. Locations of cores sampled at Cerulean Springs, Pacman Seamount	119
Figure 28. Plots of Mg, Ca and K in the pore fluids from Big Blue Seamount and Cerulean Springs showing the effects of alterations in the surface sediments	125

	Page
Figure 29. Plots illustrating the relationship between Na and Cl in pore fluids from Big Blue Seamount and Cerulean Springs on Pacman Seamount	128
Figure 30. Variations in Rb and Cs in pore fluids recovered from Big Blue Seamount and Cerulean Springs	131
Figure 31. Trace element patterns at Big Blue Seamount and Cerulean Springs	133
Figure 32. Rb/Cs sytematics of the Mariana Forearc mud volcanoes	149

List of Tables	Page
Table 1. Statistical results of the 1% dilution HR-ICP-MS method	50
Table 2. Statistical results of the 10% standard addition HR-ICP-MS method	50
Table 3. Statistical results from the 8-Hydroxyquinoline (8-HQ) extraction of 4 mL samples and subsequent analysis by HR-ICP-MS	61
Table 4. Estimates of the depth to the subducting slab under sample sites	110
Table 5. Results of flow modeling based on concentrations of Rb in the pore fluids recovered from Cerulean Springs	119
Table 6. Major element composition of the upwelling fluids across the Mariana Forearc	141
Table 7. Minor and trace element composition of the upwelling fluids across the Mariana Forearc	146
Table 8. Transition metal concentrations in the upwelling pore fluids across the Mariana Forearc	151
Table 9. End-member REE composition (pmol/kg) of the upwelling pore fluids within the Mariana Forearc serpentine mud volcanoes	153

I. Introduction:

1. The Significance of Subduction Zones

Recycling and concurrent fractionation of the earth's crust occurs within subduction zones. As the Earth's crust sinks, it is subject to increases in temperature and pressure that remobilize elements and transfer them back to the upper crust. Water plays the principal role in the transfer of elements by several distinct processes: dissolution of material in the sediments (Benton et al., 2001); serpentinization of the overlying mantle (Fryer et al., 2000); and metasomatism during arc magma generation (Peacock, 1990). Subduction zones vary globally in; trench geometry, convergence rates, slab dip angle, age, crustal composition, sedimentation rates, bordering plate boundaries, and the size and type of orographic features on the subducting plate (Stern, 2002). These factors influence the elemental flux mechanisms within each subduction zone by affecting subsurface pressure-temperature (P-T) conditions, mineral composition and pathways for fluid migration through the crust and mantle. Examining the flux of elements through subduction zones is integral to models elemental recycling (Bebout, 1999; Chan

and Kastner, 2000; Dominik and Holloway, 1996; Fryer et al., 1999; Mottl, 1992; Peacock, 1993; Spivack, 2002; Stern, 1991; You et al., 1996). Because the processes that govern elemental recycling occur at depths unreachable within the present limits of the Ocean Drilling Program (ODP), direct observation of P-T conditions, mineral phase changes, and slab geometry is not possible. To understand these processes researchers rely upon seismic and tomographic imaging, geochemical balances of subduction inputs and outputs, deep sea drilling, and the examination of exposed paleosubduction zones when constructing models of elemental recycling.

Fluids play the most critical role in convergent margins, especially in recycling mobile elements and generating of arc magmatism (Peacock, 1990). The released fluids can affect the thermal conditions within accretionary prisms (Stein, 2003), provide nutrients for biological communities, and may trigger partial melting of the overlying mantle (Peacock, 1990). Hydrous minerals in older, cooler subduction zones travel primarily through the blueschist facies and can subduct to depths below the zone of arc magmatism. Deep inside the upper mantle, hydrous minerals dehydrate to release significant amounts of water

and dissolved elements (Peacock, 1993; Domanik and Holloway, 1996). Therefore, fluids not only play a significant role in arc magmatism but may affect the composition of mantle plumes (You et al., 1996).

Fluid recycling in convergent margins occurs over thousands of square kilometers of ocean crust and involves many processes including; heating, compression, dehydration, diagenesis and magmatism. The focus of this study is to explore fluid processes within the forearc that fractionate the subducting slab through a succession of dehydration reactions well before reaching the zone of arc magmatism. Within the outermost forearc, vast amounts of fluids being released at low temperatures through sediment compaction can influence the geometry of the accreting wedge (Moore and Vrolijk, 1992). As the slab continues to subduct, dewatering of clays and mafic minerals within the ocean crust contributes an additional greater volume of fluids to the forearc and subarc mantle through prograde metamorphism up to depths of 260-360 km (Domanik and Holloway, 1996). During this release of fluids, extensive removal and fractionation of mobile elements occurs, specifically B, N, As, Be, Cs, Li, Pb, Rb, and the rare earth elements (REEs) (You et al., 1996; Bebout et al.,

1999). While some elements are mobile at these conditions (e.g. Li, B, Be), the degree of mobility is largely controlled by the flow regime (You et al., 1996). A detailed understanding of the fluid interactions and transport processes is necessary to determine the nature of elemental recycling in the forearc setting.

The primary hypothesis of this thesis is that the composition of chemical species within upwelling fluids in the Mariana Forearc serpentine mud volcanoes reflects the depth to the subducting slab, which we use as a proxy for temperature. Investigating this connection between forearc fluid composition and slab depth is made possible in the Mariana forearc because of its unique geometry, lack of an accretionary prism, and the occurrence of active serpentine mud volcanoes. These mud volcanoes bring fluids to the seafloor that originated along the décollement, possibly at depths up to 30 km (Fryer et al., 2000). To comprehensively examine this scenario, the degree of activity for each mud volcano is measured by combining geomorphology with precision geochemical sampling. Additionally, the hypothesis that fractionation of fluid-mobile elements within the subducting slab occurs as the Pacific Plate descends into the mantle is tested by

measuring the composition of upwelling fluids in serpentine mud volcanoes at varying distances from the Mariana Trench axis.

2. A Comparison of Three Convergent Margins

2.1. The Nankai Trough

The Nankai Trough (Figure 1) is characterized by highly lateral fluid movement along lithologic layers, and there is presently no evidence for active fluid flow along the décollement (Spivak, 2002). This implies that fluid flow occurs episodically and could correlate with periodic large magnitude earthquakes. Drilling in the Nankai Trough during ODP legs 190 and 196 produced a transect from seaward pre-subduction reference sites to the region above the seismic interface (Figure 2). Cores in the area of the proto-thrust zone penetrated the highly fractured décollement. This provided the necessary reference for correlating the décollement with a seismic interface and mapping a trace of it on the seismic profile (Moore, 2001; Figure 2).

Pore water chemical compositions from both surveys exhibited a complex chlorinity profile that varied both with depth below sea floor and with depth to the

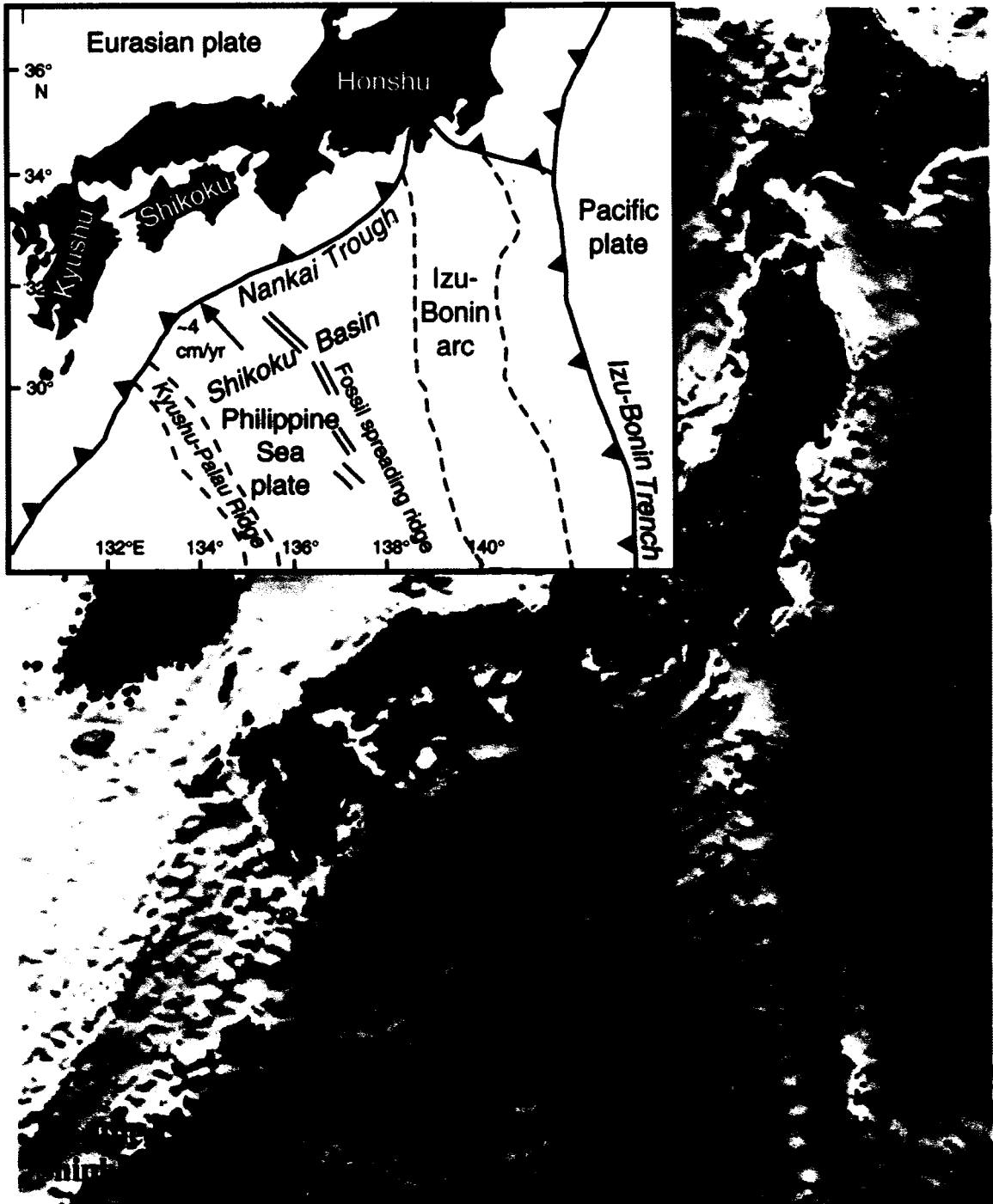


Figure 1. Shaded relief map of the Nankai Trough region produced from the Hydrographic Department of Japan's topographic data set (500-m grid interval). The inset shows a tectonic map of the northern Philippine Plate with the names of major orographic features and adjoining plates. Line AB is the location of the seismic profile in Figure 2.

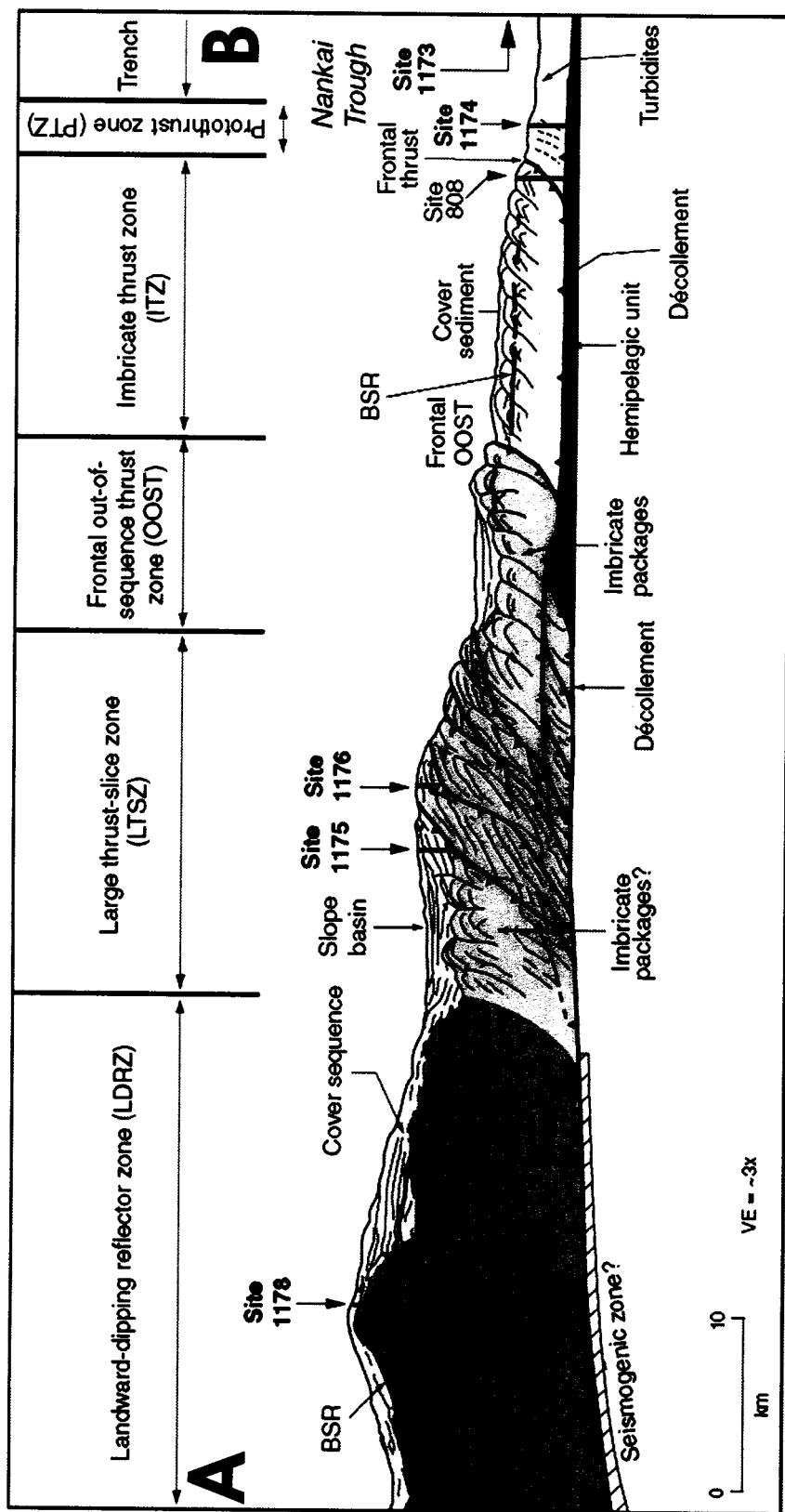


Figure 2. Interpretation of a seismic profile transecting the sites drilled in ODP Legs 190 and 196. The figure is divided into zones of sediment deformation within the accretionary prism. Growth of the accretionary prism begins at the frontal thrust. Imbricated packets of accreted sediments occur 20 km up slope and are replaced by large out of sequence thrust slices. Tilted sediment beds and fault traces were imaged beneath the inner forearc where the initiation of the seismogenic zone probably occurs. From Mikada et al., 2002.

décollement (Mikada et al., 2002; Spivak, 2002; Moore, 2001). Results from ODP Legs 190 and 196 show: a broad zone of low-chlorinity pore fluid below the décollement; a local chlorinity high within the décollement; and a local chlorinity low directly above the décollement (Mikada et al., 2002; Spivak, 2002). These anomalies indicate that fluid flow may be episodic, which would account for broad areas where fluid is diffusing out from previously localized flow and apparent lack of fluid flow at present along the décollement (Spivak, 2002). Isotopic analysis of chloride in the Nankai pore fluids suggests that exchange occurs between seawater and mineral components (Spivak, 2002). The exchange and fractionation along the path of fluid egress, which is increased by periods of stagnating fluid, would make it difficult to trace a fluid sample to its source and impossible to make conclusions about the physical properties of the source region.

2.2. The Costa Rica Margin

In the Costa Rica margin (Figure 3), faulting of the deformed sedimentary wedge allows for vertical migration of fluids, with a significant amount of fluid transport along the décollement (Bolton et al., 2001; Silver, 2001). While exploring the Costa Rica margin, ODP Leg 170 drilled a

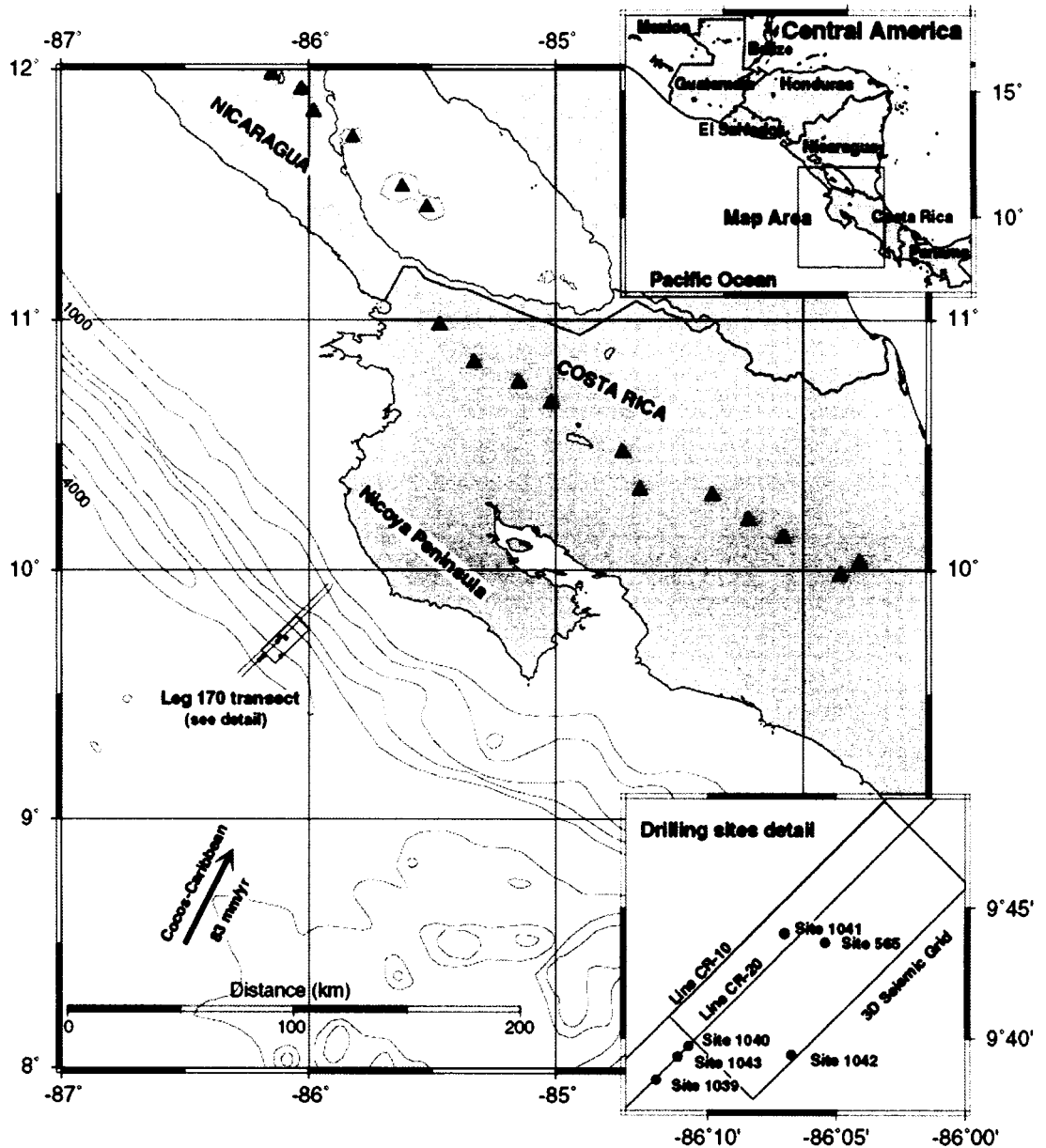


Figure 3. Map of the Costa Rica Margin showing; the location of Leg 170 drill sites, the relative plate motion of the Cocos Plate converging with the Caribbean Plate, 1000 m bathymetric contours, and arc volcanoes (triangles). From Silver, 2001.

transect from the pre-subduction crust to the landward portion of the deformation wedge (Figure 4a). Fluids in the deformed accretionary prism and overlying sedimentary apron of the Costa Rica subduction margin displayed low chlorinities, resulting from the release of fresh water from gas hydrates and clay dewatering along the décollement (Silver, 2001). Mechanisms of fluid migration were studied in detail and three distinct hydrologic systems were found (Bolton et al., 2001, Figure 4b). The upper plate was found to contain conduits for fluid flow that are fault related and release fluid as a combination of tectonic squeezing and overburden of sediment (Bolton et al., 2001; Silver, 2001). The décollement showed evidence of fluid flow, although the amount varied considerably due to variances in porosity and episodic expulsion (Bolton et al., 2001). The fluid from this zone may be derived from the dewatering of clays that are subjected to tectonic squeezing (Silver, 2001). Hemipelagic sediments atop the underthrust plate are progressively dewatered and show little fault-related flow as a result of decoupling of the two plates (Bolton et al., 2001).

Chemical analysis of pore waters from the Costa Rica margin reveals that several fluid-sediment interactions

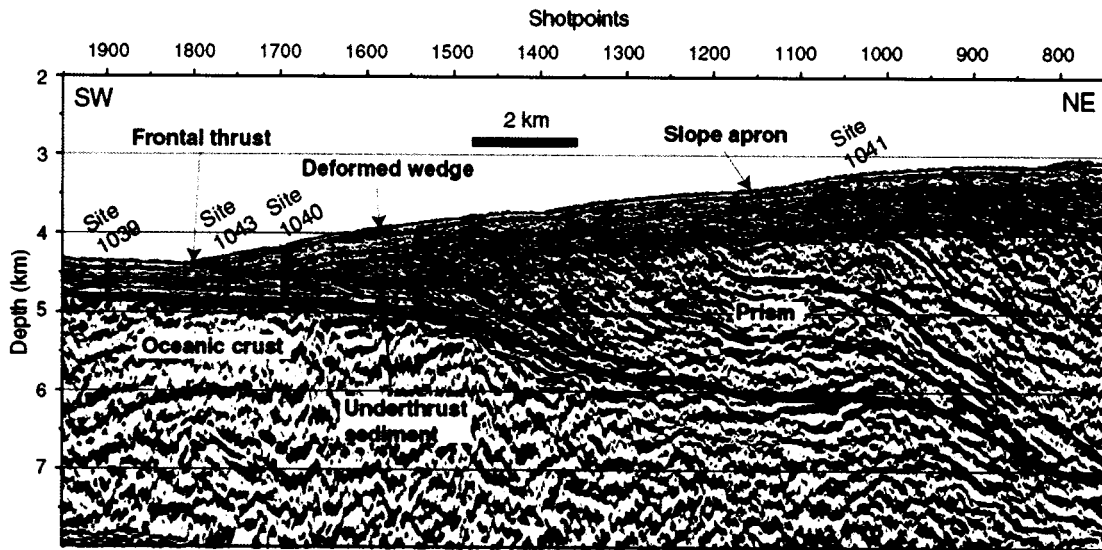


Figure 4a. Depth-corrected multichannel seismic profile of the Costa Rica Margin interpreted from the results of ODP Leg 170. The 500 m of subducting sediment can be seen compacting landward of the frontal thrust. Poor seismic resolution and a lack of deeper core samples preclude knowledge of the lithology of the larger prism. From Silver, 2001.

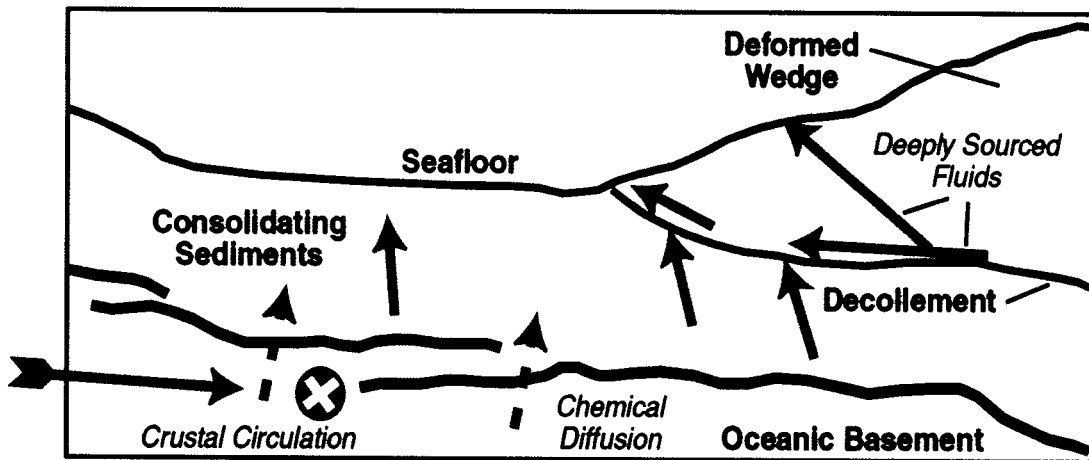


Figure 4b. Schematic cross section of the Costa Rica Margin depicting the proposed fluid pathways within the subducting ocean lithosphere and overlying forearc wedge. Arrows indicate direction of fluid flow, which is channeled along the decollement and fault offsets within the accretionary prism. From Moore and Silver, 2002.

occur; clays exchange ions with ammonium in the uppermost layers, volcanic ash undergoes alteration at depth, and seawater advects laterally through the accretionary wedge (Chan and Kastner, 2000). Deep-sourced fluids were found to be contributing to the regional hydrologic cycle. The origin of the fluids was estimated to be at temperatures between 100-150°C, depths of 10-15 km and distances of 40-60 km west of the trench axis (Silver, 2001; Chan and Kastner, 2000). Mass balance calculations indicate that about half of the Li subducted in this zone is recycled in the volcanic arc and up to a quarter is recycled into the ocean through exchange with seawater, primarily along the décollement (Chan and Kastner, 2000).

2.3. The Mariana Forearc

The Mariana Forearc (Figure 5), nearly devoid of an accretionary prism, channels fluids and erupting serpentine muds along fault-generated vertical conduits within mud volcanoes (Fryer et al., 1985, 1992, 1997, 1999, 2000; Phipps and Ballotti, 1992; Figure 6). The unique construction of the Mariana Forearc enables direct observation of conditions deep within the Earth that drive the recycling of elements. The extensive faulting of the forearc region and lack of an accretionary prism allows for

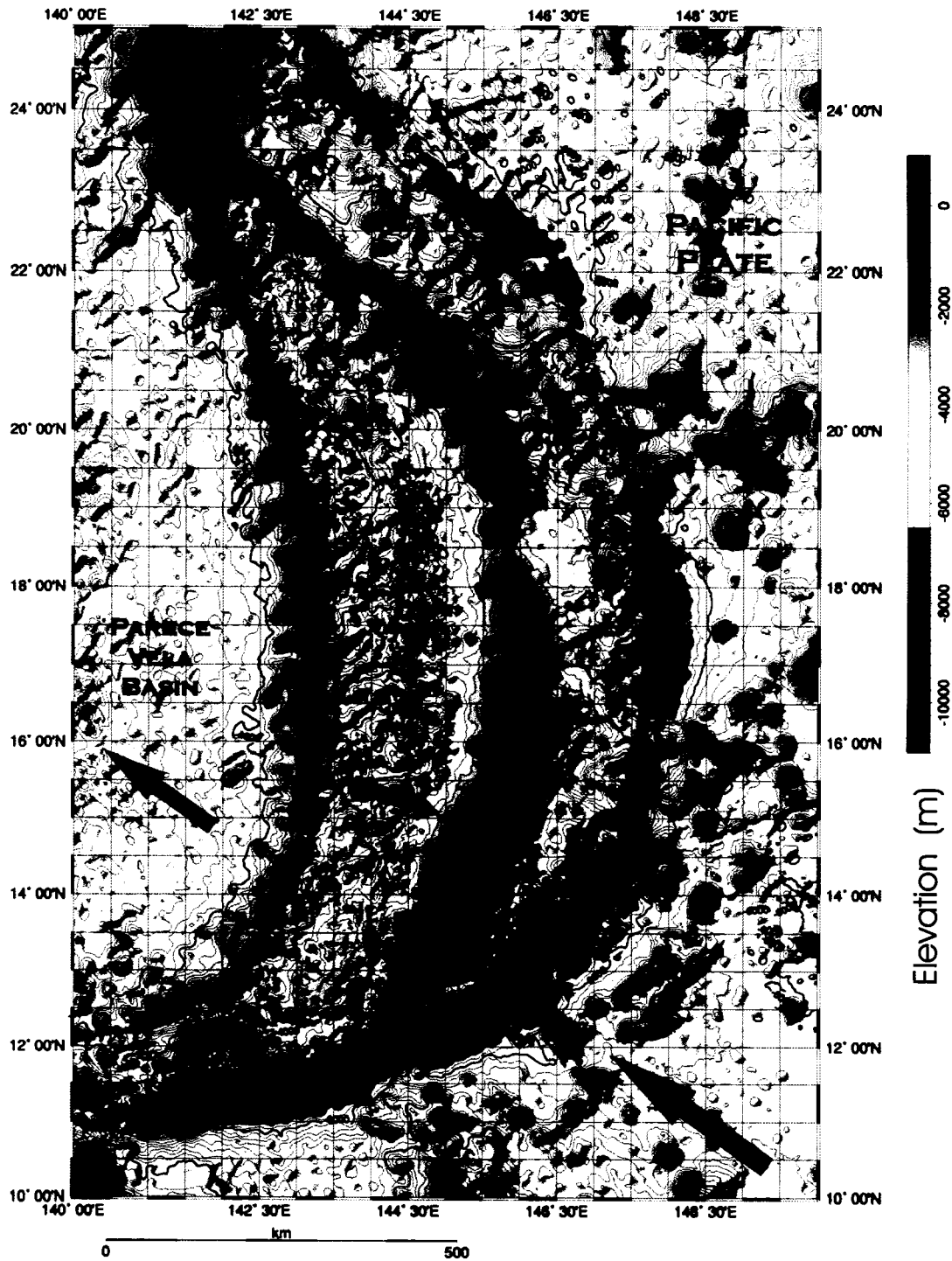


Figure 5. Overview of the Mariana Subduction Zone from the trench to the back-arc basin. Arrows represent absolute plate motion directions and are scaled to the magnitude of plate motion. Data from Geoware 1 minute combined observed and predicted topography. Contours every 250 m.

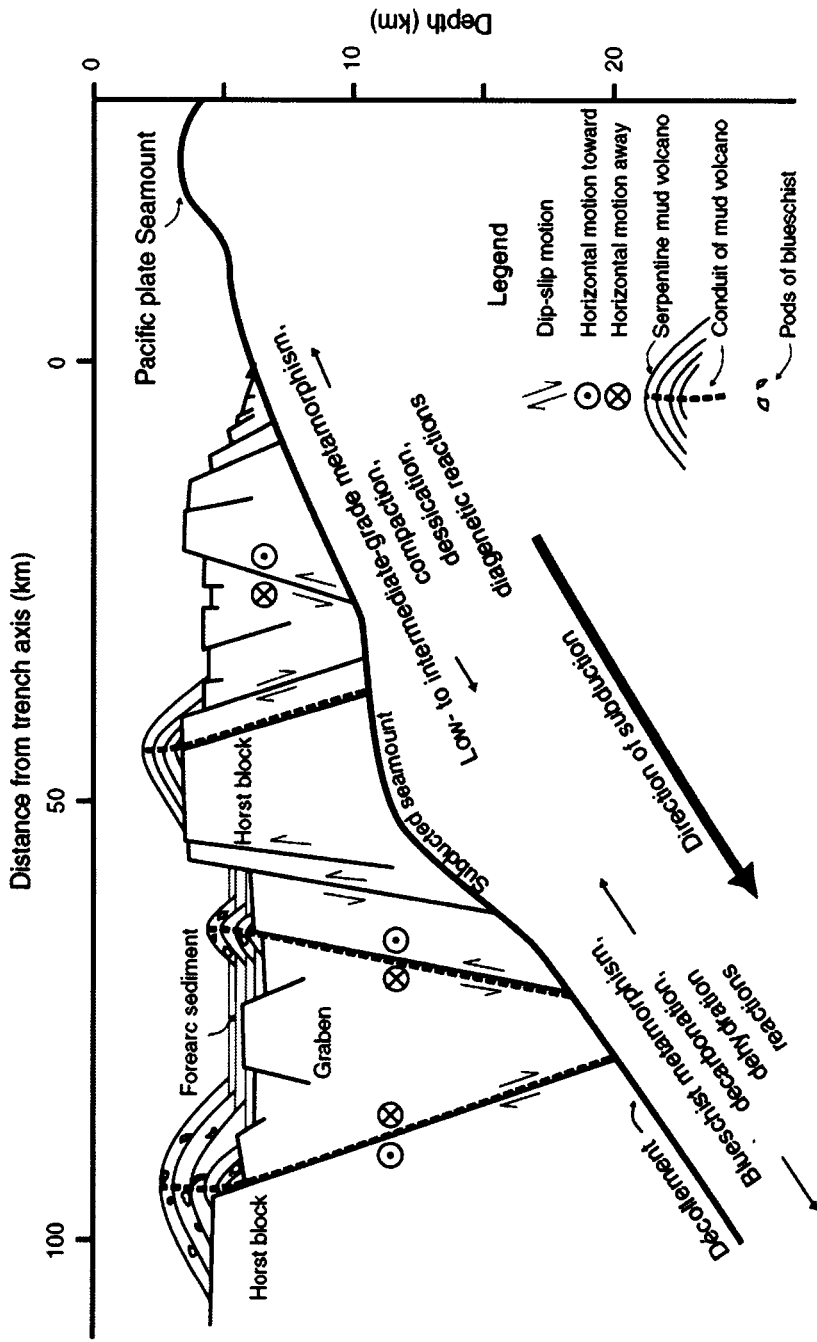


Figure 6. Schematic illustration of the basement beneath the Mariana Forearc. The sediment-starved region cannot maintain an accreting prism which places ultramafic mantle blocks at a close proximity to the trench axis. Subducting seamounts and normal faulting fracture the upper mantle allowing fluids from the dehydrating Pacific Plate to serpentinize the forearc basement. The low-density serpentine, pieces of metamorphosed oceanic crust and dehydration fluids are extruded along the fault zones forming serpentine seamounts along the outer forearc. From Fryer et al., 2000.

the direct transport of material to the seafloor with minimal alteration. Faulting of the overriding plate occurs from the combined effects of extension of the crescent-shaped arc and the subduction of numerous seamounts (Fryer et al., 2000; Fryer, 2002). The Mariana Forearc has the most direct fluid recycling pathways, but variation in the fluid formation depth can result in significantly differing fluid composition from one seamount to another (e.g. Fryer et al., 1999). The ability to assess the approximate depth of formation fluids makes it possible to understand the relationship between P-T conditions during fluid regeneration and how this affects the recycling of elements in a forearc environment.

2.4. Summary

In comparing the results of these three convergent margins, it becomes evident that there are many factors that affect how fluids are recycled and what elements are mobilized. In the Nankai Trough, an environment of episodic fluid flow exists, and lateral flow appears to be dominant (Spivak, 2001). Fluids there pass through many different lithological layers and exchange elements with each type of lithology along the path of flow. Varying P-T conditions along the broad fluid source zone and the

exchange of elements along the path are coupled with potential hydration-dehydration or recrystallization reactions, thus obscuring many potential geochemical tracers. The Costa Rica margin has a more simplified flow regime, but a combination of multiple diagenic processes creates a setting where numerous variables control fluid compositions (Chan and Kastner, 2000).

In contrast, crust-mantle conditions of the Mariana Forearc are ideally suited for elucidating chemical exchanges in subduction zones through the study of active serpentine mud volcanoes that exist at a range of depths to the décollement. There is evidence of significant recycling of elements by fluids in all three of these settings demonstrated by elevated concentrations within migrating fluids (You et al., 1996; Chan and Kastner, 2000; Mottl, 1992); but the steep angle of fluid pathways within the mud volcanoes (Figure 6) allows for transporting minimally altered fluids from the mantle to the seafloor above the region of formation as opposed to lateral flow through differing lithologic layers.

3. A Geological Description of the Mariana Forearc

3.1. Tectonics of the Mariana Forearc

The Mariana Trench delineates the active plate boundary between the subducting Pacific Plate and the overriding Philippine Plate with initial convergence occurring at least 40 Ma (Stern et al., 1991; Fryer, 1996; Figure 7). The northern and southern extent of the Mariana Trench are the Izu-Bonin trench and the intersection of the back-arc spreading center with the trench axis, respectively. The curvilinear geometry of the Mariana Convergent Margin results in transtensional stress fields which, when coupled with a high density of subducting seamounts, creates a horst and graben geomorphology throughout the Mariana Forearc (Fryer et. al., 1985; Figure 6). The forearc seamounts are spatially distributed primarily along the upper (horst-side) boundary of fault blocks (Fryer et. al., 2000) and are aligned within two sets of primary and conjugate stress fields (Fryer pers. com, 2004).

3.2. Mechanisms for Serpentine Mud Volcanism

The Mariana Forearc contains a phenomenon, referred to as serpentine mud volcanism (Fryer and Mottl, 1997; Fryer et al., 1999; Fryer et al., 2000; Mottl et al., 2003), that

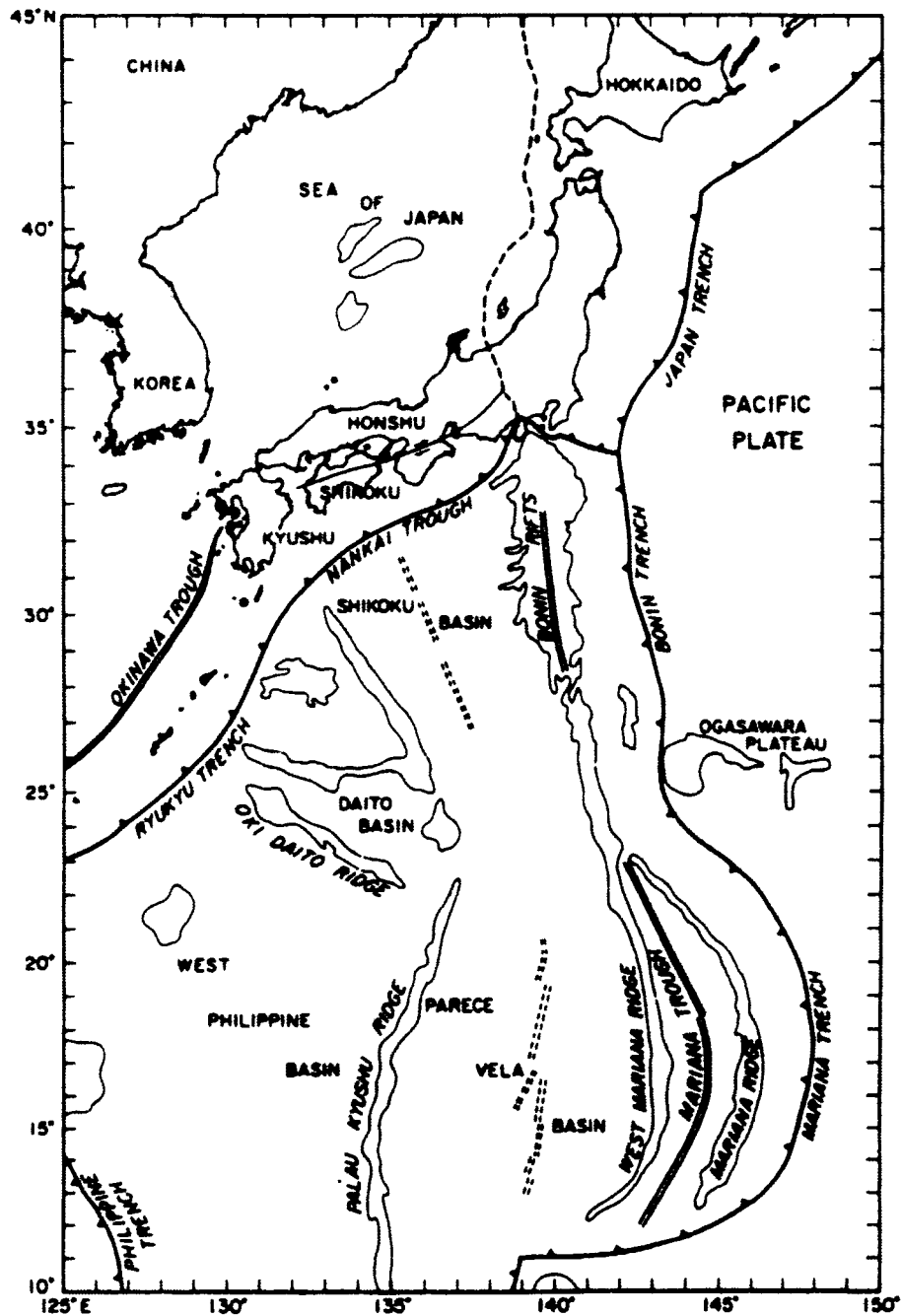


Figure 7. Diagram of the major tectonic features west of the northwestern Pacific Plate boundary. Topography is depicted by the -3000 m contour for the Mariana, West Mariana, and Izu-Bonin ridges. The -4000 m contour is used for the remaining basins and ridges. Barbed lines point to the overriding plate. Parallel lines follow active backarc spreading centers. Dashed parallel lines outline extinct backarc spreading centers. From Fryer et al., 2000.

exposes mantle-sourced serpentine muds, blueschist facies metamorphosed mafic clasts, and slab-sourced fluids at the sea floor in the form of large serpentinite seamounts. Little or no accretionary prism is coupled with extensive faulting of the overlying plate, creating conditions for the focused release of volatiles and other materials to the sea floor (Fryer, 1985). Mud volcanism in the Mariana Forearc focuses vertically along tectonic faults reaching far below the seafloor down to the décollement (Fryer et al., 1999). In addition, as water is released from sediment and dehydration reactions at depth, this water hydrates the overlying mantle to form serpentine and other metamorphic minerals (Peacock, 1993; Hyndmen and Peacock, 2003). This mixture of serpentinite and fluids erupts onto the seafloor in multiple flows creating massive mud volcanoes resembling magmatic shield volcanoes up to 3 km high and 50 km in diameter (Fryer et al., 2000; Phipps and Ballotti, 1992).

Water removed from hydrated clay minerals, upon reaching critical temperatures and pressures, serpentinizes the overlying mantle harzburgite and dunite (Fryer and Mottl, 1992). Tectonic movement along faults mylonizes the serpentine (Fryer, 2002), which combines with additional

fluids to form saturated muds with densities 0.7 to 1.3 g/cm³ less than the density of the surrounding peridotite (Phipps and Ballotti, 1992). The erupting mud often carries larger serpentinite clasts or small blueschist-facies pebbles to the seafloor as the mud volcanoes erupt in a series of episodic flows (Fryer and Mottl, 1997; Fryer et al., 2000). The active region of mud volcanism can migrate along a fault during the formation of a serpentinite seamount. When combined with a proclivity for mass wasting, the resulting seamounts appear in a variety of geomorphologies (Figure 8).

Metamorphosed wall-rock conduits can be established through these seamounts down to the décollement through which fluid can flow up to the seafloor without the fluid composition altering beyond recognition (Mottl, 1992; Mottl et al., 2004). The mineral assemblage of the Mariana Forearc mud volcano sedimentary serpentinite comprises: medium blue-green to dark blue serpentine dominated by lizardite; veins or precipitates of chlorite, brucite, magnetite and Cr-spinel; moderately to completely serpentinitized ultramafic harzburgite and dunite clasts containing olivine and orthopyroxene with lesser amounts of clinopyroxene; and calcite and aragonite carbonates

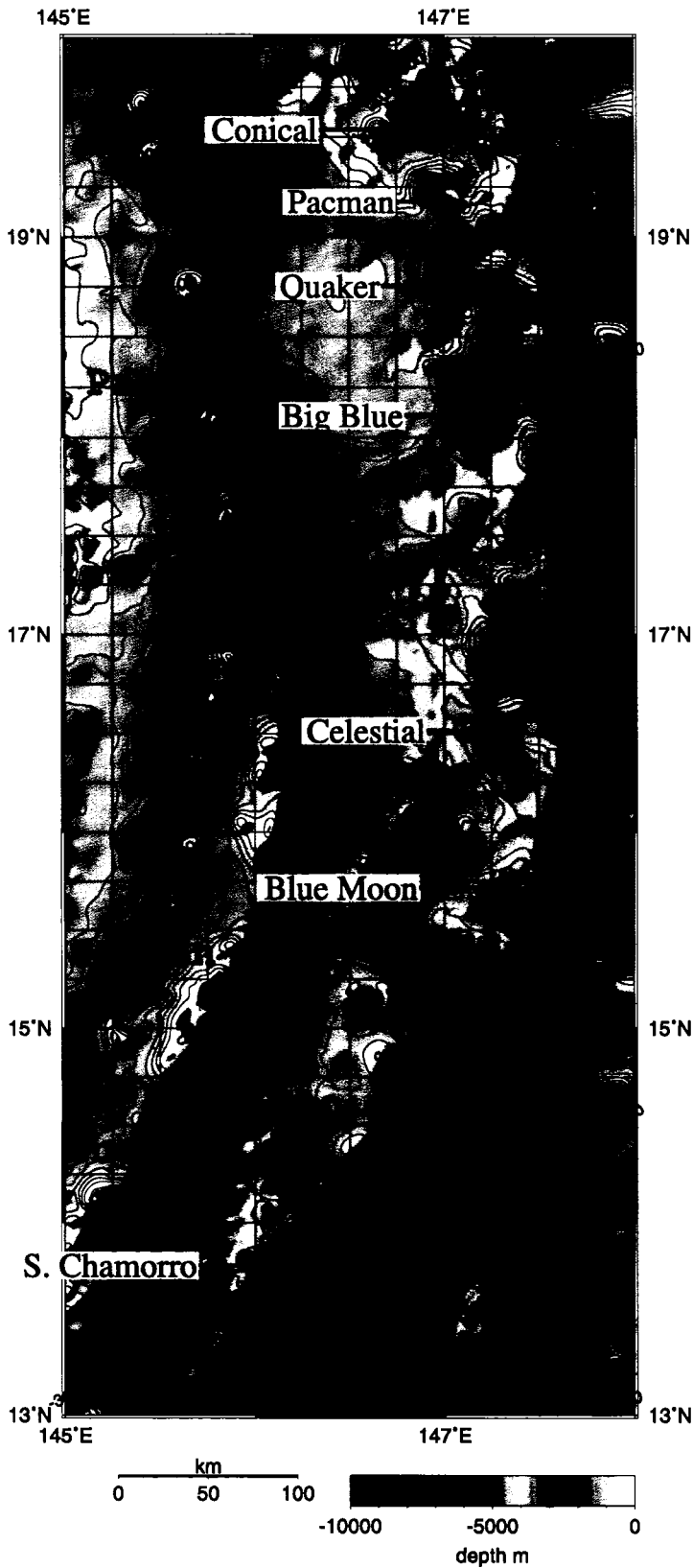


Figure 8.
 Bathymetry of the Mariana Forearc from combined ETOPO 1 and multibeam sonar surveys gridded at 10 arc second resolution. The names and locations of known active serpentine mud volcanoes are shown. Contours every 250 m.

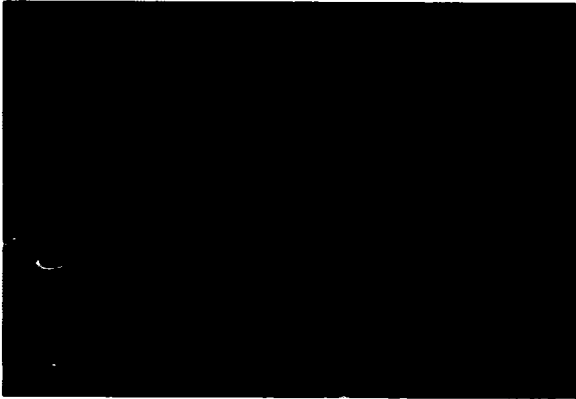
(Salisbury et al., 2002). Thus, the rapidly ascending fluidized material contacts primarily serpentized harzburgite and minimal exchange of elements occurs before erupting onto the seafloor (Mottl, 1992; Fryer et al., 1999; Mottl et al., 2004).

3.3. Fluid Flow in the Mariana Forearc

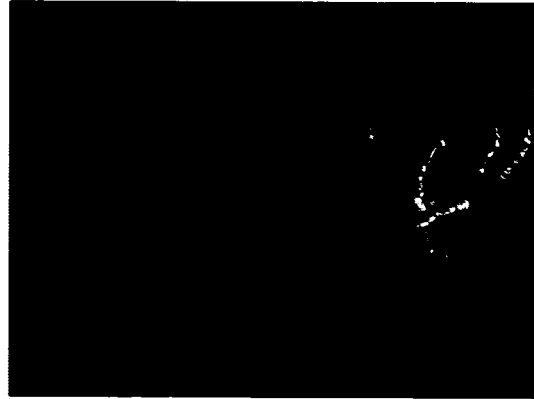
Evidence of fluid flow through serpentine mud volcanoes in the Mariana Forearc is manifest in several forms: geophysical surveys of multibeam bathymetry, sidescan sonar reflectivity, and multichannel seismic reflection image geomorphologies indicative of diapirism and mudflows (Fryer et al., 2000); carbonate and brucite chimneys form at the summit of the active mud volcanoes when highly altered upwelling fluids react with seawater (Figure 9 a-c); the presence of chemosynthetic microbial or macrofaunal communities of mussels, tubeworms, whelks, and archaea (Fryer and Mottl, 1997; Mottl, 2003; Figure 9d); and the growth of precipitates within a three-week period on the inside rim of an open borehole (Figure 9e).

Geophysical surveys highlight areas of recent mud volcanism by imaging slumps, channels, regions of high backscatter, and low density zones indicative of erupted material (Fryer et al., 2000). Areas of extensive mass

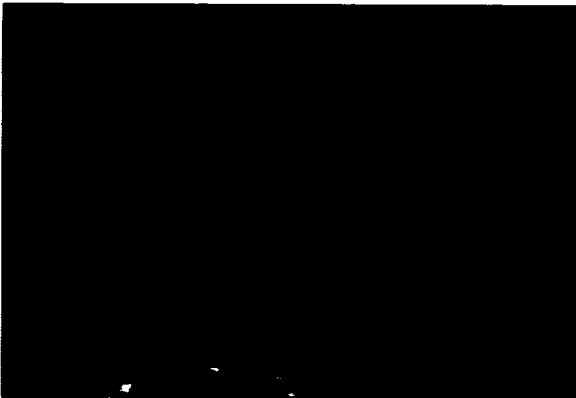
9a



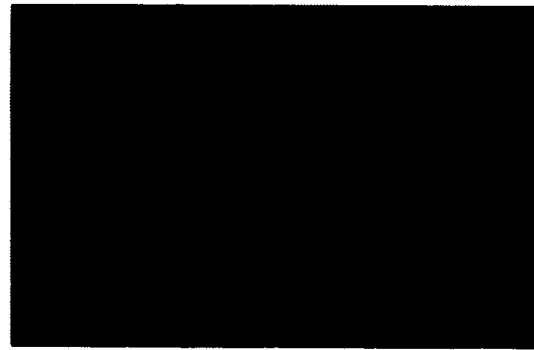
9b



9c



9d



9e



Figure 9.

Frame grabs of ROV Jason2 (9a-c and e) and Submersible Shinkai 6500 (9d) dives on serpentine seamounts in the Mariana Forearc.

9a) Brucite chimneys at Cerulean Springs 9b) Cold vent field at the summit of Quaker Seamount. 9c) 2 m chimney at the summit of Conical Seamount.

9d) Chemosynthetic megafaunal community at the summit of S. Chamorro Seamount. From Fryer and Mottl, 1997.

9e) Precipitates on the rim of an open borehole at ODP Site 1200, S. Chamorro Seamount.

wasting in the form of mudflows, were imaged by multibeam and sidescan sonar surveys on the south west side of South Chamorro Seamount (Fryer et al, 2000). An MR1 sidescan survey of Peacock seamount displayed the highest level of backscatter covering the entire edifice. Because fluid flow and the associated precipitates are limited to the seamount summits in this environment, the high backscatter indicated intense deformation of surficial sediment caused by uplift of the seafloor through diapirism (Fryer et al., 2000). However, subsequent gravity coring of Peacock Seamount yielded no evidence of fluid flow or recent activity. Seismic surveys in the Mariana Forearc show a unit of low density material on the summit of Big Blue Seamount (Figure 10), which was determined to be actively venting (Fryer et al., 1999).

Previous direct seafloor explorations by submersibles, ROV, and gravity coring discovered active fluid venting throughout the Mariana Forearc. The submersible Alvin surveyed active mud volcanism on Conical Seamount and discovered carbonate chimneys (Fryer et al., 1990). The ROV Shinkai 6500 was deployed in 1995 to investigate the conditions on S. Chamorro Seamount near ODP Leg 195 Site 1200 and discovered the only known megafaunal community

Big Blue Seamount Summit

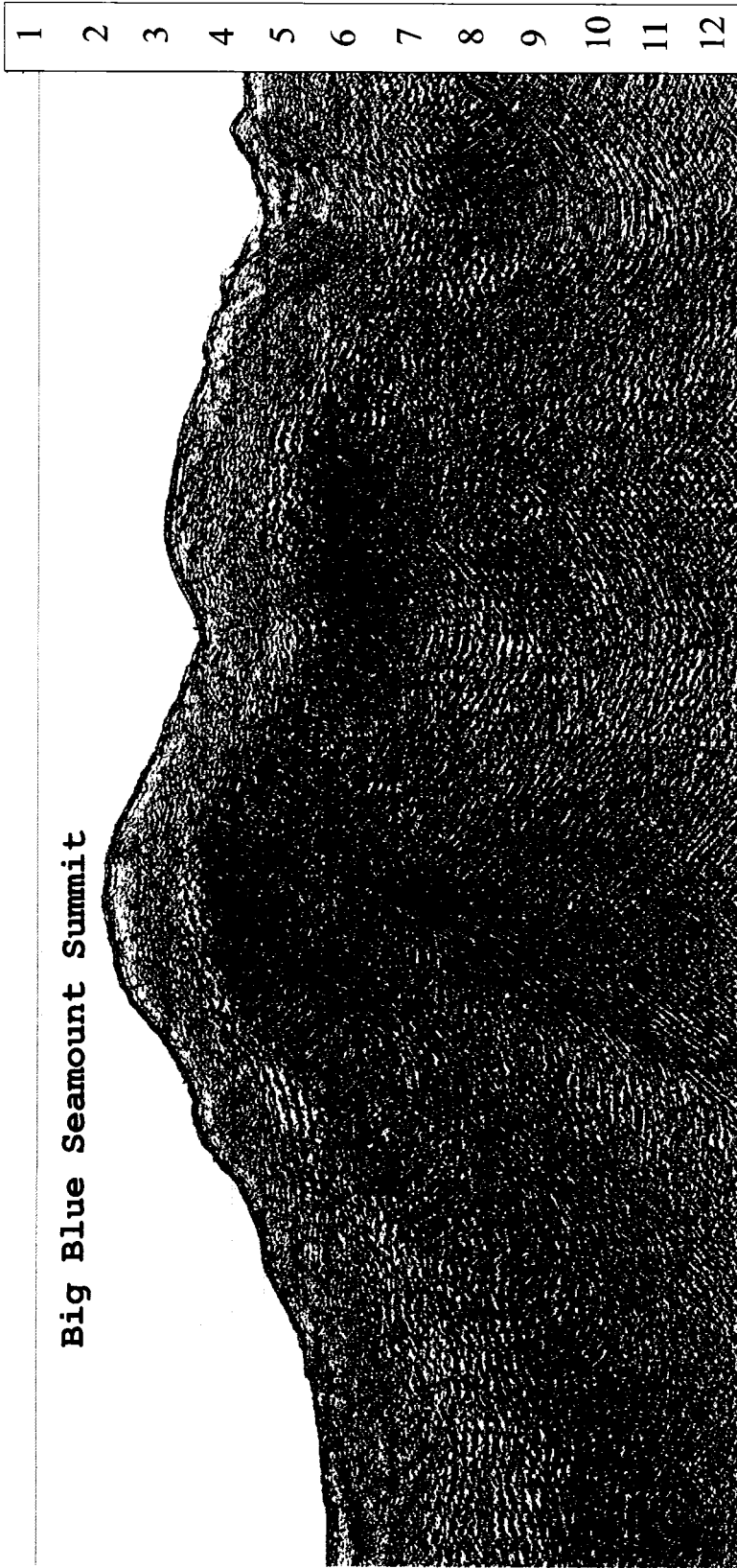


Figure 10. Seismic reflection profile of Big Blue Seamount, an active serpentine mud volcano. Data was collected by Taylor et al. (2002) aboard the R.V. Maurice Ewing. A bright low density zone can be seen near the summit. This indicates the presence of diffuse fluid flow within the summit dome. Scale represents 2-way travel time in seconds.

associated with serpentine mud volcanism (Fryer et al., 1997). Pacman Seamount was surveyed with the ROV Jason-Medea in an area of high backscatter where active fluid seeps, the Cerulean Springs, produce thin brucite chimneys almost 1 m in length (Fryer et al., 1999). Coring was conducted during the Jason-Medea expedition and the pore fluids recovered indicated upflow through surface sediments. The combined evidence determined that upwelling fluid flow was actively occurring at a minimum of seven seamounts; South Chamorro, Conical, Quaker, Big Blue, Blue Moon, and Pacman.

4. Pore Fluid Chemistry of Serpentine Seamounts

Pore fluid flowing through sedimentary serpentine seamounts contains valuable information on the conditions that exist in the mantle below, and the flux of elements from the slab and mantle to the seafloor. Results from chemical analyses of pore fluids and the serpentinite host have concluded that the fluids are not significantly altered on their migration to the surface through serpentinitized peridotite conduits, and that their composition represents conditions deep within the subduction zone (Benton et al., 2001; Mottl, 1992; Savov et

al., 2004). The isotopic compositions of the fluids strongly suggest that the fluids originate from the dehydration of hydrous minerals at depth (Benton et al., 2001). The chemical signature of the fluids in the Mariana Forearc are unique in many ways. Some of the variances relative to seawater include; an increase in carbonate alkalinity, methane, ethane, propane, sulfate, H_2S , B^{3+} , Na^+ , K^+ , and Rb^+ , and a decrease in Cl^- , Br^- , Li^+ , Ca^{2+} , Sr^{2+} , and Ba^{2+} relative to bottom seawater (Mottl, 1992; Benton et al., 2001; Fryer et al., 1999).

Alkalinity levels, increase dramatically in seamounts far from the trench, while closer seamounts, such as Blue Moon can be depleted in alkalinity relative to seawater in the surface sediments (Fryer et al., 1999). This trend is consistent over the forearc and has been accredited to a decarbonation zone or zone of carbonate dissolution that is estimated at a depth to slab between 15 km and 22 km (Fryer et al., 1999; Mottl et al. 2003). At this depth, the increase in temperature causes subducting carbonate to dissolve, releasing aqueous carbonate to the fluids. Experiments with equilibrium computer models concluded that mineral transformations within the subducting slab consume Ca^{2+} , allowing subducted carbonates to dissolve (Mottl et

al., 2004). Therefore, serpentine mud volcanism creates an input of carbon into the oceans that previously has not been addressed. The magnitude of this flux has not been constrained because of a lack of understanding of subduction zone chemical cycles.

High-pH of (up to 12.5) has been measured in upwelling pore fluids, regardless of distance from the trench and is the result of serpentinization reactions at depth (Mottl et al, 2004). The reaction that causes this high pH is defined as $2(\text{Mg}_{1.8}\text{Fe}_{0.2}\text{SiO}_4)$ (Olivine) + $2.483\text{H}_2\text{O}$ + 0.45Cl^- + 0.45H^+ = $\text{Mg}_{2.7}\text{Fe}_{0.3}\text{Si}_2\text{O}_5(\text{OH})_4$ (Serpentine) + $0.45(\text{Mg}_2(\text{OH})_3\text{Cl})$ (Mg hydroxide-chloride) + $0.033\text{Fe}_3\text{O}_4$ (Magnetite) + 0.033H_2 (Janecky and Seyfried, 1986). Also note that while chloride is consumed in the reaction, studies have found that this depletion is not significant when compared to the amount of freshening of the pore waters found in the Mariana Forearc (Mottl, 1992). The chlorinity values showed a general decrease where ever fluid flow exists, which is consistent with previous conclusions that the fluids are slab-derived dehydration products (Mottl, 1992).

Hydrogen gas produced directly from serpentinization, and the thermogenic methane produced, from the reaction of hydrogen with CO_2 by the Fischer-Tropsch reaction, has a

significant effect on observed hydrogen sulfide levels. The Mariana Forearc is depleted in organic carbon with only 13 of 49 samples from ODP Leg 195 containing detectable (>0.01 wt.%) levels (Mottl et al., 2003). Despite a lack of organic carbon, intense microbial sulfate reduction occurs in the sediments. This is indicated by the reduced zones containing up to 5.6 mmol/kg dissolved hydrogen sulfide. The microbes responsible for this reaction were determined to be Archaea deriving its source of carbon from the inorganic methane generated at the slab-mantle interface where serpentinization occurs (Mottl et al., 2003). Little is currently known about the species of Archaea found in these high pH pore fluids and their physiological mechanisms of respiration.

Many other chemical constituents are mobilized within the Mariana Forearc through the process of serpentine mud volcanism, as noted above. Depletions can occur by adsorption of ions onto sediments early in the subduction process or precipitation into carbonates. In contrast, increases in porewater concentrations are associated with; the leaching of mantle rocks, remobilization of slab materials with increased temperature, reactions associated

with sulfate reduction and the exchange of ions within carbonates.

There is currently much interest in the use of rare earth elements (REEs) as geochemical tracers of alteration processes (Williams-Jones and Wood, 1991; Stern et al., 1991; Johannesson et al., 1997), but their behavior in subducting systems is not known. The Mariana Forearc, due to its differing pore water chemical composition and P-T conditions, has the potential to increase the understanding of how REEs behave under conditions not previously reproduced in laboratory experiments. The effect of pH on REE complexing with CO_3^{2-} and PO_4^{3-} has been studied (Lee and Byrne, 1991) and one would expect the relative enrichments of REEs in the pore water samples to reflect this. There are, however, the factors of temperature and pressure to consider. Lee and Byrne (1994) conducted laboratory experiments on Gd^{3+} complexing at pressures between 1-600 atm and found a five-fold increase in the level of gadolinium carbonate complexation at high pressure. The active precipitation of carbonate could deter the mobilization of REEs, however, by sequestering them into the solid phases. Gammons et al. (1996) conducted laboratory experiments on neodymium chloride complexing at

temperatures between 25°C and 300°C and found that at elevated temperatures these complexes appear at much greater levels than at ambient temperatures. The possibility therefore exists for REE mobilization in excess of bottom seawater concentrations by complex formation at elevated temperatures and pressures. Slab depths of 30 to 40 km below the Mariana Forearc can produce temperatures as high as 550°C and pressures as high as 10 kbar (Fryer et al., 1985). These pressure conditions exceed those previously studied in REE reactions and thus make the Mariana Forearc an ideal location for *in situ* observation of speciation under extreme conditions.

II. Methods

1. Cruise Overview

A multi disciplinary survey of the Mariana Forearc, from March 23rd through May 4th of 2003, focused on the biogeochemical properties of the Mariana Forearc mud volcanoes in unprecedented detail. R.V. Thomas G. Thompson, a 274-foot research vessel, transited the forearc from South Chamorro Seamount to Conical Seamount (Figure 8) conducting geophysical and gravity coring surveys. Using the survey data to predict the location of active seeps, ROV investigations with the Jason2/Medea and navigated gravity coring surveys were conducted on the returning southward transit from Conical Seamount back to South Chamorro Seamount. The principal investigators for the expedition were P. Fryer, M. Mottl, and C.G. Wheat.

2. Swath Mapping Survey Methods

2.1. Multibeam Sonar Details

The R.V. Thompson is equipped with two multibeam sonar instruments, the ATLAS Hydrosweep and the SIMRAD EM-300, for mapping bathymetry. The KRUPS-ATLAS Hydrosweep has a swath angle of 90 degrees, which allows mapping a distance equal to twice the water depth. Two hydroacoustic

transducer arrays are mounted on the ship's hull parallel to the ship's transverse and longitudinal axes. Each transducer consists of multiple individual modules capable of recording 59 discrete depths for each sounding. By measuring the 59 depths parallel to the ship's longitudinal axis, it is possible to calculate the water-column sound velocity profile and correct for refraction of the outer portions of the sound beam. The geographical position, gyro-compass heading and ships longitudinal and latitudinal velocities were recorded from the ship's navigation computer. Ship roll, pitch and heave were recorded from a sensor platform. All of these data were stored on magnetic tape and on the ship computer's data drive. This instrument was used primarily for surveying in >4000 m water depths.

For water depths <4000 m, the Kongsberg® SIMRAD EM 300 multibeam echo sounder was used for more detailed imaging of bathymetric features. The EM 300 operates at a frequency of 30 kHz with a swath angle of 150 degrees. There are 135 beams dynamically steered to account for water depth, heave, pitch and roll. This is done to maximize the number of useful beams and enable the accuracy of depth measurements to be nearly independent of beam

pointing angle. Navigation information was recorded from the ship's navigation computer and stored with the sounding data on magnetic tape and the ship computer's data drive.

Raw bathymetry data from both multibeam instruments were processed using MB-System (www.ldeo.columbia.edu/res/pi/MB-System/), a UNIX-based open-source program designed by D. Caress and D. Chayes for editing and displaying multibeam and backscatter data. MB-System allows for editing ship navigation, sound velocity profiles, and depth recordings using both command-line and x-windows graphical interfaces. The soundings were visually inspected in a whale-bone profile, and individual depth measurements were deleted based on anomalous deviations from surrounding depth measurements. The accepted measurements were exported as latitude, longitude, and depth binary data files for gridding and display.

Generic Mapping Tools (GMT), another UNIX-based, open-source program, was used for gridding and displaying the exported files. Regional maps of the surveyed seamounts were compiled in GMT from EM 300, Hydrosweep, and historical datasets by overlaying 1 arc-second grids. The grids were produced by averaging soundings based on a gaussian nearest-neighbor calculation. For data sets of

resolutions less than the desired output, data cells were interpolated using the GMT program `grdfilter`. The grids were overlaid in the following order from top layer to bottom layer: EM 300 -> Hydrosweep -> historical data. Detailed scripting methods for this process are presented in Becker (2005).

2.2. Sidescan Sonar Details

The DSL-120 sidescan sonar, operated by the Woods Hole Oceanographic Institute (WHOI), is a towed sidescan sonar instrument capable of operating in depths up to 5700 m. The towed instrument contains two sidescan sonars for a total of 4 transducers operating at 120 kHz. The beam swath angle is 50 degrees with a swath width of 1.7 degrees. The sound level is 218 dB with variable levels of sound pulse duration and receiver amplitude gain. The DSL-120 also contains a 2-axis clinometer, gyro compass, and pressure depth sensor accurate to <1 m. These sensors are used to correct for random motion of the towed instrument relative to the seafloor.

The raw backscatter signal received from the DSL-120 was recorded directly to a chart paper recorder and to an Exabyte tape recorder along with sensor data and sonar system parameters. The backscatter data were corrected for

bottom track and amplitude gain using UNIX software developed by Hawaii Mapping Research Group (HMRG). The same software package was used by Akel Sterling (HMRG) to mosaic the backscatter, producing 1 m and 0.5 m resolution, georeferenced raster images. The raster images were combined with the bathymetry using a GMT script by Becker (2005) that adjusted the backscatter contrast and illuminated color-contoured multibeam bathymetry with the backscatter image.

3. Sampling Procedures

3.1. Shipboard Coring Methods

Sediment sampling equipment, provided by C. Moser, Oregon State University, centered around a piston and gravity coring apparatus capable of up to 2,700 kg total weight for maximum penetration. The weight was adjusted by placing steel plates of various thicknesses onto the core body. Sections of steel core barrels 3.05 m in length were attached to the core body, and 10.1 cm diameter PVC core liner with a core catcher and stainless-steel beveled tip were inserted into the core barrel. Due to the resistivity to penetration of the serpentine muds, minimal (\approx m) recovery was obtained using the gravity core, so the piston

coring apparatus was adopted for the majority of the cruise.

The piston corer operated by means of a plunger attached to a steel cable and inserted into the PVC core liner. The cable was then attached to a trigger core similar in design to the gravity corer but with a smaller weight. The trigger core was lowered below the main piston core so that it contacted the seafloor first, causing the piston core to be released and free-fall. The length of the trigger cable was carefully measured, so the plunger would be pulled into the core tube when the piston core reached the seafloor drawing the sediment into the core liner. Two sections of steel pipe lined with a section of PVC pipe were used on the main piston core sampler, and the maximum amount of weights were placed on the core body. The trigger core sample was collected as well to verify the depth of the sampled sediment horizons.

Once the core was triggered, the coordinates of the ship and the transponder on the core were recorded prior to pull-out. In cases when a long baseline (LBL) transponder net was deployed in the sample region, it was possible to navigate the descending coring apparatus to within a few meters of a target. A transponder was attached to the

cable above the corer, and the descent of the corer paused shortly before reaching the seafloor. This allowed the wire to straighten and the ship to be maneuvered above the desired target. Once in position, the corer was lowered at 50-60 m/min until penetrating the seafloor.

An additional method of gravity coring implemented on this expedition was the break-away core (BAC). For this method, a circular plate was attached to the upper end of the core barrel to prevent over-penetration into the seafloor. The core barrel was attached in a way that would allow it to release from the weight upon penetrating the seafloor leaving only the PVC liner attached to the weight. This enabled a core sample to be recovered while simultaneously emplacing a small well on the seafloor intended to channel upwelling fluid for future collection by ROV or submersible. BAC were equipped with a marker that consisted of a 3 lb dive weight, poly pro line, and a white plastic 5-gallon bucket lid with a cut-out number in the center.

Upon recovery of the cores, the PVC liner was withdrawn from the barrel in 2m sections and cut off with a hacksaw. The liner sections were longitudinally bisected with a circular saw and transported to the ship science

laboratory for examination and sub-sampling. Once in the laboratory, the sediment was bisected with monofilament fishing line and laid out in two halves on the laboratory bench. Notes were taken on the color and consistency of the sampled sediment and measurements were made of the depths of the various sediment horizons. Discrete sub-sampling intervals were marked on the core and recorded as depths below the top of the core sample. The exposed surfaces of the core-halves were scraped away and discarded to avoid sample smearing between depth intervals. The remaining sediment was scooped into acid-washed polycarbonate centrifuge tubes using Teflon-coated stainless steel spatulas. Sediment within 0.5 cm of the PVC liner was discarded to avoid sample smearing and contamination from the core wall.

Sediment-filled centrifuge tubes were immediately placed in a standard freezer for 25 minutes, which is enough time for the sediment sample to cool to 2 - 4°C. Once removed from the freezer the centrifuge tubes were placed in a rotor that was in the freezer for more than an hour and cooled to -20°C. Cooling the rotor counters the warming effects during centrifugation. The rotor was then placed in the centrifuge and spun for 5 minutes at >10,000 rpm. Pore

fluid was siphoned off the top of the sediment using acid-washed high-density polyethylene (HDPE) syringes with 3 cm of acid-washed flexible Tygon tubing attached to the intake. The tubing was removed from the syringe once the pore fluid was collected, and a 0.45 micron filter was attached in its place. Pore fluid was then filtered into acid-leached HDPE sample collection vials and glass ampules. The glass ampules were sealed with a propane torch for later O and H isotopic analysis. The volume of pore fluid recovered varied based on the sediment porosity. The residual sediments were archived for future petrographic and mineralogic analysis.

3.2. ROV Surveys

The ROV Jason2/Medea, operated by WHOI, was employed for the 2003 Mariana Forearc expedition. Capable of operating at depths up to 6500 m, the ROV Jason2/Medea is equipped with 2 manipulator arms, a gyro compass, crossbow accelerometer attitude sensor, 120 kHz acoustic altimeter, pressure sensor, six video cameras, and one electronic still camera. A long baseline (LBL) transponder net was deployed in the survey region prior to ROV deployment enabling vehicle navigation with <1 m accuracy. The payload capacity for sample collection was 130 kg with one

large forward sample drawer and two smaller swing-out side drawers.

A rack containing eight push cores was mounted in the forward sample drawer. The push cores were constructed from 7 cm ID polycarbonate tubing that were acid-leached and sealed in plastic bags prior to the cruise. Three lengths of push cores, 30, 60 and 90 cm, were made, and each core was beveled on one end for penetrating the seafloor. T-handles attached to the tops of the push cores by means of a plastic stopper with a rubber flapper-valve and a hose clamp. Beveled rubber stoppers inside 10 cm ID PVC sleeves were mounted to the sample rack with bolts, and the base of the push cores were firmly seated around the stoppers. The manipulator arm on the ROV would insert the cores into the sediment and immediately replaced the sample-filled cores on the rubber stoppers.

Upon resurfacing, the PVC sleeves were immediately transported to a walk-in freezer maintained at a temperature of 4°C. The freezer contained a device designed to extrude the sediment in an anoxic atmosphere and is fully described in Appendix A. A plastic glove bag was flushed with nitrogen gas 3 times and then a 10 cm slit was made at the bottom center. The push core inserted into the

slit and was taped in place to seal the glove bag, which was inflated with nitrogen gas. The push core then mounted to a concave block by means of hose clamps attached to the block's sides. A rod with a PVC plunger screwed on the tip was inserted into the bottom of the core and sealed with a silicon rubber o-ring. The plunger rod inserted vertically into a plastic block that screwed onto a gear-driven chain. A 110 volt AC gear motor was controlled by a foot pedal and could accurately position the plunger at 2 mm increments. The foot pedal control allowed the sampler's hands to remain in the glove bag while extruding the core.

The core was inspected through the clear tubing and a drawing was made with a description of the color and grain texture (see Appendix B). Push cores were then sectioned into approximately 3 cm vertical intervals, depending on the fluid content and the presence of rocks or precipitates. A note-taker recorded the sample intervals and noted any rocks that were found or the presence of hydrogen sulfide odors as the core was being processed. Sections of each core were sampled only from the center of the core, and the top of each section was scraped away to avoid contamination from the sectioning plate. Sediment samples were placed in acid-washed polycarbonate centrifuge

tubes and capped within the nitrogen-filled glove bag. The centrifuge tubes were centrifuged and processed in the same method as the gravity core samples.

4. Chemical Analysis

4.1. Shipboard Chemical Analysis

After pore fluid separation from the sediment, aliquots of the fluid were taken for preliminary analysis. Chlorinity was measured by titration with silver nitrate (Knudsen et al., 1902) conducted by automated electrochemical titration and calibrated with International Association for the Physical Sciences of the Oceans (IAPSO) standard seawater. This method sums the values of chlorine, bromine, and fluorine and can be affected by the presence of sulfides. In order to minimize sulfide artifacts, the 100 μ L aliquots were evaporated overnight and then re-dissolved in NaNO₃ solution. pH was measured on 2 ml aliquots by a calibrated pH electrode and the samples were then titrated with 0.1 N hydrochloric acid to measure the alkalinity by the Gran function method (Stumm and Morgan, 1981). Hydrogen sulfide concentrations were measured by the photolorimetric method developed by Cline (1969). These measurements were used as a guide for

choosing which samples to analyze in detail. After preliminary analysis, subsamples were acidified by addition of subboiled, concentrated (6N) HCl Optima from Fisher Scientific to a concentration of 4 ml HCl Optima per 1 L sample to prevent the formation of oxides that could precipitate with trace elements. Some samples with pH values greater than 11 required additional amounts of acidification to lower the pH below 2.

4.2. ICP-AES Analysis

The major elements Ca, Mg, Na, K, S, Sr, and Li were measured in 0.1 ml aliquots of the filtered pore fluids. A solution of 50 $\mu\text{g/L}$ Yttrium for internal standardization was prepared in 1% subboiled, concentrated (14.7N) nitric acid Optima from Fisher Scientific diluted in 18.2 M Ω MQ water. The 0.1 ml aliquots were then diluted in 10 ml of the Y solution. Standards were prepared from differing aliquots of IAPSO seawater in a method identical to the samples. For high levels of K, 1 g/L Claritas PPT[®] standards from Spex CertiPrep were added to the dilution solution in amounts paralleling the IAPSO volumes. The minor elements Sr, Li, Ba, B, Mn, Fe, and Si were measured in 0.35 ml aliquots of the filtered pore fluids. The aliquots were diluted in 3.625 ml of the Y solution used for major

element dilutant. Standards were prepared for each element by adding 0.175 ml of 1 g/L Claritas PPT[®] standards from Spex CertiPrep to 0.35 ml filtered deep sea water in 3.625 ml of dilutant to minimize salt matrix effects. The prepared samples and standards were analyzed with an inductively coupled plasma atomic emission spectrometer (ICP-AES) by Soil Control Lab, Watsonville, CA.

4.3. Dilution HR-ICP-MS Analysis

Fluid samples were selected for high-resolution inductively coupled plasma mass spectrometry (HR-ICP-MS) analysis based on significant variations from sea water concentrations of pH, alkalinity, chlorinity, and hydrogen sulfide. In addition, elements analyzed on the ICP-AES were used to verify these variations and indicated upwelling fluid activity. If no upwelling signature was apparent in any cores from a location, at least one representative core series was selected from that location for quantification. All dilutions were carried out in 10 ml/L subboiled, concentrated (14.7N) nitric acid Optima from Fisher Scientific diluted in 18.2 M Ω MQ water (1% QHNO₃). The details of settings and configurations for the HR-ICP-MS analyses are presented in Appendix C.

A standard stock solution was made by combining aliquots of Claritas PPT[®] standards for the elements of interest so that the concentration of elements in the primary standard simulated concentrations of ~500 times bottom seawater values given in the Geochemical Earth Reference Model database (<http://earthref.org/GERM/>). The standard stock was diluted in 10% and 1% North Pacific bottom seawater as well as 1% QHNO₃ to a concentration resembling ~5 times (500%) GERM seawater values. These three solutions were subsequently diluted to concentrations ranging from 0.5% to 300% GERM seawater levels while maintaining the desired matrix. The 10% seawater produced significant matrix suppression of the signal, especially at elevated concentrations regardless of the presence of an internal standard (Figure 11). The 1% seawater dilution matrix exhibited minimal differences from the salt-free matrix even at levels representing 300% GERM seawater.

Due to the signal suppression effects of high salt contents, analysis by HR-ICP-MS was conducted on 40 µL aliquots of seawater in 3.96 ml of 1% QHNO₃. A set of samples from the Mariana Forearc with varying major element

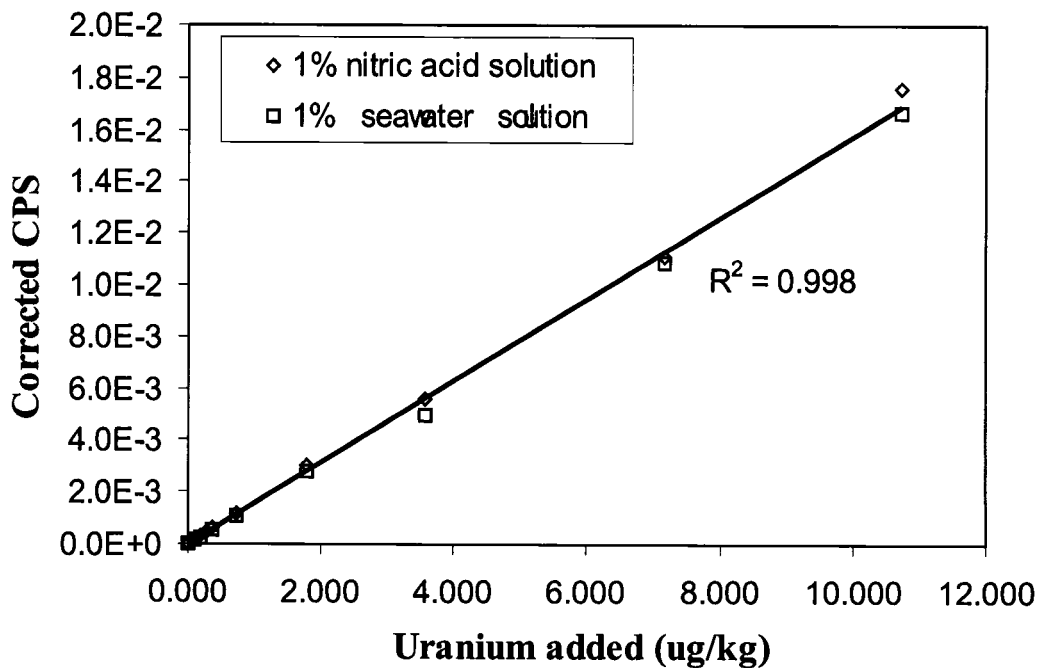
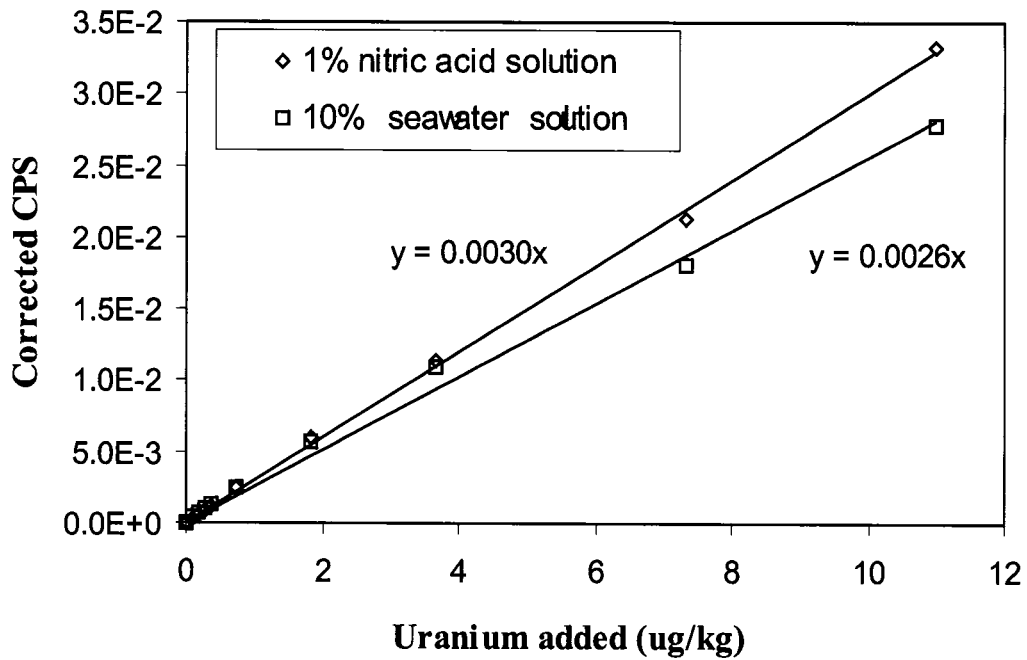


Figure 11. Results of HR-ICP-MS dilution analysis of varying U content and dilution factor. Salt contents at 10% seawater create a non-linear response for high values of U. At 1% seawater levels, the response of U is nearly identical to a salt-free matrix. Corrected CPS have been normalized by the internal standard Erbium. Normalized seawater CPS were subtracted from the 1% and 10% series.

compositions were spiked with the elements of interest at levels of 200% GERM seawater for recovery analysis to determine possible matrix interferences. Standards were prepared by addition of varying levels of the stock standard solution proportional to GERM seawater values between 2.5% and 200%. All the diluted samples along with 4 ml QHNO₃ blanks were then spiked with 0.1 ml of 25 µg/L Erbium prepared from 10 mg/L Claritas PPT[®] standard and 18.2 MΩ MQ water.

Selected samples from each site were analyzed for V, Cr, Ni, Zn, Rb, Y, Mo, Cd, Cs, Ba, and U by HR-ICP-MS. A Finnigan Element 2 HR-ICP-MS, located at Moss Landing Marine Laboratories (MLML), Moss Landing, CA, was used for all the analyses. The samples were introduced into the HR-ICP-MS through a CETAC Aridus desolvating nebulizer system fitted with a 100 µL/min nebulizer to minimize the amount of interfering oxides and hydrides within the plasma interface. Normalization of the data over varying plasma conditions was achieved by dividing the average counts per second (CPS) by the CPS of the internal standard Er. Blank correction was done by subtracting the normalized blank from the normalized sample results. This reduced the y-intercept of the standard curve to zero allowing

calibration of the normalized results by simple multiplication by the slope of the quantity of standard added over the normalized CPS.

It was not possible to resolve standard curves for the transition metals V, Cr, Ni, Zn, Y and Cd due to low CPS at the 1% dilution level relative to the blank. However, modification of the HR-ICP-MS method may enable resolving some of these elements at 1% dilution levels. Recovery analysis for Mo, Cs, Ba, and U were all within 95% over varying matrix conditions and near 99% in bottom seawater (Table 1). Accuracy of the results was determined by analysis of 2 sets of previously analyzed samples: Mo and U measured in Baby Bare hydrothermal spring water (Wheat et al., 2002); Rb, Cs and Ba measured in pore fluids from ODP site 1200F (ODP Leg 195 Shipboard Scientific Party, 2002; Mottl et al., 2004). The average percent error between the two method analyses for each set of samples ranged between 0.7% for Rb and 8.2% for Mo (Table 1). Precision was calculated as the normalized percent standard deviation of six repeated analyses of Pacific deep water subsamples inserted into the analysis sequence throughout a sample run. Barium had the best precision (1.2%) while Uranium was the least precise (2.4%). Detection limits, defined as

	Rb	Mo	Cs	Ba	U
bottom seawater (nmol/kg)	1370	120	2.2	140	13.5
% recovery in 1% seawater	99.9	98.9	100.1	99.7	99.5
% accuracy	0.7	8.1	5.0	5.5	6.7
% precision	1.9	1.5	2.2	1.2	2.4
detection limit (nmol/kg)	2.9	1.5	0.02	1.8	0.02

Table 1. Statistical results of the 1% dilution HR-ICP-MS method. Accuracy is the percent difference of measured values at Moss Landing over values measured at: Oregon State University for Mo and U (Wheat et al., 2002); University of Hawaii for Rb and Cs (Mottl et al., 2004); and ICP-OES aboard the JOIDES Resolution for Ba (ODP Leg 195 Shipboard Scientific Party, 2002). Precision determined from repeated analysis of subsamples of bottom seawater. Detection limits are defined as 3 times the standard deviation of a 1% Q-HNO₃ blank.

	V	Cr	Co	Ni	Cu	Zn
NASS-4 SRM (nmol/kg)		2.212	0.153	3.885	3.588	1.759
bottom seawater (nmol/kg)	38.4		0.03	13	5.6	10
% accuracy	4.4	1.5	28	58	14	39
% precision	2.6	8.0	28	106	24	59
detection limit (nmol/kg)	0.16	0.26	0.05	9.2	1.5	2.1

Table 2. Statistical results of the 10% standard addition HR-ICP-MS method. Accuracy was determined for V by the percent difference of measured values in bottom water with values measured at Oregon State University (Wheat et al., 2002). Accuracy for the remaining transition metals was determined by analysis of NASS-4 certified reference material (National Research Council of Canada). Precision is the normalized percent standard deviation of repeated measurements of NASS-4. The detection limit is 3 times the standard deviation of a 10% metal-free seawater matrix blank produced by 8-hydroxyquinoline extraction.

3 times the standard deviation of the blank, were determined on 22 blanks and converted to nmol/kg by the same standard calibration as the samples.

4.4. Standard Addition HR-ICP-MS Analysis

Standard addition was performed on 10% dilutions of samples in 1% Q-HNO₃ to increase the detected CPS for the transition metals V, Cr, Co, Ni, Cu, Zn and Y. Standards were prepared from Claritas PPT[®] standards in 1% Q-HNO₃ in amounts proportional to naturally occurring abundances. The stock standard solution had the following concentrations of elements in $\mu\text{mol/L}$ solution: V (100), Cr (12.5), Co (1), Ni (60), Cu (15), Zn (50), and Y (1). This stock solution was diluted to 20% and 50% in 1% Q-HNO₃ for the standard additions. Each sample was added by 200 μL aliquots to four vials containing 1.5 ml Q-HNO₃. The three standard solutions were added to 3 of the vials in 200 μL aliquots, and to the fourth vial, 200 μL of Q-HNO₃ was added. A metal-free seawater solution was produced by collecting 8 ml of bottom seawater extracted through the 8-hydroxyquinoline (8-HQ) column, as described in Appendix D. This solution was diluted in the same manner as the samples with the exception that only Q-HNO₃ was added, not the standards.

Rhodium was added to all of the dilutions as an internal standard (100 uL of 50 mg/L).

Introduction of the 10% standard additions was done through a 100 μ L/min nebulizer into a Teflon PFA spray chamber. This was done due to avoid possible carrier effects within the Aridus desolvating nebulizer from the higher salt content of the samples. A series of 10% dilutions of the metal-free seawater blank were introduced into the HR-ICP-MS for 1 hour prior to the start of the series due to observations in early experiments of rapidly decreasing sensitivity as the sample inlet cones on the HR-ICP-MS become laden with salts. A steady state was observed after 1 hour, with little appreciable signal loss over the remaining sample series even for a 10-hour series. The dilutions were analyzed and the average CPS data was normalized by dividing by the Rh average CPS. The normalized blank results were subtracted from all the sample and standard addition results. The blank-corrected, normalized values were plotted against the amount of standard added to the dilution for calibration. Quantification of the results was calculated as the negative y-intercept for the equation of a line with the

corrected CPS on the x axis and the standard concentration on the y axis.

Accuracy of the standard addition analysis was determined by comparing the measured values of bottom seawater (Wheat et al., 2002) for V, and NASS-4 (National Research Council of Canada) standard reference material (SRM) for the remaining metals (Table 2). The accuracy of Cr was the best (1.5% at 2.2 ng/kg) while the poorest was Ni (58% at 3.9 ng/kg). Precision was determined by the normalized percentage standard deviation of the results of 8 repeated standard addition analyses of bottom seawater (V) and NASS-4 (Cr, Co, Ni, Cu, and Zn). Precision was better than accuracy for V and Cr, but considerably worse for Ni, Cu, and Zn. The detection limits were determined from 3 times the standard deviation of the metal-free bottom water blank calibrated to nmol/kg by multiplication by the slope of the bottom seawater standard addition curve. Co detection limits were the lowest at 0.05 nmol/kg while Ni detection limits of 9.2 nmol/kg exceeded the concentration of NASS-4 (3.9 nmol/kg).

The inability to accurately analyze low levels of Ni by this method were brought about by high blanks produced from the nickel composition of the sample inlet cones.

This problem may be corrected by use of aluminum or platinum sample cones, but this was not tried in these experiments. As mentioned before, attempts were made to analyze Y by this method, but it became apparent that while the results were very accurate for a constant seawater matrix, variable levels of Sr in the Mariana pore fluids influenced the Y results by irresolvable interferences with Sr hydrides. Interferences could be minimized by modification of the method to lower (2-5%) dilution levels enabling the use of the desolvating system. More dilute samples may also result in much lower blank levels and lower the detection limit to a greater degree than the amount of signal loss from lower concentrations in the analyte.

4.5. Extraction HR-ICP-MS Analysis

Because of their minimal concentrations and susceptibility to interferences from the salt matrix contained in seawater, it was necessary to extract the rare earth elements (REEs) and the transition metals Y and Cd from the seawater matrix. The extraction procedure centered around the 8-Hydroxyquinoline (8-HQ) functional group immobilized onto TSK Fractogel, using a method first developed by Landing et al. (1986) and further refined by

Dierssen et al. (2001). The 8-HQ functional group preferably binds to transition metals, REEs, and heavy-metal cations over alkali, alkaline-earth cations, and especially anions (Landing et al., 1986), thus allowing the removal of the salt matrix from the sample solution. The specific resin used for this study is referred to as Resin D in Dierssen et al. (2001) and uses the commercially available TSK Fractogel AF-Epoxy-600M to bind directly to the 8-HQ ligand. The immobilized 8-HQ was subsequently added to a column of Teflon wool contained within a 5 cm section of 2 mm ID silicon peristaltic pump tubing.

The extraction apparatus is illustrated in Appendix D and was constructed inside a class-100 laminar flow clean bench at MLML. Initial construction of the apparatus was guided by a system developed for in-line preconcentration of iron for spectrophotometric analysis (Measures et al., 1995); but extensive modification was required to control both the volumes of sample taken up and eluate collected for later analysis. The apparatus consisted of two VICI Valco 4-port, 2-position, Cheminert injection valves and one VICI Valco 8-port, 2-position, Cheminert valve each controlled by a microelectric actuator. Switching of the valves was controlled by computer via a serial connection

daisy-chained to the 3 valves. A software program to automate the switching of the valves was written in the Microsoft Visual Basic programming language for operation on a Windows platform. This enabled the creation of a simple, user-friendly graphical user interface (GUI) that could dynamically adjust the parameters controlling sample uptake volumes, column rinse times, and elution volumes. A peristaltic pump placed outside the clean bench was used to push the samples and reagents into tubing ported through small holes on the wall of the clean bench and into the apparatus.

To maximize the binding ability of the 8-HQ column the samples were first buffered to a pH of 5.3 by in line addition of Optima glacial acetic acid and allowed to mix in a 0.5 m knit capillary tubing mixing coil. This pH value was selected after experiments by Sohrin et al. (1998) with 8-HQ under variable pH ranges showed the maximum amount of recovery for REEs and many transition metals occurs at a pH near 5.3. The buffer concentration was determined empirically by adding acetic acid and ammonium hydroxide to a volume of acidified seawater (4 ml Q-HCl/L) until the pH reached 5.3. A slightly more concentrated buffer solution than necessary was used to

ensure the complete buffering of samples. The final buffer solution was made by adding 84 ml ammonium hydroxide Optima (Fisher Scientific) and 45 ml acetic acid Optima (Fisher Scientific) to 121 ml 18.2 MΩ MQ water. This buffer was first pumped through an 8-HQ column to remove possible contaminants and then added inline to the sample at a ratio of 1 part buffer to 8.3 parts sample. After buffer addition, the solution was mixed in a 0.5 m knit capillary tubing mixing vector. The buffered sample was then loaded onto the 8-HQ sample column at 0.56 ml/min, allowing the undesired salts to pass through the column while collecting the REEs and transition metals. Once a 4 ml volume of sample was introduced, the column was rinsed with 3 ml of 10% buffer solution diluted in MQ water to remove any salts that may be remaining on the 8-HQ column.

After rinsing the column, air from inside the clean bench was pumped into the column to purge the rinse solution from the column and extract outflow tubing. The eluant used to extract the elements was made by adding 20 ml Q-HNO₃ to 230 ml MQ water producing a 1.12 N Q-HNO₃ solution. After the column and tubing were purged with air, 0.5 ml of eluant was introduced at a rate of 0.1 ml/min into the column. To enable internal standardization

of the extract during HR-ICP-MS analysis, 40 μL of 5 $\mu\text{g/L}$ Rhodium was added to acid-cleaned, 0.6 ml HDPE microcentrifuge vials prior to sample collection. The 0.5 ml eluates were collected by free-falling from a section of Teflon capillary tubing into the collection vials within the laminar flow hood.

Between each sample extraction, the column and outflow tubing were rinsed with 1.12 N Q- HNO_3 for 10 minutes while the remaining sections of the apparatus were rinsed with 0.3 N Q- HNO_3 . The column was then rinsed with the dilute buffer solution for 1 minute prior to the next sample extraction to restore the pH of the column to 5.3. The combined weight of the sample and vial was recorded before and after extraction to accurately quantify the amount of sample being analyzed. The sample weight was also monitored for fluctuations that could be adjusted by increasing or decreasing the rate of the peristaltic pump. This enabled the reaction times within the column to remain constant even under variable column compaction or expansion conditions while maintaining a constant volume of sample and extract. Periodically, the buffering effectiveness of the apparatus would be tested by collecting the normally

discarded salt solution that passes through the column and measuring its pH.

Standards of Y, Cd, and the REEs were made from Claritas PPT[®] standards of varying concentrations. Individual standards of Cd, La, Nd, Gd, Dy, Er, and Yb were added to a multi-element standard containing all the REEs and Y at high concentrations. A 1 ml aliquot of this concentrated standard solution was added to 249 ml of filtered, acidified Pacific bottom seawater in order to maintain a salt matrix within the standard solution. Concentrations of these elements in the maximum standard are presented in table 3. The maximum standard solution was diluted to 1%, 10%, 25%, and 50% by addition of the same bottom seawater. All of the standards were extracted in the same manner as the samples before and after extracting a sample series. This was done to ensure consistency throughout the extractions and subsequent HR-ICP-MS analysis. Procedural blanks were produced by extracting 4 ml of MQ water into a vial containing an internal standard in the same method used for the samples and standards. Analysis of the eluates by HR-ICP-MS was conducted through the Aridus desolvating nebulizer as described for the 1% dilution method.

All of the statistics for this analysis are presented in table 3. Recovery analysis of the 8-HQ column was assessed by collecting 2.5 ml of eluate in 0.5 ml intervals after loading the column with 4 ml of the 100% standard solution. Each of these five subsamples were analyzed to ensure that the elements were being quantitatively collected in the first 0.5 ml of eluate. Recovery within the first 0.5 ml was generally better than 97% ranging between complete recovery of Ho and only 95% recovery of Ce. The low Ce recovery may be an artifact created by high background levels of Ce, which is used during the HR-ICP-MS initial calibration sequence. Accuracy of the method was determined by analyzing a Pacific bottom water sample that had been previously analyzed as Oregon State University (Wheat et al., 2002) by preconcentration of 10 ml by a Dionex ion chromatograph before elution into an ICP-MS. The accuracy can only be regarded as relative to this one method, which itself had accuracies of only 20% to 30% when compared to isotope dilution analyses conducted at the University of Cambridge. In order to quantify the true accuracy of this method, it will be necessary to obtain a certified reference material for the REEs.

	bottom seawater (pmol/kg)	recovery (%)	accuracy (%)	precision (%)	detection limit (pmol/kg)	Max Standard (pmol/L)
Y	327	99	3.9	4.0	1.8	22
Cd	1039	97	13	1.9	18	8896
La	43.8	99	20	5.5	1.3	377
Ce	4.66	95	30	21	1.6	14
Pr	5.25	98	37	4.2	0.19	14
Nd	24.0	99	14	7.4	0.51	363
Sm	4.00	97	42	2.0	0.16	13
Eu	1.22	98	19	5.8	0.053	13
Gd	7.42	98	15	4.6	0.19	77
Tb	1.03	99	40	4.8	0.022	13
Dy	9.16	99	24	1.6	0.15	74
Ho	2.43	100	19	5.4	0.028	12
Er	9.01	99	12	1.2	0.077	72
Tm	1.32	99	22	3.2	0.012	12
Yb	9.49	99	14	3.3	0.11	70
Lu	1.65	99	14	1.8	0.021	11

Table 3. Statistical results from the 8-Hydroxyquinoline (8-HQ) extraction of 4 mL samples and subsequent analysis by HR-ICP-MS. Accuracy was determined by analysis of a Pacific bottom seawater sample that was previously analyzed at Oregon State University (Wheat et al., 2002) and comparing the percentage difference between the two methods. The values of bottom seawater presented are those measured in this study. Precision was determined from repeated analysis of subsamples of the same bottom seawater and given as the percent normalized standard deviation of the pmol/kg results. Detection limits were established as 3 times the standard deviation of the procedural blank. The procedural blank was produced by extracting 4 mL of 18.2M Ω milli-Q water through the 8-HQ apparatus by the same method as the samples.

Precision, as determined by 7 repeated analyses of Pacific bottom seawater, was considerably better than accuracy, and should better reflect the abilities of this method. One exception to this was Y with an accuracy of 3.9% but a precision of only 4.0%. This is likely attributed to better accuracy of the values published in Wheat et al. (2002) resulting from the higher levels of Y relative to the REEs. The detection limits were determined as 3 times the standard deviations of 8 procedural blanks and were calibrated by the standard curve. Thulium is the rarest of naturally occurring REEs and detection limits were proportionally the lowest at 0.012 pmol/kg. Cadmium detection limits, although higher than most (18 pmol/kg), still were very low when compared to its natural levels in seawater (1039 pmol/kg). Cerium detection limits (1.6 pmol/kg) were the highest relative to its natural abundance in bottom seawater (4.7 pmol/kg).

III. Results

1. Geophysical data

Multibeam surveys conducted at 7 seamounts and a small group of emergent diapirs illuminated many previously unrecognized features of the Mariana Forearc. Use of the 30kHz EM300 multibeam allowed gridding of bathymetry data at a resolution of 15 m as opposed to previous data sets of a maximum resolution of 50 m (e.g. Fryer et al., 2000). Smaller areas were surveyed with the towed 120 kHz sidescan sonar, DSL-120, at the summits of 5 seamounts. The combination of these data sets allowed pinpointing potentially active fluid vents for subsequent sampling via ROV and coring. A complete set of maps produced from these surveys are presented in Appendix E.

Conical Seamount, the northernmost of those surveyed, sits within a stepping series of grabens (Figure 12). The eastern base of Conical Seamount terminates at the upper footwall of a deep (-5750 m) trapezoidal graben, while the entire seamount rests atop a larger down-dropped block 60 km in length. With a diameter of 20 km, the seamount forms a nearly symmetrical cone starting at -4500 m elevation and continuing up to -3050 m at the summit. The eastern flank

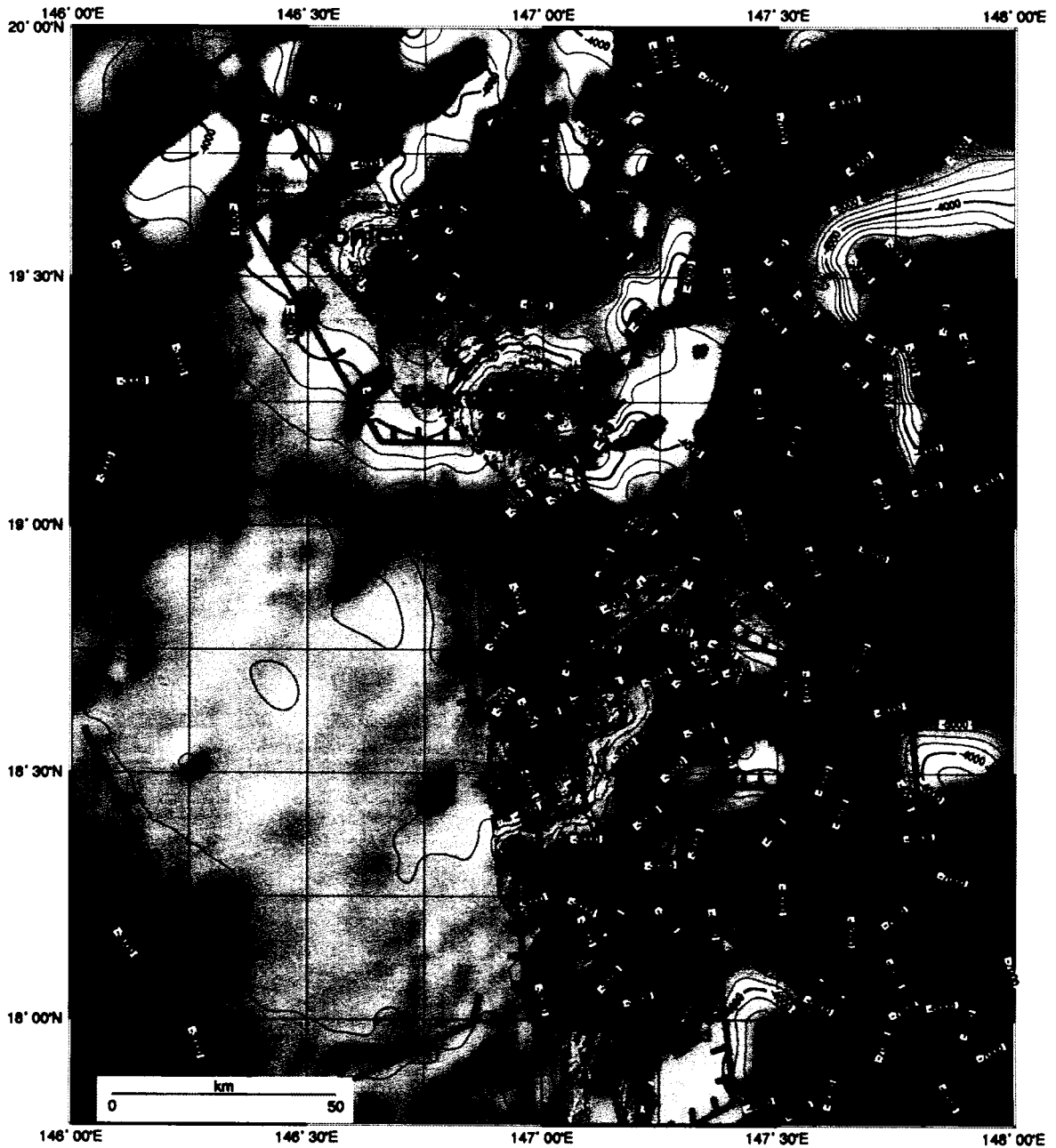


Figure 12. Sunshaded bathymetry of the northern serpentine seamounts in the Mariana Forearc combining Em300 and Hydrosweep surveys with Geoware 1 minute data. Surveyed mud volcanoes are labeled. Fault-related structures are outlined with tic marks pointing toward the downslope direction. The Mariana Trench axis is delineated by a solid line. Contours every 250 m.

has a nearly constant slope of 10 degrees from horizontal from the summit to the base, while the remaining flanks show a marked decrease in slope at less than -4000 m. Numerous channels are visible spiraling outward from the summit in a primarily counter-clockwise direction. They extend to depths of at least -4000 m where the resolution of the 300 kHz sonar diminishes. The flattened and irregular summit of the seamount where the ridges converge has a diameter of 3.2 km and roughly follows the -3200 m contour.

Pacman Seamount (Figure 12), so named for its C-shaped outline (Fryer et al., 1995), is located 45 km to the south of Conical seamount with half of the seamount resting on the same large tectonic block as its northern neighbor, and the other half atop the adjoining horst block (Fryer et al., 2000). The complex seamount has a maximum diameter of 35 km and contains a small 2 km trapezoidal graben within the eastern half. The summit reaches an elevation of -2750 m along the western ridge, and the northern and eastern flanks descend to depths as great as -4500 m where they contact adjoining grabens. A series of pressure ridges radiate from the eastern flank of the summit ridge and cascade down into the small graben contained within the

seamount. The flanks of the summit ridge lie at an average angle of 9 degrees from horizontal, with higher angles of 16 degrees along the southern boundary of the internal graben. At the southeastern tip of Pacman Seamount lies a structure, referred to as Baseball Mitt (Fryer et al., 1999), which was mapped in detail with the 120 kHz sidescan sonar. The 0.5 m resolution reflectivity images, when overlaid on a bathymetric grid of the area, highlighted 2 distinct, circular features of high backscatter 200-300 m in diameter. The larger, more distinct of these features is the location of previous submersible and ROV dives (Fryer et al., 1995; Fryer et al., 1999) where brucite precipitates were found protruding from the sea floor and is named Cerulean Springs (Fryer et al., 1999).

Quaker Seamount (Figure 12) is composed of a 20 km maximum diameter ovoid dome with a 24 km long wedge-shaped ridge extending to the northeast of the summit. The entire structure sits upon a regional horst block and is surrounded on three sides by grabens. The elevation of Quaker Seamount ranges from a minimum of -3450 m to a maximum of -2170 m from the western base to the summit of the ovoid mass. The average slope of the flanks of this feature is 9 degrees with distinctive flattening occurring

at the summit, which is the focus of outward-radiating pressure ridges. The southeastern flank, located above a deep graben, is truncated relative to the western flank. Steep angles of 16 degrees occur along the wedge-shaped northeastern ridge following the upper, horst-side boundary of another graben. A DSL-120 survey of the summit shows in greater detail the many smaller ridges radiating from a 1.5 km diameter dome at the summit abutting a 40 m high by 1 km long east-west oriented scarp.

A group of small 1-3 km in diameter circular domes were mapped within the NE-SW trending graben east of Quaker Seamount. The summit elevations of the 3 dome-like features ranged between -3000 m and -3600 m and their heights between 100 and 300 m. These tiny seamounts are barely perceptible and can be distinguished from the surrounding morphology only by anomalous contours along otherwise linear features. No detailed sidescan surveys were conducted on these features, so the nature of their geomorphology is as yet unknown.

Big Blue Seamount (Figure 12) possesses a similar overall structure to Quaker Seamount with a wedge-shaped ridge extending northeast of a central dome. The central dome of Big Blue is considerably larger; however, with a

maximum diameter of 50 km and a water depth range of -4000 m to -1240 m. The summit is relatively flat, but a mean slope of 9 degrees is maintained throughout most of the remaining edifice. Big Blue Seamount is similar to other seamounts in the Mariana Forearc in that it has radiating channels and steeper slopes along the eastern flanks. A sidescan sonar survey of the 2.5 km diameter by 200 m high dome at the summit revealed 3 additional domes at the apex of the seamount. These domes ranged in sizes of 150 m to 450 m in diameter and heights of 20 m to 40 m.

Celestial Seamount (Figure 13) closely resembles Conical Seamount with the exception of a crescent-shaped flattened summit. The maximum diameter of Celestial Seamount is 21 km and elevations on the seamount range between -4000 m and -1850 m. A large set of gullies and ridges radiate clockwise from the summit and extend to the base of the seamount along the southwestern flank. Additional smaller ridges can be seen radiating from the summit with a concentration to the northeast. Higher than average slopes of 12.5 degrees are maintained around most of the flanks of Celestial Seamount with the exception of the region south of the large set of gullies with a slope of 9 degrees. A DSL-120 sidescan survey of the summit showed a chaotic

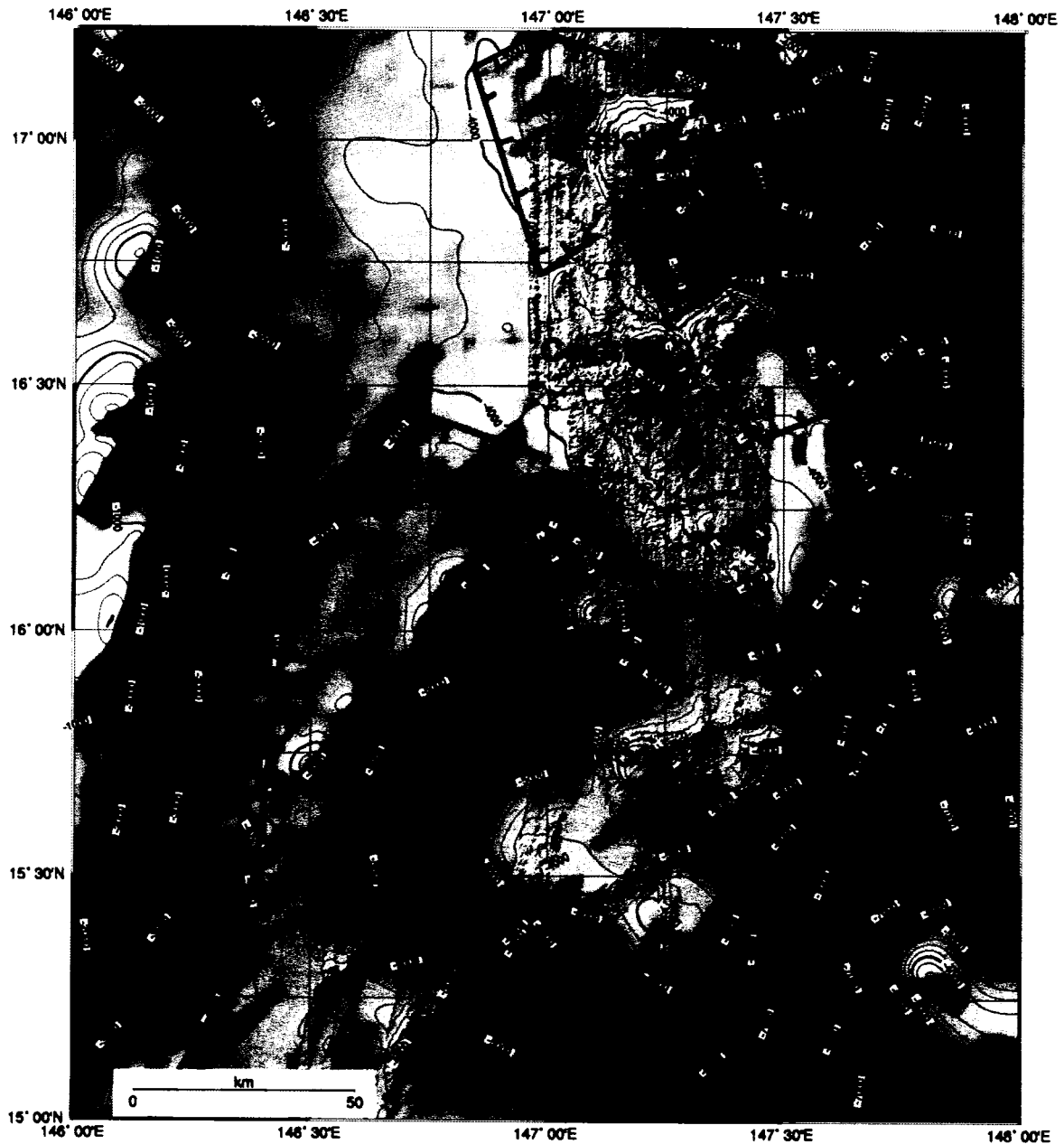


Figure 13. Sunshaded bathymetry of the central serpentine seamounts in the Mariana Forearc combining Em300 and Hydrosweep surveys with Geoware 1 minute data. Peacock and Turquoise seamounts were not surveyed in the 2003 expedition because no evidence for activity was found on previous surveys. Fault-related structures are outlined with tic marks pointing toward the downslope direction. The Mariana Trench axis is delineated by a solid line. Contours every 250 m.

terrain with small ridges roughly following the crescent shape of the low-backscatter flat top.

Blue Moon Seamount (Figure 13) lies in the deepest water depths of the seamounts in this survey despite its location on a horst block straddled by two grabens. Of interest is the dual-nature of the seamount composed of a smooth western half contrasting the hummocky eastern half with a blocky ridge extending to the northeast. Water depths up to 5000 m are at the maximum depth capabilities of the EM300 multibeam, which makes interpreting the data difficult, however faint channels can be seen radiating from the broad summit. The maximum diameter of Blue Moon Seamount approaches 25 km, and the elevation ranges from -5000 m at the base to -3600 m at the summit. The slopes of the flanks are highly asymmetrical varying from 5 degrees along the eastern flank to 20 degrees along the south. The summit forms a plateau along the western half with a series of depressions that approach a scarp oriented NE-SW at the apex of the seamount. This scarp forms a boundary between the smooth and hummocky halves of Blue Moon Seamount.

South Chamorro Seamount (Figure 14) is located at the southernmost end of the Mariana Forearc less than 40 km from the 3000 m contour of the Mariana Ridge. To the east

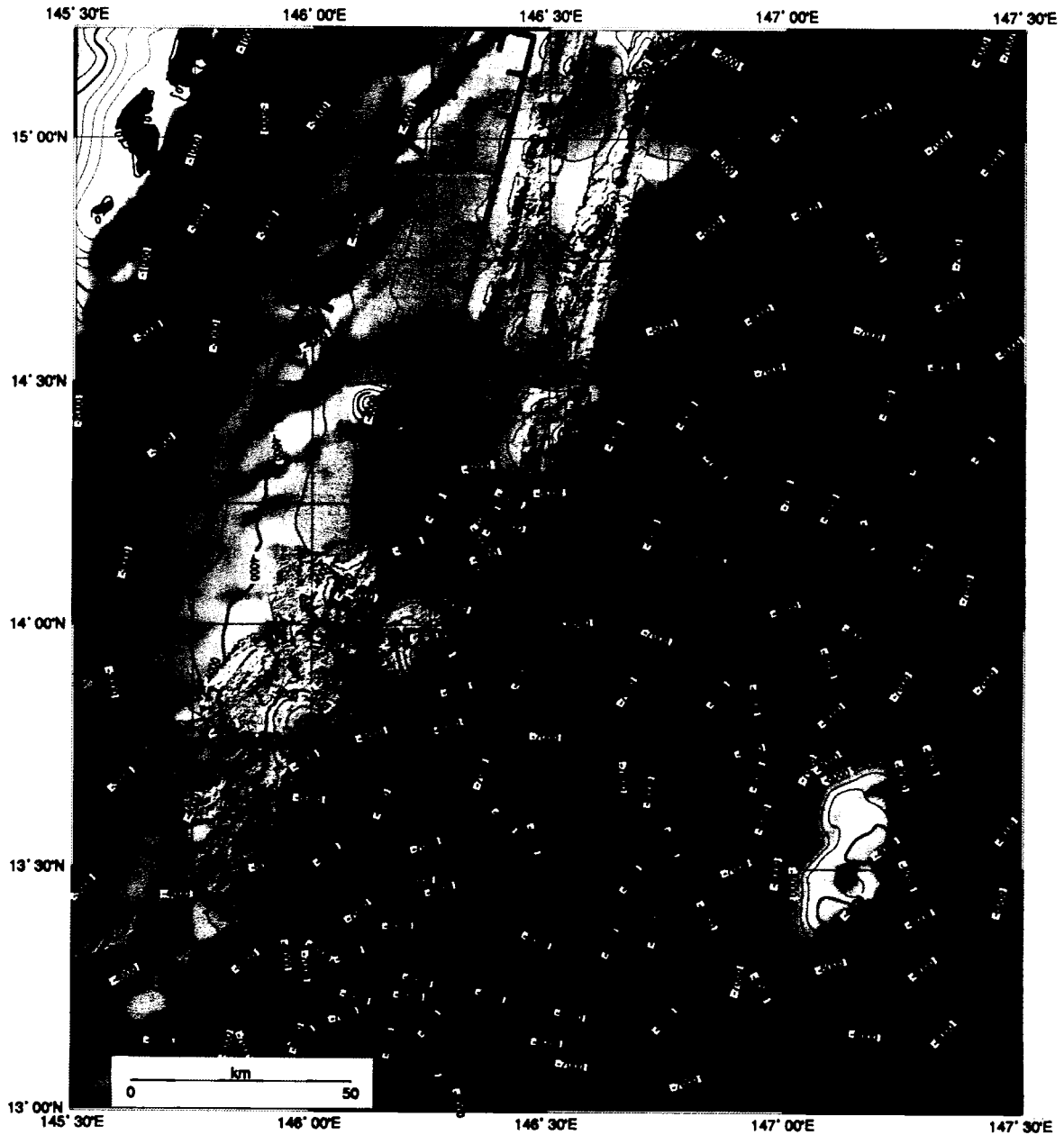


Figure 14. Sunshaded bathymetry of the southernmost serpentine seamounts in the Mariana Forearc combining Em300 and Hydrosweep surveys with Geoware 1 minute data. No evidence of recent activity was found at N. Chamorro Seamount on a previous survey (Fryer et al., 2000). Fault-related structures are outlined with tic marks pointing toward the downslope direction. The Mariana Trench axis is delineated by a solid line. Contours every 250 m.

of S. Chamorro, a 35 km long slope drops 4500 m into a graben located at -8000 m on the inner wall of the Mariana Trench. Flow lines are visible cascading down this slope and are likely the cause of the asymmetrical shape of S. Chamorro Seamount. The western flanks lie at an average angle of 7 degrees, compared to the eastern flank with slopes as great as 20 degrees and an average of 15 degrees along the trench slope break in this area. Similar to many other seamounts in the Mariana forearc are the pressure ridges emanating from the seamount summit. The size of S. Chamorro Seamount is also similar to many of the Mariana seamounts with a diameter of 20 to 25 km and elevations of -4500 m at the base and -2910 m at the apex. A detailed DSL-120 sidescan sonar survey of the circular peak at the southeastern summit of S. Chamorro displayed the extent of numerous smaller pressure ridges surrounding the summit.

2. ROV Exploration

The ROV Jason2/Medea was used to survey a total of 7 of the Mariana Forearc Serpentine seamounts during 12 dives. Objectives for these dives were to; explore previously unexplored seamounts, return to the location of 2 Ocean Drilling Program sites, and sample the serpentine

sediments wherever there was evidence of fluid egress such as chimney structures or fissures. These surveys were conducted following the swath-mapping surveys in order to navigate along the seamounts and illuminate scarps, high backscatter features or dome structures that could be associated with fluid flow. Any such features observed in the sidescan and multibeam surveys were designated as primary dive objectives prior to launch.

A dive on Conical Seamount (J32) located various features of interest including chimneys and the site of ODP Leg 126 drilling activity. A large chimney greater than 3 m in height and approximately 40 cm in diameter was located 1 km south of the summit (Figure 9c). The chimney consisted of a central circular trunk with an upward-reaching branch near the top 1 m. Other chimneys were either much smaller or lying prone on the sea floor. On approaching the summit, numerous serpentine boulders appeared with an increasing occurrence towards the apex of the seamount. A series of stair-stepping scarps oriented NE-SW and 5 m in height were found extending north of the summit, but no evidence of fluid flow was found in this area.

The dive on Pacman Seamount (J31) explored the circular high-backscatter features on the Baseball Mitt. Small chimneys of brucite, averaging 20 cm in length, were sampled at Cerulean Springs (Figure 9a). Much of the sea floor at this site was hardened from the extensive amount of precipitation as exotic fluids mixed with seawater. At the other high backscatter site on Baseball Mitt no chimneys were observed, but a white precipitate was found and sampled within a fissure. Evidence of fluid egress appeared to concentrate along the perimeter of the high backscatter areas.

Two dives (J34 and J36) were conducted to explore the domes mapped at the summit of Big Blue Seamount. The first dive surveyed the 2 km extent of the larger summit dome searching for fluid activity and observing structures across the dome. The topography of the summit was highly irregular with the common occurrence of scarps and gullies. Within the gullies, small serpentine clasts and pebbles were observed to accumulate. Along the slope of the summit, 1-5 m rectilinear slabs of sedimentary serpentine were separated by small ~1 cm cracks. Nearby a series of ripples in the serpentine sediment ran parallel to the contour of the slope indicating a front of the mudflow.

Serpentine boulders up to 20 m high also were distributed around the summit. The second dive targeted the largest of the 3 domes at the apex of the seamount for sampling. While conducting a 300 m transect of 8 push cores across this feature, a fissure of fresh serpentine mud completely devoid of pelagic sediment cover was found at the center.

Two dives on Quaker Seamount (J33 and J37) discovered a unique formation of carbonate chimneys with a structure not previously seen in the Mariana Forearc (Figure 9b). These were found at the base of the scarp running along the summit in a cluster around 20 m in diameter. The groups of chimneys consisted of many small appendages that appeared to grow at a slow rate to a structurally unsound height of ~1 m. Numerous fallen appendages created a central mound upon which additional appendages would grow. The substrate surrounding the chimneys was a mixture of a precipitate pavement and serpentine mud. Farther from the chimneys the substrate consisted of a thin pelagic layer draping serpentine silt and mud. A transect along the summit scarp located isolated chimneys similar to the type found within the mounds as well as a medium-sized chimney similar to the type found on Conical Seamount.

A single dive on Celestial Seamount (J38) traversed the well-sedimented summit in search of fluid activity.

Despite the ubiquitous presence of scarps, no signs of recent activity were found after extensive exploration.

A dive on Blue Moon Seamount (J40) focused on the western, smooth half of the summit, approaching from the south. South of the Summit scarp, in a depression between two parallel ridges, fresh serpentine sediment was found and sampled. Upon transiting over the summit ridge and down the scarp another local depression was observed. Within this depression, patches of small (~1 cm), spherical globules of flocculated detritus accumulated. There was, however little evidence of recent fluid activity in this area of the summit. Serpentine siltstone outcropped at the southwestern tip of the summit scarp.

Four dives took place on S. Chamorro Seamount (J27-29 and J41) with the first 3 centering on borehole CORK operations for ODP Site 1200. Flow meters were placed around the summit and a borehole CORK was removed on the first dives prior to the transit across the forearc. Upon returning one month later, the borehole was found to be venting cold fluids, and precipitates were growing along the rim of the open borehole (Figure 9e). Attempts were

made to sample the precipitates, but they were not found within the sample box upon ROV recovery. This, along with the occurrence of hydrocarbons (Mottl et al., 2003) suggests that the precipitates were gas hydrates. The fluids were sampled with a titanium water sampler on the ROV, and the borehole was subsequently re-sealed. Chemosynthetic muscle beds near the borehole that had been previously discovered (Figure 9d) were replaced by a scattering of empty shells. This may have resulted from drilling disturbances and the resulting re-direction of fluid flow into the borehole.

3. Pore Fluid Chemistry

Sediment coring throughout the Mariana Forearc in 2003 covered a total of 15 geologic features related to serpentine mud diapirism. Cores recovered in this survey totaled 13 gravity cores, 14 piston cores, 2 break-away cores, and 51 push cores (Figure 15). Vertical sections of these cores were taken and the extracted pore fluids totaled 474 discrete samples. In addition to sediment cores, water samples were taken by ROV within a venting borehole at S. Chamorro seamount. All of these samples were analyzed for the major constituents Ca, Mg, K, Na,

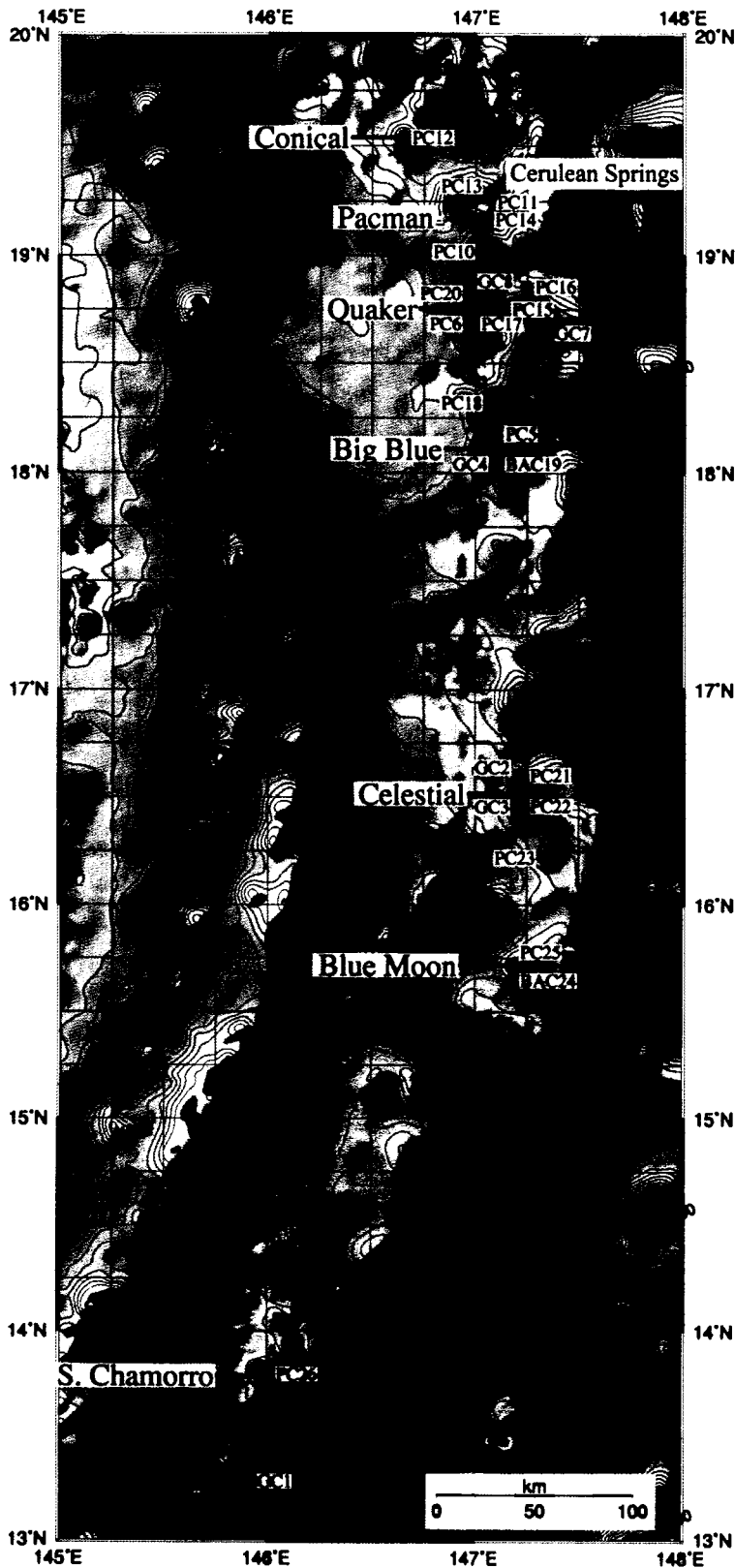


Figure 15.

Location of sampling that occurred during the 2003 Mariana Forearc expedition. Dots indicate where gravity (indicated by GC), piston (PC), and break-away (BAC) cores were taken. Black lines point to the locations of push cores taken by the ROV Jason 2. Background map data from combining EM-300, Hydrosweep, MR1, and ETOPO 1 datasets and gridding at 10 arc-second resolution. Contours every 250 meters.

sulfate, chlorinity, alkalinity, and pH. Profiles exhibiting chemical characteristics indicative of fluid flow were further analyzed for a host of minor and trace elements. A total of 42 chemical species were analyzed within the highest priority samples. The complete results of these analyses are presented in appendix F.

The major element chemistry exhibited clear variations from surface values to deeper within the sediment that showed the presence of upwelling fluids of differing compositions from one site to another (Figure 16). Throughout the forearc, Mg was found to be depleted in the source fluids, and asymptotically approached a zero value with the exception of Blue Moon Seamount which approached a minimum value of 5 mmol/kg relative to surface values of 52 mmol/kg. In contrast, levels of Ca in the pore fluids varied from 0 mmol/kg at Big Blue Seamount to 75 mmol/kg at Nip Seamount, which is over 7 times the average bottom seawater values. The pH of upwelling fluids increased at all active sites with the exception of Blue Moon Seamount which remained nearly constant. Maximum pH values of 12.3 were measured at Big Blue Seamount while pH at the remaining sites approached either 11 or 9. Sulfate and K

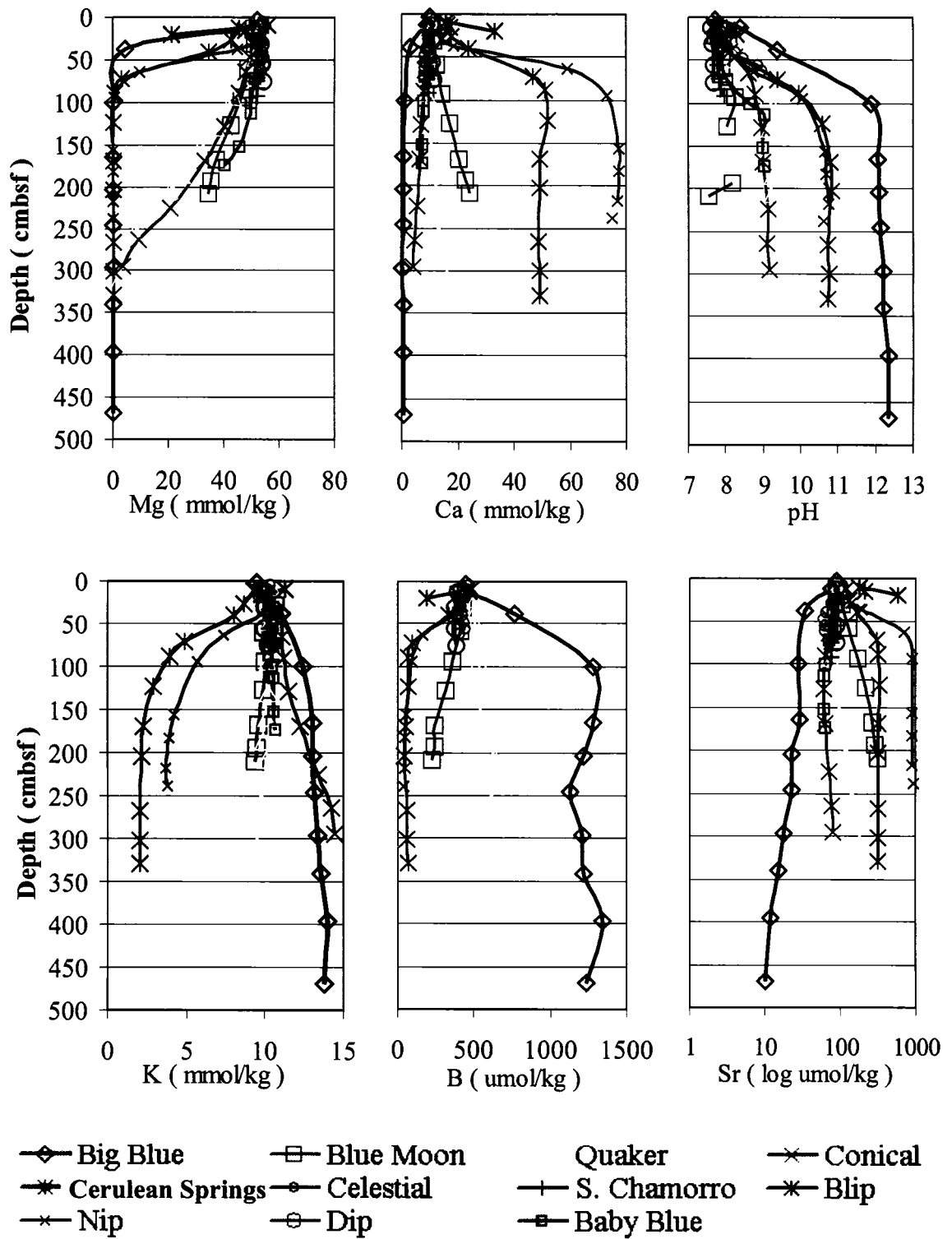


Figure 16. Results of major and minor elemental pore fluid chemistry from selected gravity and piston cores that represent the greatest variation down-section.

behaved inversely to Ca, and while seemingly independent of Na and Cl separately, Na/Cl showed the same inverse trend.

Minor element chemistry, or elements within the $\mu\text{mol/kg}$ range, behaved both similar to and independent of the major element components (Figures 16 and 17). Boron trends roughly followed those of the major ions Sulfate, K and Na/Cl with concentrations ranging 2 orders of magnitude between 15 $\mu\text{mol/kg}$ at Cerulean Springs on the eastern end of Pacman Seamount to 1500 $\mu\text{mol/kg}$ at the summit of Big Blue Seamount. Strontium concentrations mirrored those of Ca except for never reaching zero values and also varying over 2 orders of magnitude inversely to B. Lithium profiles were an anomaly in relation to the other minor and major elements, especially at Quaker seamount where values up to 113 $\mu\text{mol/kg}$ were measured in the deepest sections of the cores. The majority of the remaining seamounts were depleted in Li relative to a bottom seawater value of 26 $\mu\text{mol/kg}$.

Trace elements, or those existing at sub- $\mu\text{mol/kg}$ levels in the pore fluids, also commonly showed distinctive down-core trends from one location to another (Figure 17). Rubidium levels changed in a consistent manner down-core at all of the sample sites. Upwelling fluids from the three

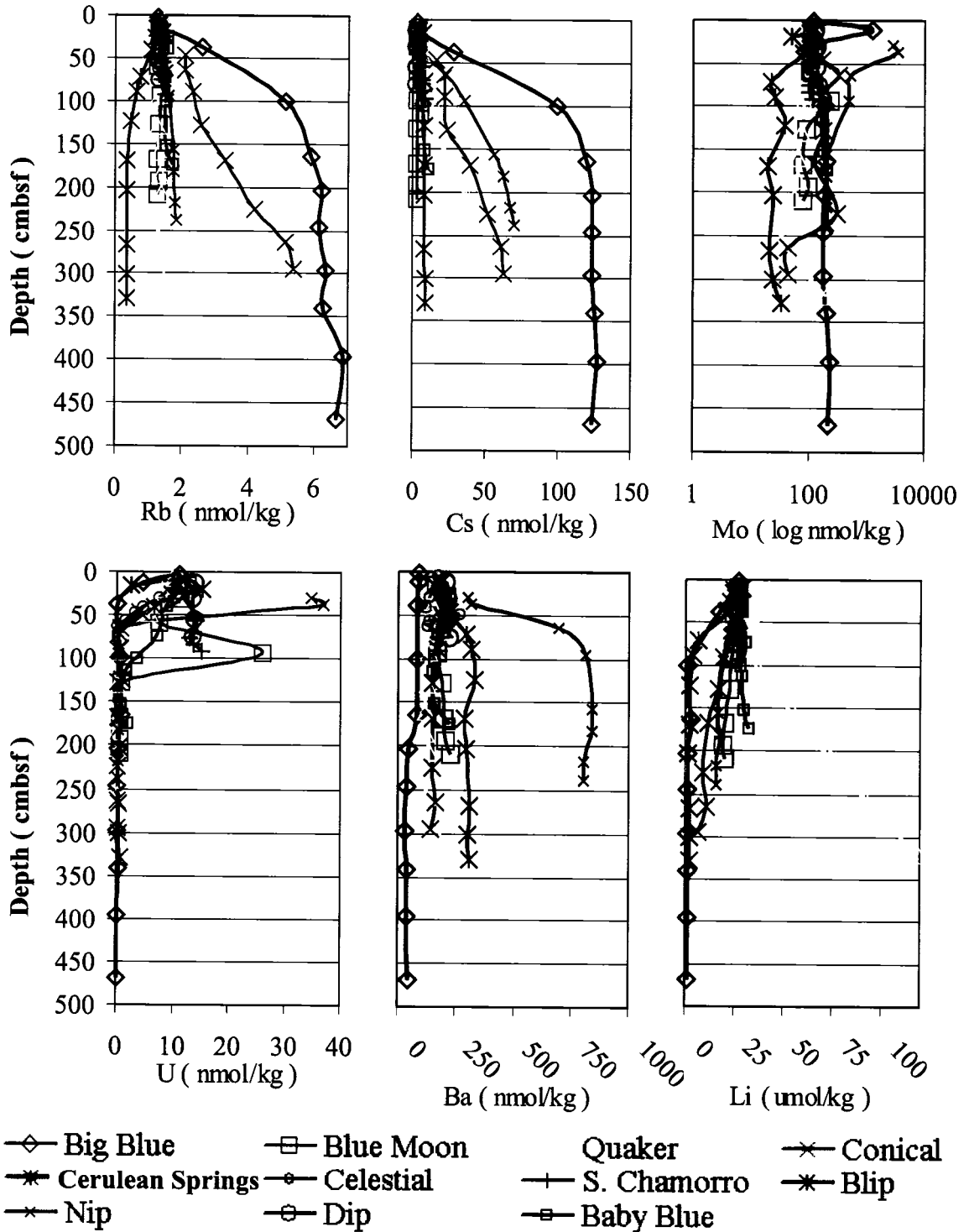


Figure 17. Results of minor and trace elemental pore fluid chemistry from selected gravity and piston cores that represent the greatest variation down-section.

seamounts Blue Moon, Pacman (at Cerulean Springs) and Blip were depleted in Rb relative to seawater. Measured values of 0.45 $\mu\text{mol/kg}$ Rb at Cerulean Springs were less than half the surface pore fluid values of 1.37 $\mu\text{mol/kg}$. The highest concentration of Rb sampled in the Marina Forearc sediment during the 2003 survey was 6.65 $\mu\text{mol/kg}$ on Big Blue Seamount. Cesium concentrations in pore fluids followed Rb, but were enriched at all of the Seamounts, except possibly Blue Moon. Another contrast in Cs concentrations compared with Rb, was the more drastic increase downcore. Cesium levels ranged from 2.7 nmol/kg at Blue Moon Seamount to 123 nmol/kg at Big Blue Seamount (bottom water concentration of 2.2 $\mu\text{mol Cs/kg}$), yet the maximum Rb concentration increased by only a factor of 5. Average surface sediment pore fluid concentration of Cs matched bottom seawater levels of 2.2 nmol/kg.

Some of the other trace elements, Mo, Ba and U, showed a marked degree of mobilization and irregular variation in the upper most sediment, but still approached asymptotic levels deeper in the sediment (Figure 17). Molybdenum concentrations at Big Blue Seamount rose as high as 6,420 nmol/kg in push core samples from the summit, but deeper piston core values converged at a much lower level of 220

nmol/kg. Down-core values at Nip and Baby Blue Seamount also approached concentrations of 200 nmol/kg. The remaining seamounts trended towards lower concentrations with depth, averaging around 40 nmol/kg at the deepest section of the core despite significant enrichments within shallow sections. Near-surface pore water values were near 110 nmol/kg, consistent with Pacific bottom seawater concentrations. Barium levels ranged from depleted levels of 43 nmol/kg at Big Blue Seamount to highly enriched concentrations of 800 nmol/kg at Nip Seamount. Uranium concentrations within the upper sediments exceeded 40 nmol/kg in a push core from the summit of Big Blue seamount and were significantly enriched at Nip Seamount and Blue Moon Seamount. Despite the surface enrichments, down-section pore- fluid values asymptotically approached zero at all the sampled sites with active fluid flow. This was the only element other than Mg to consistently approach zero values within the upwelling fluids of all the active mud volcanoes.

The complex behavior of the transition metals can be attributed to the changing redox potentials within the sediment column. The degree of fluid flux within the upper sediment column affects the redox gradients and can compact

the vertical profiles of these elements (Figures 18 and 19). These elements also responded to variations in sulfur and alkalinity. The most abundant transition metals in the sediments, Fe and Mn, behaved nearly as mirror images to each other within the sediments. Often there were two distinct zones of enrichment as well as depletion in the vertical profiles. Extreme Co enrichment up to 22 nmol/kg in the pore fluids occurred in the upper sediments of Big Blue Seamount as high sulfate and alkalinity fluids upwelled. Higher rates of upwelling compressed the vertical zone of reactivity, but slower rates of fluid flux appeared to allow a greater degree of mobilization. Copper also underwent a greater degree of mobilization under lower fluid flux conditions at the summit of Big Blue Seamount. Chromium was mobilized in the upper sediments at Big Blue Seamount independent of fluid flow rates, while high flow rates produced the greatest degree of V enrichment.

Lower sulfate and much less alkalinity in the pore fluids at Pacman Seamount had a noticeable affect on the transition metal behavior at Cerulean Springs on Pacman Seamount. While Fe and Mn were mobilized in the sediments there, the degree of mobilization was nearly an order of magnitude less than at Big Blue Seamount. Cobalt enrichment

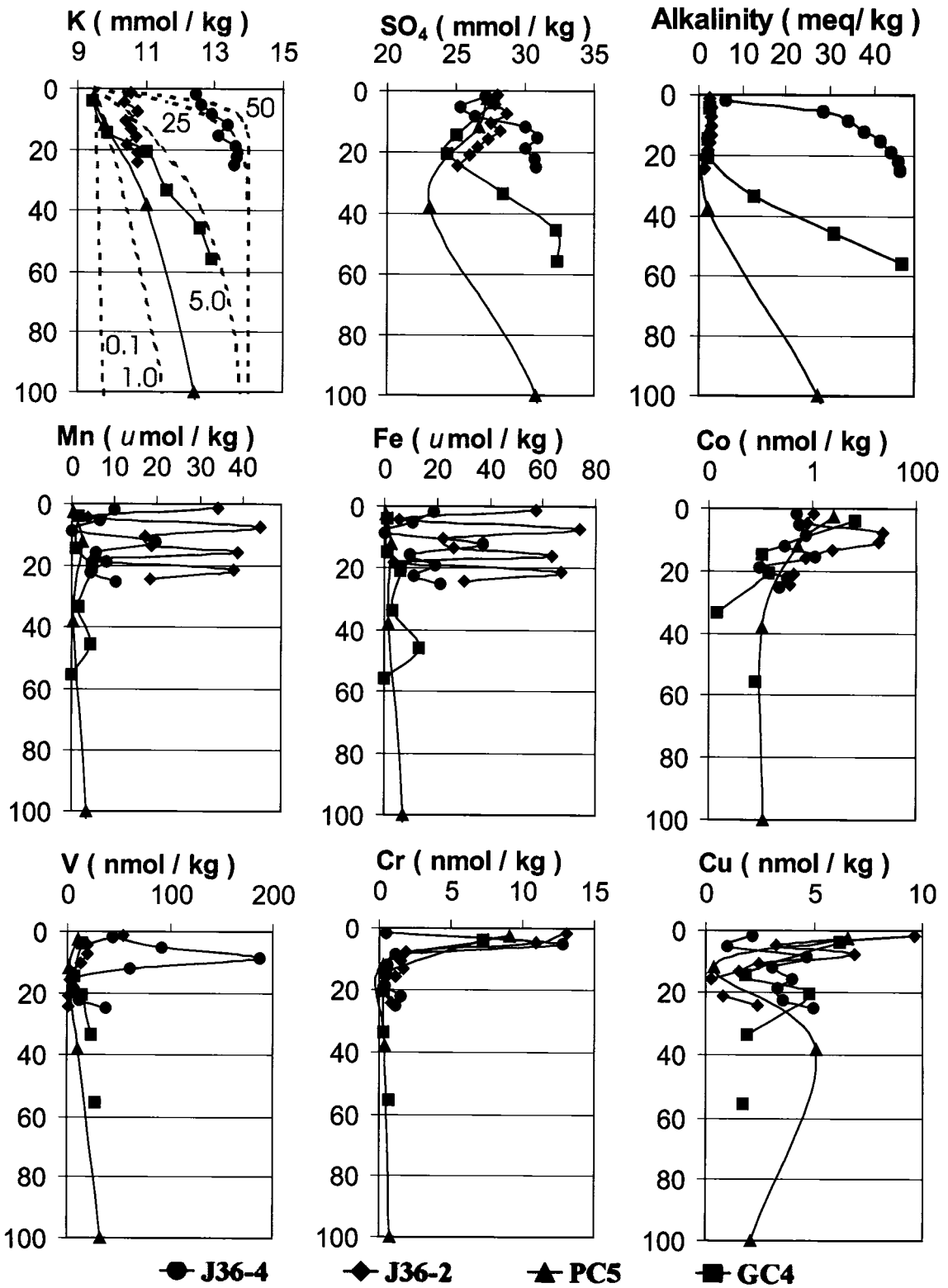


Figure 18. Depth profiles of redox sensitive elements and K at Big Blue Seamount. Flow model estimates in cm/yr are shown as a function of K.

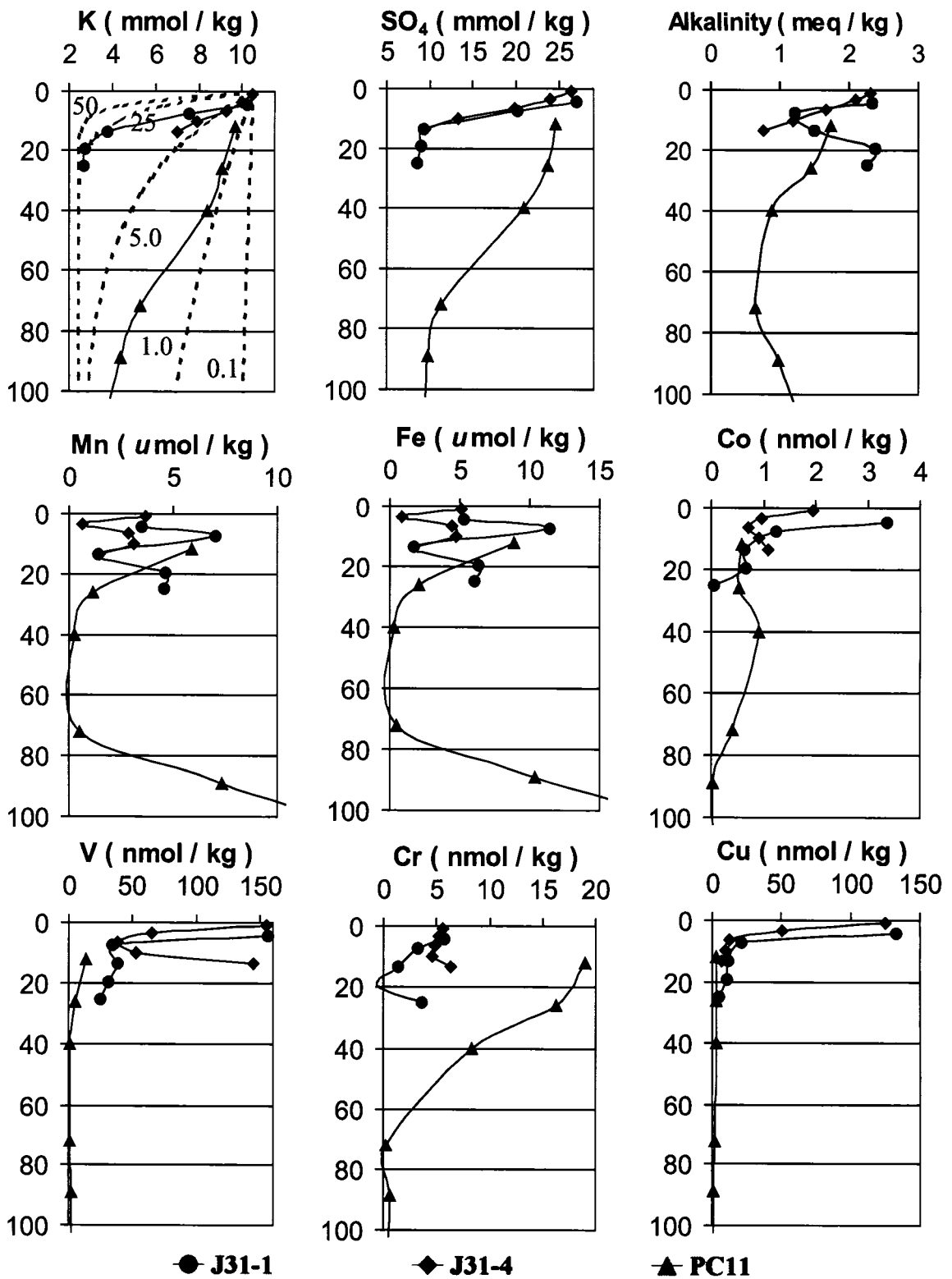


Figure 19. Depth profiles of redox sensitive elements and K at Cerulean Springs, Pacman Seamount. Flow model estimates in cm/yr are shown as a function of K.

was also much less and greatest in the most rapidly upwelling fluids. The degree of mobilization of V and Cr at Cerulean Springs was similar to Big Blue Summit, except that higher flow rates resulted in a lower degree of Cr enrichment. Copper levels at Cerulean Springs, in contrast to Mn, Fe, and Co, were more than an order of magnitude enriched relative to Big Blue Seamount and highest in the zones of greater fluid flux. Concentrations of all the transition metals measured in the deepest levels of the sediments were depleted relative to the surface with the exception of Fe and Mn at Cerulean Springs.

The entire suite of rare earth elements (REE) and Y were measured for 5 of the Mariana Forearc seamounts in pore fluids near the surface of the seafloor and within the deeper sections of the sediment cores. Fluids sampled from the venting borehole at S. Chamorro Seamount were also analyzed for concentrations of these components. The results were normalized by N-MORB concentrations (Hoffman, 1988; Hart et al., 1999) to produce a flattened pattern and show the degree of relative enrichment or depletion. The REE concentrations at Big Blue Seamount summit were studied in great detail and show a progressive depletion with greater degrees of fluid flow (Figure 20). Pore fluid

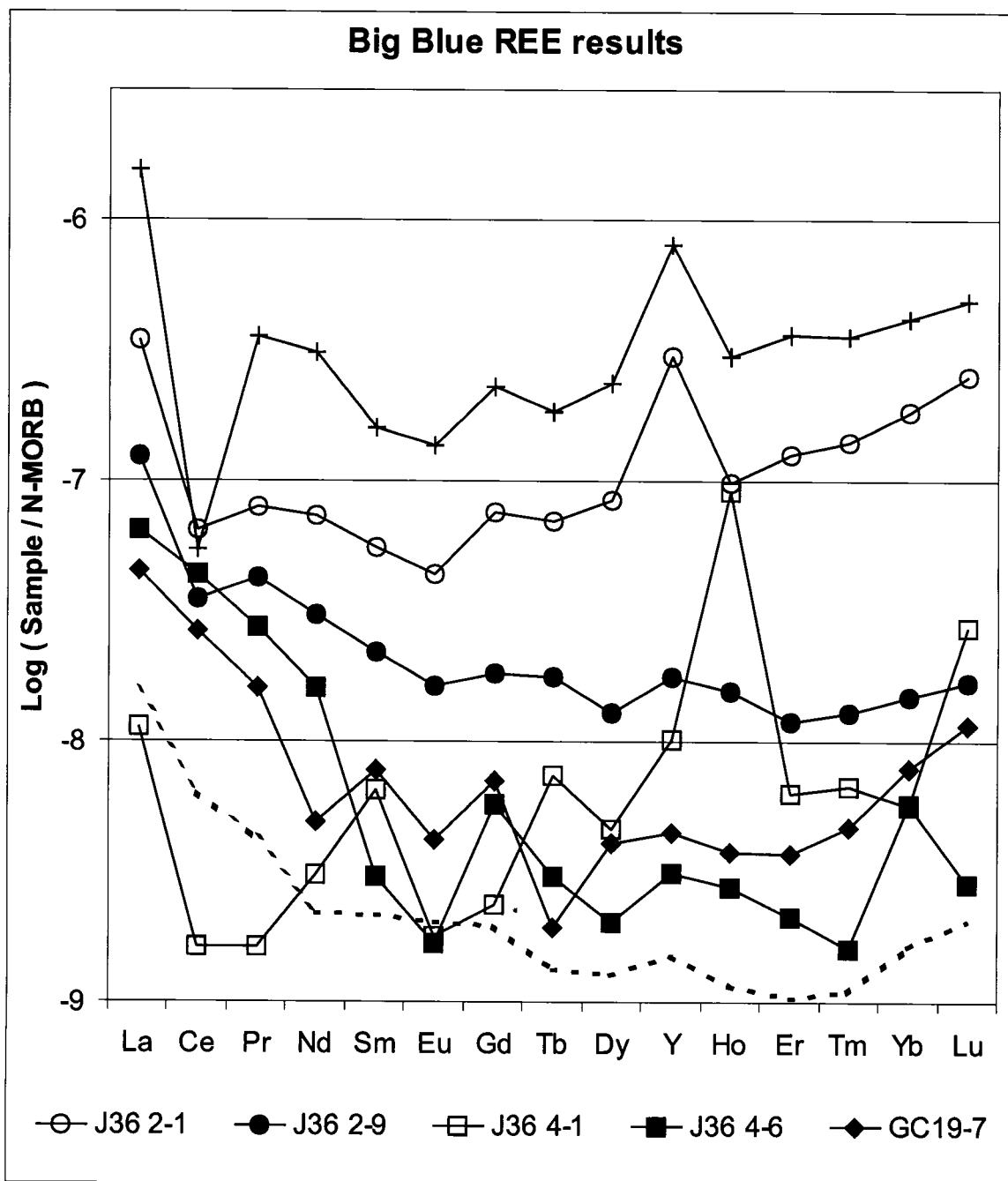


Figure 20. Results of HR-ICP-MS analysis of serpentine seamount pore fluids at Big Blue Seamount from two push cores (J36-2 and J36-4) and a gravity core (GC19). Values are normalized to N-MORB (Hoffman, 1988; Hart et al., 1999) and shown on a log scale. Pacific bottom seawater results are shown as a reference. The dashed line shows the standard deviation of the procedural blank also normalized to N-MORB.

concentrations near the surface of low-flow areas (J36-2) approach bottom seawater values while deeper samples and those within high flow zones are depleted one to two orders of magnitude relative to bottom seawater. Of particular interest is the pushcore profile from the highest fluid flow zone (J36-4), which shows a reversal of light REE (LREE) depletion near the surface to heavy REE (HREE) depletion at depth. The pattern of HREE depletion relative to LREE also is observed within gravity core (GC19) pore fluids at depth from Big Blue Seamount. A positive Gd anomaly relative to N-MORB and bottom seawater patterns can also be seen in the upwelling fluids at this site.

Examination of the REE concentrations from the deepest fluids within sites of the greatest fluid flux reveals the elemental fingerprint of each seamount (Figure 21). Cerulean Spring contains the highest concentration of REEs distributed in a slightly LREE enriched pattern. Blue Moon Seamount is the only seamount in the Mariana Forearc with a positive Eu anomaly in the upwelling fluids. These two aforementioned seamounts are also the only seamounts without a distinct positive Gd anomaly. Nip Seamount contains the lowest measured levels of La and the only positive Ce anomaly. The fluid venting from a borehole at

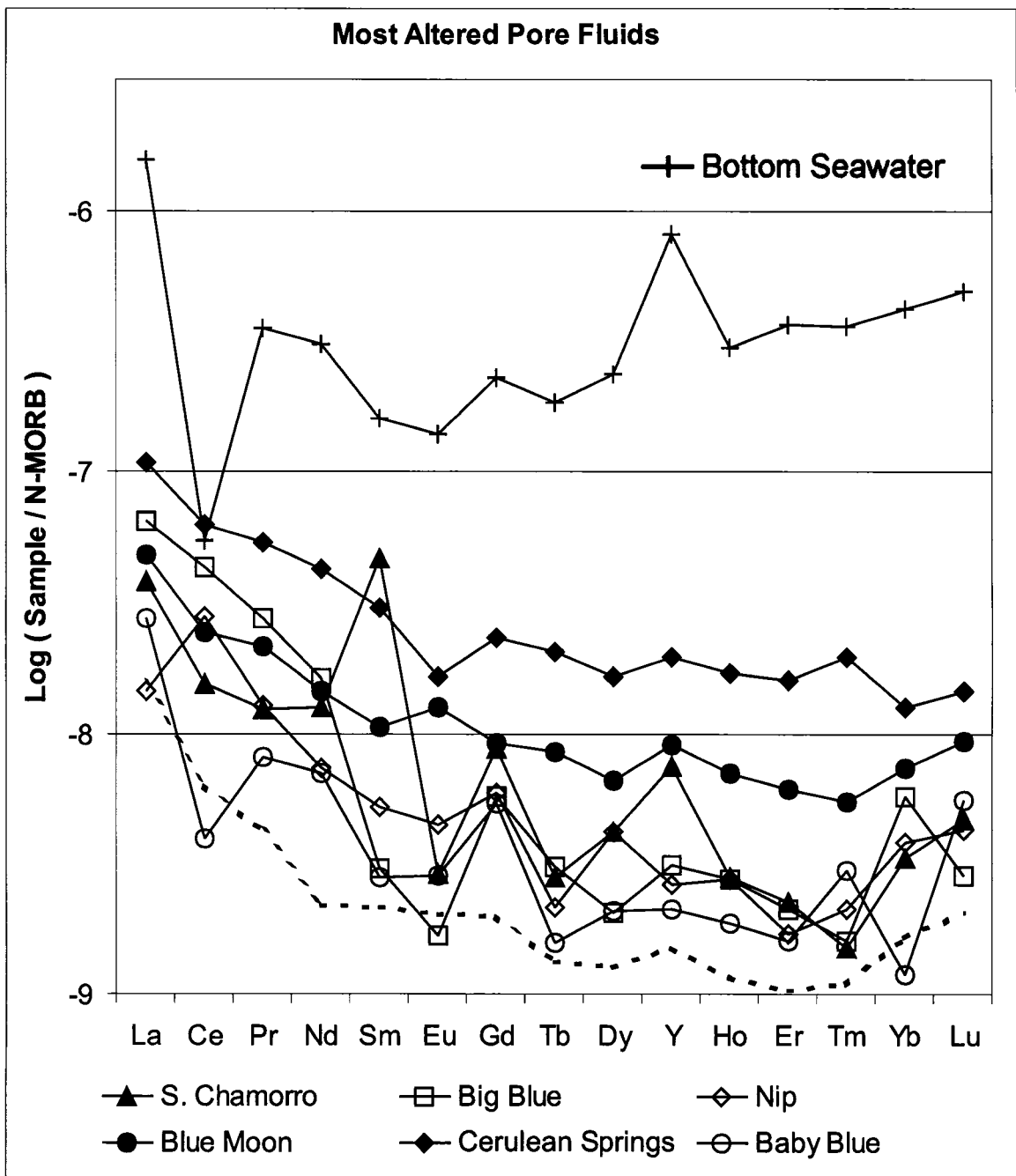


Figure 21. Results of HR-ICP-MS analysis of serpentine seamount pore fluids from the deeper core sections. Values are normalized to N-MORB (Hoffman, 1988; Hart et al., 1999) and shown on a log scale. Pacific bottom seawater results are shown as a reference. The dashed line shows the standard deviation of the procedural blank also normalized to N-MORB.

S. Chamorro Seamount shows a HREE depletion along with a strongly positive Sm anomaly. Big Blue Seamount, as mentioned before is LREE enriched and shows a positive Gd anomaly along with S. Chamorro, Nip and Baby Blue seamounts.

IV. Discussion

1. Tectonics and Geomorphology of Serpentine Mud Volcanism

1.1. Tectonics of the Mariana Forearc

An investigation into the regional tectonic forces across the Mariana Forearc was conducted on four 70,000 square kilometer sub-regions of the Mariana Forearc. These were first mapped using data provided by Geoware (www.geoware-online.com) containing 1 minute bathymetry created from combining observed soundings with predicted bathymetry from gravitational, magnetic and satellite sea surface observations. Additional higher resolution multibeam data was overlaid on the maps for available areas surrounding the more recently surveyed seamounts. Despite the scarcity of geophysical data to model the underlying structure of the Mariana Forearc at this time, this study clearly demonstrated a shift in the orientation of fault-related structures from one indicative of trench-parallel extension to one of a strain that is trench-perpendicular. This can be attributed to an increase in convergence southward as well as an increase in the degree of radial extension within the forearc northward.

To facilitate the interpretation of the geomorphology in Mariana Forearc and determine the tectonic processes

involved in serpentine mud volcanism, it was necessary to map the trends of the horst and graben blocks and fault scarps (Figures 12-14 and 22). The lengths of these structures were measured to determine which trends were dominant in each region. To avoid the uncertainties involved in how subducting seamounts impact the geomorphology of the inner trench wall, features located on the trench wall were excluded. Features in the arc and back arc were also excluded because the forearc is the locus of all the serpentine mud volcanoes, the focus of this study. For each mapped region the lengths and orientations of individual strikes were measured. The lengths were summed in 20-degree intervals relative to true north to simplify the interpretation process. The resultant summed lengths were normalized by the most dominant trend in the region in order to compare forearc regions of differing spatial dimensions. The trench axis was plotted on the regional maps and the strike averaged across each region. Rose diagrams were constructed for each region by plotting the normalized length of each strike in two directions opposed 180 degrees. The average



Figure 22. Sunshade bathymetry of the northernmost Mariana Forearc from Geoware 1 minute data with 250 m contours. Inferred fault structures within the forearc are outlined with tic marks indicating the downward slope direction. The trench axis is delineated by a solid line. Stippled area shows the location of a survey by Wessel et al. (1994).

trench axis strikes were plotted on the rose diagrams because the tectonics within the forearc are strongly influenced by the convergent margin. Plotting the trends of the structures within the Mariana Forearc showed a distinct progression from north to south along the trench axis (Figure 23). The cause of this shift in the trend of fault-related structures from north to south along the Mariana Forearc can be attributed to two competing extensional forces (Fryer pers. com. 2004).

At the northern end of the forearc (Figure 22), the dominant strikes run perpendicular to the trench axis (Figure 23a), which is in good agreement with the results of a high-resolution sidescan survey analysis within that region (Wessel et al., 1994). In the previous study, bathymetry, reflectivity and seismic reflection data were used to determine the orientations of the fault systems and use the results to deduce the tectonic stresses from the back arc to the forearc. As was described by Wessel et al. (1994), the northernmost portion of the Mariana convergent margin is currently restricted by the subduction of the Ogasawara Plateau (Figure 7). The direction of convergence in this region is nearly oblique to the trench axis and the rate of convergence was estimated at 4.4 cm/yr (Eguchi,

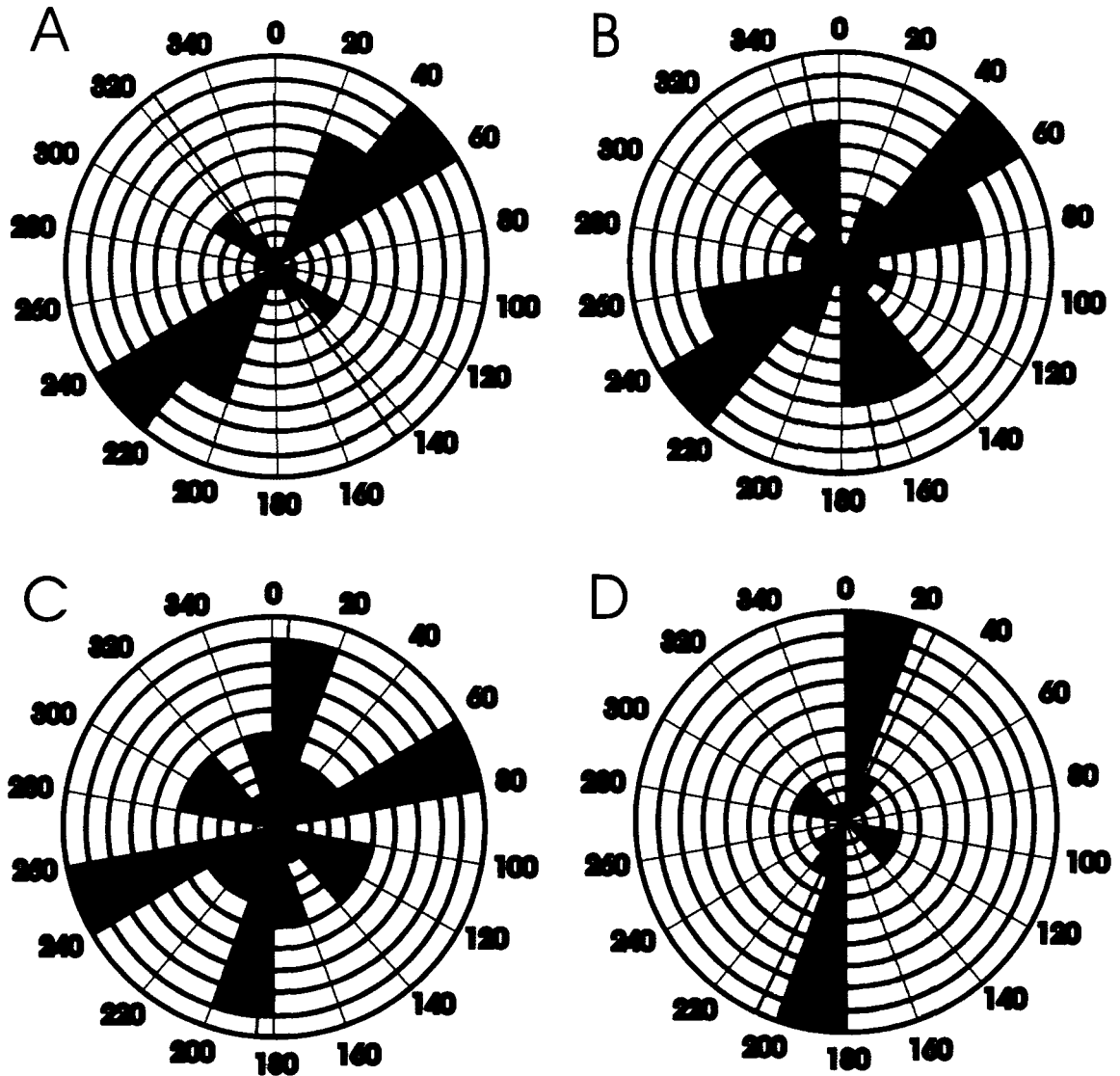


Figure 23. Rose diagrams showing orientations of apparent fault strikes across the Mariana Forearc. Orientations were grouped in 20 degree sets and the lengths of each group summed. The summed lengths were normalized by the value of the dominant alignment to minimize effects of differing forearc widths. The average trench axis orientation is shown in red for each region. All trends are referenced to true north. The regions of study and apparent fault strikes are shown in previous figures. A) Figure 22: northern Mariana Forearc. B) Figure 12: north-central Mariana Forearc. C) Figure 13: south-central Mariana Forearc. D) Figure 14: southern Mariana Forearc.

1984). A combination of asymmetrical backarc spreading and the pinning of the northern end of the convergent margin result in nearly double the convergence rate to the south (Fryer et al., 1985). The asymmetrical rates of convergence along the margin cause the faulting in the north to be controlled by radial extension parallel to the trench axis rather than interaction between the overriding and subducting plates (Wessel et al., 1994).

The presence of a significant number of strikes paralleling the trench axis begins to appear in the northern-central forearc (Figures 12 and 23b) suggesting the presence of an additional strain component. Seismic surveys of the region (Hussong and Fryer, 1981; Fryer and Pearce, 1992) have found primarily normal faulting to occur. The dominance of normal faulting in the region shows that the auxiliary strain component is most likely extensional as well. In the southern-central forearc region (Figure 13) both trench-perpendicular and trench-parallel strikes of nearly equal magnitude are present along with minor components of conjugate faulting in the NW-SE direction (Figure 23c). These faults may be occurring from the transfer of stress from one extensional direction to another. The central forearc contains the

majority of serpentine diapirs, so it appears that the transfer of strain between orthogonal extensional forces plays an important role in serpentine mud volcanism.

At the southern end of the Mariana Forearc (Figure 14), nearly all the structures parallel the trench axis with a minor number of fault-related structures oriented perpendicular to the trench axis (Figure 23d). Additional studies of outer trench walls have shown that extensional strain perpendicular to the trench axis dominates within subducting slabs (Masson, 1991). If decoupling between the converging plates is limited, which may be enhanced by the subduction of numerous seamounts, this strain could be transmitted to the overriding plate. Trench rollback along the Mariana Trench would also introduce a perpendicular extensional stress component to the overriding plate under conditions of limited decoupling. The observed results of this transfer of stress to the upper plate would be the occurrence of trench-parallel faults within the forearc region.

While the findings in this study do present a number of interesting questions regarding the tectonic processes producing serpentine mud volcanoes, caution must be taken due to the limited resolution of the data used in this

study. However, the low-resolution, large-scale analysis of the northern forearc does produce very similar results to the high-resolution, small-scale analysis done by Wessel et al. (1994), adding confidence to the interpretations. It is uncertain if the orientation of all these scarps, horsts and grabens can be inferred to result from underlying faults, but previous seismic studies of selected regions have confirmed the presence of normal faults below some of these structures (Hussong and Fryer, 1981; Fryer and Pearce, 1992).

Despite the scarcity of geophysical data to model the underlying structure of the Mariana Forearc at this time, this study clearly demonstrated a shift in the orientation of fault-related structures from one indicative of trench-parallel extension to one of a strain that is trench-perpendicular. This can be attributed to an increase in convergence southward (Eguchi, 1984; Fryer et al., 1985) causing an increase in the degree of radial extension within the forearc northward (Wessel et al., 1994) and possibly trench rollback along the southern margin.

1.2. Serpentine Seamount Distribution and Geomorphology

There have been no serpentine seamounts discovered in the northern region of the Mariana Forearc. Due to minimal

exploration in the region the possibility of serpentine diapirism activity does exist, so this possibility must be left to future studies. The northern-central region of the Mariana Forearc contains the highest density of active serpentine seamounts (Figure 12). Four serpentine seamounts have been discovered in the southern-central Mariana Forearc (Figure 13), but only Blue Moon is known to be active based on core sampling and ROV surveys.

Conical Seamount, located at the lower edge of a large half-graben, is symmetrical in shape, resembling a terrestrial cinder cone volcano. Higher slopes of 10 degrees on the southeastern flank of Conical bordered by a deep graben may result from the continued growth of the graben. The contact along this fault is a likely source for the deep fluids and serpentine mud. A large pressure ridge emanating from the flattened top continues to the base of the seamount. It is likely that this ridge represents a headwall for slumping of the eastern flank into the graben. Fluid flow, as documented by large chimneys and the pore fluid chemistry, is concentrated near this headwall. While the summit and northern flanks also contain extensive scarps, no evidence of fluid flow was found there. This suggests that the large headwall is the

expression of a deeper fault that is currently channeling fluid and serpentine mud from the forearc basement and mantle.

Pacman Seamount is located in the southern corner of the same half-graben as Conical Seamount. The location of both active seamounts at the corners of this graben reiterates the importance of dual fault systems in serpentine mud volcanism. Pacman Seamount has been partially bisected along an east-west (E-W) axis through continued faulting (Fryer, 1996). Fluid flow has been observed both at the summit on the western half and within the Baseball Mitt feature at the southeastern extremity. The Baseball Mitt has much higher rates of fluid flow than the summit, and the chemistry shows a separate source of fluid at each feature. The path of serpentine diapirism at the summit is probably from a fault system related to the large graben structure containing Conical Seamount. Baseball Mitt lies above a separate fault system that is related to separate down-dropped block near the inner trench wall. Circular depressions within the Baseball Mitt highlight the fluid activity at this site.

Quaker Seamount sits atop a horst block with a NE-SW trending ridge along the northeastern flank. The summit is

separated from this ridge by a small E-W scarp and a flattened region nearly 5 km wide. At the summit is another E-W oriented fault scarp and numerous chimneys were found along its base. A large headwall runs along eastern perimeter of the southern flank from the summit to the base. The southeastern flank lies above a deep graben, which apparently undermines the flanks resulting in a significantly steeper slope on this side. The source of fluids here is likely the E-W trending fault system that passes through the summit and forms the northern boundary of a small graben.

Big Blue Seamount is the largest of all the known serpentine mud volcanoes, with a maximum diameter of 50 km, and similar to Quaker Seamount, contains a NE-SW trending ridge along the northeastern flank. Another ridge extends east below the summit and follows the headwall of a graben located south east of Big Blue Seamount. What is unique about Big Blue, other than its size, is the occurrence of multiple domes at the summit. Three resurgent domes protrude from a larger dome at the summit. The source of fluid and serpentine expulsion at Big Blue could be from the intersection of two fault systems that follow the ridges that emanate from the seamount's center.

Serpentine seamounts within the south-central Mariana Forearc are primarily dormant based on previous sampling (Fryer et al., 1999; Fryer et al, 2000) and the results of this study. Turquoise Seamount is located on the eastern edge of a half-graben near the inner trench-slope break and contains NE-SW trending ridges similar to other active seamounts such as Big Blue and Quaker. Celestial Seamount is also inactive, based on the results of this study, and rests on a large SE-NW oriented horst block. Despite the appearance of many pressure ridges along the flanks, ROV and coring surveys of the crescent-shaped flat summit failed to discover any evidence of fluid flow. Peacock Seamount is a small diapir at the base of a long (>70 km) scarp within a graben. Peacock Seamount was initially presumed to be an emergent diapir (Fryer et al., 2000), but has since failed to exhibit any chemical or other evidence of fluid activity.

Blue Moon Seamount is near the inner trench-slope break and is atop a NE-SW aligned horst block. This is the only seamount in the region to exhibit evidence of recent activity in the form of fresh sedimentary serpentine exposures and exotic pore fluids. The southern flank is significantly steeper and is bordered by a graben that sits

above the inner trench slope. Fluid activity was restricted to the southwestern summit where two parallel NE-SW trending scarps expose fresh serpentine. The source of mud volcanism at Blue Moon Seamount is probably from a NE-SW fault system that borders the graben below the southeastern flank.

The southern Mariana Forearc contains two serpentine diapirs, North and South Chamorro seamounts. These two seamounts are above a scarp with over 4000 m of vertical relief descending into the Mariana Trench. The trench axis here has a complex structure with apparent horst blocks oriented parallel to the trench axis. Of these two seamounts, South Chamorro Seamount is actively venting fluids and is the only place where chemosynthetic macrofauna have been discovered in association with serpentine mud volcanism (Fryer and Mottl, 1997). The activity at S. Chamorro Seamount is focused at the southeastern summit, from which numerous scarps and pressure ridges emanate. The southern Mariana Forearc contains almost solely structures oriented parallel to the trench axis. However, the only serpentine diapirs discovered here (North and South Chamorro seamounts) occur near the intersection of 3 strikes of differing trends and

the trench axis makes an abrupt bend just seaward of these diapirs. The presence of mudflows along the southeastern flanks of S. Chamorro Seamount (Fryer et al., 2000) add to the possibility that the source of fluid and serpentine for this seamount is the intersection of N-S and NE-SW fault systems related to the offset in the trench axis.

While there is evidence that the eruptions occur along normal faults (Fryer et al., 1999), many of the mudflows are so extensive that they mask the underlying structures and the exact location of the fault block boundaries. Despite a masking of boundaries at the peripheral of the seamounts, features apparent on the summits, such as stair-stepping scarps and the head scarps of large gullies parallel the local orientations of tectonic block boundaries in many cases. This shows that the underlying tectonic forces can be transferred through the serpentine structures and expressed on the seafloor. Finally, the high density of serpentine seamounts within regions containing nearly equal components of trench-parallel and trench-normal faulting highlights the importance of interactions between these tensional fields in producing serpentine mud volcanism. What still remains uncertain is whether the occurrence of these cross-cutting structures

are facilitating serpentine mud volcanism, or if the extensive hydration of the mantle and overriding plate weakens the forearc crust to the point that this fracturing can occur.

1.3. Model of Slab Depth

Geochemical evidence from the Mariana mud volcanoes shows that with varied depth to the décollement, and thus differing formation conditions, significant compositional differences in upwelling pore fluid occurs (Fryer et al., 1999; Mottl et al., 2004). To test the effects of the depth to the slab on the chemical composition of the fluid at depth, it was first necessary to construct a model to approximate the depth of the décollement. The parameter chosen as a proxy for depth is the distance from the Mariana Trench axis. First, the distances for each sample location were quantified using a vectorized trace of the Mariana Trench axis. Using the commercial GIS software package ArcView8, a grid was produced where each cell contained a value representing the shortest distance to the trench vector (Figure 24).

Existing estimates of distances and accompanying depths based on geophysical and chemical evidence were used to verify the accuracy of the model and calculate the slope

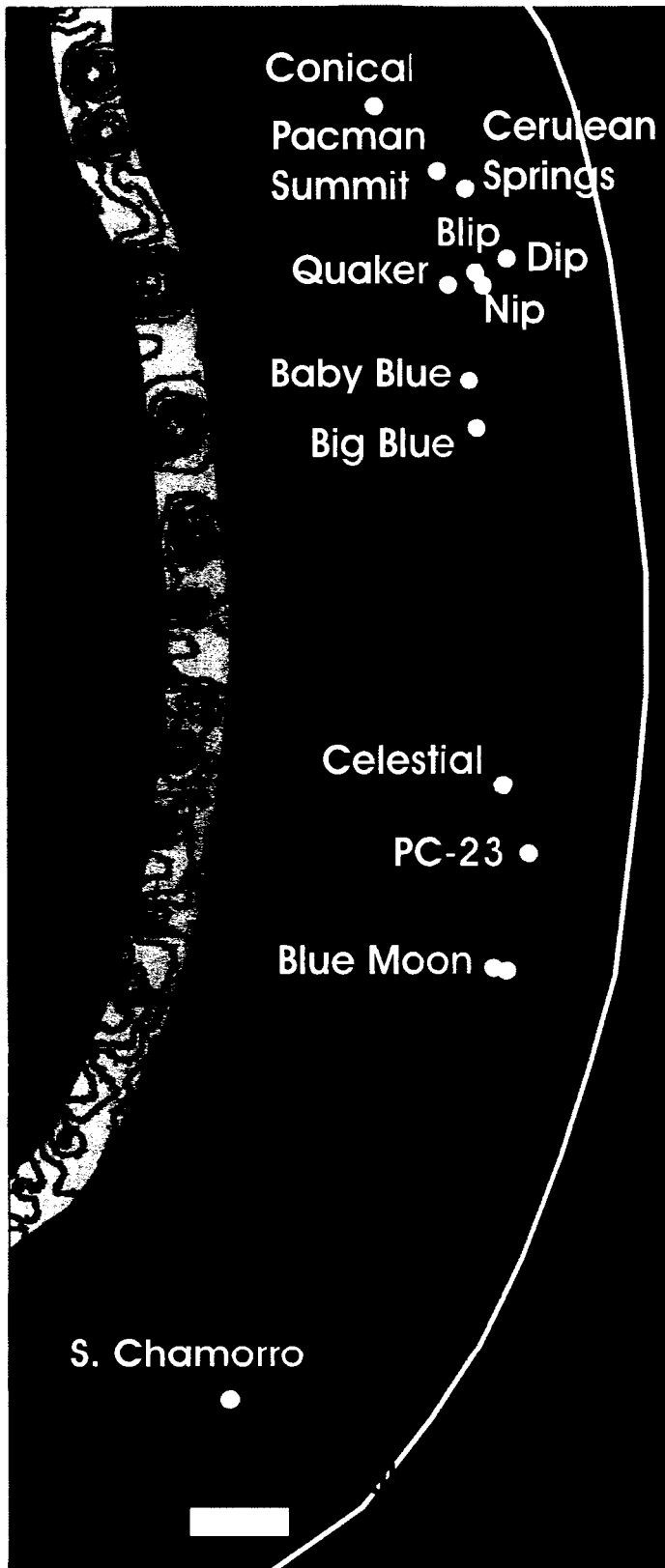


Figure 24.

Model of distance to Mariana Trench axis. Wide color bands represent 35 km intervals and narrow color bands are 15 km. The names of serpentine seamounts that were sampled or surveyed in the 2003 R.V. Thompson expedition are shown next to the location of the sample sites. One unnamed feature was sampled by piston coring (PC-23), but no evidence of activity was found. Contours for the basemap are every 500 m.

of the slab as a function of distance to the trench axis (Fryer et al., 1985, 1999, 2000; Mottl et al., 2002). A correction was applied to account for bathymetric variations of up to 3 km between sample locations. Errors on the order of 4 km may result when estimating slab depths because of the presence of subducting seamounts that alter the shape of the trench axis and elevate the depth to the décollement. The estimates of depth to the slab along with the horizontal distance to the Mariana Trench axis are presented in Table 4 and will be used in the next section to discuss the geochemical conditions within the subducting slab and upper mantle.

	Distance to Mariana trench axis (km)	Depth to the subducting slab (km)
PC-23	47	8
Dip Seamount	47	9
Blue Moon Summit	55	13
Cerulean Springs	60	16
Nip Seamount	61	17
Celestial Seamount	62	19
Blip Seamount	63	18
Pacman Summit	70	22
Baby Blue Seamount	72	24
Big Blue Seamount	72	25
Quaker Seamount	76	26
S. Chamorro Seamount	78	26
Conical Seamount	86	30

Table 4.

Estimates of the depth to the subducting slab under sample sites. The estimates are based on combining the distance from the trench axis with estimates of the slab dip angle under the forearc (Fryer et al., 1985). Corrections based on the elevation of each seamount were made to account for up to 3 km variations in seamount summit heights. The names of the sampled features are given. PC-23 is a piston core sample of a feature that did not exhibit any evidence of fluid activity.

2. Geochemistry

2.1. Modeling Flow Rates of Upwelling Fluids

Quantification of the rate of upwelling fluids at each site is essential for describing the degree that the fluids are altered as they ascend through the Mariana Forearc basement. Slower flow rates mean longer residence times in the sediment column, resulting in additional chemical exchange with the sediments (e.g., Wheat and Mottl, 2000). Slower rates also allow for the downward diffusion of seawater that mixes with the exotic pore fluids, forming secondary minerals such as carbonates. By quantifying the rates of flow at multiple locations within a seamount and assessing the systematic variations in pore water chemical profiles, the degree of alteration of certain elements becomes apparent. Cores that sample the highest rates of flow can then be chosen to make estimates of the composition of pristine fluids at depth.

The flow model used in this study examines the variable composition of chemical species under conditions of diffusion and advection. If the concentration of an ion is a function of diffusion alone, the chemical profile will be linear, provided sediment thermal and physical properties do not change with depth. Under advective flow

conditions either upwelling or downwelling, the concentration at depth is non-linear, resulting in a concave-up or down profile. Under extreme flow rates (~100 cm/yr for this model), the advecting fluids will overwhelm the diffusive effects, forcing the chemical gradient to the upper few millimeters of the sediment, resulting in what appears as a uniform concentration down-core.

In practice most elements will react with sediment, forming precipitates or dissolving minerals that alter the fluid composition. This underscores the importance of choosing conservative (non-reactive) elements as tracers to model flow within the sediments. Details of chemical reactions within the serpentine sediment of the Mariana Forearc mud volcanoes will be discussed in a later section. For now it is only important to understand the theory of flow modeling and the results of these calculations.

The general equation for pore water flow is described by Berner (1980). This general equation was simplified for this application and identical to the simplified equation used to model the flow of pore water in low temperature hydrothermal systems (Wheat and Mottl, 1994; Wheat and McDuff, 1995). In the simplified model the concentration [C] of an element within the sediment column is

$$C = \beta(e^{vz/Ds} - 1) + C_0$$

where; v is the velocity of fluid flow, z is the depth within the sediment, Ds is the sediment diffusion coefficient of the modeled ion, C_0 is the concentration of the ion in bottom seawater, and β is a function of the parameters above and explained in more detail below.

The variable Ds is itself a function of the conditions of the sediment

$$Ds = Dw \cdot v \cdot 10^{-6/f \cdot p}$$

where; Dw is the molecular diffusion coefficient of the element in seawater at 4°C (Li and Gregory, 1974), v is the viscosity of the fluid (0.95 at 0°C; Li and Gregory, 1974), f is the sediment formation factor, and p is the porosity. Values for the formation factor and porosity were taken from ODP Leg 195 results of drilling on South Chamorro Seamount, a serpentine mud volcano in the southern Mariana Forearc. The average formation factor and porosity were 3.5 and 0.55 in the upper 5 m of the sediment column (Shipboard Scientific Party, 2002).

The β parameter is a function of the composition and depth of the end member fluid within the sediment

$$\beta = (C_f - C_0) / (e^{v \cdot z \cdot \epsilon / Ds})$$

where; C_f is the ion concentration of the end member fluid at a depth of Z_f . A depth of 60 m was chosen for these models to ensure the theoretical profiles were far below the sampled depth.

Quantification of flow rates using this model is achieved by iteratively calculating the sum of the residuals between the observed and theoretical concentrations. An initial estimate of flow rate is entered and the rate varied until a minimum value for the residual sum is reached. Note that this model also can be used to estimate the rate of flow into a sediment column.

Calculations based on this model and measured data are shown in Figure 25 for two of the sample sites, Big Blue Seamount and Cerulean Springs. Rubidium was used in these models, because it is the least affected by reactions in the serpentine matrix. End-member Rb concentrations for each site are based on asymptotic concentration in the deepest sections of the sampled sediment column. As the rate of upwelling increases, the curvature of the chemical profile increases as well. When the flow rate approaches ~100 cm/yr, the profile is essentially a straight line due to the limited resolution of the sampling methods in the upper few millimeters of the sediment column where all of

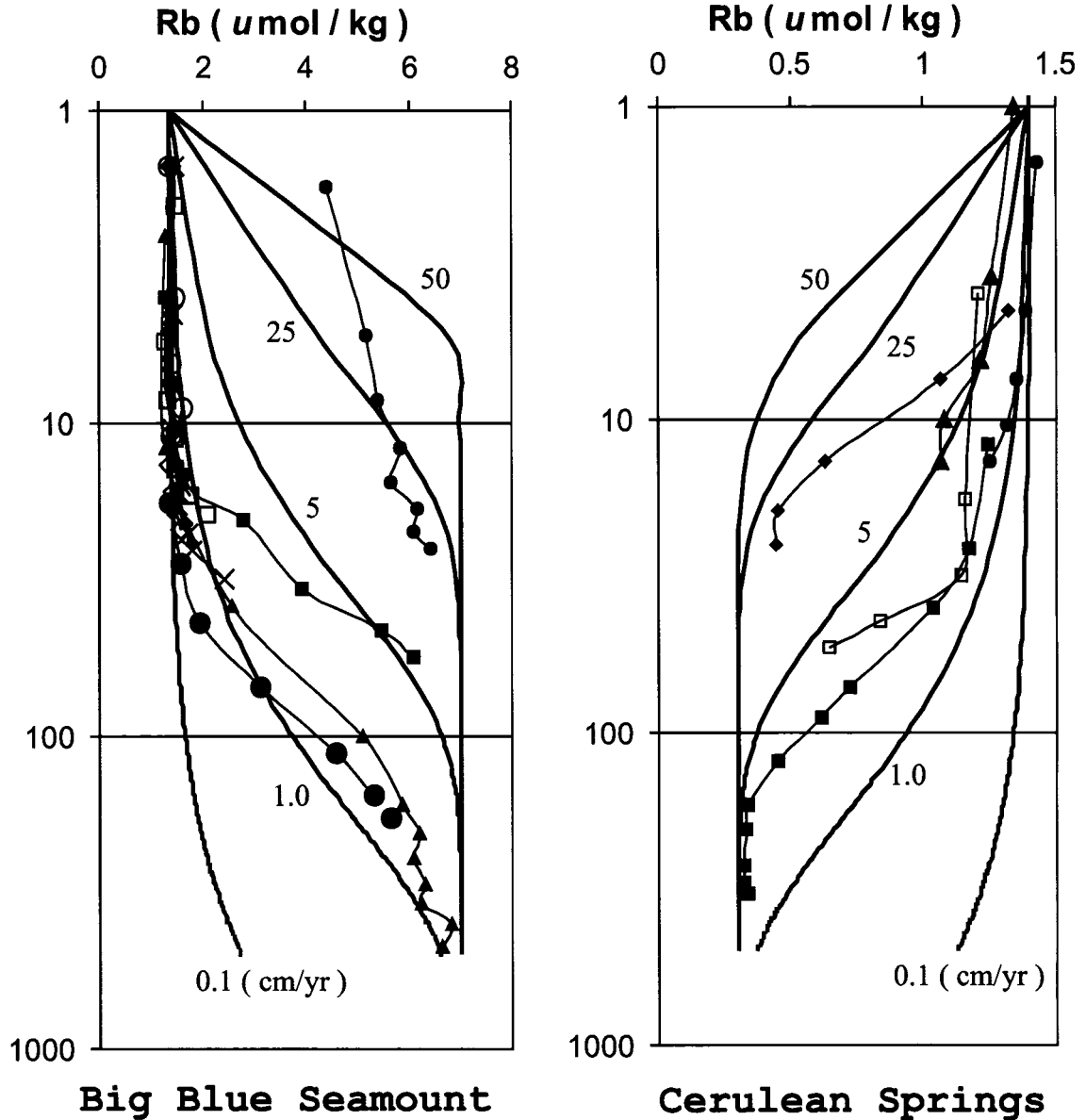


Figure 25.

Pore fluid diffusion/advection flow models used to calculate flow rates at Big Blue Seamount and Cerulean Springs, Pacman Seamount. All the pore fluid data from both sites are presented. Flow rates are calculated by minimizing the sum of the differences between the observed profiles and theoretical models at variable flow rates. Theoretical flow models and sample flow rates in cm/yr are given for reference.

the curvature is constrained. None of the Rb profiles from this study approach such a fast upwelling speed. As demonstrated in Figure 25, the ability of the model to estimate flow is independent of whether the advecting fluid is enriched or depleted. All that is required is that the end-member concentration is different from that of bottom seawater and that this difference can be resolved analytically.

Estimates of fluid flow were calculated for pore fluids from a transect across Big Blue Seamount (Figure 26), based on the elements Rb, K, and Na. These elements were chosen because they showed minimal alteration effects even at slow rates of flow. Calculated profiles based on flow rates that resulted in minimal residuals between the theoretical curve and measured values also are shown in Figure 26 for comparison. Results from the 3 elements generally agreed, with the exception that the K data generally result in higher estimates than those calculated from the other two elements. This difference results from the non-conservative nature of K as a consequence of K removal into the sediments within the gravity and piston cores as they warmed during recovery, a process that took at least one hour. In contrast, push cores were

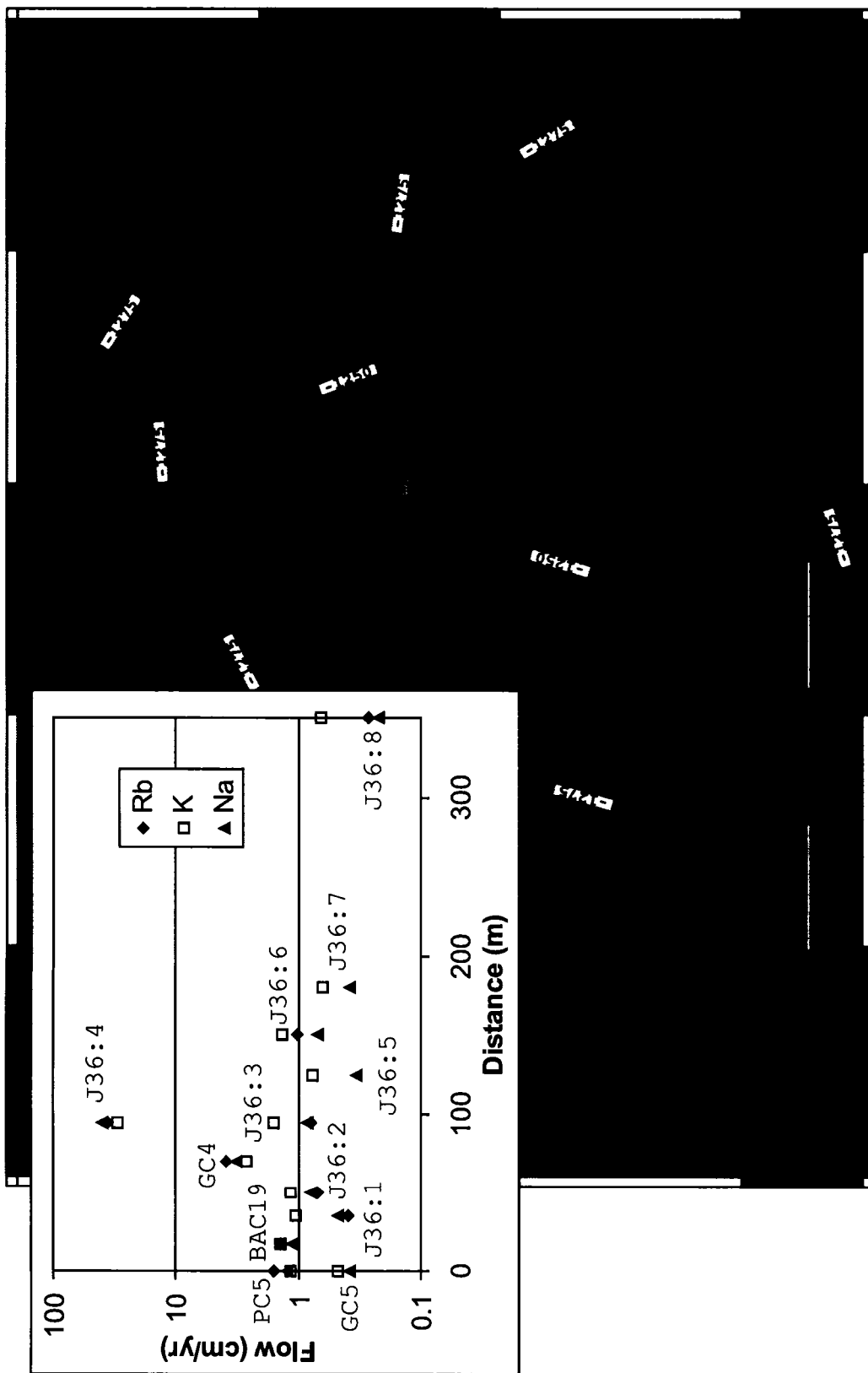
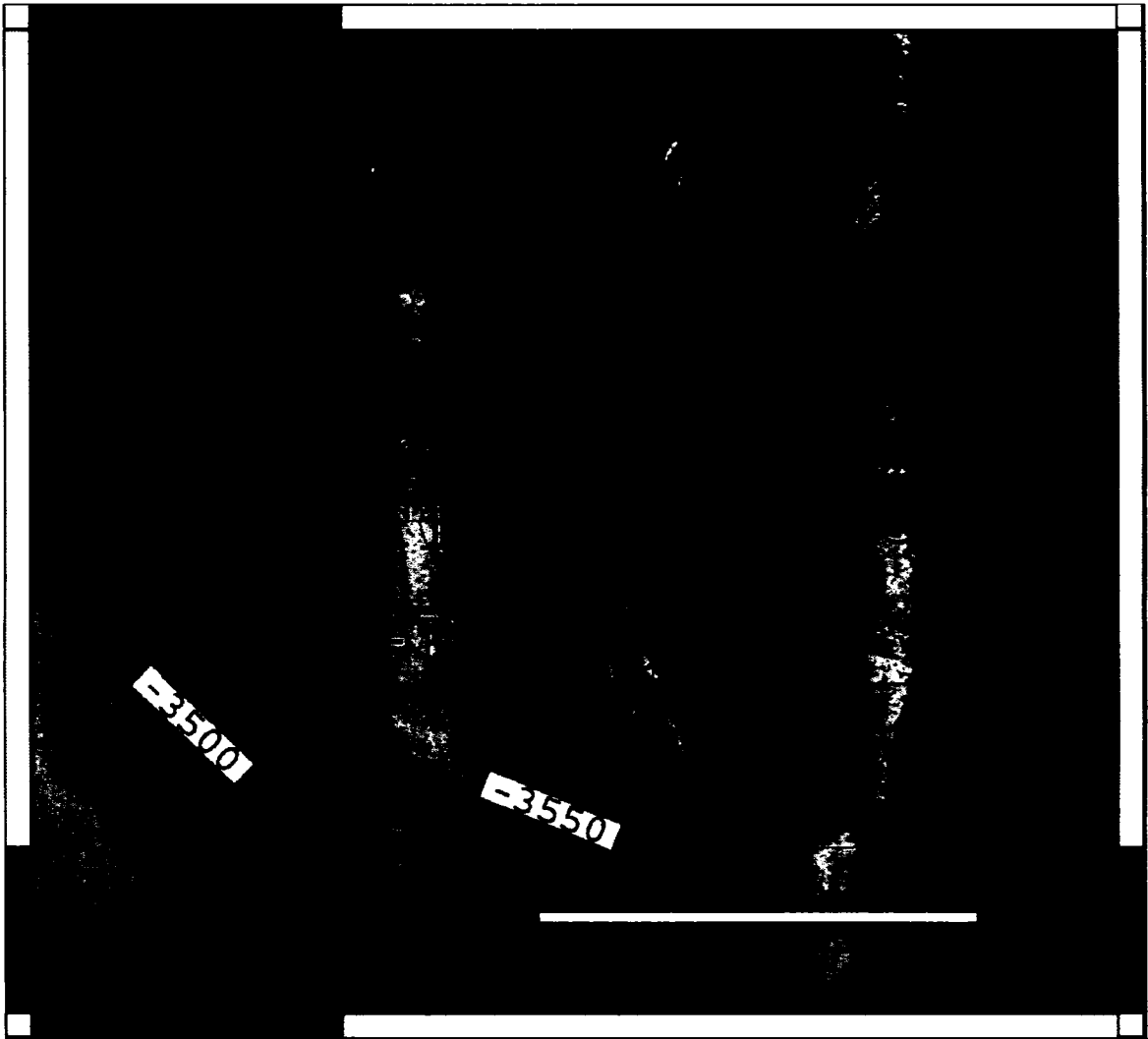


Figure 26. Location of transect conducted across Big Blue Seamount summit. Numbers show push cores taken from Jason2 dive #36. The inset shows results of flow rates calculated by 3 elements (Rb, K and Na) as a function of distance from PC5.

immediately taken from the ROV and brought to a 4°C cold room for processing.

Results of modeling the other elements Na and Rb agree and demonstrate that flow is focused towards the center of a dome at the summit of Big Blue Seamount (Figure 26). The highest rates of flow are measured near the center of the dome in push core J36:4 (36 cm/yr) and gravity core GC4 (3.9 cm/yr). Average flow rates in other cores across the dome were between 0.5 (J36:1) and 1.6 cm/yr (PC5). Flow rates from a push core taken to the side of the dome (J36:8) were the lowest at ~0.3 cm/yr. The rate of flow is also highly variable at a smaller scale. For example cores J36:3 and J36:4 were taken only a few meters apart yet they exhibit very different rates of flow (~1 cm/yr vs. 36 cm/yr). Focusing of fluid flow within this dome structure is consistent with geologic observations of recent activity, implying flow is highly channelized and intimately linked to processes that form serpentine mud volcanoes such as Big Blue Seamount.

Cerulean Springs, located at the eastern end of Pacman Seamount, is another site with high rates of fluid flow (Figure 27). Springs lie within a circular depression nearly 300 m in diameter, and a group of cores were taken



Core ID	Flow Rate (cm/yr)
J31:PC-1	13.0
J31:PC-4	5.5
J31:PC-3	1.6
PC-11	2.4
GC-11	2.9

Table 5.
Results of flow modeling based on concentrations of Rb in the pore fluids recovered from Cerulean Springs. Higher flow rates occur along the perimeter of Cerulean Springs.

Figure 27. Locations of cores sampled at Cerulean Springs, Pacman Seamount. J31 samples are push cores from Jason2 dive #31. Push core J31-PC2 was not recovered. Location of PC11 (piston core) was the same as GC11. Background shows DSL-120 sidescan reflectivity data overlaid on EM-300 multibeam bathymetry. Contours every 10 m.

from within this depression. The element chosen for modeling flow at Pacman is Rb, because it exhibits minimal perturbations in vertical profiles with differing flow rates. Results from models based on Na are not shown but produced similar results. Flow rates in 3 push cores (J31:1, 3 and 4), 1 gravity core (GC11), and a piston core (PC11) show an inverse trend from that at Big Blue Seamount summit (Figure 27, Table 5). Rather than flow focusing near the center of the depression, flow rates increase near the walls of the scarp along the peripheral. Maximum flow rates at Cerulean springs are from the two push cores, J31:1 and J31:4 with upwelling speeds of 13 and 5.5 cm/yr, respectively. Near the center of the depression flow rates range between 1.6 and 2.9 cm/yr. This focusing of flow along the base of a head scarp at Cerulean Springs could result from mass wasting occurring as fluids from within the seamount vent. Therefore, while the summit of Big Blue is currently in a constructive phase, Cerulean Springs may be in a cycle of destruction.

This model to estimate the rate of fluid flow was applied to all of the sample sites across the Mariana Forearc. Rubidium was chosen as the element to model, because Rb appears to be the most conservative element

within this geologic context. For 3 of the seamounts, Pacman summit, Quaker Seamount and Baby Blue Seamount, Rb concentrations in the upwelling fluids were indiscernible from bottom seawater values. For these seamounts, Cs was used to model flow because of its much higher concentration in the upwelling fluids and its generally conservative nature in this setting. Pore waters from the cores with the highest flow rates from each seamount were used to estimate the composition of the upwelling fluid. Flow rates and end-member compositions are presented later in this section after a discussion of pore water-sediment reactions in the sampled section so that an assessment of these reactions on the estimated end member composition can be addressed.

2.2. Chemical alteration of upwelling fluids

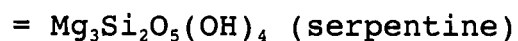
2.2.1. Major elements

Pore fluids within the Mariana Forearc serpentine mud volcanoes offer a glimpse into the conditions and reactions occurring deep within the subduction zone. In order to decipher this information from pore water chemistry, it is first necessary to examine reactions between pore fluids and the surround solid matrix as these fluids rise from the subducting slab. The original end member fluid composition

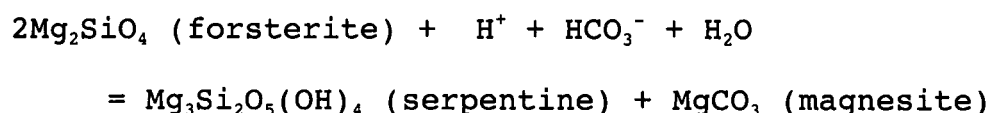
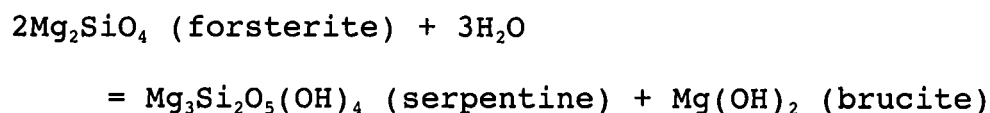
is thought to reflect slab dehydration reactions that are constrained by temperature and pressure conditions along the décollement (Mottl, 1992; Fryer et al., 1999; Mottl et al., 2004). Alteration of this fluid first occurs in the mantle above the subducting slab during the production of serpentine (e.g., Scambelluri et al., 2001; Mével, 2003). These reactions continue until the seafloor, where bottom seawater diffuses into the near-surface sediments, forming a number of alteration products (Mottl et al., 2004). By examining a wide variety of chemical species it is possible to estimate the degree of alteration and where these alterations occur that potentially mask important geochemical signals.

All the active seamounts in the Mariana Forearc contain upwelling fluids that are depleted in Mg relative to seawater, and down-core concentrations at all but Blue Moon Seamount approach an asymptotic concentration of 0 mmol/kg. The primary process that affects Mg concentrations in this system is serpentinization. If the mantle were composed of equal amounts of the magnesian end-members forsterite and enstatite, they would combine with water to form serpentine with no secondary minerals.

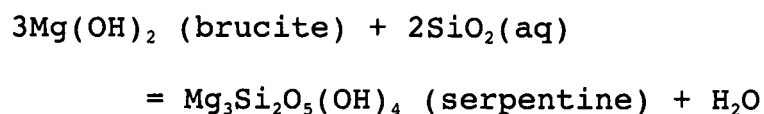




However, the depleted mantle beneath the Mariana Forearc is primarily harzburgite and dunite containing up to 99% olivine (Fryer, 1996; Parkinson and Pierce, 1998). Serpentinization of these protoliths creates a Mg excess that is then incorporated into secondary phases such as brucite or magnesite.



Brucite formation is favored under high pH and olivine-rich conditions (Bach et al., 2004) and has been observed at many of the seamounts (Fryer and Mottl, 1992; Fryer et al., 1999). Yet, brucite is almost never observed in oceanic peridotites. Snow and Dick (1995) suggest that brucite dissolves at the seafloor and reacts with dissolved silica to form serpentine plus water.



As noted above, brucite is observed in Mariana Forearc serpentinites, suggesting that the lack of brucite in ancient uplifted deposits results from retrograde reactions

during uplift with a potential source of dissolved silica coming from either terrigenous or planktonic sources.

An examination of the Mg-Ca systematics at two seamounts of differing fluid compositions shows that a significant amount of alteration of these two elements occurs in the cored sediments (Figure 28). Cerulean Springs is located at the eastern edge of Pacman Seamount and the upwelling fluid composition is high in Ca and depleted in Mg. In contrast, pore fluids from Big Blue Seamount are depleted in both Ca and Mg, but contain appreciable levels of alkalinity (>68 meq/kg). Near the surface of Big Blue, Ca in the seawater reacts with the high alkalinity to form carbonates (Mottl, 1992; Fryer et al., 1999; Mottl et al., 2003).

A closer inspection of the Ca-Mg relationships shows that Mg mobilization and removal is ongoing within the pore fluids. At Cerulean Springs, Mg removal from the fluids is apparent throughout the sediment column. In the upper 2 cm of the sediments at a site of low fluid upwelling, a depletion of nearly 3 mmol/kg of Mg occurs. In fact, none of the surface pore fluids at Cerulean Springs reach seawater values of 52.4 mmol/kg (Figure 28a). In contrast, surface concentrations of Mg at Big Blue Seamount exceed

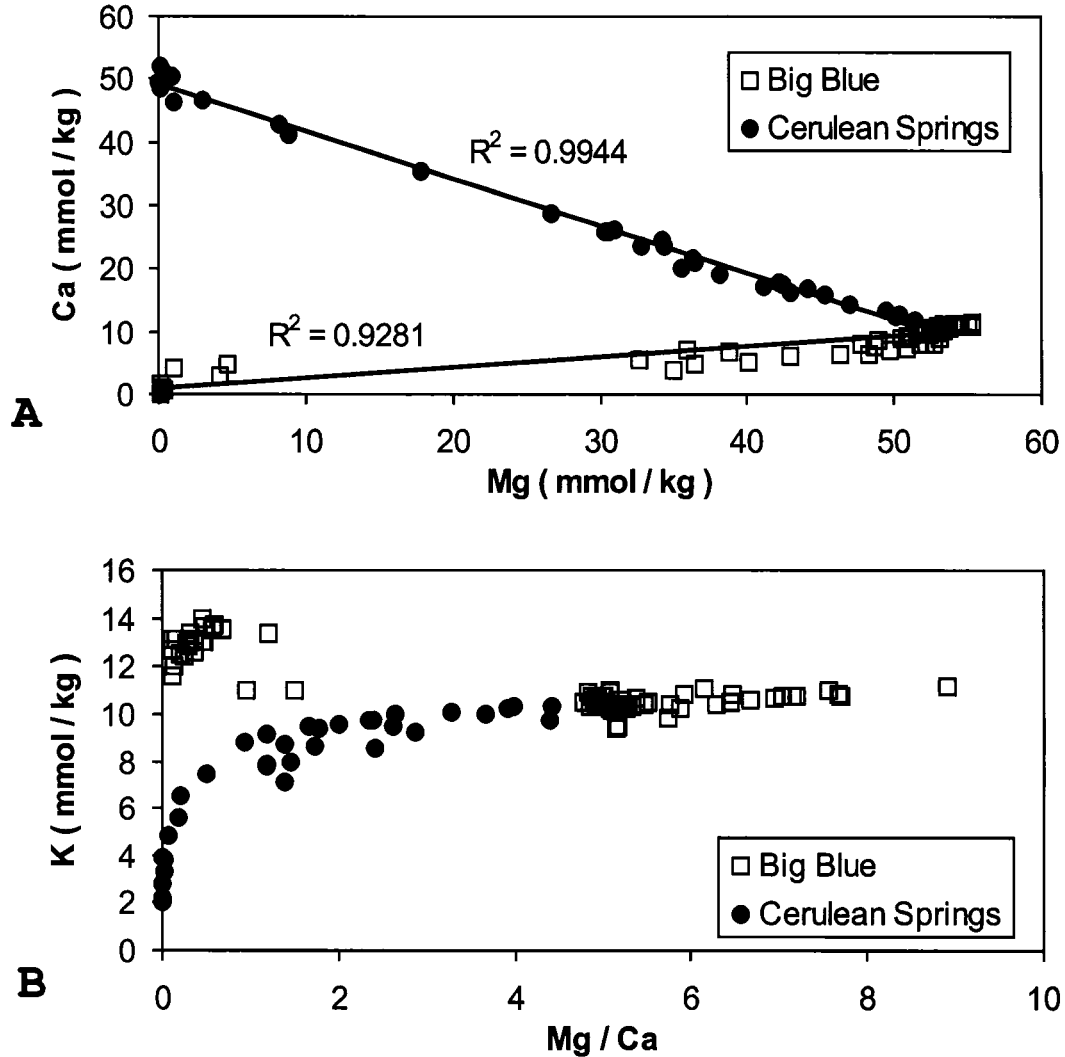


Figure 28. Plots of Mg, Ca and K in the pore fluids from Big Blue Seamount and Cerulean Springs showing the effects of alterations in the surface sediments. A) A plot of Mg vs. Ca at the two seamounts highlights the similar low Mg composition and the opposite Ca trends in the sediments. B) Plotting the more conservative element K against Mg/Ca shows how Ca is lost to carbonate precipitation at the surface of Big Blue while Mg is taken up over Ca at Cerulean Springs.

bottom seawater levels by at most 3 mmol/kg (Figure 28a). The active precipitation of brucite in the deeper sediments at both seamounts can be inferred by Mg concentrations that are completely depleted before asymptotic Ca concentrations are reached.

Potassium in the ascending fluids varies dramatically across the forearc from depleted concentrations relative to bottom seawater near the Mariana Trench (e.g. Cerulean Springs) to enriched concentrations farther from the trench (e.g. Big Blue). This trend is the result of increasing temperatures in the subducting slab, but is not associated with serpentinization reactions (Mottl, 1992; Janecky and Syfried, 1986). By plotting the conservative component K against Mg/Ca (Figure 28b), the reactions in the surface sediments at Big Blue and Cerulean Springs become even more apparent. As noted above, loss of Ca to carbonate formation in the near surface at Big Blue causes a dramatic rise in Mg/Ca. Below this zone, Mg is quickly consumed by brucite formation. At Cerulean Springs, which has low alkalinity pore fluids, the shallow slope of K vs. Mg/Ca in the near surface is the result of rapid Mg loss from the fluid, probably due to brucite precipitation.

Chlorinity values at the majority of the Mariana Forearc serpentine mud volcanoes decrease down-section, implying a freshened fluid source at depth (Mottl, 1992; Mottl et al., 2003, 2004; Fryer et al., 1999). This condition is violated at Big Blue Seamount and brings to question possible alteration reactions that may affect the chlorinity of these fluids. Sharp and Barnes (2004) examined reactions within serpentine systems that affect dissolved chloride concentrations. They found significant amounts of chloride are incorporated into serpentine both as water-soluble salts and within the serpentine lattice. The subducting oceanic crust possibly contains regions where seafloor serpentinites formed prior to subduction. For example, halite (NaCl) formation is associated with mid-ocean ridge hydrothermal processes (Sharp and Barnes, 2004). As these deposits are exposed to fluids released from the dehydration of surrounding clay minerals, soluble chlorides are mobilized and carried to the seafloor.

Experiments by Janecky and Seyfried (1986) showed that while Na and Cl can vary during serpentinization reactions, Na/Cl is conserved. Sodium vs. Cl at Big Blue and Cerulean Springs show two contrasting profiles (Figure 29). There is a high linear correlation coefficient (0.9968) between

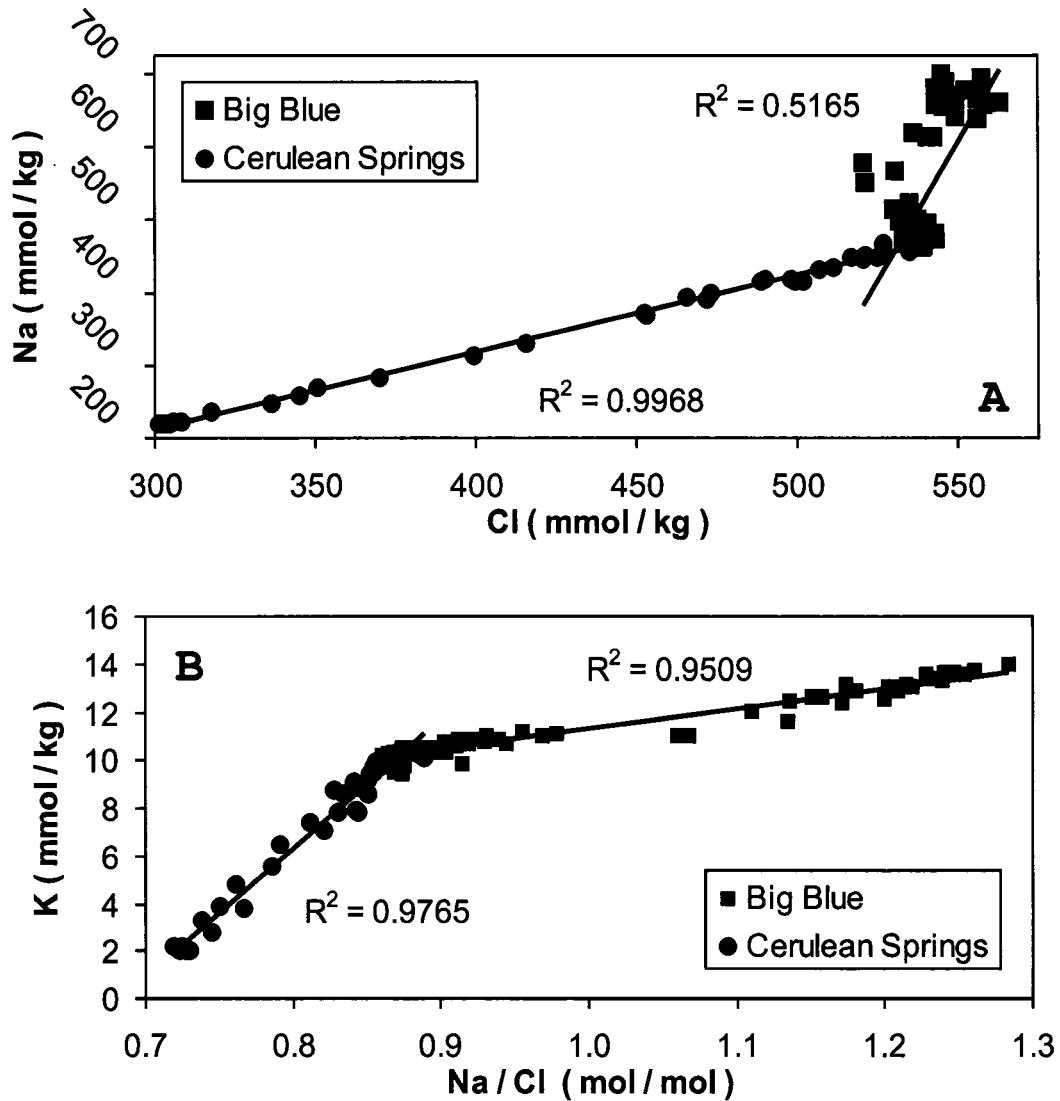


Figure 29. Plots illustrating the relationship between Na and Cl in pore fluids from Big Blue Seamount and Cerulean Springs on Pacman Seamount.

A) Na and Cl have a linear relationship at Cerulean Springs, but the low correlation at Big Blue illustrates the effect of alteration reactions.

B) Plotting K vs. Na/Cl produces linear trends for both Big Blue and Cerulean Springs illustrating the covariation of Na and Cl in the surface sediments.

Na and chlorinity at Cerulean Springs. This trend is consistent with these two species being relatively unreactive and conservative in the upwelling fluids, and easily explained by the conservative mixing of two end members; fluid from depth and bottom seawater. In contrast, the behavior of these two components at Big Blue Seamount is non-linear, indicating that at least one of these elements is not conservative in the sampled section, implying some degree of alteration must occur. One possibility is that chloride is removed in the sampled sediment from the precipitation of chloride-bearing minerals such as iowaite ($\text{Mg}_3\text{Fe}^{3+}(\text{OH})_8\text{Cl}\cdot 2\text{H}_2\text{O}$) (Sharp and Barnes, 2004). Another possibility is that Na is substituted for Mg and/or Ca in surficial sediments, thus maintaining charge balance (e.g., Mottl et al., 2004). Magnesium is universally depleted in the upwelling fluids and is not the likely cation involved with Na exchange. In contrast, Ca-Na exchange has been observed in sediment pore water (e.g., Wheat et al., 2000). Even though Ca varies dramatically with increasing distance from the Mariana Trench axis, the Ca concentration is too low at Big Blue for the required exchange with Na. Therefore, the change in the Na/Cl ratio likely results from the removal of Cl

and a charge balance that is maintained by an increase in alkalinity.

2.2.2 Trace elements

Concentrations of Rb and Cs in sediments and subducting oceanic crust vary as a function of K concentrations during reactions involving potassic minerals (Sadofsky and Bebout, 2003; Barr et al., 2002). The behavior of Rb and Cs within the sediment column at Big Blue Seamount and Cerulean springs was analyzed to test if their original compositions are conserved in the sampled section (Figure 30). Rubidium concentrations at the two sites varied in a manner similar to K, while Cs was enriched in the upwelling fluids at both localities (Figure 30a). The linear relationship of Rb vs. Cs under these differing conditions confirms that their concentrations are minimally altered within the upper sediment column.

Mobilization of Cs in the uppermost (<10 cm) sediments at Big Blue Seamount with no corresponding increase in Rb was observed within cores taken from the most active zones of fluid flow, but the overall conservative behavior of the two elements was not violated in the deeper core sections.

Experiments of hydrothermal fluids reacting with décollement sediments under varying temperatures showed the

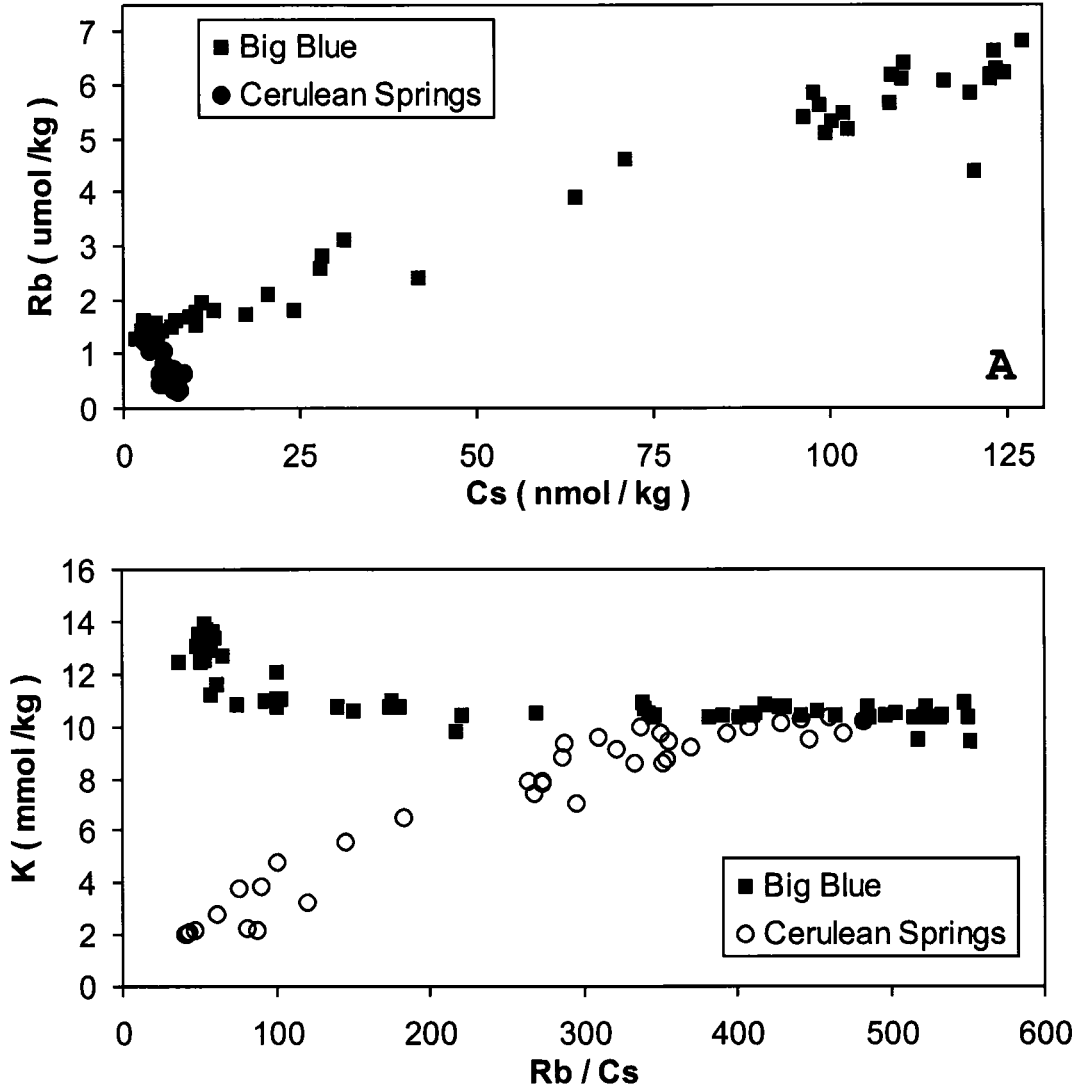


Figure 30. Variations in Rb and Cs in pore fluids recovered from Big Blue Seamount and Cerulean Springs. A) While exhibiting opposite trends in Rb, both sites show linear relationships with Rb vs. Cs throughout the sediment column. B) Rb/Cs decreases down section at both sites due to extensive Cs mobilization. Rb depletion at Cerulean Springs produces a lower final Rb/Cs ratio than Big Blue Seamount where significant Rb mobilization occurs.

progressive mobilization of Cs and Rb (You et al., 1996). In these experiments, Rb/Cs decreased continuously by the higher relative degree of Cs mobilization until reaching temperatures over 300°C. At higher temperatures, Rb mobilization outpaced Cs, producing higher Rb/Cs ratios. Thus, we can use the Rb/Cs ratio to constrain the temperature at depth. Given that the percent change in Cs is always greater than Rb, temperatures at depth must be less than 350°C. Sediment is the only source for these elements as these elements are not mobilized from peridotite.

The linear relationship between these two elements confirms the conservative properties of Rb and Cs in the upwelling fluids. We can then use the conservative nature of Rb versus other trace elements to examine the behavior of other trace elements. For example, U is uniformly depleted in upwelling fluids throughout the Mariana Forearc, but significant levels of enrichment are observed in surface sediments. A plot of U vs. Rb at Big Blue Seamount and Cerulean Springs clearly illustrates this behavior (Figure 31a). Uranium in surface pore waters from Big Blue Seamount are enriched by a factor of 3.5 over bottom seawater concentrations, while no significant

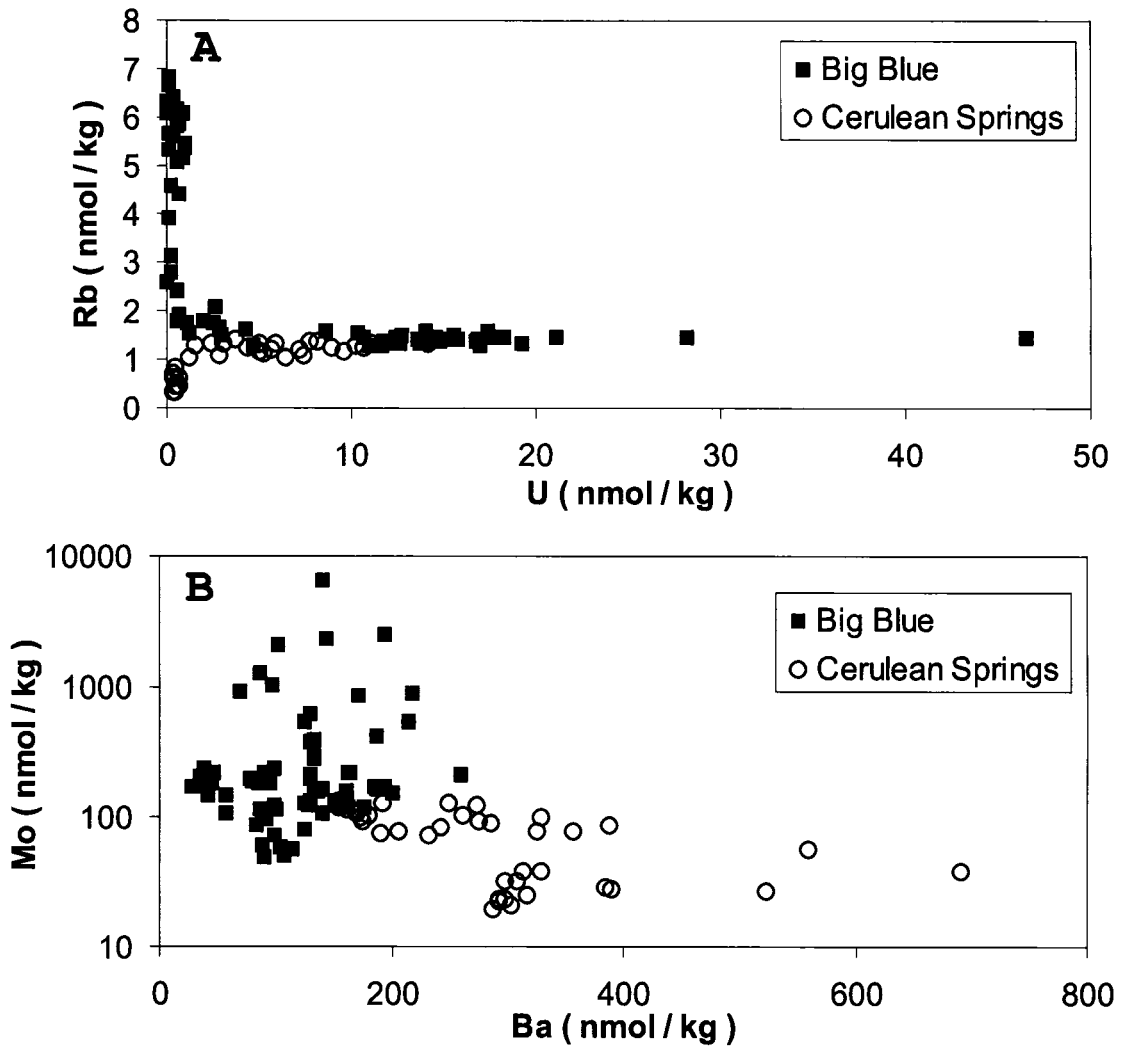


Figure 31. Trace element patterns at Big Blue Seamount and Cerulean Springs. A) Uranium concentrations at both seamounts approach zero values at depth. The presence of carbonate ions at Big Blue allows for increased levels of U to concentrate within the upper sediments. B) Each seamount exhibits distinctive patterns of Mo vs Ba as a result of differing sulfur species. Low sulfate at Cerulean Springs allows for Ba to remain mobile in the sediments. Sulfide production at Big Blue Seamount mobilizes Mo to two orders of magnitude above seawater levels.

mobilization of U occurs at Cerulean Springs. These distributions are related to microbially-mediated redox conditions with U being released during Mn and/or Fe oxidation.

Additional trace elements experience differing degrees of mobilization based on interactions with major species present in the pore fluids. Sulfate and sulfide concentrations at Big Blue Seamount and Cerulean Springs have a marked affect on the degree of Mo and Ba mobilization (Figure 31b). At Cerulean Springs, depleted sulfate levels (8.5 mmol/kg) allow Ba mobilization that is normally inhibited by the formation of barite (BaSO_4). Enhancing Ba mobilization are elevated concentrations of Ca (49.5 mmol/kg) and Sr (0.32 mmol/kg), which saturate the solution with respect to their sulfate minerals gypsum ($\text{CaSO}_4 \cdot 2(\text{H}_2\text{O})$) and celestite (SrSO_4). The precipitation of these minerals will increase Ba mobilization (You et al., 1996). In contrast, low Ba concentrations occur at all depths in cores recovered from Big Blue Seamount, which has elevated levels of sulfate relative to seawater (30 vs. 28 mmol/kg). Here, the precipitation of witherite (BaCO_3) in these high alkalinity fluids could potentially remove additional Ba.

Molybdenum mobilization occurs dramatically (up to 6,420 nmol/kg) at Big Blue Seamount. The Mo mobilization appears in intervals with increased concentrations of dissolved Mn. Previous studies described the mechanism of removing Mo from solution by adsorption onto Mn oxyhydroxides (e.g. Bertine and Turekian, 1973; Emerson and Husted, 1991). This suggests that Mo mobilization is related to microbially-mediated dissolution of oxyhydroxides. Minimal Mo enrichment relative to the bracketing core intervals is apparent at Cerulean Springs and also is associated with Mn mobilization.

The observed surface sediment enrichments and depletions in Ba and Mo at both seamounts are mirrored in the composition of the upwelling fluids. Concentrations of Ba and Mo in the deepest core sections at Big Blue Seamount converge at values of 47 and 220 nmol/kg, respectively, and concentrations of Ba and Mo at Cerulean Springs converge at inverse values of 297 and 20 nmol/kg, respectively (Figure 31b). This is of great interest because it implies that processes that occur in the surface sediments may also be occurring at depth where the fluids are produced from a sediment matrix.

Mobilization patterns in pore fluid profiles for Mn and Fe display a large degree of symmetry, many of the remaining transition metals (Co, V, Cr and Cu) display profiles that appear to behave opposite to or independent of Fe and Mn (Figures 18 and 19). The underlying reason for the observed profiles in the upper sediment section are related to microbially-mediated redox states that in part result in the consumption of Fe-Mn oxyhydroxides and the precipitation of metal sulfides (Poulton et al., 2004). The reduction of oxyhydroxides result in the mobilization of Fe and Mn, which can then react with dissolved hydrogen sulfide to precipitate pyrite and metal sulfides. The presence of large amounts of carbonate and hydroxide ions further complicates the shape of the profiles, by increased metal-carbonate and metal-hydroxide complexing and precipitation (Zachara et al., 2000).

Reactions among Fe, Mn, carbonates, oxyhydroxides and sulfur species impact the degree of mobility for a variety of other transition metals. For example, at Big Blue Seamount, Co enrichment occurs within the zone of Fe and Mn depletion (Figure 19). Experiments by Zachara et al. (2000) demonstrated the preferred dissolution of Co(II) over Fe(II) from oxyhydroxides. Nickel showed the same

behavior as Co under these conditions, and shows significant mobilization along with Co at Big Blue Seamount. In contrast, pore fluids from Cerulean Springs do not show the same magnitude of Co enrichment, and samples that are enriched do not exhibit significant Ni mobilization. Instead, a correlation between Co and Cu exists at Cerulean Springs (Figure 19). This suggests the possibility of remobilization of chemical species that were incorporated into serpentine at depth under reducing conditions can be mobilized at the surface.

Serpentinization at depth has a significant effect on the transition metals because the fluids are reducing and hyperalkaline. Water reacting with basaltic crust will rapidly become acidic causing metals to mobilize, but serpentinization consumes metals sequestering them into native and sulfur species depending on water-rock ratios (Palandri and Reed, 2003). High water-rock ratios release additional sulfur into the system, which is reduced and forms metallic sulfides. Low water-rock ratios in serpentinizing fluids are also reducing, but in the absence of available sulfur will form native metals and/or oxyhydroxide species.

2.2.3. Rare Earth Elements

The rare earth elements (REE) constrain valuable parameters for conditions at the décollement, because REEs have a unique chemical fingerprint afforded by similar but different atomic properties. The mass-dependent and redox-sensitive properties of REEs have been studied in the laboratory under ambient temperature and pressure (25°C, 1 atm) (e.g. Millero, 1992; Byrne and Li, 1995; Lee and Byrne, 1991; Liu and Byrne, 1997; Luo and Byrne, 2003) with limited studies at higher temperatures and pressures (e.g. Gammons et al., 1996; Williams-Jones and Wood, 1991; Lee and Byrne, 1994). Unfortunately, no studies have been conducted at the extreme pressure (1 GPa) and temperatures (100–300°C) that likely exist beneath the Mariana Forearc along the décollement. It is, however, possible to compare the theoretical behavior of the REEs to observed patterns of REE in pore fluids from Mariana Forearc mud volcanoes to assess how REEs respond under these physical conditions.

Complexing of the REEs with many of the major ions present in the pore fluids has the potential to enable their mobilization. Carbonate complexing often dominates in high pH solutions such as those found in the Mariana Forearc (Schijf and Byrne, 2003; Lee and Byrne, 1991;

Millero, 1992). Lee and Byrne (1994) conducted experiments on Gd carbonate complexing at 500 atm and discovered a 5-fold decrease in carbonate complexing. Pressures at the slab mantle interface below the Mariana mud volcanoes are more than 20 times this experimental pressure, implying decreased mobility because of carbonate complexing. Yet the elevated temperatures increase complexing and mobility. The combination of the increase in temperature and pressure at this site appears to minimize mobility because of the extreme pressure in this geologic setting. Another possibility is REE complexation with sulfate. These complexes are highly dependent on pH, and at the high (up to 12.5) pH conditions, sulfate complexation would have little effect on REE mobilization (Schijf and Byrne, 2003). Chloride complexes become significant at the high temperatures (150-300°C; Mottl et al., 2004), but as the pH increases, the complexing ability decreases by orders of magnitude (Gammons et al., 1996). Therefore, we only expect increased mobility in high alkalinity fluids.

Concentrations of REEs in pore fluids from Mariana Forearc mud volcanoes are uniformly depleted relative to bottom seawater (Figure 21). One possibility is that carbonates co-precipitate REEs from solution. Evidence for

carbonate co-precipitation is clear in push core J36:4, which was taken from a region of high fluid flow at the summit of Big Blue Seamount (Figure 20). Significant levels of LREE depletion are present in the uppermost sediments where the carbonate-rich pore fluids react with Ca-rich seawater to form carbonates. Scavenging by Fe-oxyhydroxides has been documented as producing positive La, Gd, Lu and Y anomalies (Bau, 1999), and must not be overlooked in this system. Another possibility is that REE are not mobilized in such settings, consistent with bulk chemical analyses of land-based blueschist formations (Bebout et al., 1999) and require much warmer temperatures for mobilization to occur (e.g. Klinkhammer et al., 1994).

3. Source of the Fluids

3.1. Major element end-members

Estimated end-member approximations for the upwelling fluid compositions are based on asymptotic profiles within cores exhibiting the fastest upwelling speed based on pore water profiles (Table 6). Concentrations of the major elements in end member fluids exhibited clear differences across the Mariana Forearc that are useful in predicting the depth to the subducting slab and P/T conditions

	(max)	(min)	Ca	K	Na	Cl	Na/Cl	pH	Alk	Sulfate	Sulfide
Flow	cm / yr	Mg	mmol / kg	mmol / kg	mmol / kg	mmol / kg	mol / mol		meq / kg	mmol / kg	umol / kg
Bottom Seawater		52.4	10.2	10.1	466	542	0.86	8.1	2.3	28	0
Blue Moon*	10.3	6.4	>54.2	<5.19	<398	<469	<0.85	>8.2	<0.3	<27	275
Pacman BB Mitt	13.6	0	49.5	2.2	220	304	0.72	10.8	2.3	8.5	0
Nip	3.07	0.2	74.8	3.7	360	501	0.72	10.7	3.1	6.9	232
Blip*	2.11	20	>33	<7.64	<420	<487	<0.86	>8.3	<1.3	<23	0
Pacman Summit*	0.31	44	<6.9	10.1	464	<525	0.89	>8.9	<1.0	<25	2
Quaker	0.56	0.5	18.1	9.39	461	427	1.08	9.2	0.8	23	0
Baby Blue*	0.36	40	<6.9	10.5	>489	<527	>0.93	>9.0	<1.0	<22	0
Big Blue	36.3	0.1	0.3	13.8	688	546	1.26	12.3	68.7	30	1320
S. Chamorro**		0	0.3	19	610	510	1.2	12.5	62	28	250
Conical*	0.49	3.44	<3.58	>14.3	<452	<427	>1.05	>9.2	>1.4	>29	0
Conical**		0.1	1	15	390	260	1.5	12.5	52	46	250

Table 6. Major element composition of the upwelling fluids across the Mariana Forearc. The maximum flow rates at each site as well as the minimum Mg are given to show the proximity to an end-member composition (ie. high flow, low Mg). Where the end-member compositions were not reached, the minimum or maximum values are shown based on the down-core asymptotic trends in composition. Conical Seamount estimates are shown along with measured end-member values from ODP Leg 125 drilling results (Mottl, 1992). * asymptote not reached ** ODP Drilling results

therein. The two most consistent major element patterns across the forearc are Na/Cl ratio, K and Na. For Example, the Na/Cl ratio shows a pattern of increasing concentrations with increasing depth to the slab (Table 4; Table 6). By using this ratio as a conservative indicator of increasing depth to the slab, errors from modeling the slab depth based on distance to the trench axis and the subduction angle are adjusted. The most obvious of these adjustments is the estimate for the slab depth below Quaker Seamount. On the basis of Na/Cl ratios, the depth to the slab is estimated to be < 25 km, but it is most probable that the depth is 23 km, which is the average depths below Baby Blue Seamount and Pacman Seamount summit. This is a correction of 2-3 km from the previous estimate of 26 km. The cause for this expected difference could be the presence of a large seamount that is being subducted below Quaker Seamount.

The increase in K across the forearc has been attributed to increasing temperature along the subducting slab (Mottl, 1992; Fryer et al., 1999; Mottl et al., 2004). These estimates of temperature are based on K concentrations from laboratory experiments conducted at much lower pressures and reactions of seawater with basalt

(Mottl et al., 2004). The experiments show K being consumed during secondary mineral formation at temperatures <150°C. At higher temperatures, K is released from the basaltic matrix, raising the K concentration above bottom water concentrations.

The Na trend across the forearc offers additional constraints for temperature and pressure based on the dramatic decrease in Na at Conical Seamount. End member concentrations of Na steadily increases with depth to the slab, likely resulting from exchange with Ca, until a drop of >200 mmol Na/kg in fluids from Conical Seamount. Albitization, which occurs when K-feldspar within the sediments consumed Na to form albite, is a potential sink for Na. If so, then this albitization coincides with the Lawsonite-Albite metamorphic phase shift, observed in Franciscan metasedimentary suites to form at ~0.7-0.8 GPa and peak temperatures of ~250°C (Sadofsky and Bebout, 2003). If albitization occurs under Conical Seamount at a depth of ~30 km, then the P/T conditions are well constrained in the décollement region. This loss of Na under Conical can also be compounded by the formation of Na-amphiboles and Na-pyroxenes, such as jadeite, which also would mark the transition to higher metamorphic facies.

The increase in alkalinity at greater distances from the trench are not the result of decarbonation from thermal sources through the mechanism described by Kerrick and Connolly (2001). The low-temperature isotherms in the Mariana Forearc inhibit devolatilization to depths possibly exceeding the depth of arc magmatism. The source of the carbonate in the Mariana mud volcanoes can thus be attributed to the dissolution of carbonates (Mottl et al., 2003, 2004). This may occur as a by-product of mineral phase shifts, or upon reaching critical water/rock ratios at a dehydration phase boundary. The formation of Lawsonite through the dehydration of zeolite minerals was described for medium-grade Franciscan metasedimentary rocks, and was thought to be associated with slight decarbonation of carbonate cements (Sadofsky and Bebout, 2003). A minimum P/T boundary for carbonate mobilization to occur is estimated at 0.3 GPa and ~100°C, based on the occurrence of unaltered carbonate cements in the Coastal Belt of the Franciscan Metamorphic Complex.

3.2. Minor and trace element end-members

The estimates of upwelling compositions of minor and trace elements within the Mariana Forearc mud volcanoes do not all exhibit the same consistent patterns across the

forearc that the major elements show (Table 7). The elements that show a lack of systematic trends are Li, Si, and Ba. Silica and Ba concentrations fluctuate widely and can be attributed to secondary reactions both at the slab-mantle interface and the surface sediments. Barium within décollement sediments exhibits mobility under experimental conditions of elevated temperature but is rapidly removed in the presence of sulfates (You et al., 1996). This can be seen in the elevated concentrations at Nip Seamount, which contains low sulfate (Table 6). This mobility at Nip Seamount does indicate temperatures greater than 150°C based on the aforementioned experiments at 800 bar. The degree of mobilization at the much greater (~5 kbar = 0.5 GPa) pressures that would occur at the estimated slab depth of 17 km, can not be determined.

The Li end-member estimates were significantly higher at Pacman Seamount summit, Quaker Seamount, and Baby Blue Seamount. Lithium was found at elevated concentrations within the solid serpentine phases at Conical Seamount (Benton et al., 2004). These enrichments occur in layers within the serpentine pointing towards episodic releases of Li into the fluids. There is currently no observed pore fluid enrichment, however, at Conical Seamount.

	(max)		(min)		Mg	B	Li	Si	Sr	Rb	Cs	Ba	U
	Flow	cm / yr	mmol / yr	umol / kg									
Bottom Seawater			52.4	410	26	190	90	1.37	2.2	140	13.5		
Blue Moon*	10.3	6.4		<7.8			>645	<0.72	<2.7	158	<0.4		
Pacman BB Mitt	13.6	0	15	2.1	2770	320	0.45	5.6	297	0.31			
Nip	3.07	0.2	36	15.3	1120	914	1.82	69.2	1025	0.12			
Blip*	2.11	20	<185	<14.2	104	>563	<1.23	>6.1	>277	<2.4			
Pacman Summit*	0.31	44	<387	>30.3	35	<56	>1.4	>9.1	<118	<0.28			
Quaker	0.56	0.5	830	119	1060	205	1.57	96.0	125	0.01			
Baby Blue*	0.36	40		>31		<61	>1.69	>10.3	216	<0.54			
Big Blue	36.3	0.1	1500	0.9	<990	10	6.65	123	47	0.08			
S. Chamorro		0**	3000**	0.4**	84.6**	10**	10**	53.5**	400**	<0.1***			
Conical*	0.49	3.44	>890	<6.4	<41	<78	>5.3	>61.6	<135	0			
Conical**		0.1	3900	1.6	60	20	7.8		100				

Table 7. Minor and trace element composition of the upwelling fluids across the Mariana Forearc. The maximum flow rates at each site as well as the minimum Mg are given to show the proximity to an end-member composition (ie. high flow, low Mg). Where the end-member compositions were not reached, the minimum or maximum values are shown based on the down-core asymptotic trends in composition. Conical Seamont estimates are shown along with measured end-member values from ODP Leg 125 drilling results (Mottl, 1992). * asymptote not reached ** ODP Drilling results *** borehole fluid sample

Benton et al. (2004) described the variable Li release as being a result of enriched sections of the mantle convecting beneath the forearc. An alternative to this however, could be a sediment source at depth. The subduction of a seamount can potentially incorporate a large mass of sediment in its wake (e.g. Lallemand et al., 1989). To produce a regional sedimentary source, it would have to cover a linear distance of over 100 km and not affect any of the neighboring seamounts. A more possible situation is that a mineral phase shift that is limited to a narrow P/T range is responsible for mobilizing Li in this region.

Strontium concentrations mirror Ca across the forearc, which can be accounted for by interactions with carbonates, and mobilization due to the transformation of smectite to illite. Uranium is universally depleted at all the seamounts, which agrees with studies of the Catalina Schist that show limited to no U mobilization at depths of 50 km and temperatures as high as 600°C (Bebout et al., 1999). This is attributed to the complexing of U into the mineral-compatible U^{4+} under reducing conditions. Boron increases continuously with increasing depth to the décollement as a

result of continued mobilization as the temperature is raised (Benton et al., 2002; You et al., 1996).

The elemental relationship between Rb and Cs has been the subject of detailed investigations into conditions within subduction zones (Bebout, 1995; You et al., 1996; Bebout et al., 1999; Busigny et al., 2003; Sadofsky and Bebout, 2003). Studies have demonstrated the increased mobility of Cs over Rb during dehydration of the subducting slab by observing increases in Rb/Cs in low-grade vs. high-grade metamorphic facies in the Catalina Schist, a low P/T paleosubduction zone (Bebout, 1995). Potassium concentrations under these conditions co-vary with Rb with increasing metamorphic grade while Cs is preferably removed from the metasedimentary rocks (Sadofsky and Bebout, 2003).

In the Mariana mud volcanoes, Cs mobilization outpaced Rb, similar to the Catalina Schist pattern, until a sudden increase in the degree of Rb mobilization at Big Blue Seamount (Figure 32). The K increase occurred prior to the Rb mobilization which points towards separate sources for fluid generation. Differences in the K/Rb ratios have been demonstrated in altered sediments vs. oceanic basalt (Plank and Langmuir, 1998). The shift from low Rb/K to higher values at Big Blue Seamount may show a transition from

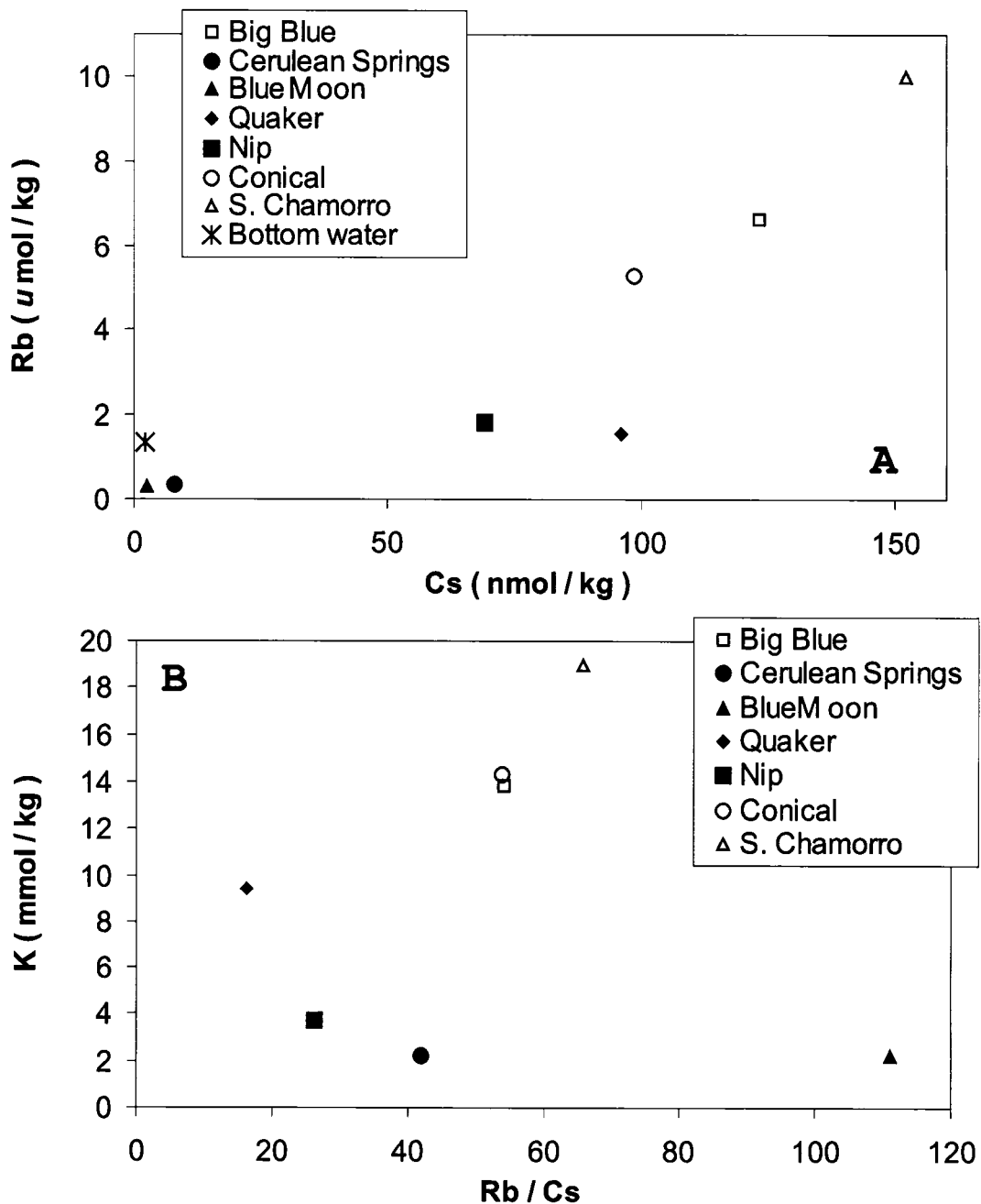


Figure 32. Rb/Cs systematics of the Mariana Forearc mud volcanoes. Cesium concentrations for Conical and S. Chamorro seamounts are from linear extrapolations with Rb end-members determined from ODP Leg 125 and 195 drilling. A) The slope of Cs vs. Rb changes between Quaker and Big Blue seamounts. B) As K increases with depth to the subducting slab Cs is preferably mobilized, lowering the Rb/Cs ratio. At Big Blue Seamount this trend is reversed as Rb mobilization increases.

dehydrating sediments to dehydration of the basaltic ocean crust. This fractionation can be facilitated by open-system behavior, compared to observations of metasediments of the Schistes Lustrés nappe that Rb/CS is conserved to depths of 90 km and temperatures of 600°C (Busigny et al., 2003). Due to the variability of concentrations within rock samples and uncertainty of paleosubduction zone open vs. closed system behavior, fractionation of these elements at shallow depths within high P/T systems, such as the Franciscan Complex (Sadofsky and Bebout, 2003), has not been discerned.

3.3. Transition metals

The transition metals, as described in the previous section, exhibited strong redox behavior and were not conservative within the sediment column. The best approximation of their activity within the seamounts can therefore only be given as the concentration within the deepest section of the core with the highest flow rate (Table 8). Higher degrees of mobilization are evident at seamounts with low flow rates. Quaker and Baby Blue seamounts both have minimal rates of flow and are enriched in almost all the transition metals. Higher flow rates such as those at Cerulean Springs (Pacman Baseball Mitt)

	V	Cr	Mn	Fe	Co	Ni	Cu	Zn	Y	Mo	Cd
	nmol/ kg	nmol/ kg	umol/ kg	umol/ kg	nmol/ kg	nmol/ kg	nmol/ kg	nmol/ kg	nmol/ kg	nmol/ kg	nmol/ kg
Bottom Seawater	38.4	4.9	<0.05	<0.005	0.03	13	5.6	10	0.33	100	1.2
Blue Moon*	1.2	0.4	2.8	0.4	0.04	2	1.4	2	0.004	30	0.011
Pacman BB Mitt	25.1	3.6	8	11.5	0.05	18	4.8	5	0.008	20	0.013
Nip	0.8	1.0	2.2	3.0	0.25	10	2.4	16	0.001	198	0.013
Blip*	40.7	2.2	0.9	1.1	0.88	62	21	44		50	
Pacman Summit*			2.5	0.5							
Quaker	80.3	14	1.6	2.5	1.7	69	14	169		36	
Baby Blue*	5.4	574			9.9	503	32	2	0.001	198	0.014
Big Blue	37	1.1	10	21	0.23	35	5.0	5	0.001	220	0.002
S. Chamorro	16.3***	1.0***	0.07**	6.9**	0.11***	4***	13***	5***	.003***	24***	0.05***
Conical*	113	25	<0.01**	2**	1.7	326	8.9	24		42	

Table 8. Transition metal concentrations in the upwelling pore fluids across the Mariana Forearc. The values given are from the deepest section of the core with the highest flow rate at each site. Asymptotic values were not reached in any of the cores due to complex gradients caused by redox reactions in the sediment column. ODP Leg 125 (Conical) and Leg 195 (S. Chamorro) drilling results are given where available. ** ODP Drilling results *** borehole fluid sample

and Big Blue Seamount produce lower concentrations of transition metals, with the exception of Fe and Mn. The high concentrations of Fe and Mn could indicate a source at depth due to the rapid flow rates. The lack of the remaining transition metals could indicate scavenging by oxyhydroxides, sulfides, or carbonates that are catalyzed by the presence of high Fe and Mn. Due to the significant mobilization of Co and Ni at Big Blue, the source fluid could also be enriched in these components. Blue Moon Seamount, with a high rate of flow is uniformly depleted in transition metals, and could reflect the source. Higher resolution sampling is needed to resolve the exact boundaries between redox zones and better interpret the data.

3.4. Rare earth element end-members

The REE concentrations within all the serpentine mud volcanoes were significantly depleted relative to bottom seawater (Table 9; Figure 21). This is the result of two possible scenarios; the REEs are being consumed by the active precipitation of carbonates and Fe-oxyhydroxides, or the depleted REE patterns reflect a depleted source at depth. If the former is the case, there should be a correlation between the concentration of dissolved iron and

	Bottom		Blue		Pacman		Baby		S.	
	Seawater	Moon*	BB	Mitt	Nip	Blue*	Big	Blue	Chamorro	
La	43.8	1.3	3.0	0.4	0.76	1.8	1.1***			
Ce	4.7	2.1	5.4	2.4	0.34	3.7	1.3***			
Pr	5.3	0.31	0.79	0.19	0.12	0.40	0.18***			
Nd	24.0	1.1	3.3	0.57	0.55	1.2	0.97***			
Sm	4.0	0.27	0.75	0.13	0.07	0.08	1.2***			
Eu	1.2	0.11	0.14	0.04	0.03	0.01	0.03***			
Gd	7.4	0.3	0.74	0.19	0.17	0.19	0.28***			
Tb	1.0	0.05	0.11	0.01	0.009	0.02	0.02***			
Dy	9.2	0.26	0.64	0.16	0.08	0.08	0.16***			
Ho	2.4	0.06	0.14	0.02	0.02	0.02	0.02***			
Er	9.0	0.15	0.39	0.04	0.04	0.05	0.06***			
Tm	1.3	0.02	0.07	0.008	0.01	0.006	0.006***			
Yb	9.5	0.17	0.28	0.09	0.03	0.13	0.07***			
Lu	1.7	0.03	0.05	0.01	0.02	0.01	0.02***			

Table 9. End-member REE composition (pmol/kg) of the upwelling pore fluids within the Mariana Forearc serpentine mud volcanoes. All the upwelling fluids are depleted relative to bottom seawater. Mud volcano pore fluids near the trench contained higher concentrations of the REE than the deeper-sourced fluids. Big Blue Seamount concentrations show a slight LREE-enriched pattern. LREE mobilization occurs at Big Blue Seamount which could reflect a slab component. * asymptote not reached *** borehole fluid sample

carbonates with REE concentrations. This is clearly not the case for concentrations of Fe in the fluids. Cerulean Springs and Big Blue Seamount both are significantly enriched in dissolved Fe, but the REE patterns and concentrations at the two sites are distinctly different. The presence of carbonate at Big Blue could be the cause of REE immobilization, but this cannot account for depletions at Nip Seamount or Baby Blue Seamount where alkalinity is drastically lower.

What could account for the REE depletion in seamounts displaying minimal alkalinity is that the reactions removing REE from solution are occurring in the slab. Some mobilization of carbonate could be occurring at depth, but it may be rapidly removed by reaction with Ca to form carbonates. In the process of doing this, the trace amounts of REE in solution could be scavenged almost completely. What this would suggest then, is that the decrease in REE concentration is an indicator of the depth at which carbon mobilization begins to occur. This carbon does not make it to the surface, but could possibly be transferred into the mantle or react with available H₂, forming hydrocarbons that are brought to the surface with the upwelling fluids.

Big Blue Seamount REE patterns, although depleted, do show an indication of LREE enrichment. This was theorized by You et al. (1996) after observing LREE mobilization under hydrothermal reaction with sediments. Given the possibility of significant depletion by carbonate formation at depth, the presence of a LREE enrichment could be significant. LREE depletion was observed in blueschist grade metasediments that formed at pressures of 0.6 to 0.9 GPa and temperatures between 150 and 300°C; but this was interpreted as the protolith REE pattern and not the result of LREE mobilization (Sadofsky and Bebout, 2003). There still remains the possibility of LREE mobilization within sediments undergoing Lawsonite-Albite to Lawsonite-Blueschist metamorphism.

Could the enrichment of REEs in solution near the trench (Cerulean Springs and Blue Moon) relative to the farther removed seamounts be the result of mobilization at the décollement? If mobilization at the hydration source were to occur, this would result from increased temperature as the slab subducts and REE concentrations would increase with distance from the trench. There is however, the possibility of separate dehydration reactions occurring at discrete depths along the subducting path that are

independent of thermal conditions. If residual pore fluids still remained in the subducting slab at the depths below Cerulean Springs and Blue Moon Seamount (~15 km) one would expect to see the REE pattern reflect that of bottom seawater. However, the formation of serpentine at depth and the strongly reducing conditions could potentially erase any Ce anomaly, and a long residence time within the subducting sediments could allow the pore fluid chemistry to reach equilibrium with the sediments. This does leave open the possibility for mechanical dehydration of pore fluids within the subducting sediments at the shallowest depths of serpentine mud volcanism, but there needs to be a mechanism for removal of significant amounts of chloride. As described earlier, significant chloride can be sequestered in serpentine, but further experiments with cold fluids and peridotites at high pressures need to be done to test this theory.

There are some minor, but significant anomalies in the REE distribution of some of the seamounts. The most evident of these, a positive Gd anomaly, occurs in all but Cerulean Springs and Blue Moon suggesting that it is tied to the mechanism of REE depletion. If the Gd anomaly is associated with the formation of Fe-oxyhydroxides as

described by Bau (1999), there would also have to be anomalies for La, Ce, and Lu. This pattern does not appear to occur at any of these seamounts when compared to bottom seawater or the two seamounts that do not display a Gd anomaly. A more likely explanation for the Gd anomaly is therefore albitization. Plagioclase contains significant amounts of Gd because of its similar ionic radius to Ca, a major component of plagioclase (e.g. Goldberg et al., 1963). As this Ca is exchanged for Na during the albitization process, Gd mobilization will occur, producing a positive Gd anomaly (Wheat et al., 2002). If albitization is occurring within the subducting slab, there must be an additional supply of Na to the fluids. Possible sources are halite or sodic amphiboles, both of which could be present within the subducting slab.

V. Conclusions

The process of crustal subduction affects 43,000 km of convergent margins (von Huene and Scholl, 1991) and plays a critical role in crustal formation (e.g. von Huene and Scholl, 1991; Le Pinchon et al., 1993; Clift and Vannucchi, 2004). The current flux of recycled fluids ($0.9 \text{ km}^3/\text{yr}$) and sediments ($1.5 \text{ km}^3/\text{yr}$) through subduction zones rivals that of new continental material generated through terrestrial volcanic activity (von Huene and Scholl, 1991).

Associated with the subduction process are large earthquakes that have devastating effects of human populations. Yet, human populations benefit from rich ore deposits associated with the concentration of materials as they are recycled, and human life may never have existed without subduction zones maintaining continental land masses (Stern, 2002).

Although the general aspects of subduction-related processes have been described, there are still many unknown and unquantified parameters associated with subduction processes and the maintenance of a global crustal balance. One such important parameter is temperature within the seismogenic zone, particularly within the shallow zone

where the two margins converge. Even though these depths (< 50km) are considered shallow compared to the 2885 km depth of the mantle where the subducting slab descends (Stern, 2002), these shallow depths still extend well beyond the current reach of ocean drilling. Thus, given the lack of direct observations within this zone, the accuracy of seismic models are still limited by models related to the estimated shear stresses along the décollement (e.g. Peacock, 1990).

The Mariana Forearc is an ideal environment for examining physical and chemical properties of a shallow subduction zone because of the lack of an accretionary prism, which obfuscates the composition of formation fluids as they ascend through a thick sedimentary sequence, and the presence of serpentine mud volcanoes, which provide a direct conduit for formation fluids and altered mantle to the seafloor (e.g. Fryer et al., 1985, 1990, 1999, 2000). Active serpentine mud volcanism has only been discovered in the Mariana Forearc, where a combination of extensional tectonic forces and subducting seamounts fracture the overlying Philippine Plate allowing serpentine and associated fluids to escape from mantle depths (Mottl, 1992; Fryer and Mottl, 1992, 1997; Mottl et al., 2004).

Serpentinite seamounts resulting from this process are distributed along the outer forearc at differing distances from the Mariana Trench axis, and as a result originate from variable depths along the subducting Pacific Plate. By examining the fluid composition within these seamounts it is therefore possible to estimate the chemical and thermal properties of the subducting slab at discrete depths as it descends towards the zone of arc magmatism. In addition, significant enrichments of fluid-mobile elements in the serpentine fluids can constrain fluxes beneath the outer forearc, increasing the accuracy of current subduction zone mass-balance estimates, which are poorly constrained in present budgets (e.g. Bebout, 1995).

In 2003, a comprehensive mapping and sampling survey of several serpentine mud volcanoes in the Mariana Forearc was conducted. Bathymetric mapping of seamounts and surrounding regions confirmed previous observations of their associations with fault structures in the forearc basement. High-resolution sidescan reflectivity measurements of summit regions indicated recent serpentine emplacement and fluid expulsion. Sidescan images were coupled with ROV and navigated piston core sampling locations to verify these features as the locus of active

fluid flow, which was confirmed with systematic variations in pore water chemical gradients coupled with theoretical advection-diffusion models to identify the most active locations for fluid transport. Fluid advection rates varied systematically in relation to the geomorphology, consistent with a point-source for fluid flow out of the serpentine mud volcanoes.

Asymptotic concentrations of elements from cores taken in high flow areas were used to predict the composition of the fluid at depth. Systematic variations were evident across the forearc as a function of distance to the Mariana Trench and/or predicted slab depth. At Blue Moon Seamount, the seamount nearest the trench, only Ca and Sr were found in concentrations greater than seawater, reflecting a fluid source from the transformation of smectite to illite. The lack of a Cs enrichment sets an upper bound on temperature at 80°C based on experimental observations summarized in Mottl et al. (2004). At Cerulean Springs, which is further from the trench axis, Cs mobilization occurs, consistent with a temperature in excess of 80°C, implying the 80°C isotherm is at 13 to 16 km below the seafloor.

Further from the trench axis, representing slab depths of 17 to 24 km, pore fluids lack significant Rb and K

enrichments relative to seawater, placing an upper bound on temperature at 150°C. Mobilization of B occurs in fluids sampled at Quaker Seamount placing this upper bound at less than 24 km slab depth, based on laboratory experiments (You et al., 1996). The REE patterns at these seamounts differs from those near the trench by the presence of a distinct positive Gd anomaly, suggesting that albitization begins at depths >16 km beneath the Mariana Forearc. The low Rb/K and Rb/Cs at all of these intermediate seamounts points towards a sedimentary source of fluids generated from the dehydration of altered clays at depth (Plank and Langmuir, 1998).

The chemical composition of upwelling pore fluids at Big Blue Seamount is consistent with higher temperatures. The depth to slab is ~25 km below the seafloor and the minimum temperature is 150°C, based on elevated concentrations of Rb and Cs (Mottl et al., 2004). At these depths and greater, carbonate in excess of Ca is released from the slab into the fluids, resulting in drastic depletions of Ca and Sr relative to bottom seawater. Sulfate levels are greater than seawater, which limits the degree of Ba mobilization; and the transition metals Fe, Mn and Co show elevated concentrations in the upwelling fluids

from these greater depths. The ratios of Rb/K begin to increase, reflecting more of a basaltic source for these fluids. Some LREE enrichment is visible at Big Blue seamount, but it was not possible to confirm this as the result of higher temperatures because of a lack of end-member samples from Conical and S. Chamorro seamounts.

These new insights into the thermal conditions and elemental mobilizations within an actively subducting slab will not only aid in modeling active subduction zones, but also interpreting exposures of paleosubduction zones around the world. A series of exposed metamorphic terrains exist along western North America where subduction occurred through much of the Mesozoic; and the thermal history was thought to be similar to those of the Mariana Subduction Zone. Sequences of previously subducted sediments and oceanic crust are now exposed due to tectonic processes associated with transform motion along the San Andreas Fault. Considerable work has been done to interpret the formation histories of these units (e.g. Coleman, 2000; Bebout et al., 1999; Sadofsky and Bebout, 2003), but some of the details of the system are unknown due to retrograde reactions that occur during exhumation from depth.

By combining the information gained through studying active Mariana Forearc serpentine mud volcanoes with the mineral assemblages of exposed metamorphic sequences, constraints on the closed vs. open system behavior of subducting slabs can be defined. It has been found that if no conduits exist in a forearc for serpentine and fluids to emanate from, the fluid-mobile elements can be subducted to the depth of the locus of arc magmatism and no mass fractionation will occur in the forearc (Busigny et al., 2003). Other observations in the Catalina Schist of southern California have shown that fractionation does occur within oceanic crust subducted to forearc depths (Bebout, 1995, Bebout et al, 1999). With the newly available information on active chemical fluxes from the Mariana Forearc, better estimates on the fluxes from paleosubduction zones can be made.

In order to further define the mass fluxes from the slab to the mantle, additional information on the serpentine host phases must be obtained. Serpentine can potentially host considerable amounts of Cs, Rb, Cl, F, Sr, B, and Li (Mével, 2003; Tenthorey and Hermann, 2004; Savov et al., 2004; Benton et al, 2004), but the degree that this impacts the composition of the upwelling fluids has not

been examined in detail. In addition, many of the metallic species can be hosted in sulfur and oxide accessory phases within serpentinite. In order to ascertain the potential magnitude of the serpentinite elemental reservoir, studies of the serpentinite muds collected at these seamounts need to be conducted. Larger serpentinite clasts within the muds can be studied by laser ablation ICP-MS and reflected light microscopy to determine how the mineral species partition various elements.

A large serpentinite body, the New Idria Serpentinite, exists in the Diablo Range of central California that possibly formed through serpentine mud volcanism similar to what is currently occurring in the Mariana Forearc (Fryer et al., 2000; Fryer and Coleman, pers. com. 2005). This body contains many metamorphosed blueschist-grade clasts representing cool thermal conditions similar to the Mariana Subduction Zone. Numerous silica-carbonate chimneys are scattered throughout the New Idria body that could be analogous to the chimneys found near cold springs on Mariana serpentinite seamounts. Detailed comparisons of the composition and mineralogy of the metamorphics and silica-carbonates found in the Mariana Forearc and New Idria may further explain the processes that occur at depth

as oceanic slabs are subducted. Verification of the emplacement mechanism for the New Idria may also be possible through geochemical tracers found in the serpentine host that are characteristic of slab dehydration rather than seawater infiltration. One such possible tracer may be Sr isotopic ratios found in the forearc fluids and the New Idria Serpentine.

The ultimate goal of developing a comprehensive mass balance for the Mariana Forearc will be possible once models of chemical species in oceanic crust, serpentinized mantle, seafloor precipitates and venting fluids are constrained. These chemical constraints will then allow more accurate predictions of the minerals formation at depth that can then be compared to exposed metamorphic terrains, placing constraints on temperature and pressure conditions at depth. These physical constraints are critical to models of seismic activity within subduction zones not only in the Mariana region, but around the world. The downdip limit is the depth to which the seismogenic zone occurs within a subduction zone and is directly related to the landward extent of subduction related earthquakes. In warm subduction zones such as the Nankai Trough, the downdip limit is considerably shallower than a

cooler subduction zone like the Japan Trench just to the north (Peacock and Wang, 1999). In addition to temperature, the presence of hydrous minerals such as serpentine, talc and brucite can drastically decrease the downdip limit (Peacock and Hyndman, 1999). With the continued addition of empirical constraints on physical properties within subduction zones, accurate and detailed seismic models may someday be able to predict the occurrence of large magnitude earthquakes. This would enable preventive measures to be taken before the catastrophic loss of lives that currently occurs as a result of subduction-induced earthquakes.

Citations:

- Barr, S.R., S. Revillon, T.S. Brewer, P.K. Harvey, and J Tarney, 2002, Determining the inputs to the Mariana Subduction Factory: Using core-log integration to reconstruct basement lithology at ODP Hole 801C: *Geochemistry Geophysics Geosystems*, vol 3, no 11, 2001GC000255.
- Bau, Michael, 1999, Scavenging of dissolved yttrium and rare earths by precipitating iron oxyhydroxide: Experimental evidence for Ce oxidation, Y-Ho fractionation, and lanthanide tetrad effect: *Geochimica et Cosmochimica Acta*, vol 63, no 1, pp 67-77.
- Bebout, Gray E., Jeffrey G. Ryan, William P Leeman, and Ann E. Bebout, 1999, Fractionation of trace elements by subduction-zone metamorphism B effect of convergent margin thermal evolution: *Earth and Planetary Science Letters*, vol 171, pp 63-81.
- Bebout, Gray E., 1995, The impact of subduction-zone metamorphism on mantle-ocean chemical cycling: *Chemical Geology*, vol 126, pp 191-218.
- Becker, N.C., 2005, Painting by numbers: A GMT primer for merging swath-mapping sonar data of different types and resolutions: *Computers and Geosciences*, vol 31, no 8, pp 1075-1077.
- Benton, Laurie D., Jeffrey G. Ryan, and Fouad Tera, 2001, Boron isotope systematics of slab fluids as inferred from a serpentine seamount, Mariana forearc: *Earth and Planetary Science Letters*, vol 187, pp 273-282.
- Benton, Laurie D., Jefferey G. Ryan, and Ivan P. Savov, 2004, Lithium abundance and isotope systematics of forearc serpentinites, Conical Seamount, Mariana forearc: Insights into the mechanics of slab-mantle exchange during subduction: *Geochemistry, Geophysics, Geosystems*, vol 5, no 8, 2004GC000708.

- Berner, R.A., 1980, *Early Diagenesis: A Theoretical Approach*: Princeton, NJ (Princeton Univ. Press).
- Bertine, K.K. and K.K. Turekian, 1973, Molybdenum in marine deposits: *Geochimica et Cosmochimica Acta*, vol 37, pp 1415-1434.
- Bolton, Alistair J., Paola Vannucchi, M. Ben Clennell, and Alex Maltman, 2001, Microstructural and geomechanical constraints on fluid flow at the Costa Rica convergent margin, Ocean Drilling Program Leg 170: Silver, E.A., Kimura, G., Shipley, T.H. (Eds.), *Proc. ODP, Sci. Results*, 170: College Station TX (Ocean Drilling Program), pp 1-32.
- Busigny, Vincent, Pierre Cartigny, Pascal Philippot, Magali Ader, and Marc Javoy, 2003, Massive recycling of nitrogen and other fluid-mobile elements (K, Rb, Cs, H) in a cold slab environment: evidence from HP to UHP oceanic metasediments of the Schistes Lustrés nappe (western Alps, Europe): *Earth and Planetary Science Letters*, vol 215, pp 27-42.
- Byrne, Robert H. and Biqiong Li, 1995, Comparative complexation behavior of the rare earths: *Geochimica et Cosmochimica Acta*, vol, 59, no 22, pp 4575-4589.
- Chan, Lui-Heung and Miriam Kastner, 2000, Lithium isotopic compositions of pore fluids and sediments in the Costa Rica subduction zone: implications for fluid processes and sediment contribution to the arc volcanoes: *Earth and Planetary Science Letters*, vol 183, pp 275-290.
- Cline, J. D., 1969, Spectrophotometric determination of hydrogen sulfide in natural waters: *Limnology and Oceanography*, vol 14, pp 454-458.
- Domanik, Kenneth J. and John R. Holloway, 1996, The stability and composition of phengitic muscovite and associated phases from 5.5 to 11 GPa: Implications for deeply subducted sediments: *Geochimica et Cosmochimica Acta*, vol 60, no 21, pp 4133-4150.

- Emerson, S.R. and S.S. Husted, 1991, Ocean anoxia and the concentration of molybdenum and vanadium in seawater: *Marine Chemistry*, vol 34, pp 177-196.
- Fryer, Patricia, 2002, Recent Studies of Serpentinite Occurrences in the Oceans: Mantle-Ocean Interactions in the Plate Tectonic Cycle: *Chemie der Erde Geochemistry*, vol 62, pp 257-302.
- Fryer, Patricia, John P. Lockwood, Nathan Becker, Stephen Phipps, and Clifford S. Todd, 2000, Significance of serpentine mud volcanism in convergent margins: Geological Society of America, Special Paper 349, pp 35-51.
- Fryer, P., Wheat, C. G., Mottl, M.J., 1999, Mariana blueschist mud volcanism: Implications for conditions within the subduction zone: *Geology*, vol 27, no. 2, pp 103-106.
- Fryer, Patricia and Michael J. Mottl, 1997, Shinkai 6500 investigations of a resurgent mud volcano on the Southeastern Mariana forearc: *JAMSTEC Journal of Deep Sea Research*, vol 13, pp 103-114.
- Fryer, Patricia and Julian A. Pearce, 1992, Introduction to the Scientific Results of Leg 125: Proceedings of the Ocean Drilling Program, *Scientific Results*, vol 125, pp 3-11.
- Fryer, Patricia and Michael J. Mottl, 1992, Lithology, Mineralogy, and Origin of Serpentine Muds Recovered from Conical and Torishima Forearc Seamounts: Results of Leg 125 Drilling: Proceedings of the Ocean Drilling Program, *Scientific Results*, vol 125, pp 343-362.
- Fryer, P., K. L. Saboda, L. E. Johnson, M. E. MacKay, G. F. Moore, and P. Stoffers, 1990, Conical Seamount: SeaMARC II, Alvin Submersible, and seismic reflection studies, in Fryer, P., J. A. Pearce, L. B. Stokking and the Leg 125 scientific shipboard party, 1990, *Proceeding of the Ocean Drilling Program: Initial Reports, Leg 125: College Station, Texas, Ocean Drilling Program*, pp 5-14.

- Fryer, P., Ambros, E.L., Hussong, D.M., 1985, Origin and emplacement of Mariana forearc seamounts: *Geology*, vol 13, pp 774-777.
- Gammons, C. H., S. A. Wood and A. E. Williams-Jones, 1996, The aqueous geochemistry of the rare earth elements and yttrium: VI. Stability of neodymium chloride complexes from 25 to 300°C: *Geochimica et Cosmochimica Acta*, vol 60, no. 23, pp 4615-4630.
- Goldberg, E.D., M. Koide, R.A. Schmitt, and R.H. Smith, 1963, Rare-earth distributions in the marine environment: *Journal of Geophysical Research*, vol 68, pp 4209-4217.
- Janecky, D. R., and W. E. Seyfried, Jr., 1986, Hydrothermal serpentinization of peridotite within the ocean crust: Experimental investigations of mineralogy and major element chemistry: *Geochimica et Cosmochimica Acta*, vol 50, pp 1357-1378.
- Johannesson, Kevin H., Klaus J. Stetzenbach, and Vernon F. Hodge, 1997, Rare earth elements as geochemical tracers of regional groundwater mixing: *Geochimica et Cosmochimica Acta*, vol 61, no 17, pp 3605-3618.
- Kerrick, D.M and J.A.D. Connolly, 2001, Metamorphic devolatilization of subducted marine sediments and the transport of volatiles into the Earth's mantle: *Nature*, vol 411, pp 293-296.
- Klinkhammer, G.P., H. Elderfield, J.M. Edmond, and A. Mitra, 1994, Geochemical implications for rare earth element patterns in hydrothermal fluids from mid-ocean ridges: *Geochimica et Cosmochimica Acta*, vol 58, pp 5105-5113.
- Lallemand, S.E., R. Culotta, and R. von Huene, 1989, Subduction of the Daiichi Kashima Seamount in the Japan Trench: *Tectonophysics*, vol 160, pp 231-247.

- Landing, William M., Conny Haraldsson, and Nicklas Paxéus, 1986, Vinyl Polymer Agglomerate Based Transition Metal Cation Chelating Ion-Exchange Resin Containing the 8-Hydroxyquinoline Functional Group: *Analytical Chemistry*, vol 58, pp 3031-3035.
- Langmuir, D., 1978, Uranium solution-mineral equilibria at low temperatures with applications to sedimentary ore deposits: *Geochimica et Cosmochimica Acta*, vol 42, pp 547-569.
- Lee, Jong Hyeon and Robert H. Byrne, 1994, Pressure dependence of gadolinium carbonate complexation in seawater: *Geochimica et Cosmochimica Acta*, vol 58, no 19, pp 4009-4016.
- Lee, Jong Hyeon and Robert H. Byrne, 1991, Examination of comparative rare earth element complexation behavior using linear free-energy relationships: *Geochimica et Cosmochimica Acta*, vol 56, pp 1127-1137.
- Li, Yuan-Hui and Sandra Gregory, 1974, Diffusion of ions in sea water and deep sea sediments: *Geochimica et Cosmochimica Acta*, vol 38, pp 703-714.
- Liu, Xuewu and Robert H. Byrne, 1997, Rare earth and yttrium phosphate solubilities in aqueous solution: *Geochimica et Cosmochimica Acta*, vol 61, no 8, pp 1625-1633.
- Luo, Yu-Ran and Robert H. Byrne, 2003, Carbonate Complexation of Yttrium and the Rare Earth Elements in Natural Waters: *Geochimica et Cosmochimica Acta*, vol 68, no 4, pp 691-699.
- Mikada, H., Becker, K., Moore, J.C., Klaus, A., et al., 2002. *Proc. ODP, Init. Repts.*, 196 [CD-ROM]. Available from: Ocean Drilling Program, Texas A&M University, College Station TX 77845-9547, USA.
- Millero, Frank J., 1992, Stability constants for the formation of rare earth inorganic complexes as a function of ionic strength: *Geochimica et Cosmochimica Acta*, vol 56, pp 3123-3132.

- Moore, Gregory F. et al., 2001, New insights into deformation and fluid flow processes in the Nankai Trough accretionary prism: Results of Ocean Drilling Program Leg 190: Geochemistry Geophysics Geosystems, vol 2, 2001GC000116.
- Moore, Casey, and Silver, Eli, 2002, Fluid flow in accreting and eroding convergent margins, in: K. Becker et al., eds, Achievements and Opportunities of scientific Ocean Drilling, Joides Journal, vol 28, no 1, pp 91-96.
- Moore, J. Casey and Peter Vrolijk, 1992, Fluids in Accretionary Prisms: Reviews of Geophysics, vol 30, no 2, pp 113-135.
- Morford, Jennifer L. and Steven Emerson, 1999, The geochemistry of redox sensitive trace metals in sediments: Geochimica et Cosmochimica Acta, vol 63, no 11/12, pp 1735-1750.
- Mottl, Michael J., C. G. Wheat, P. Fryer, J. Gharib, and J.B. Martin, 2004, Chemistry of springs across the Mariana forearc shows progressive devolatilization of the subducting slab: Geochimica et Cosmochimica Acta, vol 68, no 23, pp 4915-4933.
- Mottl, Michael J., Stephen C Komor, Patricia Fryer, and Craig L. Moyer, 2003, Deep-Slab Fluids Fuel Extremophilic Archaea on a Mariana Forearc Serpentine Mud Volcano: ODP Leg 195: Geochemistry Geophysics Geosystems, vol 4, no 11, 2003GC000588.
- Mottl, Michael J., 1992, Pore waters from serpentine seamounts in the Mariana and Izu-Bonin forearcs, Leg 125: evidence for volatiles from the subducting slab: Proceedings of the Ocean Drilling Program, Scientific Results, vol 125, pp 373-385.
- Palandri, James L. and Mark H. Reed, 2003, Geochemical models of metasomatism in ultramafic systems: Serpentinization, rodingitization, and seafloor carbonate chimney precipitation: Geochimica et Cosmochimica Acta, vol 68, no 5, pp 1115-1133.

- Peacock, Simon M., and Roy D. Hyndman, 1999, Hydrous minerals in the mantle wedge and the maximum depth of subduction thrust earthquakes: *Geophysical Research Letters*, vol 26, no 16, pp 2517-2520.
- Peacock, Simon M., and Kelin Wang, 1999, Seismic Consequences of Warm Versus Cool Subduction Metamorphism: Examples from Southwest and Northeast Japan: *Science*, vol 286, no 29, pp 937-939.
- Peacock, Simon M., 1993, The importance of blueschist -> eclogite dehydration reactions in subducting oceanic crust: *Geological Society of America Bulletin*, vol 105, pp 684-694.
- Peacock, Simon M., 1990, Fluid Processes in Subduction Zones: *Science*, vol 248, pp 329-337.
- Phipps, Stephen Paul and Dean Ballotti, 1992, Rheology of Serpentinite Muds in the Mariana-Izu-Bonin Forearc: *Proceedings of the Ocean Drilling Program, Scientific Results*, vol 125, pp 363-372.
- Poulton, Simon W., Michael D. Krom, and Robert Raiswell, 2004, A revised scheme for the reactivity of iron (oxyhydr)oxide minerals towards dissolved sulfide: *Geochimica et Cosmochimica Acta*, vol 68, no 18, pp 3703-3715.
- Sadofsky, Seth J. and Gray E. Bebout, 2003, Record of forearc devolatilization in low-T, high-P/T metasedimentary suites: Significance for models of convergent margin chemical cycling: *Geochemistry Geophysics Geosystems*, vol 4, no 4, 2002GC000412.
- Salisbury, M. H., M. Shinohara, C. Richter, et al., 2002, *Proceedings of the ODP, Initial Reports Volume 195: Core descriptions.*

- Savov, Ivan P., Jeffrey G. Ryan, Massimo D'Antonio, Katherine Kelley, and Patrick Mattie, 2004, Geochemistry of serpentized peridotites from the Mariana Forearc Conical Seamount, ODP Leg 125: Implications for the elemental recycling at subduction zones: *Geochemistry, Geophysics, Geosystems*, vol6, no 4, 2004GC000777.
- Schijf, Johan and Robert H. Byrne, 2003, Determination of $_{\text{SO}_4}\square_1$ for yttrium and the rare earth elements at $I = 0.66m$ and $t = 25^\circ\text{C}$: Implications for YREE solution speciation in sulfate-rich waters, *Geochimica et Cosmochimica Acta*, vol 68, no 13, pp 2825-2837.
- Sharp, Z.D. and J.D. Barnes, 2004, Water-soluble chlorides in massive seafloor serpentinites: a source of chloride in subduction zones: *Earth and Planetary Science Letters*, vol 226, pp 243-254.
- Shipboard Scientific Party, 2002, Site 1200. Proceeding from the Ocean Drilling Program: Initial Reports, vol 195, pp 1-173.
- Silver, E.A., 2001, Leg 170: synthesis of fluid-structural relationships of the Pacific margin of Costa Rica: Silver, E.A., Kimura, G., Shipley, T.H. (Eds.), *Proc. ODP, Sci. Results*, 170: College Station TX (Ocean Drilling Program), pp 1-11.
- Sohrin, Yoshiki, Shun-ichi Iwamoto, Shoji Akiyama, Takeshi Fujita, Toyokazu Kugii, Hajime Obata, Eiichiro Nakayama, Shiro Goda, Yukiyo Fujishima, Hiroshi Hasegawa, Kazumasa Ueda and Masakazu Matsui, 1998, Determination of trace elements in seawater by fluorinated metal alkoxide glass immobilized 8-hydroxyquinoline concentration and high resolution inductively coupled plasma mass spectrometry detection: *Analytica Chimica Acta*, vol 363, pp 11-19.
- Spivak, Arthur J., 2002, Elemental and Isotopic Chloride Geochemistry and Fluid Flow in the Nankai Trough: *Geophysical Research Letters*, vol 29, no 14, 2001GL014122.

- Stein C. A., 2003, Heat flow and flexure at subduction zones: *Geophysical Research Letters*, vol 30, no 23, 2003GL018478.
- Stern, Robert J., 2002, Subduction Zones: Reviews of Geophysics, vol 40, no 4, pp 3-1 - 3-38.
- Stern, Robert J., Julie Morris, Sherman H. Bloomer and James W. Hawkins Jr., 1991, The source of the subduction component in convergent margin magmas: Trace element and radiogenic isotope evidence from Eocene boninites, Mariana forearc: *Geochimica et Cosmochimica Acta*, vol 55, pp 1467-1481.
- Stern, Robert J., Julie Morris, Sherman H. Bloomer and James W. Hawkins Jr., 1991, The source of the subduction component in convergent margin magmas: Trace element and radiogenic isotope evidence from Eocene boninites, Mariana forearc: *Geochimica et Cosmochimica Acta*, vol 55, pp 1467-1481.
- Tenthorey, Eric and Jorg Hermann, 2004, Composition of fluids during serpentinite breakdown in subduction zones: Evidence for limited boron mobility: *Geology*, vol 32, no 10, pp 865-868.
- Wheat, C. Geoffrey, H. W. Jannasch, J. Plant, C. L. Moyer, F. J. Sansone, and G. M. McMurtry, 2000, Continuous sampling of hydrothermal fluids from Loihi Seamount after the 1996 event: *Journal of Geophysical Research*, vol 105, pp 19353-19368.
- Wheat, C. Geoffrey, Michael J. Mottl, and Mark Rudnicki, 2002, Trace Element and REE composition of a low-temperature ridge-flank hydrothermal spring: *Geochimica et Cosmochimica Acta*, vol 66, no 21, pp 3693-3705.
- Wheat, C. Geoffrey and R.E. McDuff, 1995, Mapping the fluid flow of the Mariana Mounds off-axis hydrothermal system: Pore water chemical tracers: *Journal of Geophysical Research*, vol 100, pp 8115-8131.

- Wheat, C. Geoffrey and Michael J. Mottl, 1994, Hydrothermal circulation. Juan de Fuca eastern flank: Factors controlling basement water composition: *Journal of Geophysical Research*, vol 99, pp 3067-3080.
- Williams-Jones, Anthony E., and Scott A. Wood, 1991, A preliminary grid for REE fluorocarbonates and associated minerals: *Geochimica et Cosmochimica Acta*, vol 56, pp 725-738.
- You, C.F., P.R. Castillo, J.M. Gieskes, L.H. Chan, and A.J. Spivak, 1996, Trace element behavior in hydrothermal experiments: Implications for fluid processes at shallow depths in subduction zones: *Earth and Planetary Science Letters*, vol 140, pp 41-52.
- Zachara, John M., Jim K. Fredrickson, Steven C. Smith and Paul L. Gassman, 2000, Solubilization of Fe(III) oxide-bound trace metals by a dissimilatory Fe(III) reducing bacterium: *Geochimica et Cosmochimica Acta*, vol 65, no 1, pp 75-93.

Appendix A. Push Core Extruder Design

To facilitate the sectioning of push cores in an oxygen-free environment, a device was designed and constructed by Hans Jannasch (MBARI) and Samuel Hulme (MLML). The extruder's support base can be lashed to most standard research vessel lab benches for operation while under way. A glove bag was first placed on the extruder's working surface and flushed 3 times with nitrogen gas. The push cores were placed on the plunger and secured to the extruder by means of two stainless steel hose clamps. Once the core was secured, a slit was cut in the glove bag, and the upper end of the push core inserted into the slit. The glove bag was sealed to the push core by electrical tape.

The operator's hands were then placed in the glove bag to begin the core sectioning process. The core was extruded in discrete intervals by depressing a foot pedal attached to a gear motor. The accuracy of the electric extruder was <2mm. Once the core was extruded, the operator could remove her/his hands from the glove bag and switch the device into reverse to remove the plunger from the core. The extruder could be adjusted to 3 core lengths of 12", 18", and 24" by selecting 1 of 3 holes in the plunger rod to attach to the chain drive.

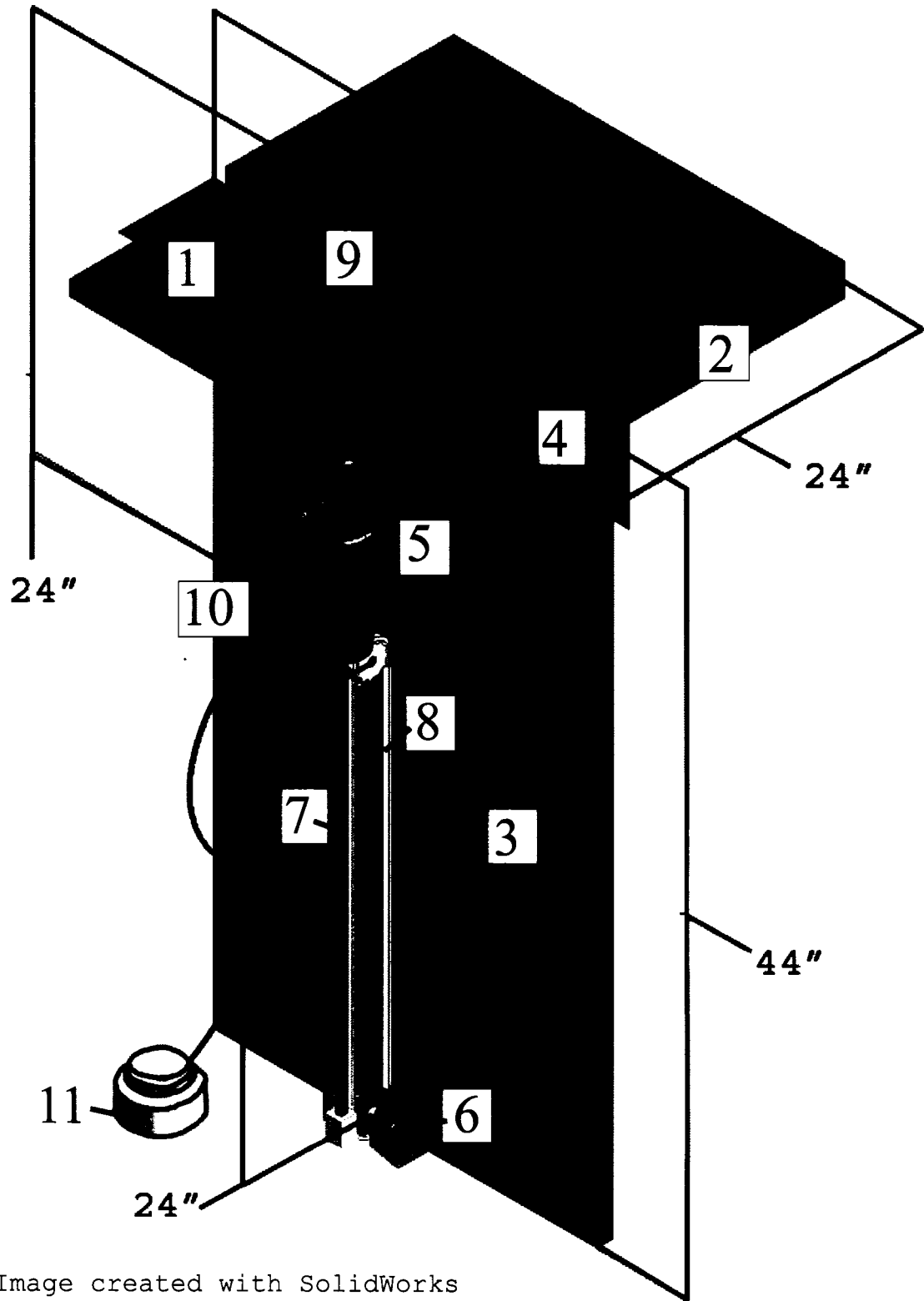
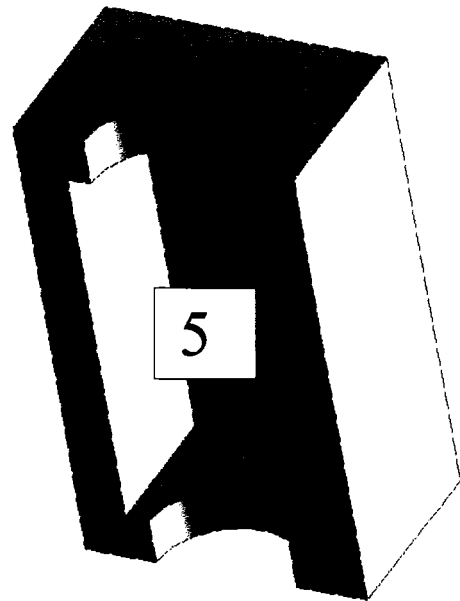
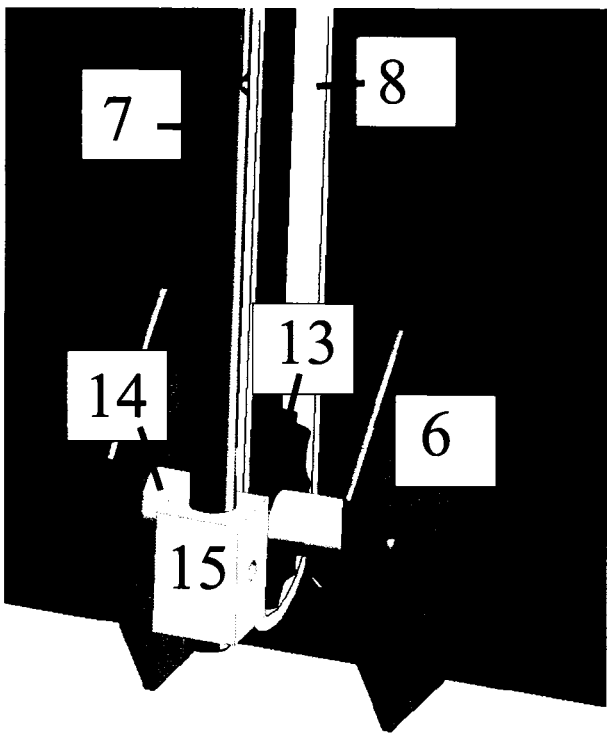
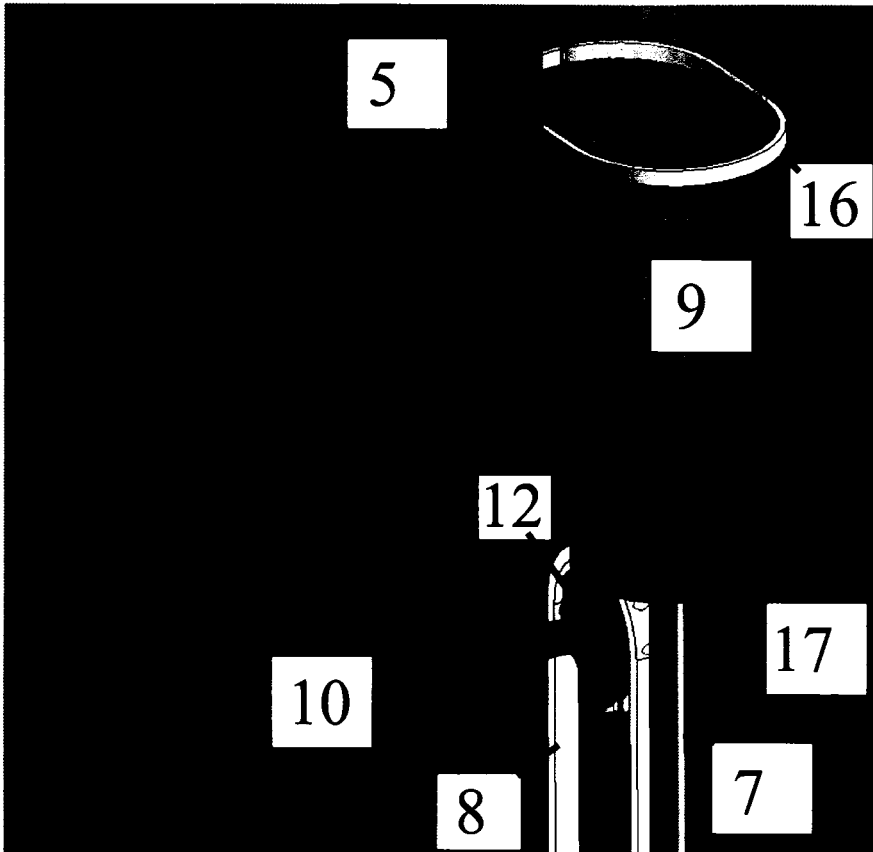


Image created with SolidWorks
mechanical design automation software.



Images created with SolidWorks mechanical design automation software.

Key to push core extruder components.

1. 24" x 24" x 1" plywood work surface with rounded slot.
2. 1/4" x 2" plywood rim.
3. 44" x 24" x 1" plywood support base.
4. 4" x 4" x 1" triangular plywood gusset
5. 4" x 7" x 10" x 1" thick plywood restraining block.
6. Aluminum chain tensioner bracket attached to support base with 2 stainless steel bolts.
7. 27" x 1/2" aluminum plunger rod threaded on one end with 3 holes at 6" intervals on opposite end.
8. Stainless steel roller chain with attachment link.
9. Polycarbonate push core with beveled edge.
10. 115 v AC bidirectional 95.5:1 gear motor from Bison Gear and Engineering Corp. (Part # 016-103-1096).
11. Stainless steel waterproof foot pedal switch.
12. Stainless steel gear pressed onto motor shaft.
13. Ceramic pulley gear with sealed bearing.
14. Nylon hollow shaft pressed into pulley gear and bolted onto chain tensioner bracket.
15. Nylon block screwed to roller chain attachment link with holes to insert plunger rod and pin.
16. Stainless steel adjustable hose clamp screwed to restraining block.
17. PVC beveled plunger puck with 2 O-ring groves and threaded hole for attaching to plunger rod.

Appendix B. Push Core Descriptions

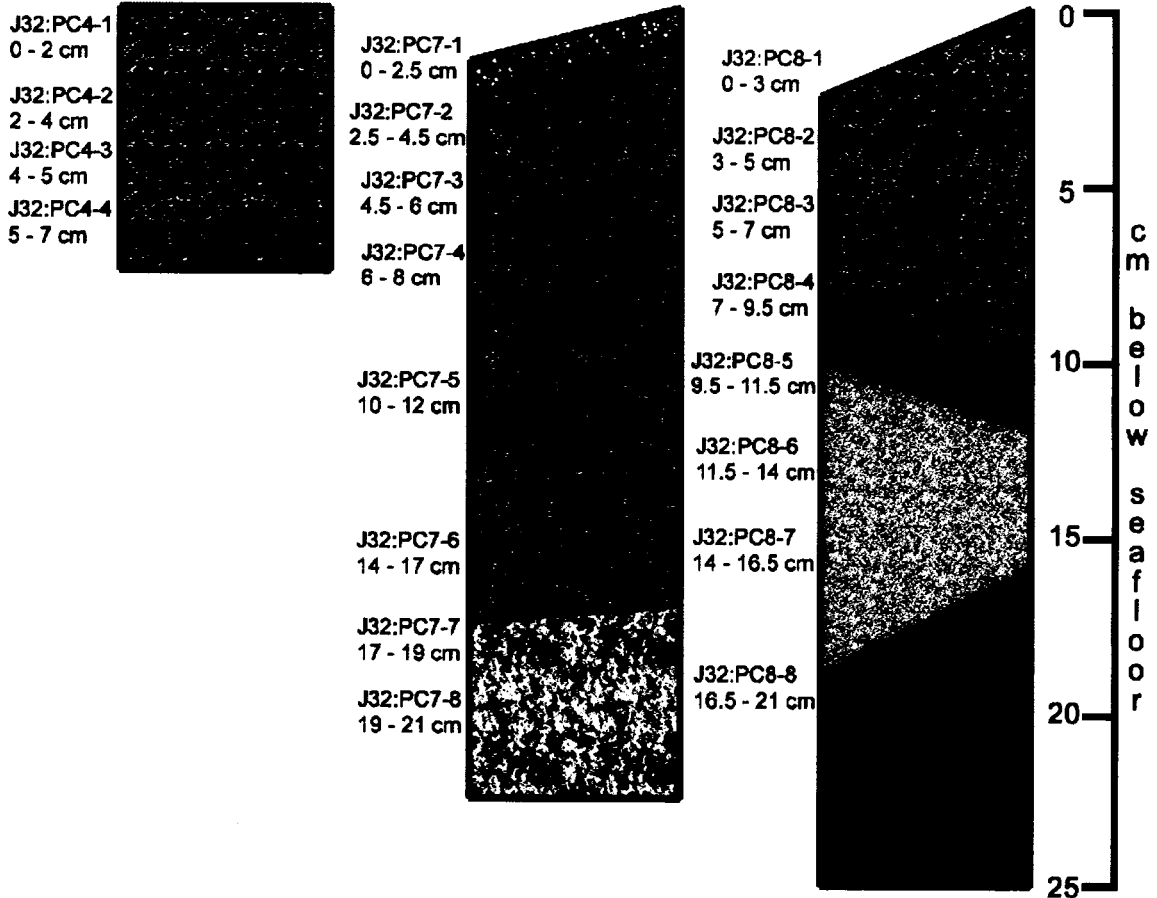
Push cores that were processed in the 4°C cold room within a nitrogen atmosphere were described based on color, texture, and the presence of clasts within the sediment. The following pages present the interpretations of the initial observations along with the sample locations and depths. The core sections and intervals are also presented with the names corresponding to those used in Appendix F.

Conical Seamount: Near the summit.

J32: Push Core #4
 19° 32.230' N
 146° 39.045' E
 -3122 m

J32: Push Core #7
 19° 32.230' N
 146° 39.046' E
 -3123 m

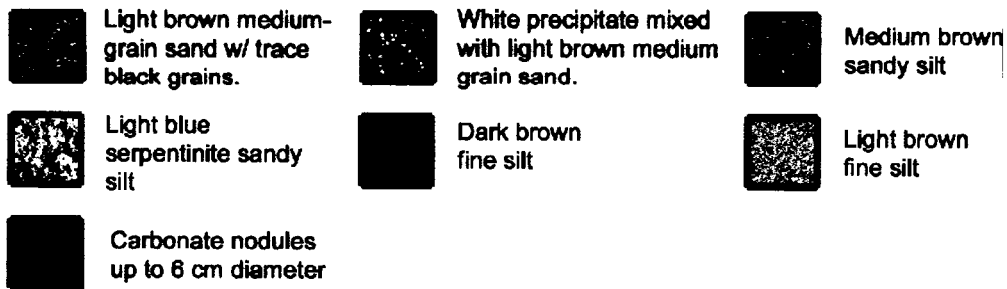
J32: Push Core #8
 19° 32.230' N
 146° 39.046' E
 -3123 m



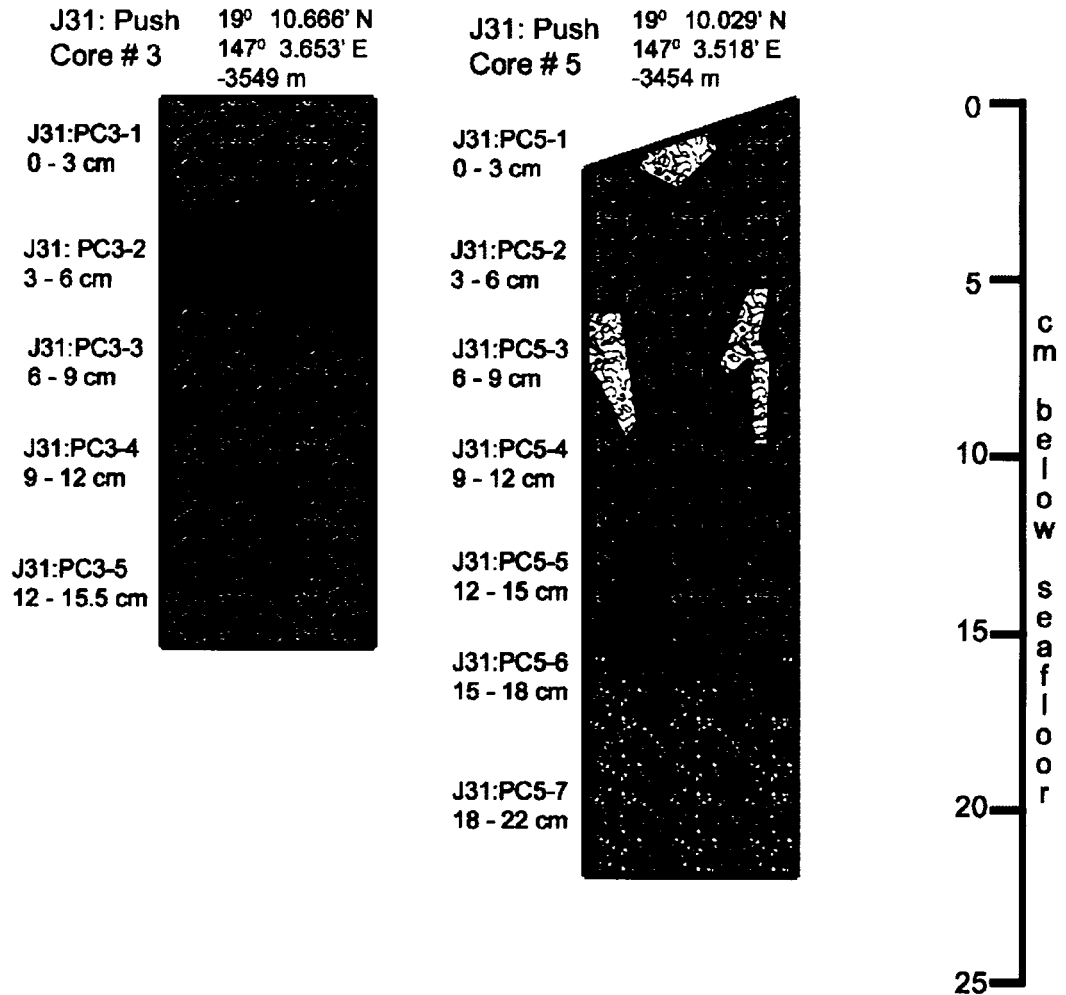
Note:

Serpentinite rocks up to 3 cm diameter found in J32:PC7 at 12 - 14 cm and in J32:PC8 at 13.5 - 17 cm below seafloor.

Key:



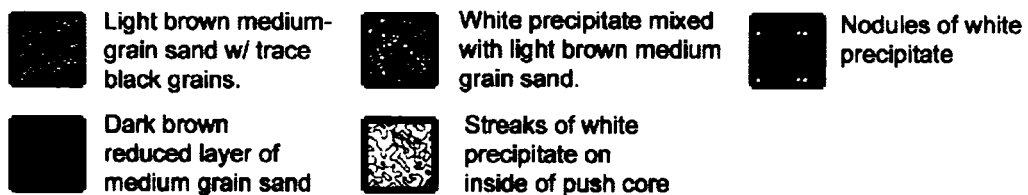
Pacman Seamount: Near Cerulean Springs on Baseball Mitt.



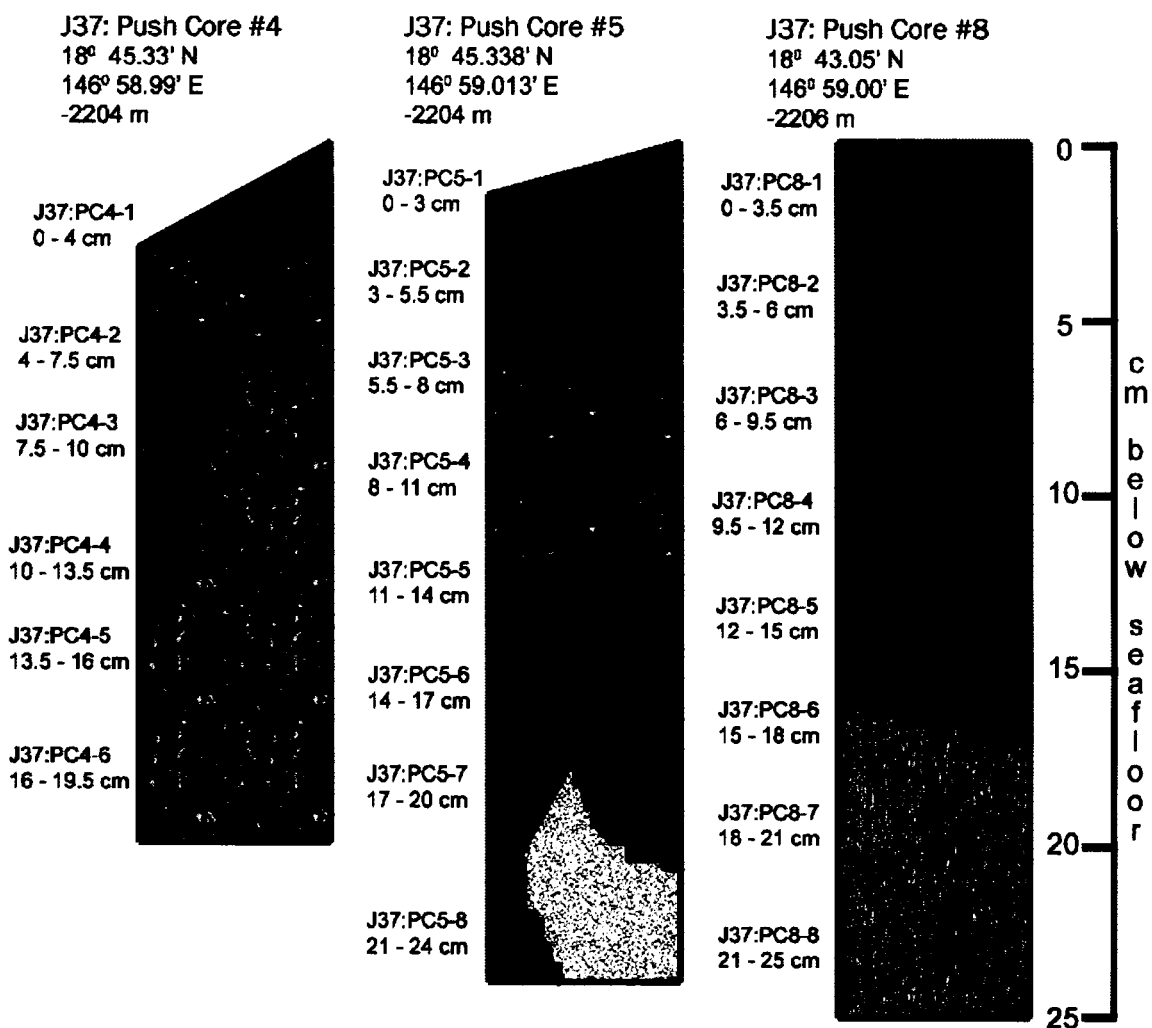
Note:

When extruding J31:PC #5 small serpentinite rocks (~ 1 cm dia.) were found at depths below seafloor of 6, 7, 10 and 13 cm.

Key:












Quaker Seamount: At the Summit. Lowering J37.



Note:

Serpentinite rock ~ 2 cm in diameter found in J37:PC5 at 6 cm below seafloor.

Key

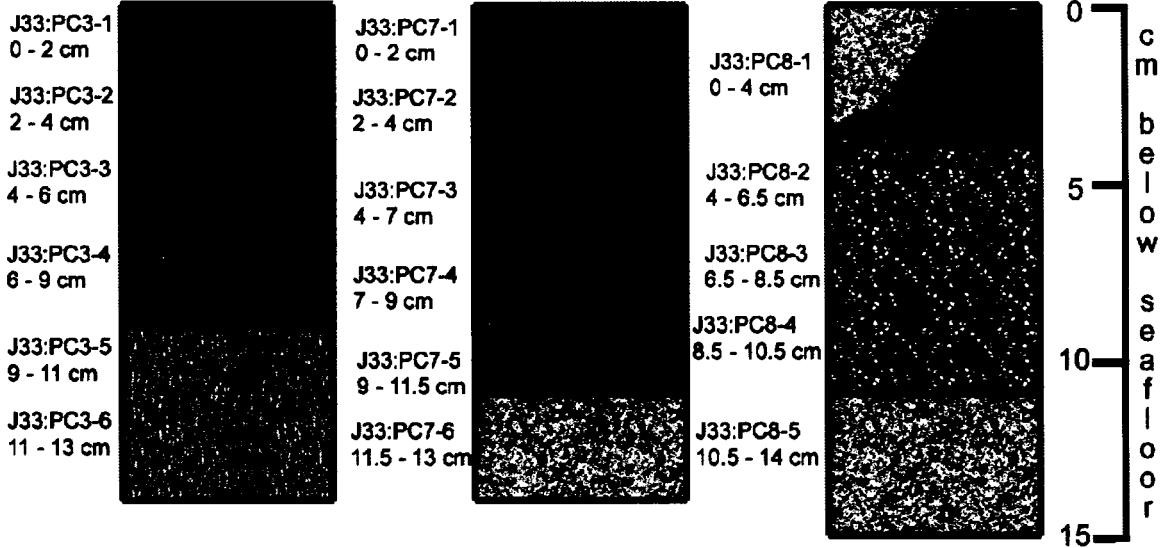
	Dark brown fine silt		Light brown fine silt with mottled light-blue serpentinite clasts		Light reddish-brown silt
	Medium brown silt with lighter red and blue mottled streaks		Dark-blue serpentinite fine silt		Medium-brown fine silt with mottled light-blue serpentinite clasts
	Medium-brown fine silt		Light-blue serpentinite fine silt		Light-blue serpentinite fine silt with orange-red streaks

Quaker Seamount: At the Summit. Lowering J33.






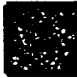

J33: Push Core #3
 18° 45.337' N
 146° 58.440' E
 -2190 m

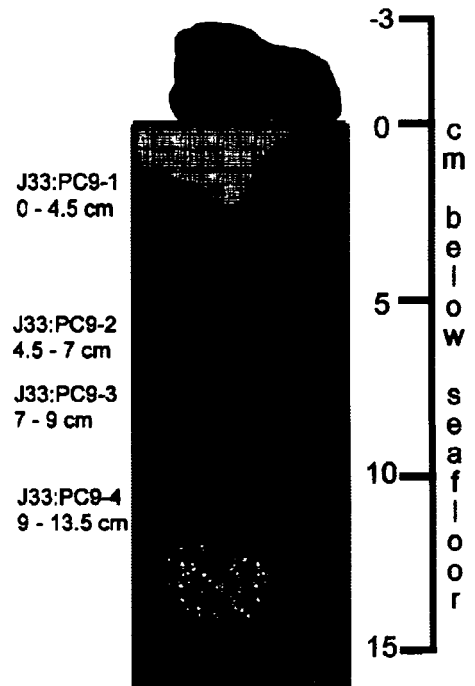
J33: Push Core #7
 18° 45.330' N
 146° 58.470' E
 -2191 m

J33: Push Core #8
 18° 45.362' N
 146° 58.991' E
 -2204 m



Key:

-  Dark brown fine silt
-  Medium brown fine silt
-  Light blue serpentinite fine silt with rust-colored streaks
-  Light brown fine silt
-  Carbonate precipitate (piece of vent chimney)
-  White precipitate mixed with light brown medium grain sand
-  White silt with trace black sand grains



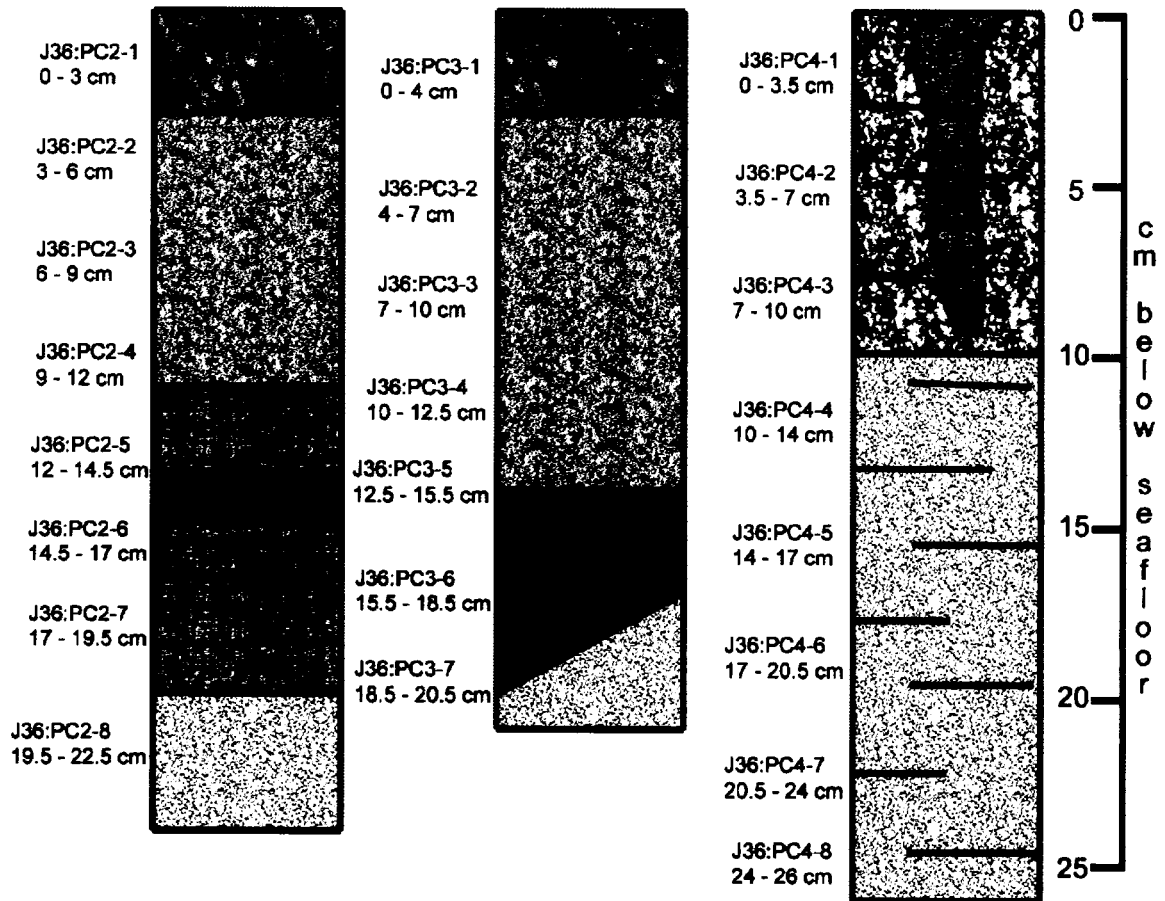
J33: Push Core #9
 18° 45.362' N
 146° 58.991' E
 -2204 m

Big Blue Seamount: Summit transect.

J36: Push Core #2
 18° 6.622' N
 147° 6.098' E
 -1239 m
 (50 m E of BAC19)

J36: Push Core #3
 18° 6.621' N
 147° 6.125' E
 -1239 m
 (71 m E of BAC19)

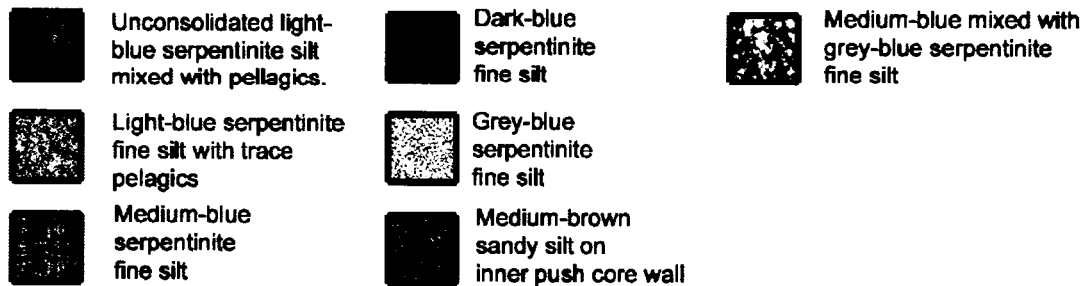
J36: Push Core #4
 18° 6.621' N
 147° 6.621' E
 -1239 m
 (75 m E of BAC19)



Note:

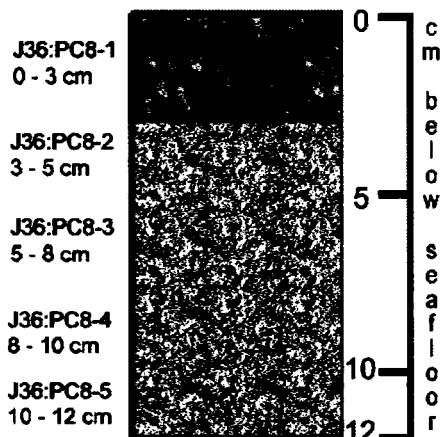
Shell found 7 cm below seafloor (cmbsf) in J36:PC2. Tube worm casing found 10 cmbsf in J36:PC3. Serpentine rock ~ 3.5 cm diameter found 18 cmbsf in J36:PC4. Expansion of gasses within J36:PC4 caused separation of sediments during ascent (indicated by horizontal lines).

Key

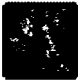



Big Blue Seamount: Summit transect.

J36: Push Core #8
 18° 6.628' N
 147° 6.03' E
 -1253 m
 (25 m W of BAC19)

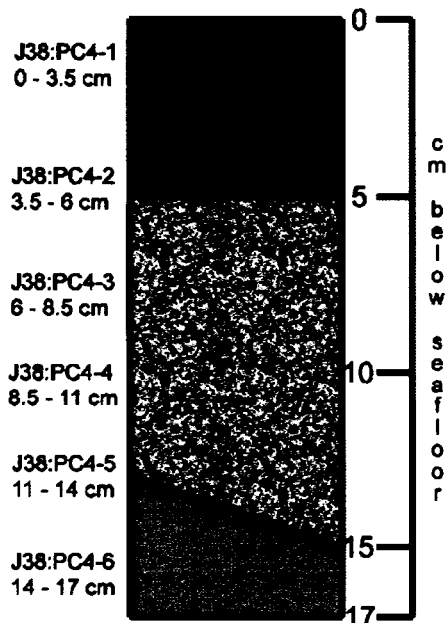


Key:




-  Unconsolidated light-blue serpentinite silt mixed with pelagics.
-  Light-blue serpentinite fine silt with trace pelagics

Celestial Seamount: Southern flank near the summit.

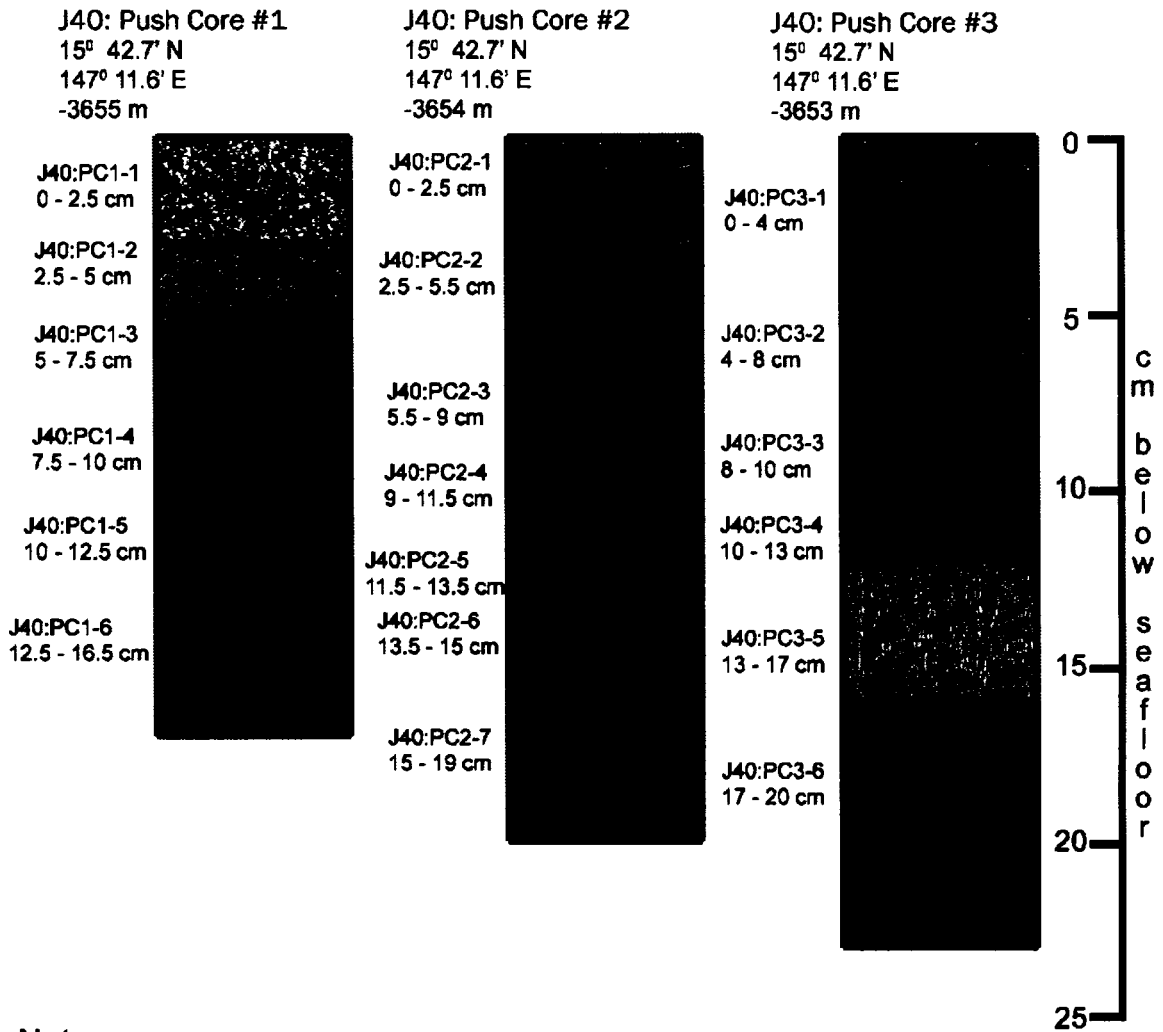
J38: Push Core #4
 16° 30.706' N
 147° 13.456' E
 -1955 m



Key:

-  Graded coarse to fine downward with thin laminae. Light-brown sandy silt with trace black grains.
-  Light-brown silt.
-  Light-blue serpentinite fine silt

Blue Moon Seamount: Near the Summit.



Note:

2 serpentinite rocks ~ 2 cm in diameter found in J40:PC1 at 14 and 15 cm below seafloor (cmbfsf).

3 Serpentinite rocks ~ 2.5 cm in diameter found in J40:PC2 at 3, 6 and 7 cmbfsf.

3 serpentinite rocks ~ 2.5 to 4 cm in diameter found in J40:PC3 at 0, 3 and 14 cmbfsf.

Key



Unconsolidated medium-brown pelagic silt



Dark-blue serpentinite fine silt



Medium-brown pelagic silt

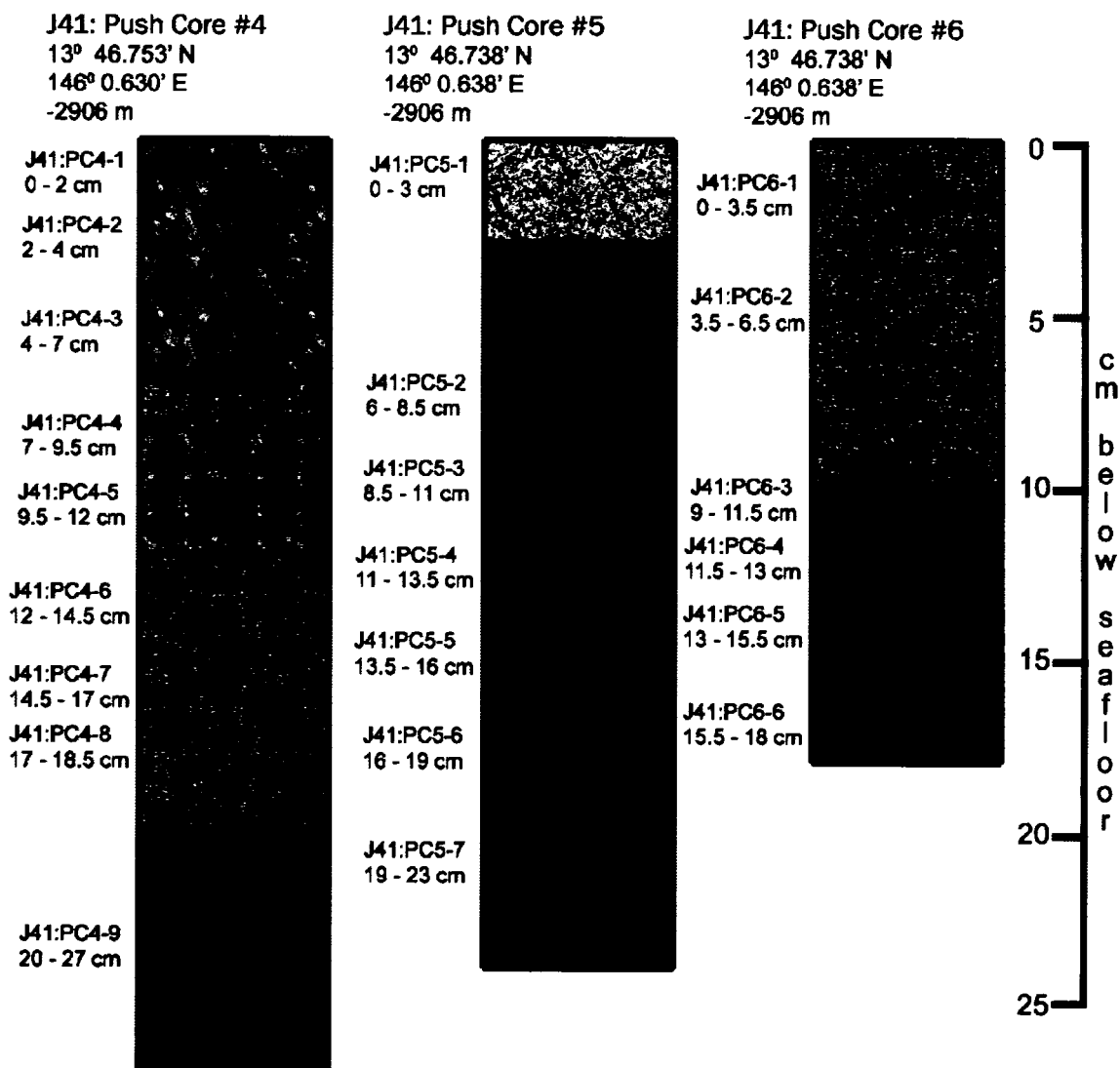


Light-blue serpentinite fine silt with orange-red streaks



Medium brown silt with light-brown and orange-red mottled streaks.

South Chamorro Seamount: Near ODP Site 1200C.



Note: 4.5 cm diameter serpentinite rock found in J41:PC4 at 21 cm below seafloor (cmbsf).
 2 cm diameter serpentinite rock found in J41:PC5 at 15.5 cmbsf.
 Serpentinite rocks and muscle shells found in top 6 cm of J41:PC6.

Key:



Appendix C. Detailed ICP-MS Methods

Trace element analyses conducted at Moss Landing Marine Laboratories were done with a Finnigan Element2 high-resolution inductively-coupled-plasma mass spectrometer (HR-ICP-MS). The instrument settings for these analyses are presented in the following tables of this appendix. For the 1% dilution and 8-HQ extraction methods, a CETAC Aridus desolvating nebulizer system was used, and the setting for this are given. Typical counts per second (CPS) of certain elements and oxides after tune optimization are given. The given tune conditions are typical but in practice could vary due to changing temperatures, sample cones, and plasma torches. Three methods were used on the Element2, and the scan settings for each are presented in table form.

Sample collection vials for long-term sample storage were extensively cleaned prior to the expedition. New HDPE vials were initially soaked in Micro laboratory soap solution mixed with distilled water according to manufacturer's instructions for 3 weeks. After this period, the vials were rinsed 5 times in MQ water and soaked for an additional 4 weeks in 10% Fisher brand trace-metal grade HCL diluted in MQ water. The vials were subsequently rinsed an additional 5 times in MQ water and place in a class-100 laminar flow clean bench to dry. When the vials were dried, they were capped and placed in two layers of Ziplock plastic bags. After the samples were collected, the vials were only opened within a class-100 laminar flow clean bench during acidification and sub-sampling. Vials used for dilutions immediately preceding

HR-ICP-MS analysis were placed in 10% Fisher brand trace-metal grade HCl diluted in MQ water and heated in a 60°C oven for two days. After cooling, the vials were rinsed 5 times in MQ water and dried in a class-100 laminar flow clean bench.

Reagent bottles used for standard preparation were cleaned in the same manner as the sample vials and either disposed of after use or re-used with the same standard solution. Blank and extraction reagent bottles were Teflon containers that had previously contained Optima acids or ammonium hydroxide. These bottles were cleaned between uses by rinsing 5 times with MQ water, as they only contained MQ water or dilute Optima reagents. The purity of the reagents in these containers were checked against the Element2 machine blank prior to use. If any contamination was found, the bottles were filled with 10% Fisher brand trace-metal grade HCL diluted in MQ water and placed in a 60°C oven for two days. The bottles were then rinsed 5 times with MQ water and re-checked for contamination.

PFA Spray Chamber Tune Parameters

Cool gas (L/min)	15
Aux gas (L/min)	0.8
Sample gas (L/min)	1
Additional gas (L/min)	0.2
Plasma power (W)	1200
Guard electrode	yes
Torch X-positoin (mm)	1.9
Torch Y-positoin (mm)	-0.5
Torch Z-positoin (mm)	-0.5
CeO/Ce for 1 mg/L Ce in 2% QHNO3 (%)	< 2
Resolution	med
2.5 mg/L Rh in 2% QHNO3 (CPS)	75,000
2.5 mg/L Rh in 10% seawater (CPS)	40,000

Aridus Desolvator Element2 Tune Parameters

Cool gas (L/min)	15
Aux gas (L/min)	0.8
Sample gas (L/min)	1
Additional gas (L/min)	0
Plasma power (W)	1200
Guard electrode	yes
Torch X-positoin (mm)	2
Torch Y-positoin (mm)	-0.2
Torch Z-positoin (mm)	-1.9
CeO/Ce for 1 mg/L Ce in 2% QHNO3 (%)	< 0.05
Resolution	low
10 mg/L Li in 2% QHNO3 (CPS)	8,500,000
10 mg/L In in 2% QHNO3 (CPS)	45,000,000
10 mg/L U in 2% QHNO3 (CPS)	75,000,000
Resolution	med
10 mg/L Fe in 2% QHNO3 (CPS)	2,500,000
Resolution	high
100 mg/L K in 2% QHNO3 (CPS)	1,700,000

Aridus Desolvating Debulizer Settings

Nitrogen gas (mL/min)	11
Sweep gas (L/min)	4.3
Sweep gas temperature (C)	175
Spray chamber temperature (C)	75

1% Dillution Element2 Method Settings

Global settings	# of scans	Instrument resolution	Scan time (s)	Sample time (min:s)	Rinse time (min:s)	Take-up time (min:s)	Scan type
	20	medium	3.581	1:12	1:30	1:00	E-Scan

Isotope	Mass window (%)	Mass Range	Settling Time (s)	Sample Time (s)	Samples per peak	Integration window (%)	Internal standard
V51	100	50.937 - 50.950	0.300	0.025	20	70	Rh
Cr52	100	51.933 - 51.946	0.001	0.035	20	70	Rh
Ni60	100	59.923 - 59.938	0.043	0.025	20	70	Rh
Cu63	100	62.921 - 62.937	0.001	0.035	20	70	Rh
Zn66	100	65.917 - 65.934	0.001	0.035	20	70	Rh
Rb85	100	84.901 - 84.922	0.068	0.020	20	70	Rh
Mo95	100	94.893 - 94.917	0.001	0.020	20	70	Rh
Rh103	100	102.892 - 102.918	0.053	0.010	15	70	
Cs133	100	132.888 - 132.922	0.067	0.035	20	70	Tl
Ba137	100	136.888 - 136.922	0.001	0.015	20	70	Tl
Tl205	100	204.948 - 204.999	0.118	0.010	15	70	
U238	100	238.020 - 238.080	0.067	0.020	20	70	Tl

Standard Addition Element2 Method Settings

Global settings	# of scans	Instrument resolution	Scan time (s)	Sample time (min:s)	Rinse time (min:s)	Take-up time (min:s)	Scan type
	40	medium	4.493	3:00	3:00	1:00	E-Scan

Isotope	Mass window (%)	Mass Range	Settling Time (s)	Sample Time (s)	Samples per peak	Integration window (%)	Internal standard
V51	110	50.936 - 50.950	0.300	0.015	20	70	Rh
Cr52	110	51.933 - 51.947	0.001	0.025	20	70	Rh
Co59	110	58.925 - 58.941	0.041	0.050	20	70	Rh
Ni60	110	59.922 - 59.938	0.001	0.015	20	70	Rh
Cu63	110	62.920 - 62.938	0.001	0.030	20	70	Rh
Zn66	110	65.916 - 65.935	0.001	0.030	20	70	Rh
Rh103	100	102.891 - 102.919	0.098	0.010	20	70	

8-HQ Extraction Element2 Method Settings

Global settings	# of scans	Instrument resolution	Scan time (s)	Sample time (min:s)	Rinse time (min:s)	Take-up time (min:s)	Scan type
	25	medium	7.401	3:05	2:00	0:30	E-Scan

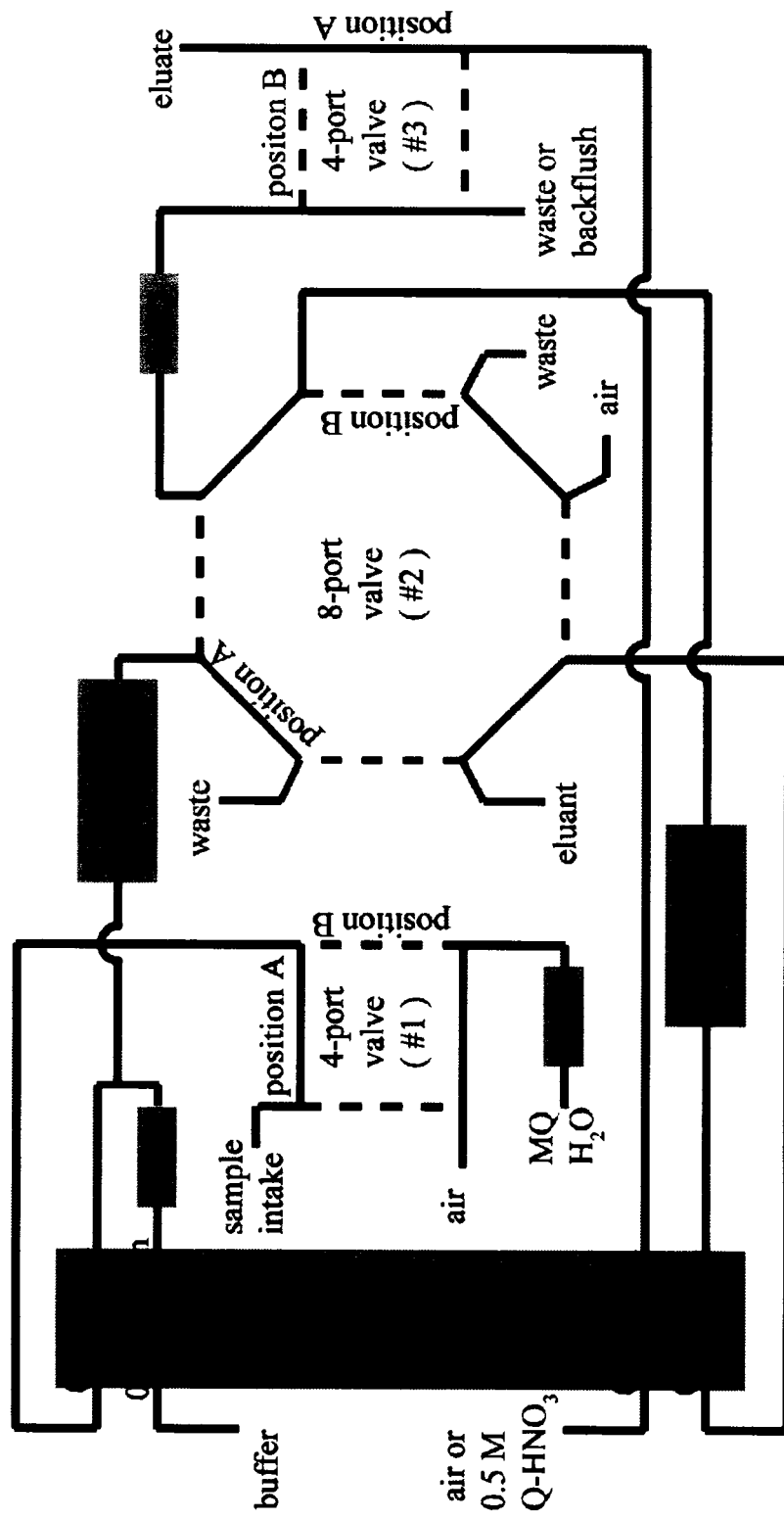
Isotope	Mass window (%)	Mass Range	Settling Time (s)	Sample Time (s)	Samples per peak	Integration window (%)	Internal standard										
								Y89	Rh103	Cd111	La139	Ce140	Pr141	Nd143	Sm147	Eu153	Gd157
	110	88.893 - 88.918	0.300	0.015	20	80	Rh										
	100	102.892 - 102.918	0.047	0.010	15	80											
	100	110.888 - 110.919	0.001	0.015	20	80	Rh										
	100	138.887 - 138.925	0.075	0.015	20	80	Tl										
	100	139.887 - 139.922	0.001	0.020	20	80	Tl										
	100	140.890 - 140.925	0.001	0.020	20	80	Tl										
	100	142.891 - 142.927	0.001	0.015	20	80	Tl										
	100	146.896 - 146.933	0.001	0.030	20	80	Tl										
	100	152.902 - 152.940	0.001	0.020	20	80	Tl										
	100	156.904 - 156.943	0.001	0.020	20	80	Tl										
	100	158.905 - 158.945	0.001	0.020	20	80	Tl										
	110	162.906 - 162.951	0.057	0.020	20	80	Tl										
	100	164.909 - 164.950	0.001	0.020	20	80	Tl										
	100	165.909 - 165.951	0.001	0.020	20	80	Tl										
	100	168.913 - 168.955	0.001	0.020	20	80	Tl										
	100	171.914 - 171.957	0.001	0.020	20	80	Tl										
	100	174.918 - 174.962	0.001	0.020	20	80	Tl										
	100	204.948 - 204.999	0.079	0.010	15	80											

Appendix D. 8-HQ Extraction Apparatus

Rare earth element and select transition metal analyses were conducted by removal of the salt matrix and preconcentrating the elements prior to analysis by HR-ICP-MS. A device was designed and constructed at MLML for this purpose and is described in this section. The three valves that directed the flow of sample and reagents were mounted in a row on a small (12" x 8" x 6") nylon table. This was placed in a class-100 laminar flow clean bench, and the cables and tubing routed out to a laptop computer and peristaltic pump respectively. The reagents and components of the apparatus are detailed in the methods section of this thesis. This appendix is designed to present a visual depiction of the device operation.

The extraction device could switch between 6 modes: loading the sample on the 8-HQ column; rinsing the salt residue from the column; purging the column and tubing with air; collection of the eluate; stopping and idling after collection; and washing the column and tubing between samples. A brief rinse of the 8-HQ column with buffer would be performed prior to sample introduction to condition the pH in the column. The normal timing of these steps were as follows: 30s rinse; 440s sample load; 195s rinse; 130s purge; 280s elution; stop until operator prompt; and wash for 10 minutes.

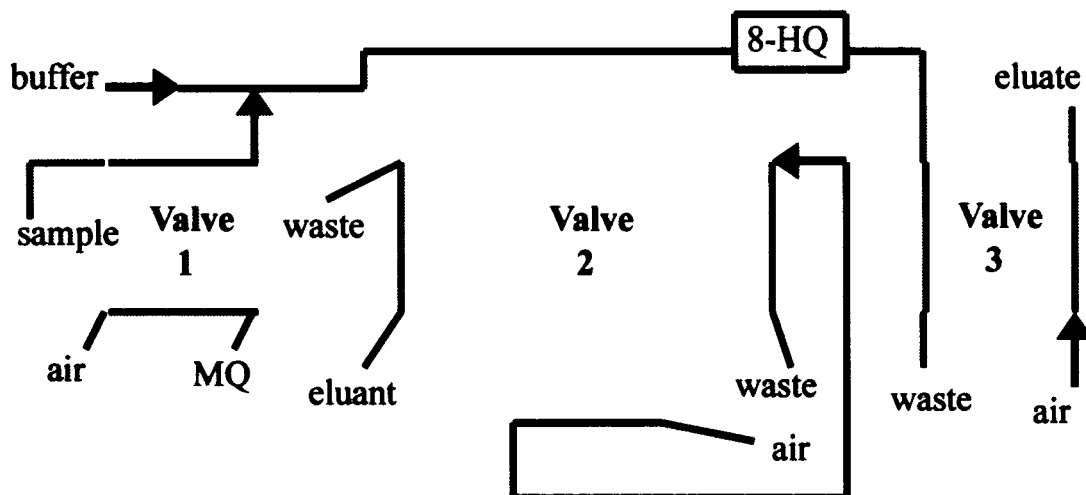
Trace Element Extraction Apparatus



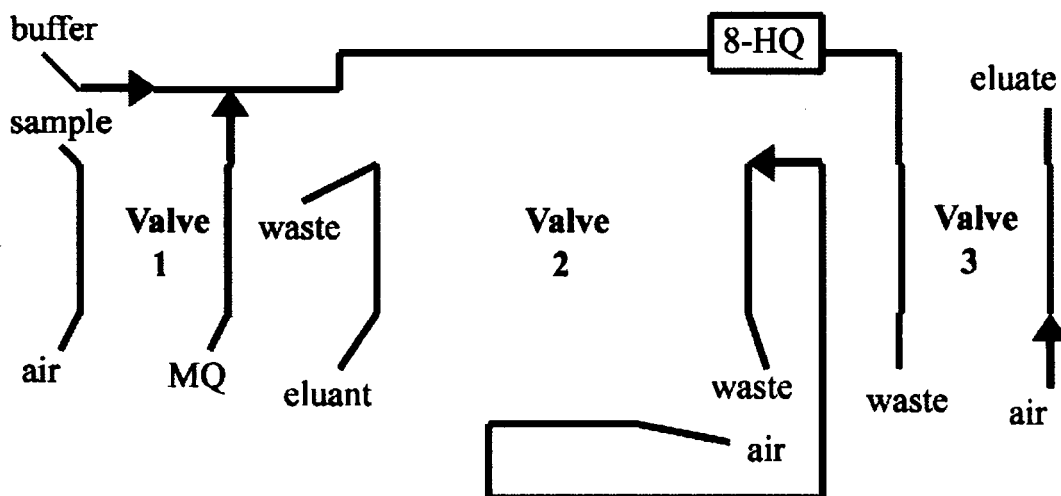
Schematic diagram of the apparatus used for extraction of trace elements from fluid samples by immobilization onto 8-Hydroxyquinoline columns (shown as 8-HQ).

Operation of Extraction Apparatus:

Load Phase- Immobilize trace elements on 8-hydroxyquinoline column



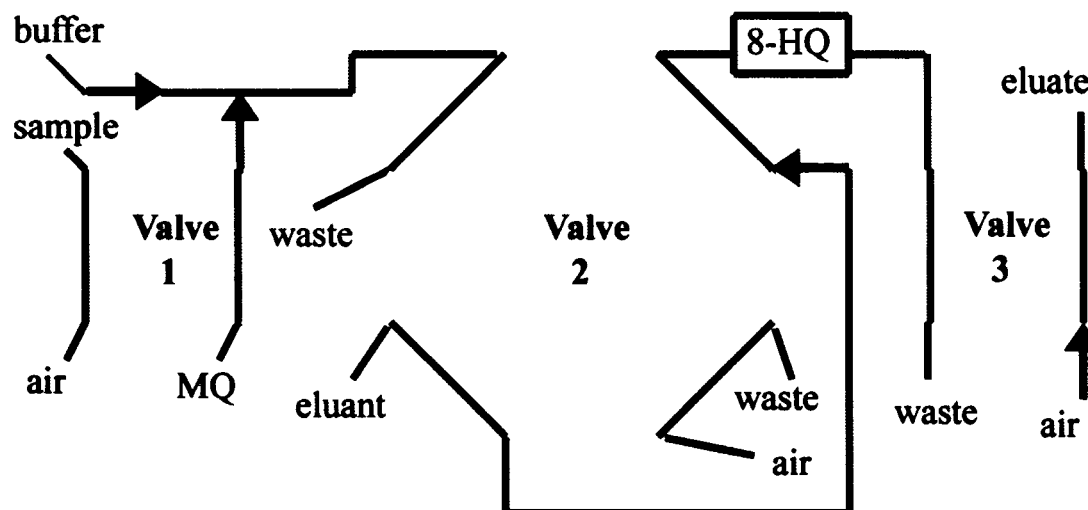
Rinse Phase- Remove salt residue from the column and condition the pH of the column before sample introduction



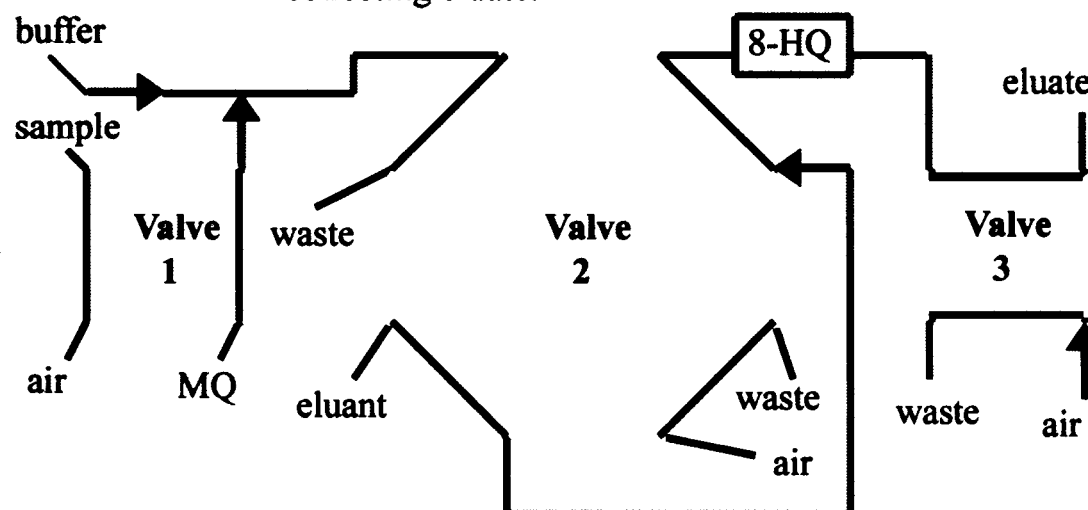
Schematic of the first two steps of the extraction process illustrating reagents and flow paths. Vector arrows represent peristaltic pump positions in flow paths and the direction of active pumping. Only active valve positions are shown for simplicity.

Operation of Extraction Apparatus:

Purge Phase- Remove excess fluid from column by purging with air from eluant loop.



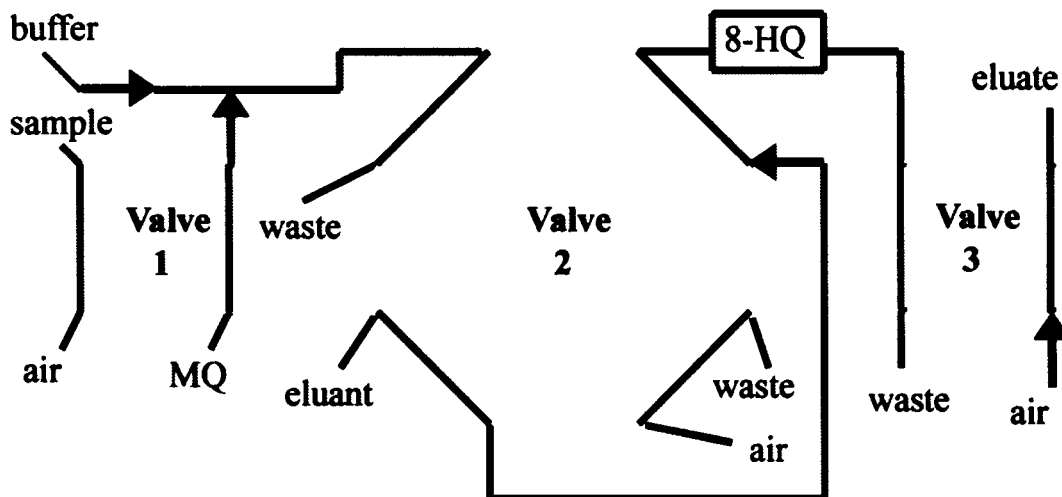
Collection Phase- When the sample column is purged of rinse fluid, begin collecting eluate.



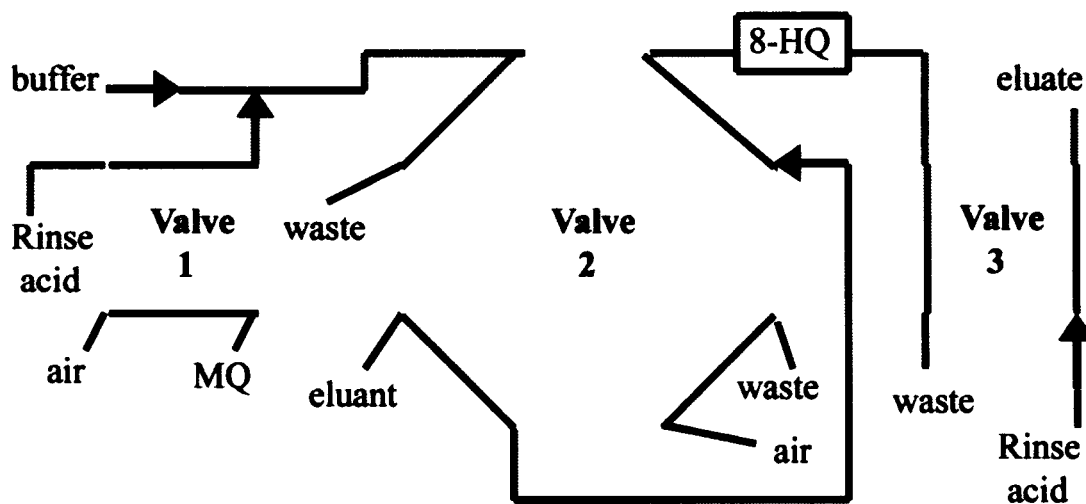
Schematic of the second two steps of the extraction process illustrating reagents and flow paths. Vector arrows represent peristaltic pump positions in flow paths and the direction of active pumping. Only active valve positions are shown for simplicity.

Operation of Extraction Apparatus:

Stop Phase- No sample is consumed nor is eluate produced. This is the last position after collecting eluate and can be used to abort an extraction.



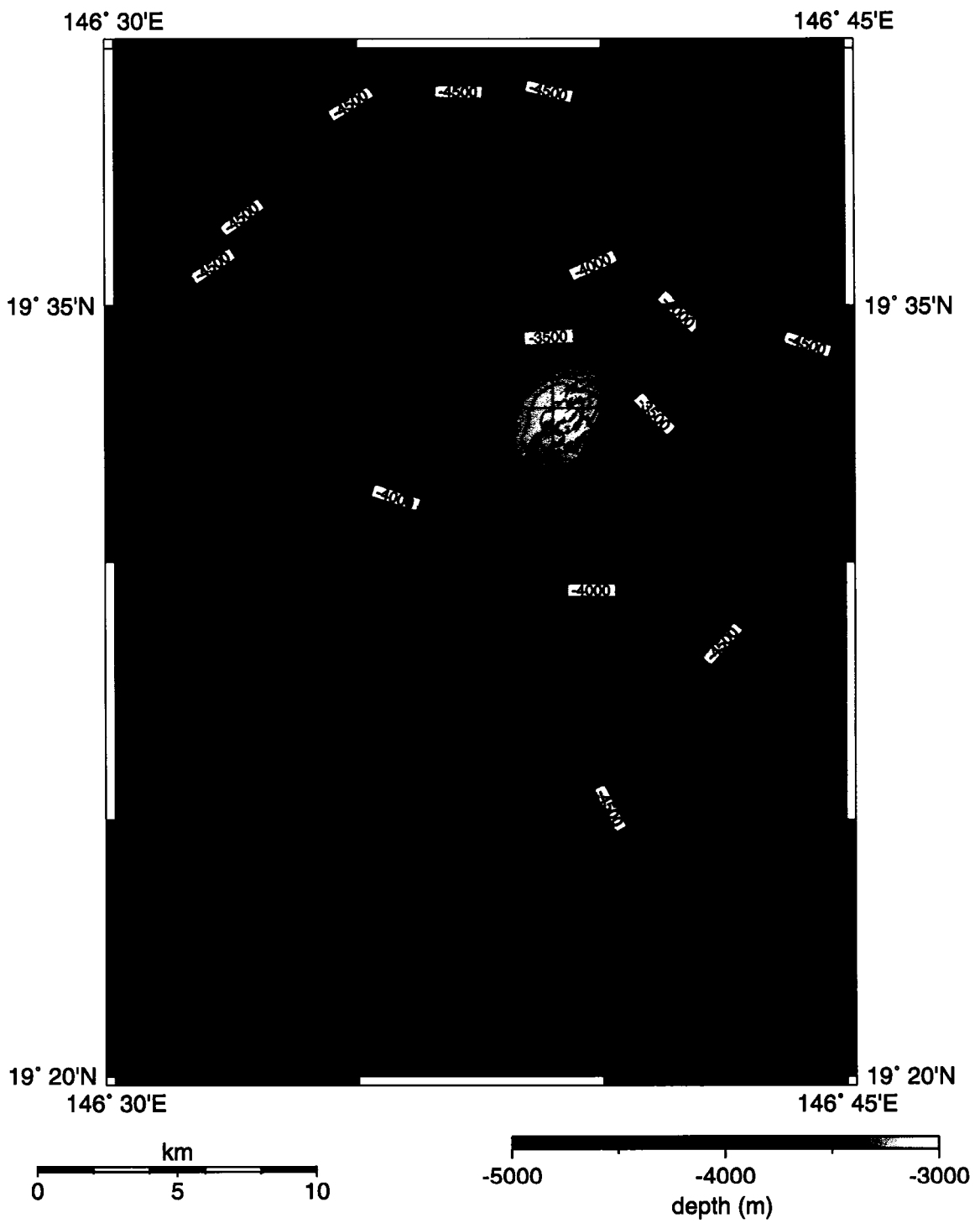
Wash Phase- Clean sample intake and eluate tubing while removing all remaining trace constituents from column.



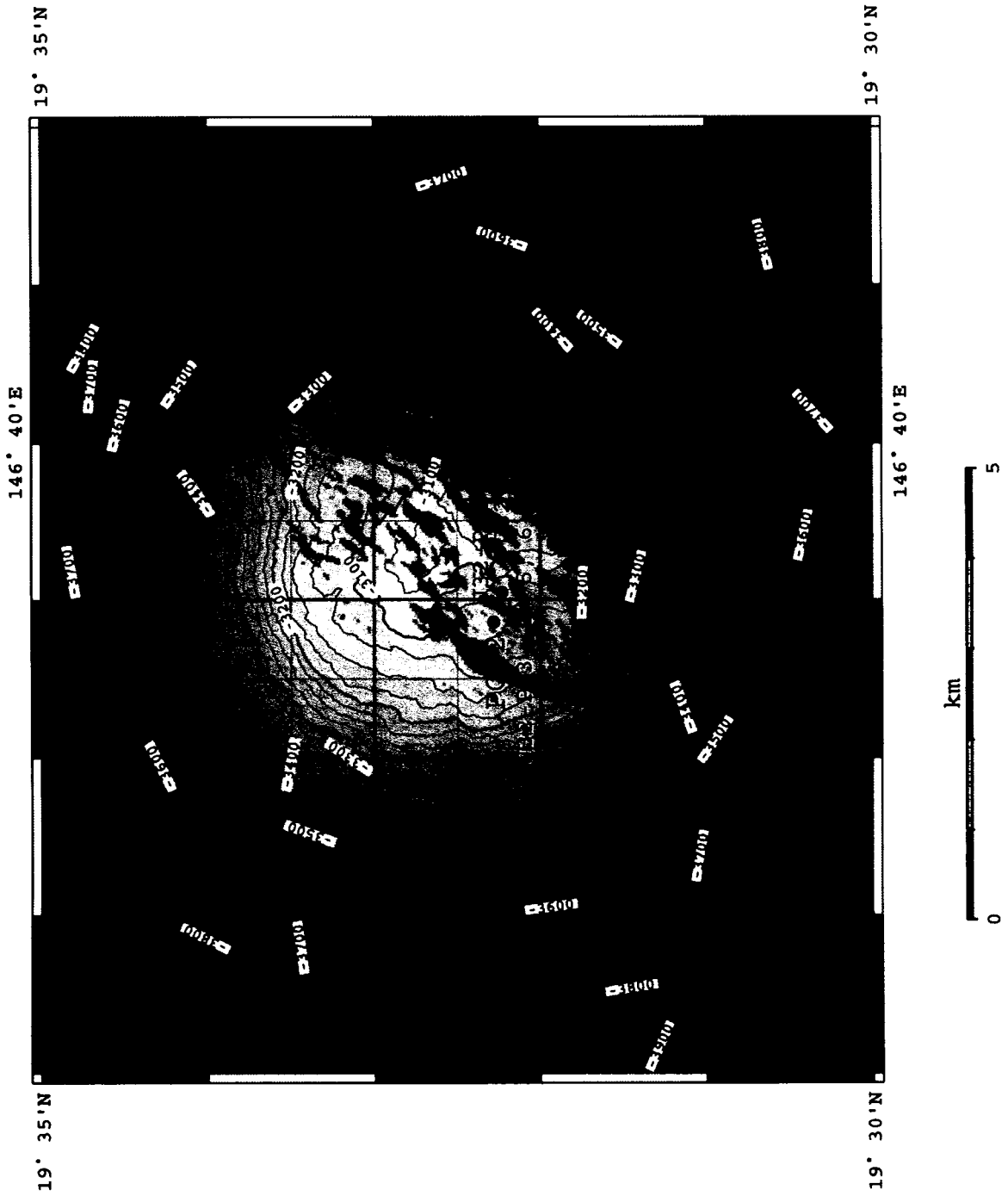
Schematic of the last two steps of the extraction process illustrating reagents and flow paths. Vector arrows represent peristaltic pump positions in flow paths and the direction of active pumping. Only active valve positions are shown for simplicity.

Appendix E. Maps of Multibeam and Bathymetry

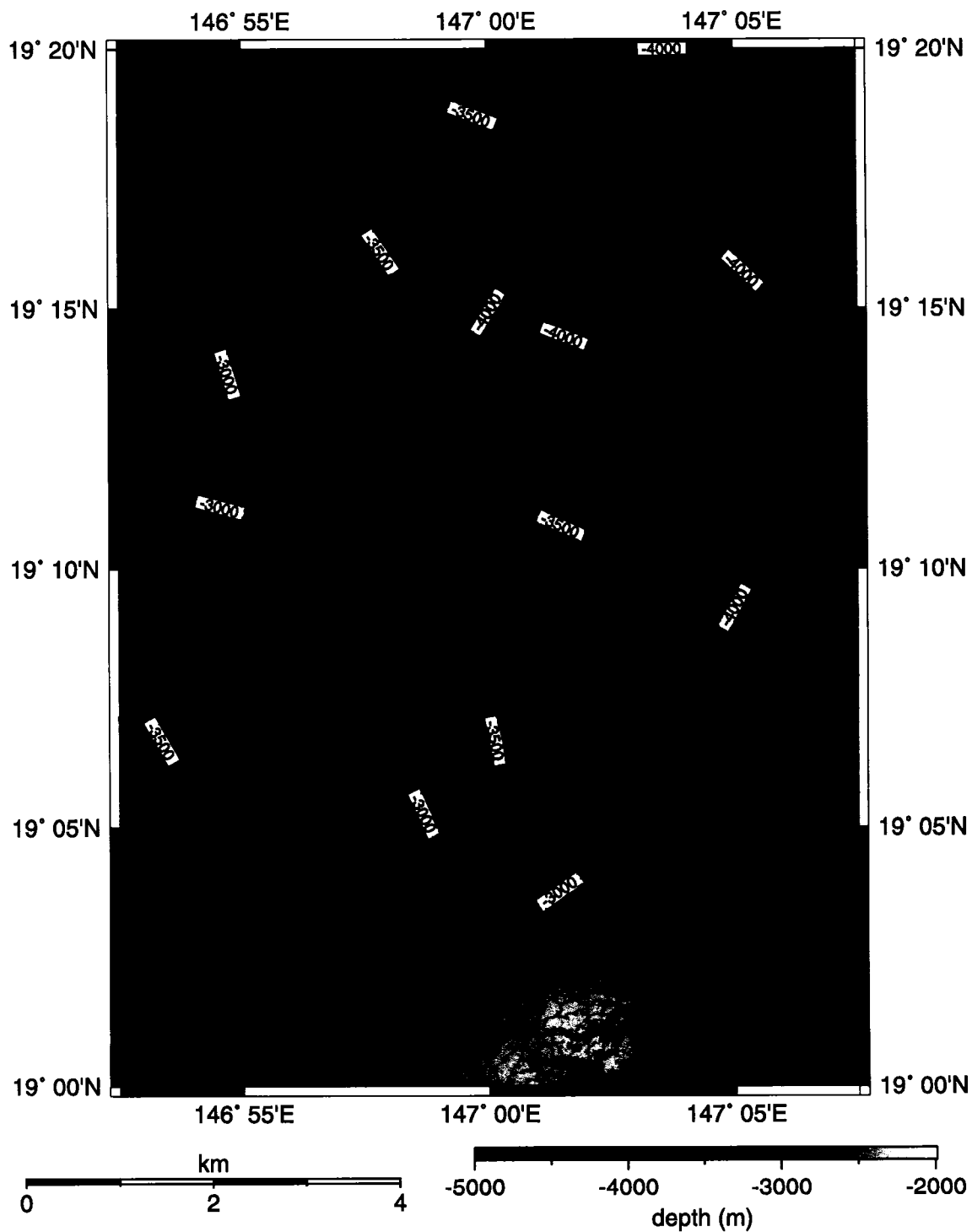
A complete set of maps for the Mariana forearc including all EM 300, Hydrosweep and DSL-120 data obtained on the 2003 expedition are presented in this appendix. The sample positions are displayed on the maps as a reference for the geochemical results. The format consists of regional maps with boxes representing the areas of small-scale map coverages. The methods for sonar data collection, processing and display are given in the methods section of this thesis.



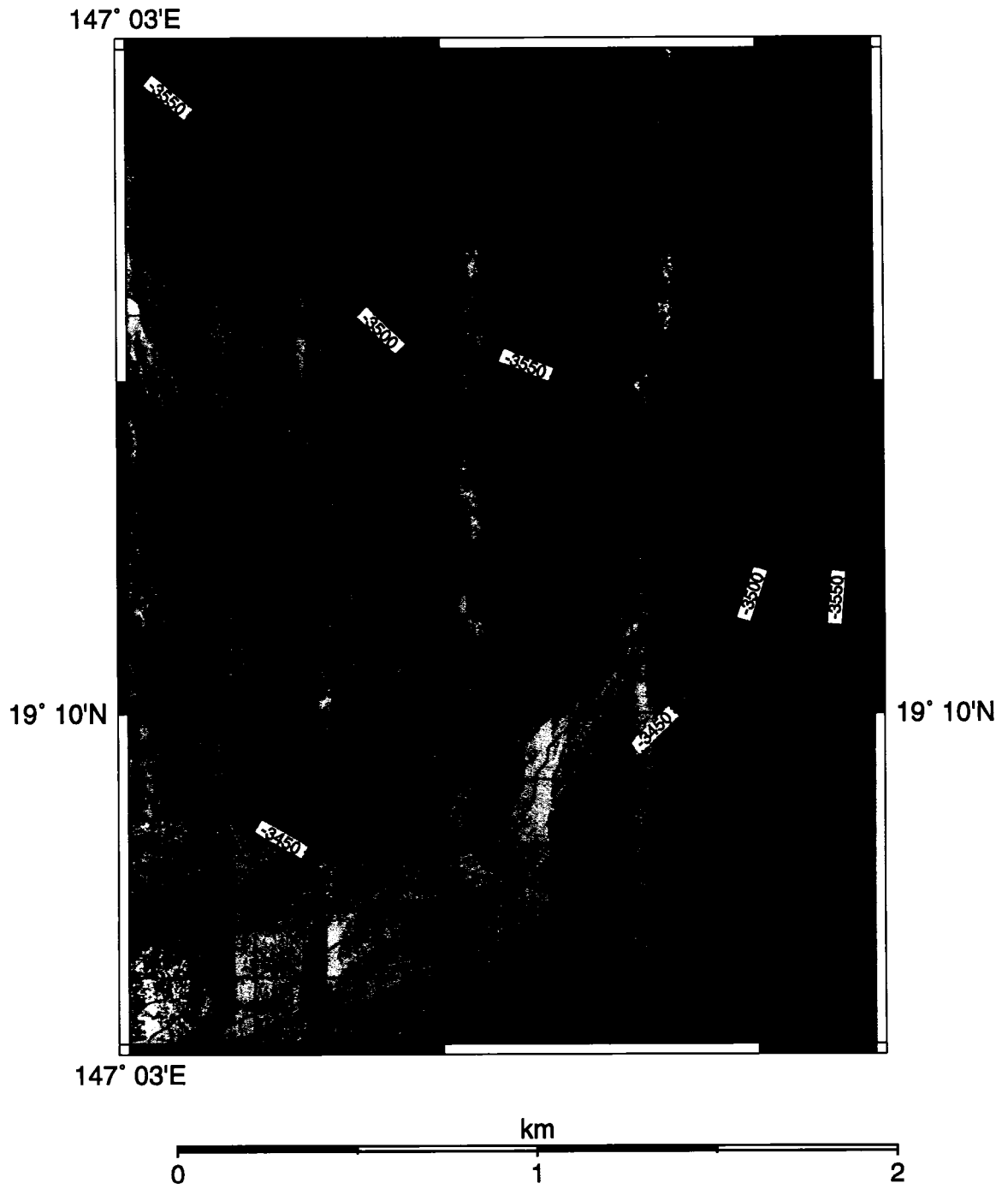
Bathymetry of Conical Seamount.



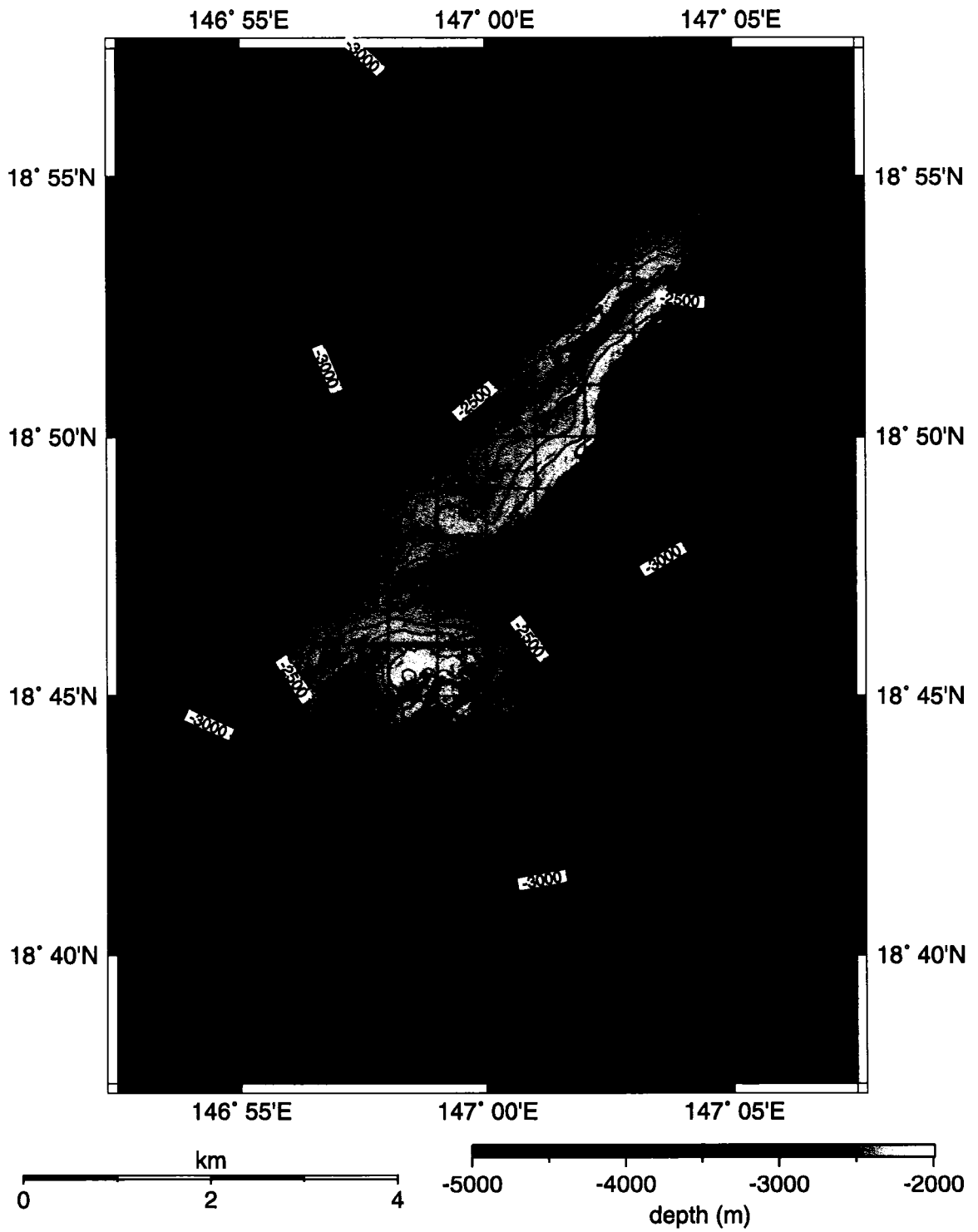
Bathymetry of Conical Seamount.



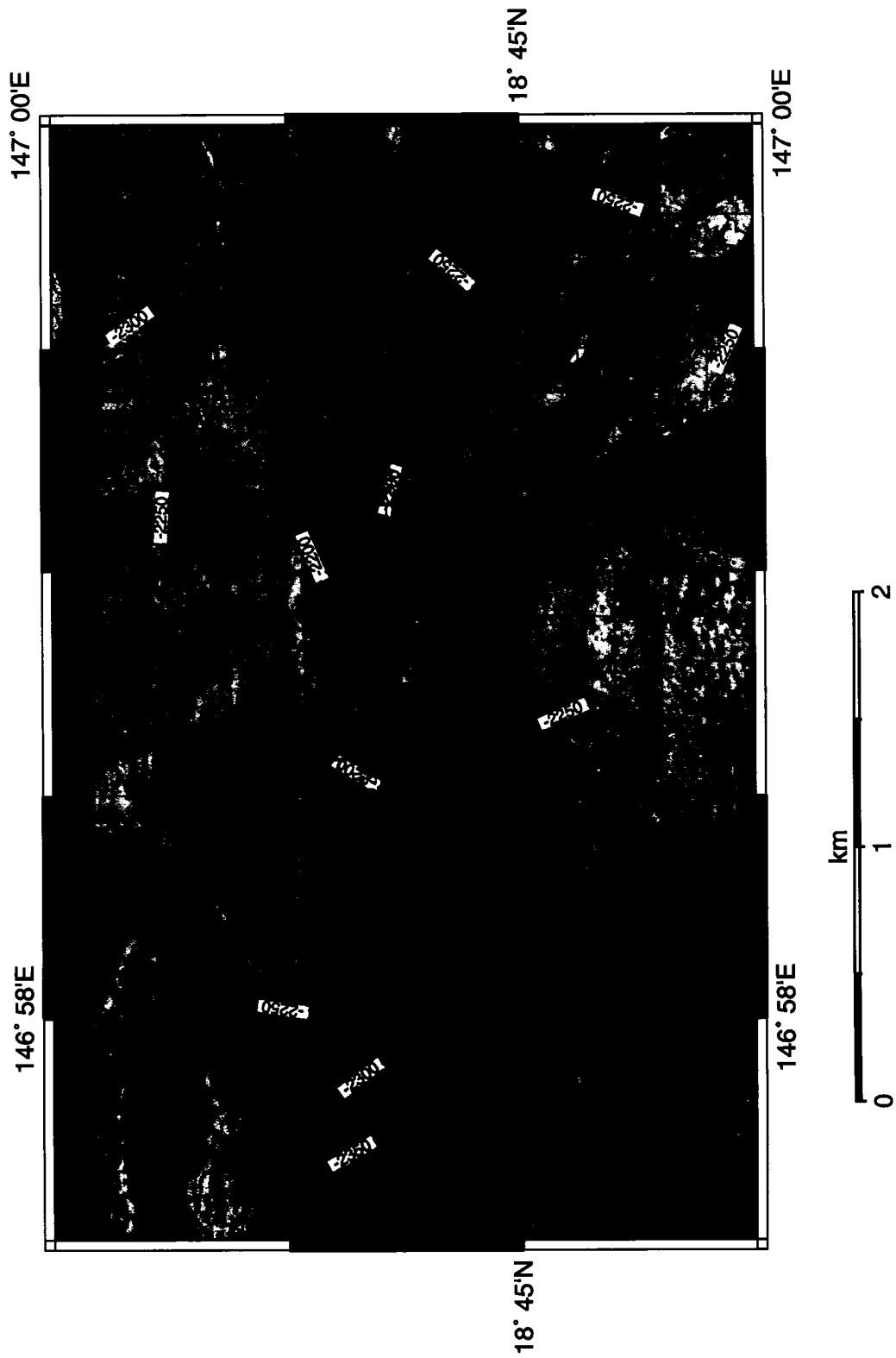
Bathymetry of the eastern half of Pacman Seamount.



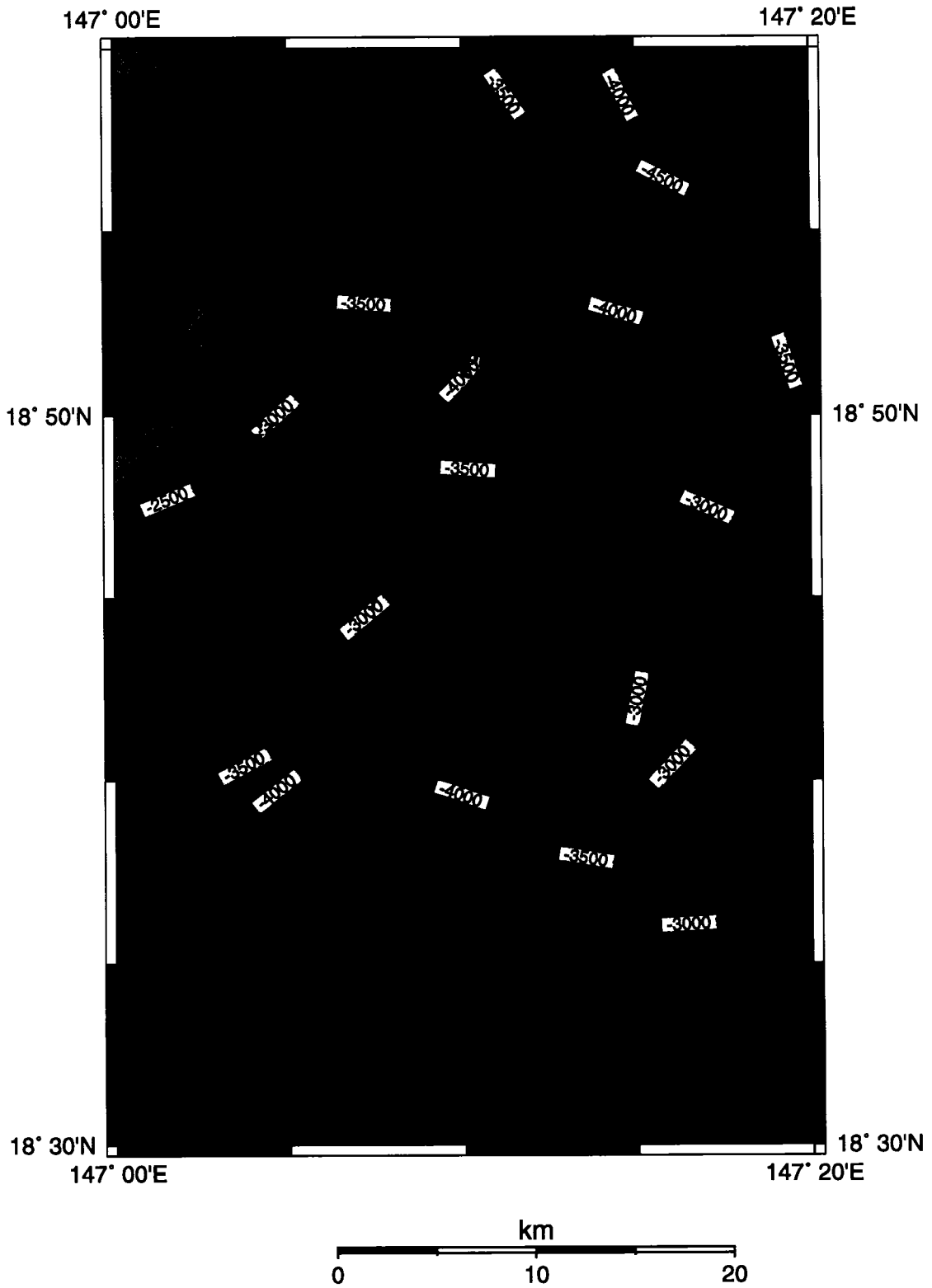
Bathymetry and reflectivity of Cerulean Springs, Pacman Seamount



Bathymetry of Quaker Seamount.



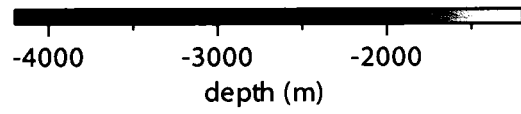
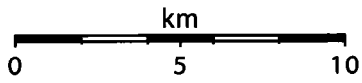
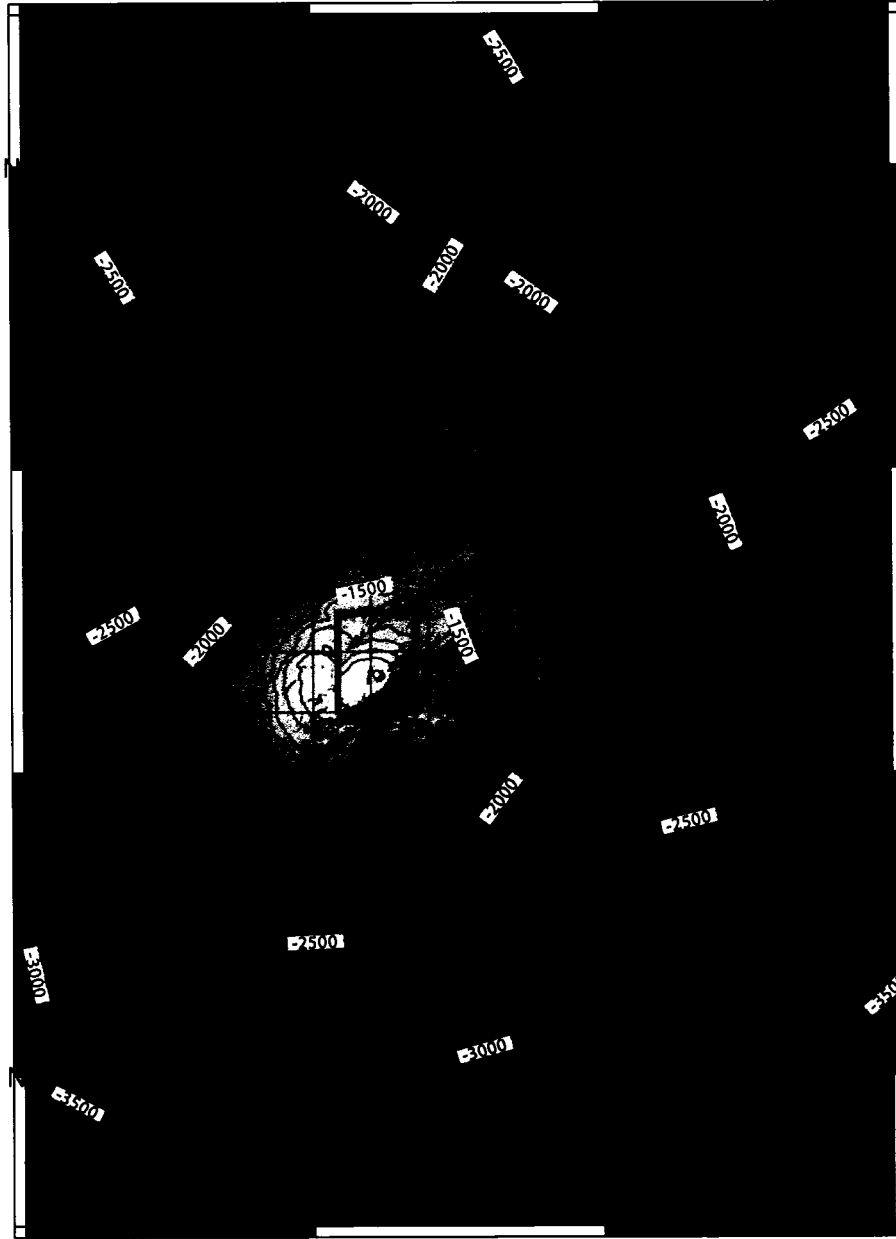
Bathymetry and reflectivity of Quaker Seamount.



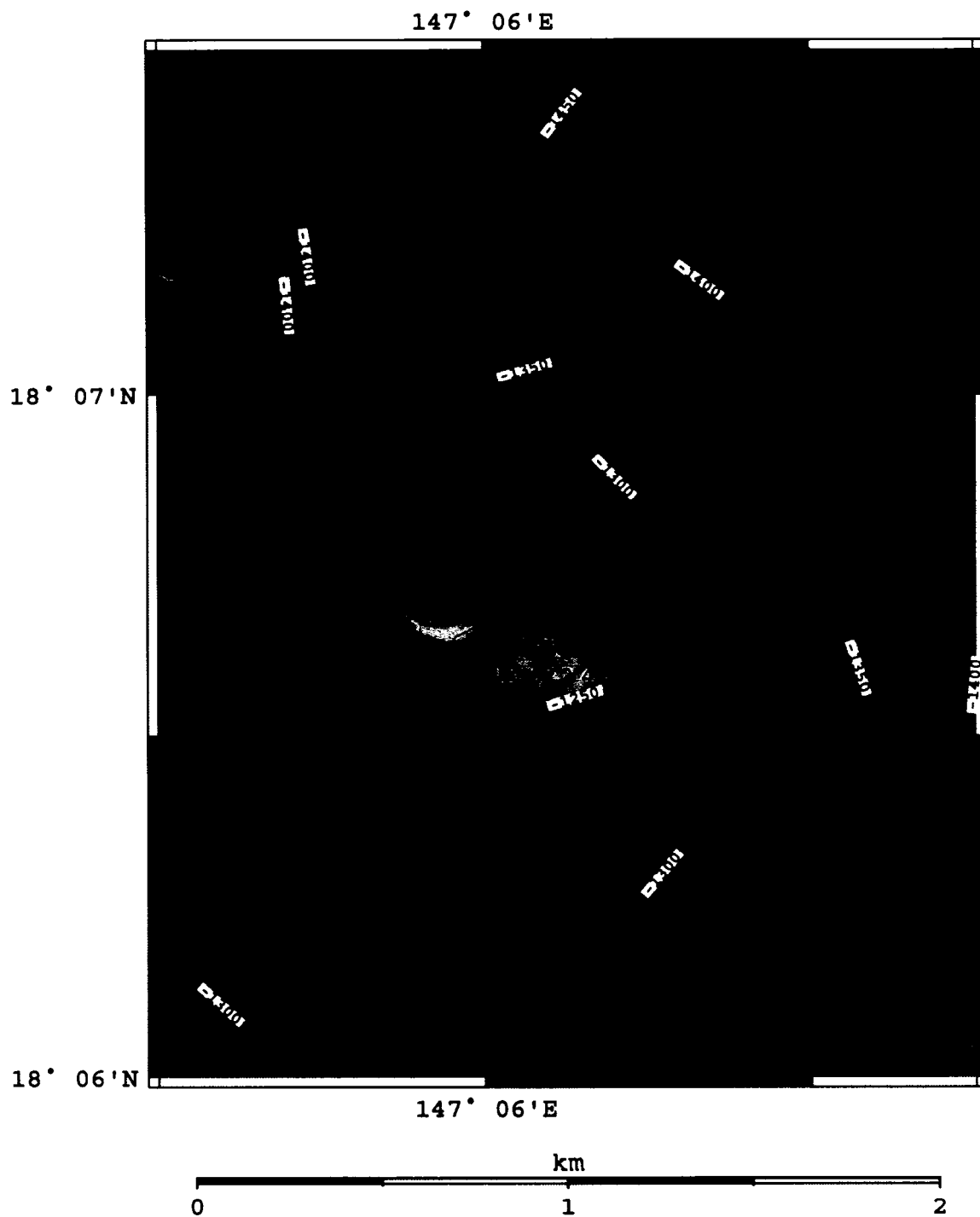
Bathymetry of a small group of emergent seamounts.

147E 00'

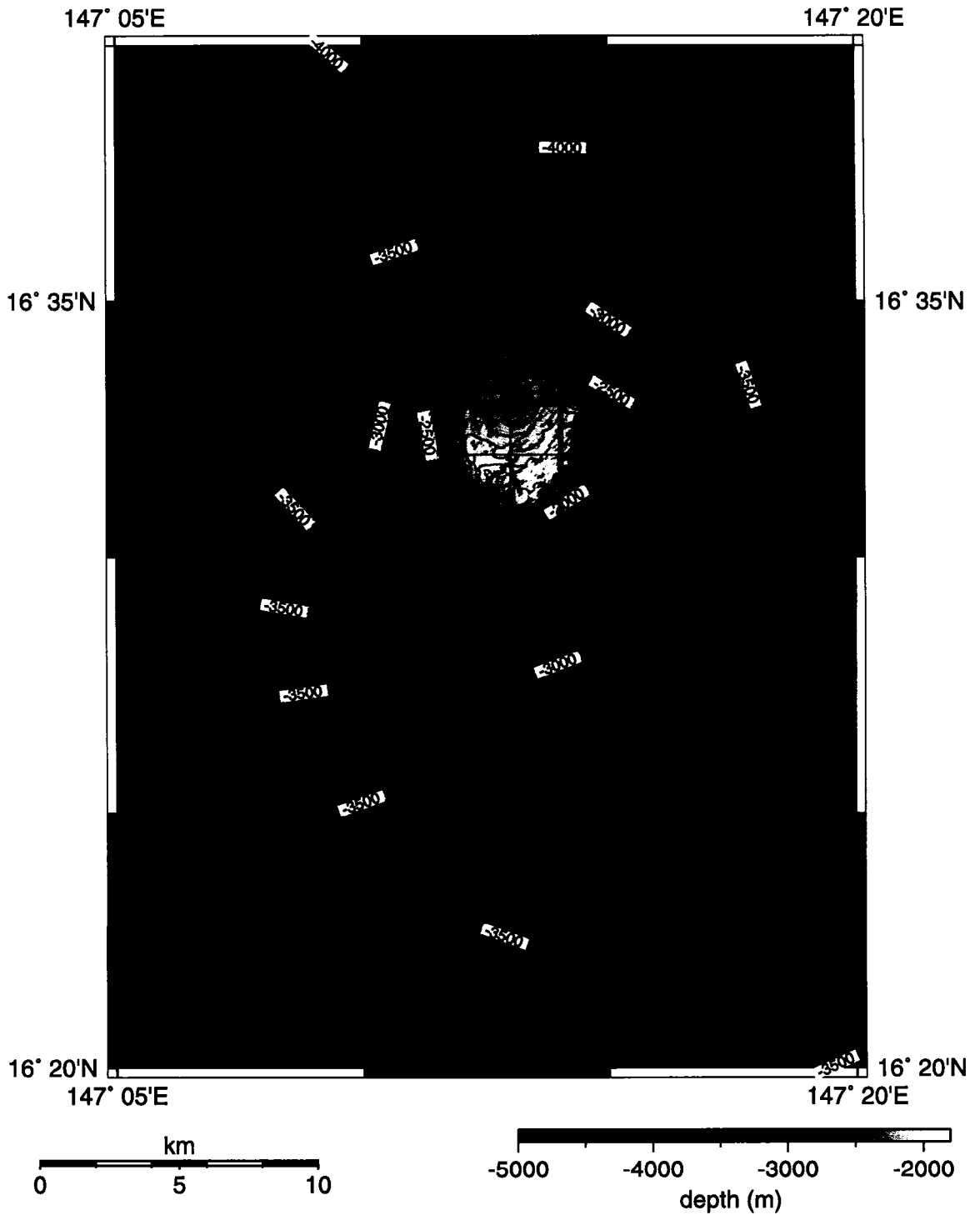
147E 15'



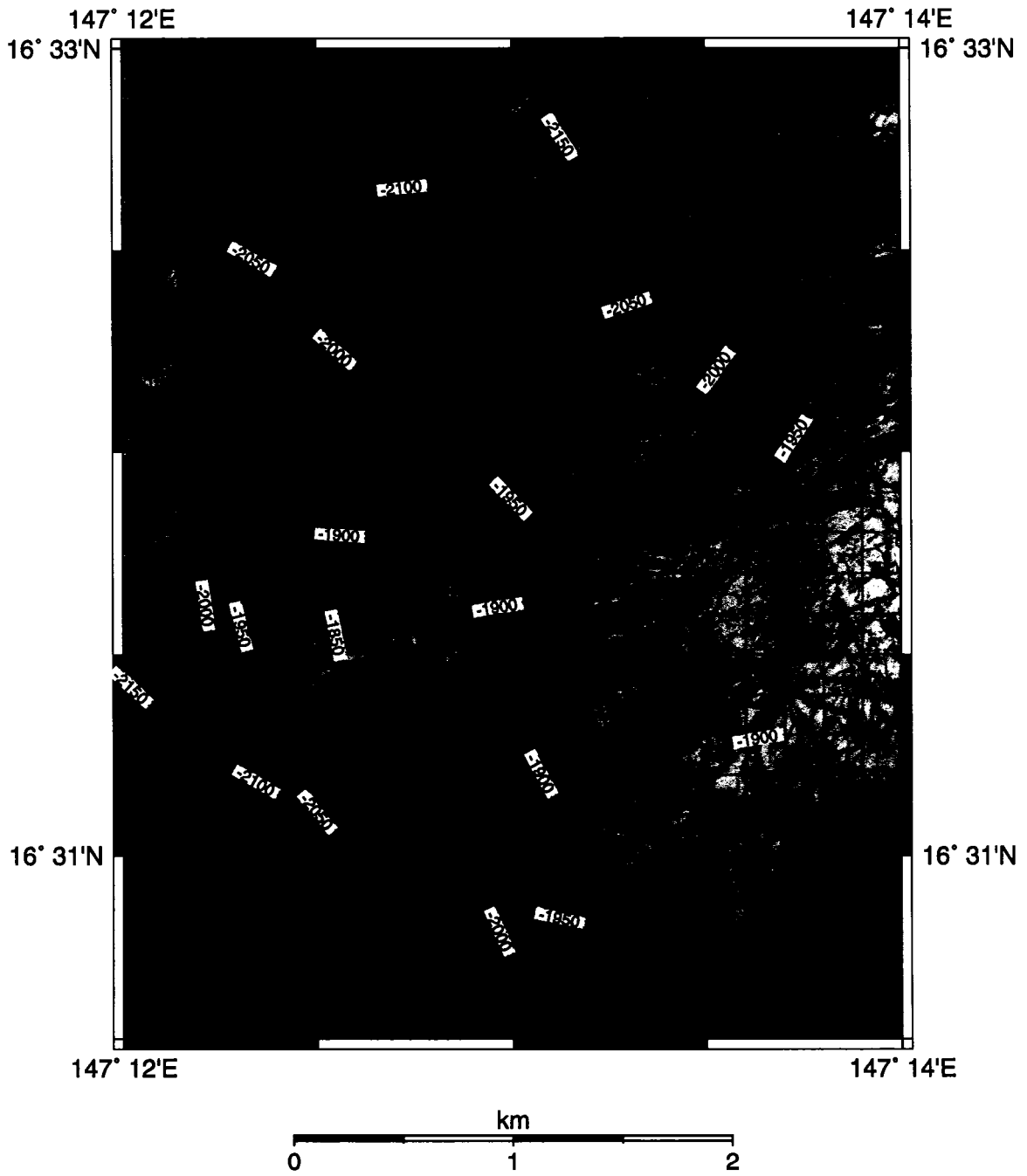
Bathymetry of Big Blue Seamount



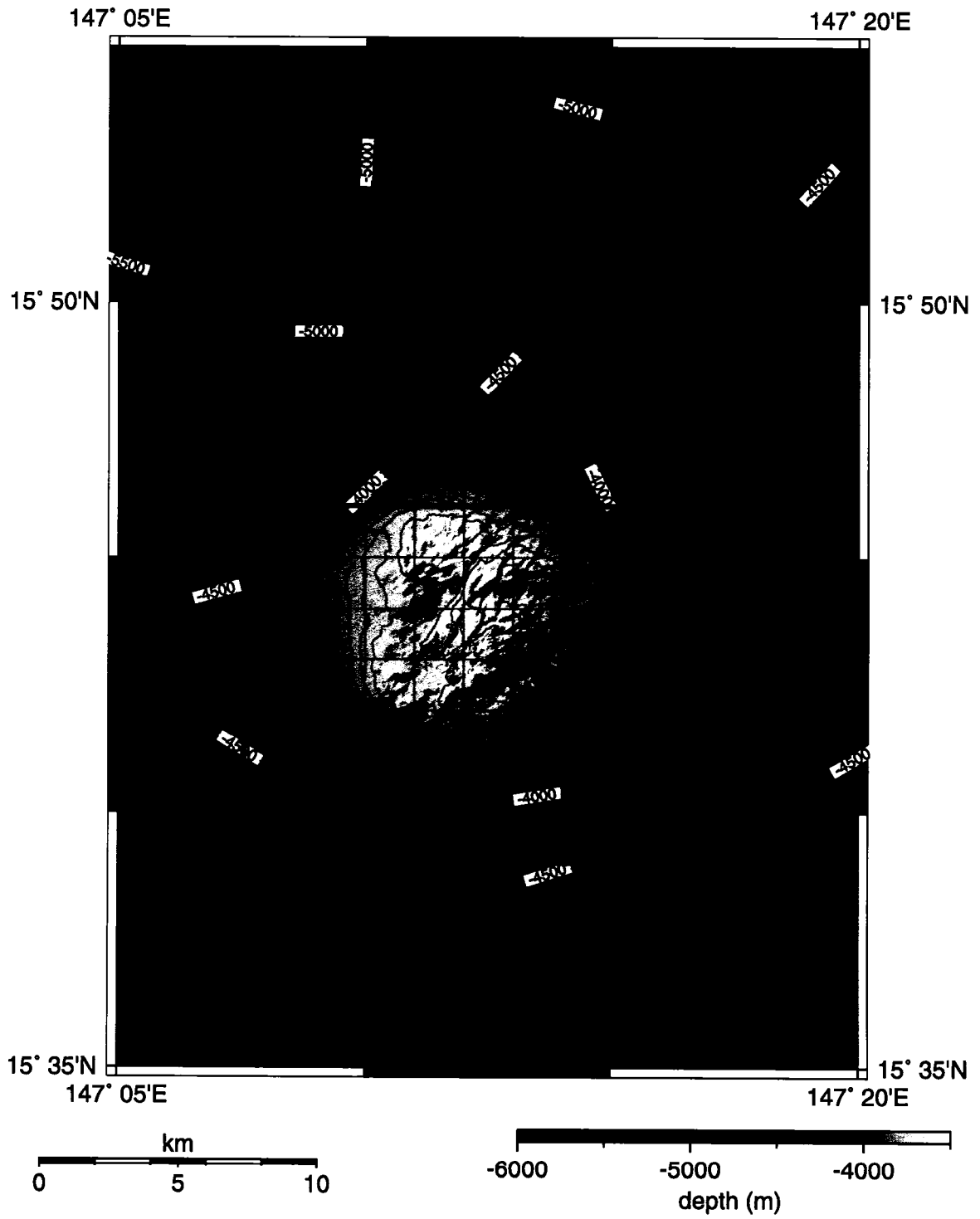
Bathymetry and reflectivity of Big Blue Seamount Summit.



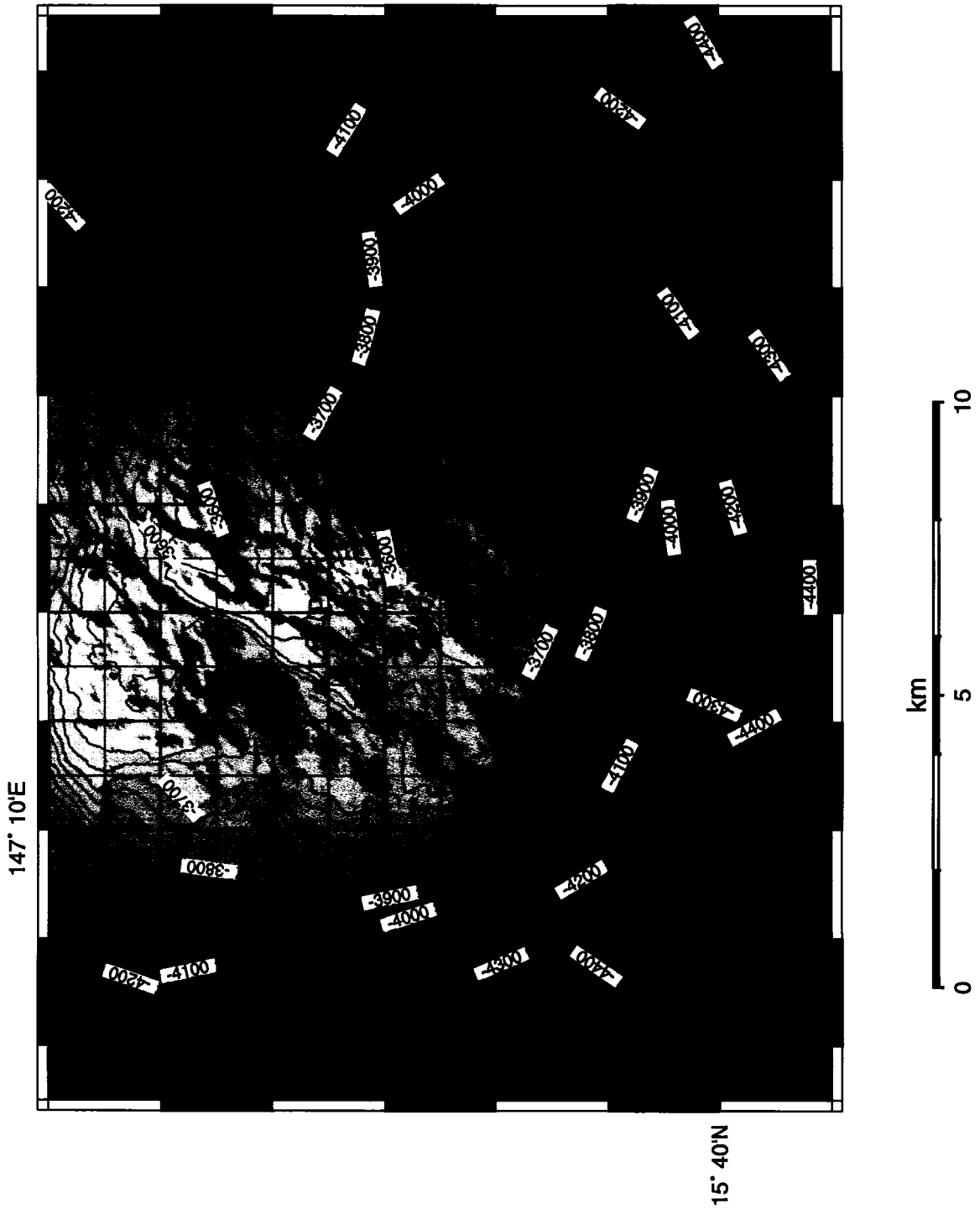
Bathymetry of Celestial Seamount.



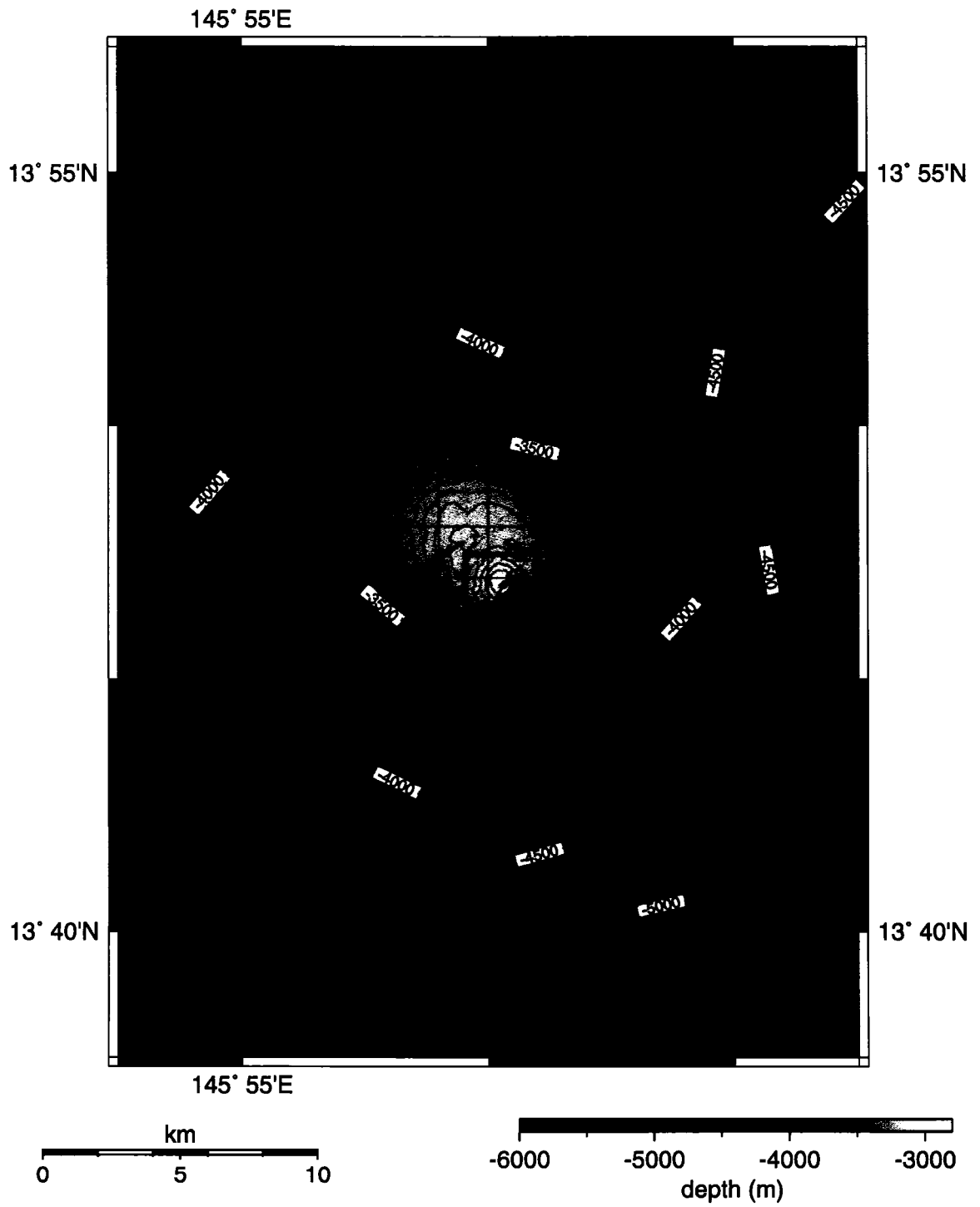
Bathymetry and reflectivity of Celestial Seamount.



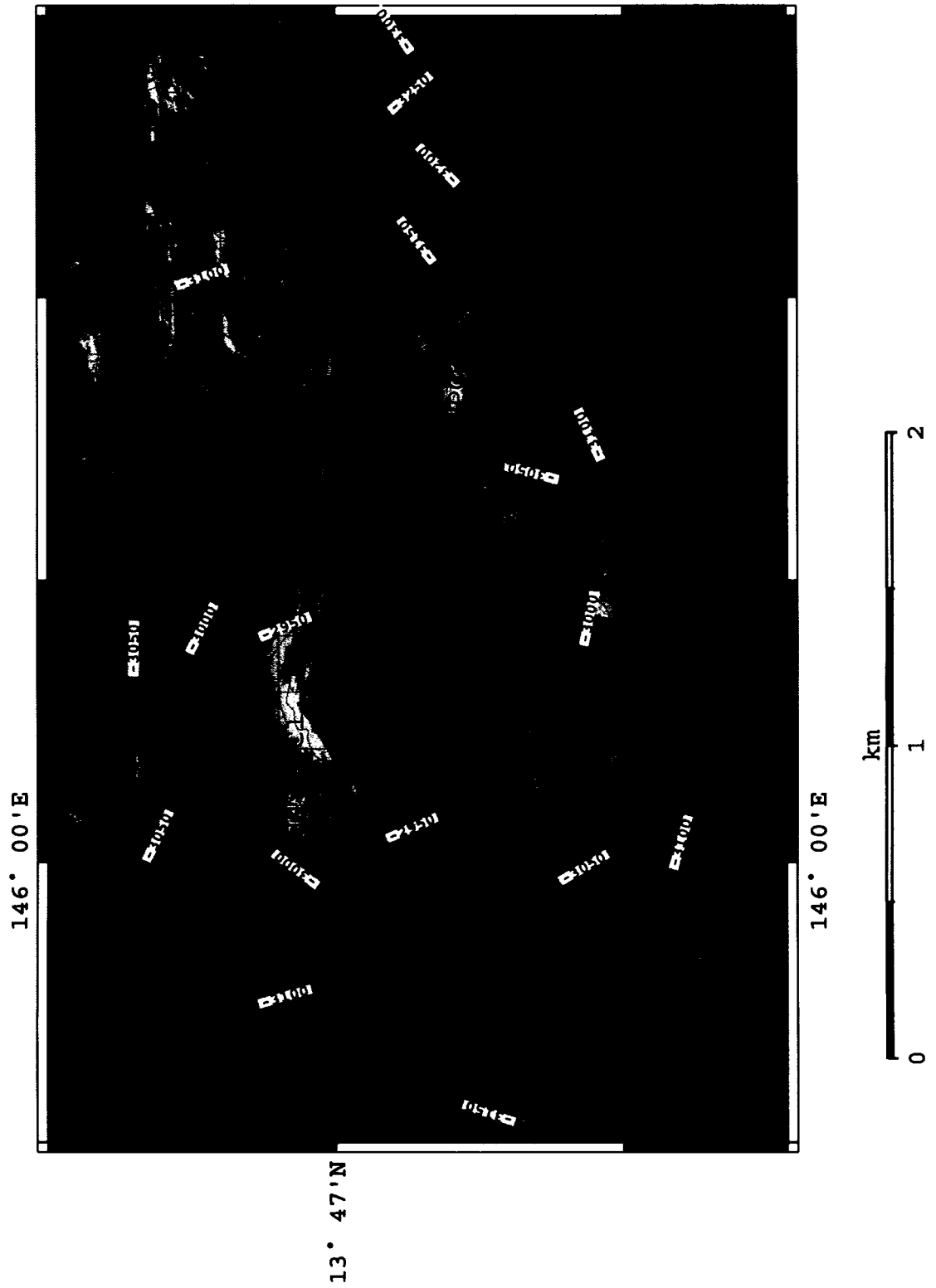
Bathymetry of Blue Moon Seamount.



Bathymetry of Blue Moon Seamount.



Bathymetry of S. Chamorro Seamount.



Bathymetry and reflectivity of S. Chamorro Seamount.

Appendix F. Complete Chemical Analysis Results

A complete listing of all the measured chemical concentrations for all the samples recovered in 2003 from the Mariana Forearc is presented in this appendix. Tables are organized by seamounts and element groups. Methods of analysis are described in the methods section of this thesis.

Conical Seamount

Sample ID	depth (cm)	pH	Alk (meq/kg)	Cl (mmol/kg)	Na (mmol/kg)	Mg (mmol/kg)	Ca (mmol/kg)	K (mmol/kg)	S (mmol/kg)	HS- (umol/kg)	Sr (umol/kg)	Li (umol/kg)
3-1	0-3	7.64	2.31	542.9	475.5	53.60	10.52	10.71	28.41		88.99	27.45
3-2	3-6	7.67	2.46	541.0	468.9	53.12	10.46	10.59	27.96		87.92	27.41
4-1	0-3	7.67	2.38	553.2	478.7	54.26	10.60	10.44	28.49		88.73	27.23
4-2	3-6			547.1	478.8	54.26	10.54	10.48	28.65		88.44	27.37
4-3	6-9	7.74	2.40	552.2	468.6	53.42	10.24	10.34	27.81		86.99	26.69
4-4	9-12			556.0	484.2	54.78	10.67	10.50	29.10		88.82	27.88
5-1	0-3	7.61	2.40	539.1	473.2	53.01	10.43	10.59	27.92		87.97	27.14
5-2	3-6	7.66	2.38	539.1	464.4	52.82	10.21	10.36	27.45		86.99	26.57
6-1	0-3	7.60	2.44	542.9	469.6	52.61	10.24	10.57	27.98		87.50	26.93
6-2	3-6	7.63	2.37	538.2	465.7	52.72	10.18	10.56	27.74		87.19	26.62
6-3	6-9	7.63	2.35	538.2	464.2	52.01	10.02	10.41	27.72		85.90	26.66
6-4	9-12			538.2	467.8	52.41	10.12	10.67	28.01		86.64	26.50
6-5	12-15	7.66	2.30	537.2	466.1	52.25	9.99	10.53	27.95		85.85	26.63
7-1	0-3	7.64	2.30	541.9	465.6	53.10	10.28	10.17	27.88		86.20	27.00
7-2	3-6	7.65	2.47	538.2	469.3	53.48	10.46	10.34	27.98		86.66	27.06
7-3	6-9	7.65	2.25	537.2	463.5	52.75	10.11	10.29	27.98		85.49	26.78
7-4	9-12	7.66	2.39	537.2	465.7	52.96	10.36	10.42	27.76		85.77	26.91
7-5	12-15	7.73	2.22	543.8	463.5	52.72	10.23	10.40	27.90		85.87	26.44
7-6	15-18	7.76	2.35	539.1	467.1	52.45	10.07	10.41	27.86		85.10	26.82
7-7	18-21			535.3	479.0	52.79	10.32	10.52	28.15		86.20	27.11
7-8	21-24	7.79	2.39	538.2	469.7	52.13	10.05	10.31	27.90		84.55	26.76

Dive
J32

Conical Seamount

Sample ID	depth (cm)	pH	Alk (meq/kg)	Cl (mmol/kg)	Na (mmol/kg)	Mg (mmol/kg)	Ca (mmol/kg)	K (mmol/kg)	S (mmol/kg)	HS- (umol/kg)	Sr (umol/kg)	Li (umol/kg)
J32												
8-1	0-3	7.68	2.52	544.73	469.38	53.05	10.34	10.56	28.14	0	87.57	27.18
8-2	3-6	7.70	2.36	541.92	476.56	52.96	10.36	10.66	28.39	0	87.07	27.39
8-3	6-9	7.71	2.21	539.10	461.33	52.42	9.97	10.17	27.8	0	85.07	26.5
8-4	9-12	7.76	2.36	536.28	477.52	53.65	10.56	10.48	28.31	0	86.79	27.34
8-5	12-15	7.76	2.32	536.28	469.17	52.4	10	10.22	27.8	0	84.88	26.74
8-6	15-18	7.75	2.26	536.28	464.08	52.26	10.1	10.19	27.94	0	83.94	26.57
8-7	18-21	7.78	2.30	538.16	470.32	52.47	10.27	10.21	28.05	0	84.88	26.82
8-8	21-24	7.80	2.36	537.22	474	52.31	10.31	10.21	27.86	0	84.85	26.83
Major		7.83	2.60	544.73							86.7	26.2
PC12												
12-1	45-49	8.23	1.74	524.45	463.29	48.97	8.37	10.97	28.37	0	72.7	26.94
12-2	62-68	8.58	1.59	521.70	466.04	47.46	8.03	11.05	28	0	68.3	24.5
12-3	85-95	8.77	1.71	519.87	464.15	45.2	7.36	11.12	25.98	0	62.5	18.75
12-4	125-132	8.94	1.47	510.70	468.8	40.17	6.48	11.48	26.92	0	58.9	16.52
12-5	166-171	8.99	1.35	492.36	465.92	32.9	6.1	12.21	26.83	0	61.7	11.38
12-6	222-228	9.1	1.37	463.94	474.99	20.33	5.31	13.35	27.73	0	68.9	8.97
12-7	260-268	9.07	1.31	438.26	465.74	8.81	4.34	14.11	29.47	0	76.6	10.64
12-8	292-298	9.16	1.41	427.26	452.04	3.44	3.58	14.32	29.15	0	78.1	6.43
GC12												
12-1	8-12	7.60	2.33	538.20	470.95	53	10.37	10.78	27.97		87.4	26.93
12-2	22-25	7.62	2.31	536.37	475.41	52.68	10.14	10.74	28.03		86.6	27.13
12-3	33-36	7.72	2.25	535.45	469.08	52.4	10.05	10.8	28.01		86	26.52
12-4	48-53	7.78	2.31	531.78	467.31	52.38	9.87	10.87	28.05		85.5	26.32
12-5	66-70	7.89	2.16	530.87	480.1	51.08	9.67	10.98	28.51		80.1	27.11

Conical Seamount

Sample ID	Rb umol/ kg	Cs nmol/ kg	Ba nmol/ kg	U nmol/ kg	Mo nmol/ kg
J32					
7-1	1.31	2.7	197	11.4	134
7-2	1.38	3.2	184	11.0	132
7-3	1.40	3.4	191	10.5	118
7-4	1.46	3.9	210	10.8	128
7-5	1.47	4.2	209	10.9	125
7-6	1.45	4.1	206	11.0	123
7-7	1.53	4.5	220	11.5	130
7-8	1.46	5.0	213	11.8	129
8-1	1.46	3.2	255	11.5	225
8-2	1.48	3.4	201	10.9	147
8-3	1.36	2.8	178	10.5	118
8-4	1.43	3.4	200	11.3	133
8-5	1.37	3.2	182	10.4	117
8-6	1.34	3.5	185	10.7	127
8-7	1.37	3.5	189	11.7	126
8-8	1.31	3.6	186	12.2	122
Major	1.31	2.3	412	15.0	169
PC-12					
12-1	2.05	16.2	220	4.0	163
12-2	2.07	20.8	199	0.4	315
12-3	2.31	21.3	168	0.1	150
12-4	2.57	23.6	147	0.0	175
12-5	3.28	39.2	146	0.1	126
12-6	4.18	50.5	147	0.1	295
12-7	5.09	60.2	158	0.0	44
12-8	5.33	61.6	136	0.0	42
GC-12					
12-1	1.63	4.6	227	11.5	134
12-2	1.46	5.0	201	10.5	111
12-3	1.63	6.4	215	11.8	125
12-4	1.62	7.2	194	12.3	121
12-5	1.80	9.2	205	11.1	118

Conical Seamount

Sample ID	B umol/ kg	Mn umol/ kg	Fe umol /kg	Si umol/ kg	V nmol/ kg	Cr nmol/ kg	Co nmol/ kg	Ni nmol/ kg	Cu nmol/ kg	Zn nmol/ kg
J32										
Major	414.6	0.0	0.3	161.3	35.1	4.9	4.88	109	64.0	1119.8
PC-12										
12-1					22.0	0.5	9.22	671	1.5	4.7
12-2					1.5	0.5	3.51	844	8.1	29.4
12-3					6.0	0.2	2.80	673	1.2	4.1
12-4					1.3	1.9	1.33	384	4.3	17.4
12-6					113.3	24.6	1.70	326	8.9	24.4

Cerulean Springs

Sample ID	depth (cm)	pH	Alk (meq/kg)	Cl (mmol/kg)	Na (mmol/kg)	Mg (mmol/kg)	Ca (mmol/kg)	K (mmol/kg)	S (mmol/kg)	HS- (umol/kg)	Sr (umol/kg)	Li (umol/kg)
1-3	3-6	7.70	2.33	526.4	452.72	51.43	11.71	9.75	26.96	0.00	95.1	26.6
1-4	6-9	7.89	1.21	452.4	371.14	32.80	23.49	7.07	20.06	0.00	168.0	18.3
1-2	12-15	10.16	1.50	336.0	247.95	1.01	46.17	3.27	9.28	0.00	300.2	3.3
1-5	18-21	10.73	2.37	308.3	221.68	0.00	49.55	2.21	8.91	0.00	313.2	2.5
1-6	23-27	10.75	2.27	304.6	220.61	0.00	49.44	2.15	8.54	0.00	319.8	2.1
3-1	0-3			526.9	466.27	50.31	12.81	10.24	26.54		100.7	26.7
3-2	3-6	7.74	2.07	520.4	444.69	42.13	18.01	9.76	24.08		133.1	22.6
3-3	6-9	7.73	1.85	511.1	435.54	36.32	21.71	9.45	21.95		155.4	21.0
3-4	9-12	7.73	1.52	498.2	418.93	30.57	25.73	9.11	20.31		180.0	18.8
3-5	12-15	7.68	1.26	489.0	414.21	26.72	28.83	8.81	19.01		197.3	17.2
4-1	0-2	7.56	2.30	535.2	458.14	49.44	13.44	9.95	26.35		108.0	25.1
4-2	2-5	7.60	2.10	525.0	448.97	44.13	16.86	9.48	24.03		131.9	23.0
4-3	5-8	7.58	1.66	501.9	415.65	34.27	24.72	8.76	19.90		184.3	18.2
4-4	8-12	7.52	1.18	452.9	367.21	17.82	35.29	7.42	13.19		250.8	13.4
4-5	12-15	7.39	0.76	415.9	328.8	8.84	41.12	6.48	9.48		293.1	9.2
5-1	0-3	8.04	2.77	537.9	468.37	51.32	11.60	10.32	27.74		90.2	29.1
5-2	3-6	8.21	2.69	534.2	462.27	50.10	12.56	10.31	27.37		92.8	28.3
5-3	6-9	8.34	2.37	526.9	467.92	47.02	14.32	10.11	27.03		96.8	28.3
5-4	9-12	8.23	1.84	521.3	452.54	42.92	16.20	9.97	25.98		101.5	28.7
5-5	12-15	8.40	1.63	516.7	448.28	41.09	17.23	9.77	25.37		103.2	25.1
5-6	18-21				448.76	38.12	19.08	9.60	25.02		109.1	24.8
5-7	23-27				434.09	35.57	20.06	9.36	24.63		110.6	24.9

Dive
J31

Cerulean Springs

Sample ID	depth (cm)	pH	Alk (meq/kg)	Cl (mmol/kg)	Na (mmol/kg)	Mg (mmol/kg)	Ca (mmol/kg)	K (mmol/kg)	S (mmol/kg)	HS- (umol/kg)	Sr (umol/kg)	Li (umol/kg)
PC-11												
11-1	10-14	7.80	1.73	506.8	430.8	45.25	15.82	9.20	24.63		118.0	24.1
11-2	24-28	7.88	1.46	490.3	417.3	42.47	17.59	8.57	23.61		127.7	22.5
11-3	38-42	8.11	0.88	465.5	392.3	34.39	23.60	7.92	20.90		164.4	19.5
11-4	68-76	9.36	0.64	370.0	281.7	3.05	46.59	4.79	11.21		295.3	5.9
11-5	85-93	9.93	0.98	345.2	258.8	0.54	50.71	3.90	9.75		315.6	3.3
11-6	120-128	10.57	1.58	317.7	236.7	0.17	51.93	2.80	9.12		324.5	1.8
11-7	168-171	10.77	2.40	305.7	221.4	0.08	49.00	2.16	8.64		313.7	1.3
11-8	200-206	10.82	2.62	303.0	220.2	0.09	48.82	2.09	8.52		311.8	1.2
11-9	264-270	10.72	3.04	302.1	218.2	0.10	48.66	2.04	8.58		309.8	1.5
11-10	298-304	10.75	2.92	301.2	219.7	0.10	48.80	2.00	8.60		312.9	1.4
11-11	325-333	10.71	2.97	302.1	219.6	0.10	48.90	2.00	8.70		312.5	1.3
GC-11												
11-1	2-6	7.55	1.50	499.5	416.8	36.50	21.17	8.61	21.51		150.5	21.2
11-2	16-20	7.70	0.96	472.8	399.2	30.94	26.32	7.87	19.74		178.1	18.9
11-3	30-33	7.64	0.92	471.9	391.8	30.31	25.75	7.81	19.53		175.9	17.8
11-4	42-46	9.09	0.57	399.4	313.7	8.26	42.86	5.56	13.08		270.1	9.4
11-5	51-55	10.11	0.89	350.7	268.9	0.92	50.27	3.82	10.22		304.7	4.0

Cerulean Springs

Sample ID	B umol/ kg	Mn umol / kg	Fe umol /kg	Si umol/ kg	Rb umol/ kg	Cs nmol/ kg	Ba nmol/ kg	U nmol/ kg	Mo nmol/ kg
J31:1-3	521	3	5	2878	1	3	249	14	131
1-4	350	7	11	3955	1	4	275	7	95
1-2	53	1	2	570	1	5	522	0	27
1-5	15	5	6	2569	0	6	384	1	29
1-6	15	5	6	1901	0	5	390	0	28
3-1	412				1	3	193	12	129
3-2	348	2	2	837	1	4	330	8	102
3-3	325	1	1	440	1	4	286	6	90
3-4	288	2	2	1658	1	4	326	5	78
3-5	266	1	1	837	1	4	357	4	79
4-1	471	4	5	1864	1	3	274	11	125
4-2	424	1	1	414	1	3	262	9	105
4-3	373	3	4	1815	1	3	389	6	87
4-4	264	3	5	2759	1	4	559	3	57
4-5	168	1	2	1165	1	6	690	1	39
5-1	451	0	0	234	1	3	155	13	122
5-2	460	0	0	218	1	3	154	10	134
5-3	474	1	1	623	1	3	161	8	117
5-4	507	1	2	1558	1	4	169	4	113
5-5	475	0	0	396	1	4	170	3	109
5-6	467				1	4	170	2	107
5-7	480				1	4	174	2	101
PC11-1	461	6	9	5002	1	3	179	11	104
11-2	404	1	2	1633	1	4	175	10	95
11-3	329	0	0	101	1	4	191	6	77
11-4	92	1	1	42	1	7	293	0	23
11-5	63	7	10	1651	1	7	316	0	25
11-6	59	19	31	7019	0	7	329	1	39
11-7	43	0	0	62	0	7	287	0	19
11-8	34	1	1	51	0	8	292	0	23
11-9	57	2	2	82	0	8	303	0	21
11-10	51	1	2	711	0	8	297	0	23
11-11	58	8	12	2772	0	8	308	0	32
GC11-1	353	0	1	238	1	3	205	7	79
11-2	363	8	12	3801	1	4	231	5	75
11-3	395	15	23	7063	1	4	242	5	84
11-4	140	4	6	2598	1	6	298	0	32
11-5	79	12	20	5643	1	8	313	1	39

Cerulean Springs

Sample ID	V nmol/ kg	Cr nmol/ kg	Co nmol/ kg	Ni nmol/ kg	Cu nmol/ kg	Zn nmol/ kg
Dive J32						
1-3	156.3	5.7	3.36	132	132.8	14.2
1-4	33.8	3.2	1.23	43	21.5	13.5
1-2	38.3	1.4	0.63	43	11.3	15.2
1-5	31.4		0.66	0	10.2	10.2
1-6	25.1	3.6	0.05	18	4.8	4.7
4-1	154.5	5.6	1.95	134	125.4	20.5
4-2	64.6	5.3	0.96	47	50.2	14.8
4-3	37.9	4.9	0.70	48	12.6	15.2
4-4	52.8	4.6	0.90	42	9.8	11.7
4-5	144.5	6.4	1.09	18	6.7	23.2
PC-11						
11-1	13.7	19.0	0.57	174	3.2	19.0
11-2	5.1	16.2	0.53	131	2.5	14.1
11-3	1.5	8.3	0.92	168	2.6	12.9
11-4	1.0	0.2	0.40	37	1.7	4.1
11-5	1.6	0.6	0.02	8	1.4	5.5
11-6	1.9	0.2	0.13	2	1.9	0.4
11-8	6.2	0.5	0.14	9	1.7	5.6
11-9	5.6	1.6	0.07	5	3.2	12.1
11-10	5.7	7.6	5.85	27	4.6	10.3
11-11	6.5	0.9	0.21	11	10.2	26.1

Cerulean Springs

		Dive J32		
		1-3	1-2	1-6
nmol/kg				
	Y	0.232	0.023	0.008
	Cd	3.08	0.02	0.01
pmol/kg				
	La	26.9	6.0	3.0
	Ce	11.0	12.2	5.4
	Pr	4.01	1.96	0.79
	Nd	20.1	9.0	3.3
	Sm	4.62	1.78	0.75
	Eu	1.476	0.592	0.144
	Gd	8.32	2.27	0.74
	Tb	1.352	0.266	0.113
	Dy	9.88	1.87	0.64
	Ho	2.399	0.339	0.137
	Er	8.41	1.07	0.39
	Tm	1.241	0.136	0.072
	Yb	9.83	1.07	0.28
	Lu	1.725	0.148	0.049

Quaker Seamount

Sample ID	depth (cm)	pH	Alk (meq/kg)	Cl (mmol/kg)	Na (mmol/kg)	Mg (mmol/kg)	Ca (mmol/kg)	K (mmol/kg)	S (mmol/kg)	HS- (umol/kg)	Sr (umol/kg)	Li (umol/kg)
Dive J33												
2-1	0-3	7.67	2.41	537.2	473.7	53.25	10.35	10.67	28.17		88.0	27.6
2-2	3-6	7.65	2.39	538.6	464.5	52.79	10.19	10.67	27.89		87.5	27.4
2-3	9-12	7.69	2.36	535.3	461.7	52.28	9.82	10.11	27.58		83.5	30.7
2-4	12-15	7.68	2.25	535.3	469.0	52.62	10.05	10.22	27.69		82.4	37.6
3-1	0-2	7.70	2.37	540.9	468.1	53.39	10.40	10.62	28.07		87.7	27.3
3-2	2-4	7.68	2.32	537.2	470.2	53.11	10.32	10.72	28.21		86.1	28.1
3-3	4-6	7.73	2.39	538.6	471.6	52.82	10.03	10.69	28.06		84.2	28.9
3-4	6-9	7.75	2.12	534.4	475.1	52.67	9.96	10.65	28.06		82.5	30.2
3-5	9-11	7.78	2.04	536.2	468.2	51.88	9.60	10.39	27.76		79.2	31.0
3-6	11-13	7.82	1.88	535.3	469.8	50.81	9.26	10.22	27.36		76.5	31.8
5-1	0-3	7.67	2.42	540.0	467.9	52.72	10.01	10.75	27.64		87.5	27.9
5-2	6-9	7.65	2.15	536.2	475.4	52.61	10.05	10.72	27.89		83.9	30.1
5-3	9-12	7.70	2.12	537.2	475.8	52.26	9.77	11.01	27.93		82.8	30.6
5-4	12-15	7.73	1.93	535.3	470.3	51.99	9.49	10.96	27.84		80.4	31.4
5-5	15-18	7.78	1.87	535.3	484.2	52.93	9.80	10.49	27.90		78.6	32.9
5-6	18-21	7.81	1.80	535.3	477.5	52.10	9.49	10.35	27.59		76.0	31.5
6-1	0-3	7.63	2.39	540.9	471.6	53.42	10.57	10.85	28.35		89.3	27.5
6-2	3-6	7.62	2.36	537.2	472.2	53.17	10.52	10.91	28.00		88.5	28.1
6-3	6-9	7.67	2.31	538.1	475.0	52.83	10.20	11.06	28.25		87.4	29.2
6-4	9-12	7.64	2.23	534.4	479.2	52.87	10.35	10.98	28.32		87.5	31.3
6-5	12-15	7.71	2.10	534.4	473.9	52.42	10.07	10.49	28.09		84.5	32.0
6-6	15-18	7.90	1.89	531.5	471.0	52.20	9.72	10.35	27.96		79.4	32.8
6-7	18-21	7.84	1.91	532.5	482.0	52.72	10.01	10.53	28.69		82.0	34.1

Quaker Seamount

Sample ID	depth (cm)	pH	Alk (meq/kg)	Cl (mmol/kg)	Na (mmol/kg)	Mg (mmol/kg)	Ca (mmol/kg)	K (mmol/kg)	S (mmol/kg)	HS- (umol/kg)	Sr (umol/kg)	Li (umol/kg)
Dive J33												
7-1	0-2	7.73	2.37	540.0	471.1	53.34	10.38	10.83	28.30		88.9	27.1
7-2	2-4	7.67	2.36	539.1	473.5	52.95	10.40	11.02	28.24		88.8	27.8
7-3	4-7	7.71	2.54	539.1	477.9	53.34	10.32	11.14	28.23		88.8	28.3
7-4	7-9	7.72	2.48	538.1	478.5	53.08	10.41	11.06	28.02		87.9	28.6
7-5	9-11.5	7.73	2.26	535.3	465.3	52.22	9.87	10.68	27.71		85.6	28.3
7-6	11.5-13	7.73	2.30	536.2	481.3	53.14	10.29	10.79	28.44		86.3	29.5
8-1	0-4	8.79	1.58	538.1	477.2	55.31	8.69	10.47	27.90		74.3	27.1
8-2	4-6.5	8.54	1.74	539.1	477.7	55.04	8.91	10.50	27.92		77.3	27.1
8-3	6.5-8.5	8.14	1.85	536.2	477.3	53.89	9.53	10.56	28.01		81.0	27.5
8-4	8.5-10.5	8.08	1.81	537.2	476.8	53.62	9.24	10.59	27.94		79.1	27.6
8-5	10.5-14	7.99	1.63	536.2	479.4	53.27	9.14	10.85	28.22		80.0	27.9
9-1	0-4.5	8.84	1.46	541.9	485.3	55.44	8.99	10.53	28.35		78.4	27.1
9-2	4.5-7	8.56	1.56	538.1	480.8	55.55	9.31	10.69	28.36		78.3	27.2
9-3	7-9	8.61	1.37	537.2	483.7	54.70	8.86	10.46	27.91		73.6	27.1
9-4	9-13.5	8.57	1.01	537.2	484.2	54.01	8.83	10.72	28.15		76.3	27.4
10-1	0-3	7.65	2.39	541.9	470.5	53.10	10.02	10.86	27.74		89.1	28.1
10-2	3-6	7.68	2.41	537.2	477.3	53.39	10.39	10.67	28.11		88.3	27.5
10-3	6-9	7.66	2.43	537.2	469.2	52.91	10.05	10.59	27.81		87.5	27.4
10-4	9-12	7.70	2.55	538.1	478.5	53.37	10.56	11.06	28.36		89.6	28.4
10-5	12-15	7.70	2.55	537.2	482.3	52.95	10.27	11.03	27.89		88.8	28.7
10-6	15-18	7.78	2.48	538.1	474.4	53.81	10.46	10.72	28.02		88.5	28.4

Quaker Seamount

Sample ID	depth (cm)	pH	Alk (meq/kg)	Cl (mmol/kg)	Na (mmol/kg)	Mg (mmol/kg)	Ca (mmol/kg)	K (mmol/kg)	S (mmol/kg)	HS- (umol/kg)	Sr (umol/kg)	Li (umol/kg)
Dive J37												
1-1	0-3	7.71	2.18	540.5	476.8	53.56	10.55	10.95	28.35		89.6	27.7
1-2	6-9	7.87	1.83	536.7	481.9	52.93	10.28	11.02	28.24		82.9	29.1
1-3	9-12	7.87	1.78	535.8	482.9	52.79	9.74	10.94	28.40		81.6	29.3
1-4	12-15	7.90	1.67	533.9	478.4	52.52	9.54	10.86	28.21		80.5	28.5
1-5	15-18	7.92	1.30	533.0	488.0	53.05	9.71	11.01	28.40		80.5	29.1
2-1	0-3	7.80	2.29	539.6	477.9	53.57	10.03	11.00	28.26		89.6	27.6
2-2	6-9	7.75	2.48	537.7	470.6	51.82	10.00	10.75	27.60		87.8	27.3
2-3	9-12	7.89	1.80	532.1	485.4	50.88	9.77	11.00	28.47		82.6	27.6
2-4	12-15	8.09	1.70	530.2	490.9	50.88	9.18	11.43	27.91		79.2	27.6
3-1	0-3	7.71	2.34	538.6	483.7	53.97	10.62	11.01	28.43		91.2	27.9
3-2	6-9	7.75	2.19	537.7	490.4	53.54	10.12	11.00	28.42		87.8	28.3
4-1	0-4	7.67	2.50	539.6	465.9	52.79	10.17	10.64	27.56		88.2	27.2
4-2	4-7.5	7.68	2.27	536.7	475.7	52.54	10.04	10.70	27.82		85.8	28.0
4-3	7.5-10	7.67	2.22	536.7	469.6	52.52	10.08	10.72	27.67		84.9	27.6
4-4	10-13.5	7.71	2.00	536.7	469.8	52.84	9.77	10.85	27.94		84.4	28.1
4-5	13.5-16			537.7	465.6	52.36	9.43	10.84	27.57		82.2	28.0
4-6	16-19.5	7.75	1.92	536.7	478.5	52.94	9.64	10.80	28.16		81.9	28.7
5-1	0-3	7.65	2.48	540.9	475.6	53.08	10.48	10.58	27.84		89.8	27.1
5-2	3-5.5	7.70	2.43	541.8	469.6	52.93	10.24	10.65	27.70		89.3	26.8
5-3	5.5-8	7.70	2.47	539.0	479.2	53.56	10.29	10.88	28.08		90.2	27.6
5-4	8-11	7.74	2.44	539.0	479.0	53.29	11.48	10.80	28.07		89.3	27.8
5-5	11-14	7.80	2.42	536.2	479.8	52.78	10.06	10.70	27.71		87.6	27.7
5-6	14-17	7.88	2.40	535.2	482.7	52.76	10.38	10.83	27.71		87.5	28.2
5-7	17-20	7.90	2.29	536.2	477.1	52.00	9.70	10.73	27.22		85.8	27.5
5-8	21-24	8.00	2.52	534.3	472.6	50.97	9.67	10.70	27.12		84.1	27.3

Quaker Seamount

Sample ID	depth (cm)	pH	Alk (meq/kg)	Cl (mmol/kg)	Na (mmol/kg)	Mg (mmol/kg)	Ca (mmol/kg)	K (mmol/kg)	S (mmol/kg)	HS- (umol/kg)	Sr (umol/kg)	Li (umol/kg)
Dive J37												
7-1	0-3.5	7.77	2.59	541.8	478.7	53.41	10.75	10.73	28.32		92.3	28.0
7-2	3.5-6.5	7.80	2.52	538.1	485.2	54.02	10.93	10.84	28.52		92.1	29.3
7-3	6.5-9.5	7.82	2.62	538.1	488.2	54.54	10.97	11.00	28.70		93.5	28.9
8-1	0-3.5	7.67	2.51	538.1	468.8	52.60	10.12	10.62	27.88		89.1	27.3
8-2	3.5-6	7.69	2.40	537.1	475.7	52.66	10.29	10.69	28.26		88.3	27.8
8-3	6-9.5	7.77	2.47	537.1	470.5	52.57	10.05	10.66	27.94		87.2	27.9
8-4	9.5-12	7.80	2.35	537.1	468.9	52.92	10.06	10.67	28.04		86.8	28.4
8-5	12-15	7.81	2.38	538.1	476.1	53.12	10.10	10.71	27.87		86.4	28.6
8-6	15-18	7.83	2.32	537.1	464.5	52.28	9.70	10.51	27.48		84.9	27.8
8-7	18-21	7.84	2.31	538.1	466.9	51.71	9.78	10.36	27.27		84.5	28.2
8-8	21-25	7.84	2.39	537.1	474.6	52.74	10.08	10.51	27.76		86.0	28.2
PC-6												
6-1	6-9	7.61	2.07	542.3	463.3	51.97	9.70	10.34	27.58		83.2	28.4
6-2	19-23	7.91	1.58	535.0	471.9	51.70	9.37	10.33	27.99		76.5	31.2
6-3	37-41	8.08	1.39	536.8	476.6	51.94	9.11	10.43	28.11		73.8	33.0
6-4	47-51	8.24	1.23	530.4	473.7	51.18	8.84	10.31	27.99		70.3	33.6
6-5	91-96	9.16	0.97	516.7	470.5	43.23	9.12	10.16	26.78		76.6	34.9
6-6	128-133	9.15	0.83	505.7	468.5	36.92	10.03	10.14	26.13		89.6	46.0
6-7	157-163	9.07	0.71	498.3	467.4	30.69	10.74	10.06	25.38		100.9	55.9
6-8	183-189	9.24	0.82	487.3	460.4	24.94	11.22	9.88	24.42		110.5	64.1
6-9	205-210	9.22	0.88	480.0	470.2	20.43	12.44	10.03	24.75		121.7	74.4
6-10	255-260			461.7	461.4	7.59	13.39	9.74	22.89		145.8	92.4
6-11	317-325			426.9	461.4	0.50	18.08	9.39	25.53		205.2	118.9
6-12	outside				472.3	38.79	10.02	10.23	26.26		87.5	43.3

Sample ID	depth (cm)	pH	Alk (meq/kg)	Cl (mmol/kg)	Na (mmol/kg)	Mg (mmol/kg)	Ca (mmol/kg)	K (mmol/kg)	S (mmol/kg)	HS- (umol/kg)	Sr (umol/kg)	Li (umol/kg)
GC-6												
6-1	10-14	7.64	2.19	541.4	480.4	53.23	10.16	10.44	28.24		85.3	28.7
6-2	22-26	7.61	2.16	535.9	477.2	53.20	10.28	10.45	28.24		85.9	28.4
6-3	38-41	8.49	1.02	529.5	478.0	50.49	8.78	10.42	27.51		68.2	35.6
6-3	57-60	9.27	1.15	516.7	477.5	42.14	9.53	10.34	25.99		80.3	47.6
PC-17												
17-1	~5	7.75	2.58	539.7	491.0	54.98	10.86	10.76	28.99		92.4	28.2
17-2	~10	7.79	2.09	540.7	476.4	53.46	10.53	10.42	28.01		89.5	29.0
PC-20												
20-1	15-19	7.71	2.31	537.7	468.7	52.71	10.23	10.74	28.58		88.1	27.8
20-2	34-38	7.72	2.21	535.8	468.3	52.35	9.94	10.50	28.17		85.8	28.7
20-3	62-67	7.87	1.94	533.0	467.9	51.63	9.48	10.22	27.88		81.5	30.9
20-4	92-96	8.08	1.75	531.1	481.2	52.56	9.49	10.53	28.98		79.3	34.0
20-5	104-108	8.27	1.51	527.4	471.5	50.47	8.99	10.23	28.43		73.4	35.5
20-6	125-128	8.94	1.08	523.6	470.7	46.90	8.77	10.25	27.11		70.8	38.5
20-7	157-161	8.99	1.06	516.1	472.4	42.73	9.41	10.19	26.87		80.0	45.6
20-8	181-187	8.96	0.92	510.5	469.7	38.51	9.84	10.23	26.00		88.8	51.8
20-9	251-257	8.99	0.91	489.0	461.8	24.96	11.30	9.93	24.97		115.6	72.3
20-10	274-278			480.5								
20-11	314-318	8.97	1.09	463.7	463.3	9.65	13.50	9.85	23.42		148.7	98.7
20-12	341-345			453.4	465.0	3.98	14.52	9.80	23.24		164.2	108.8
20-13	365-371	9.50	1.89	444.9	460.5	0.68	15.24	9.69	24.33		179.4	118.3

Quaker Seamount

Sample ID	B umol/ kg	Mn umol / kg	Fe umol /kg	Si umol/ kg	Rb umol/ kg	Cs nmol/ kg	Ba nmol/ kg	U nmol/ kg	Mo nmol/ kg
Dive J33									
3-1	539	21.7	37.6	6456	1.47	3.6	177	11.9	133
3-2	682	34.3	66.0	7047	1.50	4.3	191	11.2	121
3-3	577	16.3	27.3	1795	1.50	4.5		9.8	120
3-4	582	18.1	30.2	5844	1.45	4.5	187	9.5	123
3-5	639	21.0	34.4	1541	1.35	4.4	175	8.8	117
3-6	536	1.0	1.4	158	1.30	4.1	164	7.7	111
8-1	328	16.6	28.4	2306	1.36	2.9	143	1.5	156
8-2	315	6.4	8.4	280	1.34	2.9	165	4.0	133
8-3	451	11.1	15.8	1249	1.40	3.2	180	8.6	127
8-4	502	10.9	18.3	4393	1.45	3.4	192	7.8	130
8-5	612	10.7	18.2	5001	1.52	3.5	211	8.6	130
9-1	378	41.0	75.3	5216	1.46	3.2	158	2.3	158
9-2	351	11.3	15.6	5173	1.47	3.4	170	4.7	145
9-3	310	9.9	12.8	2553	1.40	3.2	155	1.7	140
9-4	565	53.2	105.2	5445	1.51	3.5	182	3.3	140
10-1	475	2.0	2.8	367	1.57	4.1	188	12.3	126
10-2	547	16.4	29.5	5800	1.50	3.6	199	13.0	134
10-3	447	0.5	0.7	254	1.46	3.4	183	12.5	121
10-4	698	38.6	66.7	3081	1.64	4.2	233	14.4	138
10-5	513	5.0	5.6	850	1.51	3.9	196	12.9	116
10-6	681	23.7	44.7	6209	1.49	3.7	215	13.8	135
Dive J37									
1-1	579	26.0	46.7	6167	1.50	3.3	229	12.2	134
1-2	597	28.9	55.1	6248	1.51	3.5	218	8.4	131
1-3	580	12.9	20.4	2302	1.49	3.5	197	7.2	114
1-4	665	17.2	30.6	2736	1.54	3.6	214	6.9	115
1-5	624	13.2	23.3	3467	1.51	3.4	191	6.2	107
2-1	705	45.3	91.6	6676	1.63	3.8	217	14.1	149
2-2	491	1.7	4.7	428	1.50	3.2	185	11.8	115
2-3	604	7.4	12.0	1718	1.59	3.5	193	9.0	109
2-4	763	42.1	70.1	3522	1.71	4.1	256	7.5	119

Quaker Seamount

Sample ID	B umol/ kg	Mn umol / kg	Fe umol /kg	Si umol/ kg	Rb umol/ kg	Cs nmol/ kg	Ba nmol/ kg	U nmol/ kg	Mo nmol/ kg
Dive J37									
5-1	561	16.8	28.5	5006	1.43	3.5	269	12.53	120
5-2	569	29.7	58.2	6738	1.52	3.8	228	12.81	128
5-3	686	39.0	72.0	6387	1.59	4.0	216	13.35	129
5-4	664	39.5	87.0	5006	1.64	4.1	252	14.38	132
5-5	595	18.5	29.3	3895	1.46	3.5	195	12.21	113
5-6	526	3.9	7.9	1288	1.60	4.1	222	15.20	144
5-7	556	13.2	17.9	1307	1.53	3.7	186	13.86	130
5-8	554	15.5	20.6	2297	1.50	3.7	170	13.59	117
6-1	549	14.7	22.4	1749	1.51	3.3	208	14.53	132
6-2	561	28.9	48.6	7234	1.41	3.0	198	15.06	133
6-3	464	2.2	2.9	243	1.26	2.2	164	13.84	105
6-4	711	37.2	70.2	5634	1.39	2.7	183	15.66	128
6-5	606	17.7	29.5	4192	1.47	2.7	188	16.37	143
6-6	661	39.0	76.7	5778	1.50	2.7	192	16.53	137
PC-6									
6-1	466	0.9	1.1	218	1.41	3.7	169	9.99	116
6-2	502	1.2	1.5	1497	1.30	4.5	154	8.06	112
6-3	498	1.5	1.9	1700	1.32	5.3	147	7.05	113
6-4	505	1.5	2.0	584	1.34	5.9	137	5.78	113
6-5	532	5.0	1.8	1465	1.31	12.6	131	0.06	86
6-6	545	4.5	1.4	1527	1.26	17.0	125	0.05	74
6-7	546	2.6	0.7	648	1.28	22.2	114	0.01	65
6-8	547	2.2	1.0	33	1.33	29.4	116	0.04	65
6-9	638	6.9	8.3	4493	1.37	38.1	129	0.16	56
6-10	612	0.4	1.7	113	1.31	50.8	125	0.01	36
6-11					1.57	96.0	218	2.24	200
6-12	556	7.0	8.2	3437	1.31	16.2	120	0.24	80
GC-6									
6-1	465	2.7	2.7	2011	1.35	3.1	171	10.18	118
6-2	491	5.3	8.1	4910	1.37	3.0	171	10.63	121
6-3	530	3.1	4.3	3539	1.28	6.8	133	3.56	105
6-3	553	5.2	3.0	1794	1.29	13.0	120	0.13	82

Quaker Seamount

Sample ID	B	Mn	Fe	Si	Rb	Cs	Ba	U	Mo	V	Cr	Co	Ni	Cu	Zn
	umol / kg	umol / kg	umol / kg	umol / kg	umol / kg	nmol / kg	nmol / kg	nmol / kg	nmol / kg	nmol / kg	nmol / kg	nmol / kg	nmol / kg	nmol / kg	nmol / kg
PC-20															
20-1	454	1.2	2.0	2627	1.49	4.0	192	11.78	115	59.7	33.2	0.95	123	13.8	127
20-2	474	0.7	1.1	1283	1.35	4.6	251	10.91	113						
20-3	479	0.5	3.6	155	1.28	4.6	175	10.65	113	8.0	63.7	0.36	153	1.5	16.9
20-4	755	37.8	72.6	4439	1.41	6.3	175	9.82	130						
20-5	511	1.5	1.7	222	1.35	7.3	146	5.86	106	0.8	35.9	0.69	53	1.8	1.4
20-6	525	3.5	1.9	888	1.33	11.1	121	0.15	91	2.6	2.0	5.54	612	1.0	8.5
20-7	543	5.3	2.2	1297	1.30	15.5	119	0.08	82	85	14.0	3.89	538	7.8	95
20-8	544	5.3	2.8	2200	1.39	20.4	123	0.11	76	104	18.9	3.86	599	7.7	142
20-9	558	1.3	0.4	355	1.35	33.1	113	0.00	56	16.0	14.3	1.37	454	6.4	30.2
20-10															
20-11	637	1.0	2.3	1176	1.45	62.2	123	0.06	45	70.7	11.0	1.21	168	3.0	61.7
20-12	719	2.2	3.8	3168	1.41	67.3	139	0.08	40	150	32.9	3.37	210	21.7	377
20-13	833	1.6	2.5	1060	1.37	69.4		0.09	57	80.3	13.7	1.72	69	13.7	169

Big Blue Seamount

Sample ID	depth (cm)	pH	Alk (meq/kg)	Cl (mmol/kg)	Na (mmol/kg)	Mg (mmol/kg)	Ca (mmol/kg)	K (mmol/kg)	S (mmol/kg)	HS- (umol/kg)	Sr (umol/kg)	Li (umol/kg)
Dive J34												
1-1	0-3	7.64	2.57	537.8	490.1	55.32	11.45	10.88	29.09		95.1	28.7
1-2	6-9	7.68	2.52	536.9	488.7	54.39	11.02	10.65	28.68		93.1	28.7
1-3	9-12	7.75	2.54	536.9	472.3	53.64	10.82	10.51	28.16		92.3	27.9
1-4	12-15	7.75	2.53	538.7	463.1	52.16	10.22	10.18	27.61		89.2	27.3
2-1	2-5	7.58	2.51	538.7	486.1	54.51	10.89	10.75	28.84		91.8	28.0
2-2	9-12	7.63	2.41	538.7	476.2	52.47	10.05	10.44	27.96		87.1	27.7
2-3	12-15	7.63	2.38	536.9	469.1	52.01	10.08	10.32	27.74		86.0	26.9
2-4	21-24	7.68	2.32	542.9	480.9	52.42	10.08	10.40	27.86		83.5	27.5
Dive J36												
1-1	0-3	7.68	2.49	536.6	485.6	53.71	10.88	10.57	28.57		92.7	29.5
1-2	6-9	7.72	2.59	537.5	477.1	53.42	10.63	10.47	28.65		91.5	28.5
1-3	9-12	7.73	2.48	536.6	485.7	54.12	10.85	10.73	27.97		91.3	28.9
1-4	12-15	7.78	2.52	532.9	477.5	52.49	10.31	10.44	27.78		85.6	28.1
1-5	15-18	8.02	2.39	534.7	471.0	50.87	9.31	10.42	27.15		80.4	27.1
1-6	18-21	8.23	2.28	533.8	474.5	48.96	8.51	10.38	26.26		71.8	26.3
1-7	21-23	8.52	2.14	531.9	499.3	47.82	8.06	10.87	26.35		63.3	26.1
2-1	0-3	7.68	2.58	538.5	470.8	53.55	10.93	10.54	27.94		91.9	27.7
2-2	3-6	7.72	2.72	538.5	470.7	52.42	10.67	10.34	27.81		90.2	27.9
2-3	6-9	7.78	2.68	535.7	490.5	53.79	11.02	10.73	28.64		90.9	29.2
2-4	9-12	8.04	2.64	532.9	479.7	51.66	10.21	10.38	27.47		84.8	27.9
2-5	12-14.5	8.22	2.64	536.6	483.6	52.06	9.97	10.54	28.18		81.5	27.2
2-6	14.5-17	8.36	2.52	534.7	484.3	51.76	9.62	10.69	27.32		76.5	26.6
2-7	17-19.5	8.55	2.09	534.7	477.3	48.73	7.74	10.44	26.50		59.0	25.6
2-8	19.5-22	8.72	1.42	532.9	495.0	46.37	6.45	10.75	25.96		39.7	25.5
2-9	22.5-26	8.78	1.34	534.7	505.3	40.06	5.20	10.73	25.13		33.5	24.8

Big Blue Seamount

Sample ID	depth (cm)	pH	Alk (meq/kg)	Cl (mmol/kg)	Na (mmol/kg)	Mg (mmol/kg)	Ca (mmol/kg)	K (mmol/kg)	S (mmol/kg)	HS- (umol/kg)	Sr (umol/kg)	Li (umol/kg)
Dive J36												
3-1	0-4	7.69	2.60	540.3	494.4	55.04	11.21	10.78	29.07		94.6	28.7
3-2	4-7	7.68	2.68	540.3	475.4	53.43	10.77	10.45	28.26		92.5	27.9
3-3	7-10	7.69	2.71	537.5	464.8	52.25	10.30	10.24	27.86		90.9	26.9
3-4	10-12.5	7.68	2.53	537.5	475.1	53.36	11.17	10.51	27.98		92.1	27.3
3-5	12.5-15	7.78	2.44	536.6	475.5	52.51	10.04	10.41	28.01		86.9	27.0
3-6	15-18.5	8.90	1.57	538.5	494.5	49.71	6.95	10.77	27.28		49.3	25.8
3-7	18.5-20	8.91	1.49	534.7	522.9	32.70	5.31	11.09	26.22		36.9	22.7
4-1	0-3.5	10.55	5.87	540.5	614.1	1.00	4.04	12.43	27.07	3700	51.2	8.8
4-2	3.5-7	11.82	28.18	556.4	640.5	0.28	0.78	12.60	25.26	5440	20.7	5.2
4-3	7-10	11.85	34.19	558.3	658.8	0.29	1.01	12.90	26.39	5540	17.9	5.0
4-4	10-14	11.86	37.61	557.4	687.8	0.30	0.93	13.39	29.96	5590	18.4	5.9
4-5	14-17	11.89	41.51	563.0	660.7	0.31	0.84	13.10	30.90	5430	17.3	6.1
4-6	17-20.5	11.92	43.72	557.4	695.4	0.34	0.71	13.61	30.00	4770	16.1	5.6
4-7	20.5-24	11.94	45.29	557.4	691.3	0.35	0.61	13.66	30.66	3940	14.4	5.2
4-8	24-26	12.04	45.78	552.7	678.5	0.34	0.49	13.57	30.80	1960	13.8	2.7
5-1	0-3	7.81	2.54	536.6	470.9	52.96	10.89	10.31	28.24		90.8	27.7
5-2	6-9	7.79	2.54	535.7	466.2	52.54	10.48	10.30	27.84		90.4	27.7
5-3	9-12	7.82	2.54	538.5	469.7	52.45	10.26	10.18	27.66		89.2	27.5
5-4	12-15	7.88	2.61	535.7	471.2	53.12	10.66	10.33	28.13		91.2	27.1
5-5	15-19	8.42	2.04	539.4	466.6	53.08	9.04	10.25	26.72		69.7	25.7
5-6	22-25	8.64	1.22	538.5	477.9	51.82	8.03	10.50	27.09		53.3	25.9
5-7	25-28	8.68	1.10	537.5	500.1	35.88	7.05	11	24.17		51.5	21.1

Big Blue Seamount

Sample ID	depth (cm)	pH	Alk (meq/kg)	Cl (mmol/kg)	Na (mmol/kg)	Mg (mmol/kg)	Ca (mmol/kg)	K (mmol/kg)	S (mmol/kg)	HS- (umol/kg)	Sr (umol/kg)	Li (umol/kg)
Dive J36												
6-1	0-3	7.78	2.49	537.5	473.7	53.55	10.64	10.44	28.00	0	90.7	27.6
6-2	3-6	7.90	2.53	537.5	473.1	53.33	10.67	10.52	27.76	0	88.9	27.8
6-3	9-12	8.21	2.18	534.7	479.8	52.39	9.49	10.50	27.68	1	80.5	29.3
6-4	15-18.5	8.80	1.29	534.7	482.4	52.68	7.89	10.57	27.02	69	55.9	27.4
6-5	21-24	8.74	0.97	536.6	487.1	50.85	7.23	10.71	26.48	186	51.7	27.0
6-6	24-27	8.78	1.19	535.7	493.8	48.30	6.29	10.84	26.21	560	48.0	27.1
6-7	30-33	9.08	1.70	534.7	510.7	35.07	3.94	11.18	23.73	1140	34.9	24.7
7-1	0-3	7.69	2.60	538.5	480.9	53.19	10.81	10.38	28.56		92.3	28.4
7-2	3-6	7.70	2.64	536.6	470.4	52.69	10.40	10.34	28.00		91.5	28.0
7-3	9-12	7.73	2.54	538.5	467.3	52.16	10.13	10.24	27.71		90.0	28.0
7-4	12-15	7.76	2.53	537.5	481.4	53.35	10.68	10.48	28.54		90.4	28.7
7-5	15-18	7.95	2.33	538.5	477.9	52.46	9.74	10.38	27.91		84.0	27.6
8-1	0-3	7.77	2.51	538.5	481.9	53.81	10.48	10.41	28.53		91.1	28.3
8-2	3-5	7.77	2.56	536.6	471.6	53.41	10.85	10.39	28.19		90.6	28.0
8-3	5-8	7.77	2.51	536.6	467.8	53.30	10.35	10.39	28.02		89.3	27.7
8-4	8-10	7.81	2.49	536.6	492.5	55.34	10.89	10.88	28.89		91.0	29.1
8-5	10-12	7.82	2.40	535.7	475.4	53.24	10.47	10.34	28.31		87.6	28.2
MAJOR												
GC-4		7.87	2.57	538.5							87.6	24.5
4-1	2-6	7.85	2.41	543.3	474.8	52.87	10.29	9.42	27.65	0	86.8	26.4
4-2	13-16	9.03	1.85	536.5	490.5	38.74	6.75	9.84	25.01	105	58.0	23.2
4-3	19-22	9.89	1.99	530.4	566.2	4.64	4.81	11.03	24.35	403	47.2	14.3
4-4	32-35	11.54	12.37	542.3	615.0	0.19	1.74	11.59	28.36	145	41.5	5.4
4-5	44-47	11.92	30.69	556.3	667.0	0.21	1.04	12.56	32.20	1	25.7	1.5
4-6	54-57	12.12	46.00	557.7	674.7	0.21	0.75	12.92	32.27	0	24.8	2.2

Big Blue Seamount

Sample ID	depth (cm)	pH	Alk (meq/kg)	Cl (mmol/kg)	Na (mmol/kg)	Mg (mmol/kg)	Ca (mmol/kg)	K (mmol/kg)	S (mmol/kg)	HS- (umol/kg)	Sr (umol/kg)	Li (umol/kg)
PC-5												
5-1	1-4	7.71	2.50	536.8	466.2	51.73	10.01	9.48	27.20	0	87.8	26.6
5-2	10-14	8.38	2.19	536.8	470.0	51.18	8.93	9.78	26.66	0	75.3	25.8
5-3	36-40	9.37	2.02	521.0	552.0	4.15	2.74	11.00	23.12	1320	33.6	17.5
5-4	98-102	11.88	27.16	549.2	643.4	0.19	0.79	12.42	30.76	4	27.0	1.3
5-5	164-166	12.05	43.52	549.6	670.0	0.18	0.57	13.05	32.06	0	28.2	2.9
5-6	202-206	12.09	51.13	549.6	666.8	0.19	0.42	13.02	30.98	0	22.2	0.9
5-7	243-248	12.10	57.60	549.6	666.3	0.17	0.35	13.07	30.05	0	22.2	0.9
5-8	294-300	12.19	62.71	546.0	676.5	0.17	0.14	13.34	30.03	0	17.8	0.7
5-9	337-344	12.19	65.67	543.2	681.1	0.18	0.32	13.53	30.17	0	14.8	0.8
5-10	394-398	12.34	68.20	545.1	699.9	0.18	0.40	13.94	30.52	0	11.8	0.8
5-11	466-472	12.33	68.73	546.0	688.3	0.18	0.30	13.75	30.09	0	10.0	0.9
GC-5												
5-1	6-8	7.70	2.50	540.9	482.0	53.63	10.57	10.41	27.90	0	88.7	26.3
5-2	18-20	7.82	2.36	537.7	472.6	52.20	9.91	10.24	27.43	0	83.5	25.7
5-3	26-28	8.54	2.20	535.9	484.1	50.52	8.78	10.40	26.77	16	69.0	25.8
5-4	32-34	8.97	1.73	533.1	489.7	42.90	6.17	10.67	25.42	145	46.5	22.3
BAC-19												
19-1	16-20	7.74	2.31	538.3	473.0	52.97	9.92	10.33	28.12	0	85.4	27.1
19-2	26-30	8.56	1.62	536.5	491.3	52.14	8.06	10.81	27.53	48	61.1	26.4
19-3	41-46	8.91	1.32	529.9	513.6	36.49	4.83	11.01	24.66	627	32.7	23.5
19-4	67-72	10.49	4.61	520.5	578.0	0.19	1.51	12.05	22.31	1090	23.5	13.0
19-5	110-116	11.71	22.30	536.5	621.1	0.10	0.90	12.66	27.37	77	24.1	2.8
19-6	151-157	11.92	34.03	543.0	659.3	0.09	0.78	13.16	31.00	1	22.9	2.4
19-7	180-185	11.95	39.69	545.8	656.5	0.08	0.53	13.09	30.21	0	20.2	1.9

Big Blue Seamount

Sample ID	B umol/ kg	Mn umol/ kg	Fe umol/ kg	Si umol/ kg	Rb umol/ kg	Cs nmol/ kg	Ba nmol/ kg	U nmol/ kg	Mo nmol/ kg
Dive J34									
2-1	796	27.1	50.4	5520	1.50	3.5	194	15.51	176
2-2	485	0.4	1.8	200	1.35	3.5	163	12.59	123
2-3	529	1.8	3.1	1618	1.34	3.9	177	13.73	123
2-4	605	29.3	52.6	6163	1.44	4.2	163	12.56	121
Dive J36									
1-1	903	34.1	57.0	6070	1.39	3.1	185	16.71	171
1-2	730	45.9	88.2	5776	1.39	2.7	131	14.09	137
1-3	738	22.1	39.8	4364	1.46	3.0	151	14.52	134
1-4	609	22.4	35.4	1866	1.36	3.1	128	11.69	127
1-5	645	39.7	65.8	5026	1.45	3.7	130	12.43	376
1-6	466	10.0	14.6	281	1.51	3.9	124	12.72	538
1-7	700	25.8	46.1	5152	1.57	4.6	143	14.07	2311
2-1	659	34.0	57.4	4494	1.41	2.8	200	15.79	156
2-2	491	3.8	5.4	433	1.36	2.8	130	13.70	129
2-3	694	44.1	74.1	3495	1.41	3.3	151	13.57	126
2-4	594	17.1	22.3	2153	1.46	3.6	140	12.59	107
2-5	610	18.8	26.2	2182	1.47	4.3	140	10.60	168
2-6	818	38.7	63.2	3434	1.56	4.6	134	10.29	292
2-7	561	4.6	3.4	29	1.48	6.7	88	2.88	61
2-8	684	37.9	66.7	6657	1.68	9.4	115	2.85	57
2-9	618	18.2	30.3	3914	1.80	12.9	89	1.95	49
3-1	840	49.9	105	5004	1.46	2.8	161	17.66	161
3-2	559	5.0	7.7	690	1.30	2.6	161	16.93	149
3-3	485	2.6	4.2	140	1.32	2.7	134	19.22	289
3-4	785	55.5	167	6949	1.46	3.5	187	21.13	426
3-5	591	11.4	39.4	2111	1.46	3.6	218	18.31	894
3-6	628	16.2	26.6	3721	1.75	10.1	84	2.51	187
3-7	703	38.4	72.6	7176	2.10	20.4	99	2.63	74
4-1	717	9.9	18.8	1734	4.40	120	259	0.60	212
4-2	1192	6.5	10.6	812	5.17	103	124	0.84	83
4-3	410	0.0	0.2	174	5.39	96.2	125	0.98	128
4-4	1629	19.7	37.2	3518	5.84	97.7	131	0.50	212
4-5	1336	5.6	9.8	2308	5.64	98.4	131	0.31	200
4-6	1852	8.2	19.1	8466	6.18	109	133	0.55	158
4-7	1436	4.5	11.1	929	6.10	110	104	0.10	59
4-8	1565	10.3	21.1	990	6.43	110	92	0.38	186

Big Blue Seamount

Sample ID	B umol/ kg	Mn umol/ kg	Fe umol/ kg	Si umol/ kg	Rb umol/ kg	Cs nmol/ kg	Ba nmol/ kg	U nmol/ kg	Mo nmol/ kg
Dive J34									
5-1	445	0.7	0.5	215					
5-2	546	1.3	2.1	1949					
5-3	467	0.5	0.7	175					
5-4	636	7.6	5.6	2878					
5-5	411	3.0	0.7	42					
5-6	416	2.1	0.3	0					
5-7	457	1.0	1.1	101					
6-1	894	64.1	122	5899	1.46	3.2	214	18.04	536
6-2	659	49.2	86.6	4609	1.45	3.6	195	28.20	2522
6-3	607	40.4	75.9	5948	1.44	5.3	141	46.5	6420
6-4	552	26.2	41.6	2163	1.55	10.3	97	1.17	1027
6-5	572	29.6	50.0	4351	1.73	17.2	130	1.13	623
6-6	584	32.8	68.8	5899	1.81	24.2	133	0.58	388
6-7	649	11.3	20.3	2591	2.41	41.8	171	0.51	844
7-1	558	22.1	37.5	3090					
7-2	622	19.2	34.7	4886					
7-3	570	9.0	12.0	1214					
7-4	799	47.8	83.2	5816					
7-5	623	24.5	44.4	5416					
8-1					1.37	2.6	160	14.76	145
8-2					1.46	2.7	187	15.49	165
8-3					1.41	2.7	136	15.00	161
8-4					1.60	2.9	163	17.36	218
8-5					1.41	2.7	164	16.87	218
MAJOR	415	0.1	0.2	157	1.28	2.2	258	14.62	163
GC-4									
4-1	430	1.5	1.1	1011	1.29	2.3	89	11.60	112
4-2	394	0.9	0.9	64	1.62	7.5	70	4.24	914
4-3	611	4.6	6.3	2349	2.81	28.0	95	0.21	186
4-4	985	1.6	3.1	2309	3.91	64.0	98	0.15	127
4-5	1330	4.4	12.9	6558	5.47	102	99	0.94	237
4-6	418	0.1	0.3	217	6.09	116	90	0.87	219

Big Blue Seamount

Sample ID	B umol/ kg	Mn umol/ kg	Fe umol/ kg	Si umol/ kg	Rb umol/ kg	Cs nmol/ kg	Ba nmol/ kg	U nmol/ kg	Mo nmol/ kg
PC-5									
5-1	443	0.3	0.5	265	1.27	2.5	87	11.01	117
5-2	452	2.4	2.3	654	1.29	1.8	86	4.66	1268
5-3	764	0.4	1.4	408	2.57	27.7	83	0.03	87
5-4	1276	3.3	6.8	4670	5.09	99.3	79	0.56	192
5-5	1278	1.6	5.6	3334	5.86	120	78	0.63	201
5-6	1213	0.4	2.5	1701	6.19	123	46	0.22	184
5-7	1124	0.2	0.3	33	6.10	123	36	0.00	176
5-8	1207	0.2	2.1	343	6.31	123	27	0.01	173
5-9	1214	0.2	1.6	2642	6.23	125	35	0.16	208
5-10	1345	0.2	0.7	3518	6.84	127	38	0.11	234
5-11	1237	1.1	5.0	3305	6.65	123	47	0.08	220
GC-5									
5-1	455	1.5	2.0	1014					
5-2	439	4.6	2.2	1201					
5-3	438	4.1	2.0	1102					
5-4	559	3.9	2.7	1593					
BAC-19									
19-1	1270	2.2	9.4	6501	1.34	2.4	101	11.82	118
19-2	664	35.6	56.9	3369	1.58	3.8	102	8.63	2104
19-3	939	52.9	107	5315	1.93	11.0	108	0.68	52
19-4	1015	21.5	39.3	4066	3.12	31.1	92	0.24	97
19-5	1427	18.6	33.4	5282	4.59	70.9	58	0.21	109
19-6	1320	5.2	9.4	1810	5.32	100	56	0.15	150
19-7	1265	2.5	4.7	196	5.67	109	41	0.06	149

Big Blue Seamount

Sample ID	V nmol/ kg	Cr nmol/ kg	Co nmol/ kg	Ni nmol/ kg	Cu nmol/ kg	Zn nmol/ kg
Dive J36						
2-1	53.6	13.0	1.03	397	9.7	4.2
2-2	18.8	10.9	0.77	407	3.3	34
2-3	19.0	1.9	22.6	402	6.9	40
2-4	12.6	1.5	19.4	639	2.4	39
2-5	3.9	1.7	2.42	474	1.6	20
2-6	3.2	1.1	0.72	160	0.2	7.9
2-8	1.4	0.3	0.45	48	0.8	2.4
2-9	1.5	0.9	0.38	50	2.4	4.7
4-1	44.3	0.5	0.48	47	2.2	5.7
4-2	92.2	12.8	0.55	46	1.0	9.2
4-3	187	1.1	0.74	92	4.7	16
4-4	60.1	0.5	0.29	41	3.1	8.2
4-5	3.6	0.5	1.13	55	4.0	7.0
4-6	5.9	0.4	0.09	23	3.3	3.8
4-7	11.4	1.4	0.32	32	3.6	9.6
4-8	37.4	1.1	0.23	35	5.0	5.1
MAJOR	35.2	5.1	3.56	71	62.0	421
GC-4						
4-1	14.3	7.2	6.81	555	6.2	20
4-2	6.8	0.5	0.11	68	1.8	7.3
4-3	14.5	0.3	0.14	8	4.8	13
4-4	23.4	0.2	0.01	10	1.9	15
4-6	27.5	0.6	0.08	9	1.7	12
PC-5						
5-1	9.9	9.1	2.60	741	6.6	18
5-2	1.7	0.3	0.53	360	0.3	3.2
5-3	9.8	0.3	0.11	10	5.1	7.2
5-4	32.6	0.7	0.11	19	2.1	7.3
5-6	30.2	0.3	0.15	23	4.7	31
5-7	35.6	1.1	0.83	91	2.9	13
5-8	55.6	0.7	0.19	28	2.4	48

Big Blue Seamount

	Dive J36			BAC-19	
	2-1	2-9	4-1	4-6	19-7
nmol/kg					
Y	0.122	0.007	0.004	0.001	0.002
Cd	1.617	0.003	0.008	0.005	0.002
pmol/kg					
La	9.7	3.5	0.3	1.8	1.3
Ce	5.5	3.0	0.1	3.7	2.5
Pr	1.18	0.62	0.02	0.40	0.24
Nd	5.72	2.38	0.24	1.24	0.39
Sm	1.38	0.55	0.16	0.08	0.19
Eu	0.385	0.143	0.016	0.015	0.037
Gd	2.45	0.58	0.08	0.19	0.23
Tb	0.389	0.098	0.041	0.017	0.011
Dy	3.27	0.50	0.18	0.08	0.16
Ho	0.806	0.127	0.743	0.022	0.031
Er	3.15	0.29	0.16	0.05	0.09
Tm	0.522	0.047	0.025	0.006	0.017
Yb	4.18	0.34	0.13	0.13	0.18
Lu	0.848	0.057	0.092	0.010	0.039

Celestial Seamount

Sample ID	depth (cm)	pH	Alk (meq/kg)	Cl (mmol/kg)	Na (mmol/kg)	Mg (mmol/kg)	Ca (mmol/kg)	K (mmol/kg)	S (mmol/kg)	HS- (umol/kg)	Sr (umol/kg)	Li (umol/kg)
Dive J38												
4-1	0-3.5	7.70	2.42	541.9	477.6	53.29	10.24	10.27	28.36	0	88.1	27.0
4-2	3.5-6				479.6	54.41	11.48	10.48	28.72	0	90.0	26.9
4-3	6-8.5	7.75	2.36	549.5	484.9	54.47	10.60	10.48	28.52	0	89.3	27.1
4-4	8.5-11	7.76	2.49	545.8	475.6	53.41	10.34	10.29	28.18	0	87.5	27.5
4-5	11-14	7.75	2.46	544.9	468.5	53.33	10.29	10.27	27.81	0	87.6	27.4
4-6	14-16	7.79	2.65	556.2	476.0	54.03	10.41	10.26	28.08	0	88.0	27.8
GC-2												
2-1	8-10	7.76	2.39	545.8	474.1	53.99	10.51	9.21	28.03		87.8	27.0
2-2	18-20	7.80	2.31	540.6	466.0	53.11	10.15	9.10	27.13		85.1	26.4
2-3	60-62	7.95	1.91	547.6	468.7	52.63	9.23	9.35	26.00		76.2	24.5
2-4	75-77	8.16	1.61	542.8	466.4	51.55	8.31	9.33	25.25		67.2	25.6
GC-3												
3-1	3-5	7.63	2.37	543.3	473.6	53.85	10.48	10.29	28.35		88.3	26.9
3-2	28-31	7.90	1.67	540.1	471.0	53.30	9.19	10.16	27.20		75.8	25.8
3-3	39-42	8.22	1.17	540.6	469.6	53.79	8.34	10.27	26.80		65.3	25.6
3-4	46-49	8.45	0.99	539.2	471.1	54.30	8.00	10.39	26.74		60.1	25.4
3-5	54-57	8.84	1.52	539.2	478.8	54.29	8.39	10.51	26.84		62.8	26.3
3-6	60-64	8.93	0.96	546.4	473.0	53.56	7.90	10.38	26.42		61.5	26.1
3-7	outside	8.80	0.67	557.7	487.9	52.69	8.60	10.89	25.18		63.9	23.1
PC-22												
22-1	17-23	8.00	1.70	536.0	469.8	52.41	9.40	10.10	27.15		74.5	26.1
22-2	26-29	8.32	1.16	535.0	475.6	52.41	8.98	10.17	26.75		69.2	25.8
22-3	34-37	8.11	1.18	535.0	465.7	52.19	9.28	10.12	26.36		73.4	25.8
22-4	outside	8.67	0.89	541.6	480.6	49.57	9.41	10.20	24.04		71.0	24.3

Celestial Seamount

Sample ID	B umol/ kg	Mn umol/ kg	Fe umol/ kg	Si umol/ kg	Rb umol/ kg	Cs nmol/ kg	Ba nmol/ kg	U nmol/ kg	Mo nmol/ kg
Dive J38									
4-1					1.33	3.3	174	11.45	119
4-2					1.38	3.3	240	11.18	137
4-3					1.34	3.1	159	11.54	119
4-4					1.33	3.2	175	11.36	112
4-5					1.31	3.3	155	11.79	109
4-6					1.33	3.1	160	13.80	119
GC-2									
2-1	432	1.7	2.7	1641	1.20	2.1	169	10.35	111
2-2	419	1.0	2.1	1073	1.25	2.2	165	11.48	111
2-3	404	1.5	2.4	959	1.25	2.6	150	7.40	107
2-4	389	1.3	2.9	1234	1.19	3.0	131	3.46	94
GC-3									
3-1	456	2.8	4.7	2120	1.30	2.2	169	11.01	125
3-2	412	1.1	2.2	184	1.20	2.5	130	7.55	109
3-3	420	1.7	2.9	752	1.29	3.0	117	4.50	109
3-4	423	4.0	7.8	826	1.27	3.2	261	3.16	110
3-5	431	4.4	6.4	3419	1.30	3.6	130	1.46	115
3-6	399	2.6	1.7	78	1.26	3.6	122	0.05	98
3-7	333	4.5	2.3	1099	1.33	7.5	113	0.12	84
PC-22									
22-1	406	1.4	3.1	2322	1.28	2.6	212	7.04	120
22-2	396	2.3	4.1	1709	1.32	2.9	144	3.04	124
22-3	388	3.1	5.4	3958	1.24	2.7		4.09	144
22-4	328	3.2	1.9	369	1.24	4.4	168	0.11	92

Blue Moon Seamount

Sample ID	depth (cm)	pH	Alk (meq/kg)	Cl (mmol/kg)	Na (mmol/kg)	Mg (mmol/kg)	Ca (mmol/kg)	K (mmol/kg)	S (mmol/kg)	HS- (umol/kg)	Sr (umol/kg)	Li (umol/kg)
Dive J40												
1-1	0-2.5	7.65	2.46	544.7	463.2	51.42	11.37	10.32	27.33		102.1	27.2
1-2	2.5-5	7.65	2.31	538.2	462.9	49.73	12.71	10.29	27.26		119.1	27.4
1-3	5-7.5	7.65	2.26	534.4	464.6	47.47	14.70	10.16	27.44		148.3	27.0
1-4	7.5-10	7.70	2.07	530.7	468.2	45.02	17.54	10.03	27.78		183.9	25.9
1-5	10-12.5	7.76	1.91	525.1	462.0	42.43	20.11	9.93	27.68		217.3	24.9
1-6	12.5-16	7.73	1.86	528.3	459.7	40.84	21.20	9.84	27.57		233.2	24.3
2-1	0-2.5	7.64	2.28	534.4	463.0	46.87	15.96	10.05	28.03	0	160.2	25.1
2-2	2.5-5.5	7.65	2.08	526.0	451.5	43.63	18.14	9.44	27.51	0	189.5	24.0
2-3	5.5-9	7.64	1.52	511.0	435.1	34.62	27.23	8.19	27.22	0	300.1	18.8
2-4	9-11.5	7.71	1.15	493.2	425.6	23.02	38.61	7.10	27.73	14	445.7	14.5
2-5	11.5-13	7.74	0.74	482.4	409.8	15.20	45.00	6.20	27.49	92	528.9	11.4
2-6	13-15	6.43	0.45	473.5	405.7	9.23	51.88	5.44	27.96	163	620.1	9.0
2-7	15-19	7.40	0.26	469.7	398.6	6.49	54.61	5.19	27.33	275	645.4	7.8
3-1	0-4	7.73	2.28	538.2	467.9	50.91	12.05	10.23	27.58		110.1	26.7
3-2	4-8	7.71	2.31	535.4	481.9	51.30	13.60	10.48	28.29		123.7	27.3
3-3	8-10	7.73	2.20	531.6	467.6	48.59	14.84	9.97	28.18		143.7	26.0
3-4	10-13	7.80	2.12	526.0	460.6	43.70	19.24	9.44	28.00		198.8	24.2
3-5	13-17	7.79	1.76	514.7	447.7	37.79	24.84	8.58	27.55		274.3	20.5
3-6	17-20	7.88	1.60	513.3	440.9	36.54	25.30	8.56	26.91		279.0	19.6

Blue Moon Seamount

Sample ID	depth (cm)	pH	Alk (meq/kg)	Cl (mmol/kg)	Na (mmol/kg)	Mg (mmol/kg)	Ca (mmol/kg)	K (mmol/kg)	S (mmol/kg)	HS- (umol/kg)	Sr (umol/kg)	Li (umol/kg)
Dive J40												
4-1	0-3	7.66	2.41	543.8	471.0	52.35	10.22	10.93	28.06		88.2	27.8
4-2	3-6	7.69	2.24	542.9	468.4	52.17	10.33	11.10	27.95		89.0	27.9
4-3	6-9	7.74	2.34	540.1	475.9	52.52	10.62	10.72	28.16		90.7	27.7
4-4	9-13	7.73	2.46	539.1	466.1	52.42	10.66	10.55	27.77		91.9	27.2
4-5	13-16	7.74	2.48	541.0	472.5	52.22	10.85	10.47	27.75		93.9	27.5
4-6	20-23	7.77	2.48	540.1	467.7	51.75	10.98	10.35	27.47		96.6	27.2
4-7	23-26	7.80	2.43	539.1	473.0	52.07	11.16	10.43	27.73		97.9	27.3
4-8	26-29	7.79	2.35	539.1	466.6	51.57	10.96	10.36	27.50		96.9	27.0
5-1	0-3	7.61	2.23	539.3	469.6	53.04	10.18	10.62	27.70		87.0	27.6
5-2	3-6	7.70	2.26	539.3	469.3	52.65	10.05	10.76	27.62		86.9	27.7
5-3	9-12	7.65	2.23	540.2	468.5	52.96	10.16	10.77	27.71		88.3	27.3
5-4	15-18	7.67	2.26	540.2	472.1	52.87	10.28	10.84	27.95		90.2	27.8
5-5	22-25	7.70	2.33	539.3	473.2	51.93	10.33	11.43	27.82		91.8	28.6
5-6	29-32	7.73	2.38	539.3	479.2	52.67	10.61	11.36	28.26		93.8	28.7
5-7	35-39	7.77	2.32	538.4	471.4	52.00	10.47	11.49	27.95		94.1	28.6
6-1	3-6	7.68	2.33	538.4	467.3	52.74	10.40	11.12	27.80		87.0	27.3
6-2	6-9	7.71	2.29	539.3	467.6	52.69	10.20	11.01	27.64		86.6	27.3
6-3	12-15	7.74	2.40	539.3	467.8	52.71	10.22	11.14	27.68		86.9	27.2
6-4	18-21	7.71	2.23	539.3	470.2	52.44	10.17	11.10	27.79		86.2	27.5
6-5	24-27	7.74	2.29	539.3	474.1	52.81	10.29	11.26	28.19		87.8	27.9
6-6	30-33	7.74	2.22	539.3	470.9	52.72	10.20	11.10	27.89		86.8	27.4
6-7	36-39	7.76	2.17	538.4	474.4	52.43	10.16	11.17	27.99		86.7	27.5

Blue Moon Seamount

Sample ID	depth (cm)	pH	Alk (meq/kg)	Cl (mmol/kg)	Na (mmol/kg)	Mg (mmol/kg)	Ca (mmol/kg)	K (mmol/kg)	S (mmol/kg)	HS- (umol/kg)	Sr (umol/kg)	Li (umol/kg)
Dive J40												
7-1	2-5	7.69	2.36	538.4	470.5	51.93	10.26	11.09	27.95		87.0	29.2
7-2	5-8	7.71	2.41	539.3	476.1	52.01	10.25	11.36	27.99		86.9	29.4
7-3	11-14	7.81	2.36	539.3	468.0	51.56	9.92	11.35	27.63		85.9	28.8
7-4	17-20	7.77	2.36	538.4	476.8	52.59	10.42	11.00	28.24		86.7	28.6
7-5	23-26	7.77	2.52	538.4	474.5	52.38	10.42	11.05	28.11		87.3	28.3
7-6	29-32	7.82	2.54	538.4	475.0	52.58	10.47	10.93	28.11		87.4	28.1
7-7	35-38	7.81	2.54	537.4	469.5	51.92	10.21	11.18	28.06		86.6	28.1
8-1	2-5	7.65	2.30	541.2	471.0	53.13	10.36	10.86	27.92		87.4	27.2
8-2	5-8	7.72	2.31	539.3	474.5	52.71	10.09	10.81	27.93		86.4	27.4
8-3	8-11	7.71	2.33	539.3	478.1	53.12	10.42	10.96	28.17		86.9	27.7
8-4	11-14	7.74	2.32	539.3	475.4	53.54	10.31	11.36	28.32		87.9	30.0
8-5	14-17	7.74	2.36	538.4	472.2	52.91	10.20	10.86	28.13		86.7	27.6
8-6	17-20	7.76	2.34	539.3	471.5	52.99	10.33	10.84	27.97		87.1	27.4
BAC-24												
24-1	11-16	7.83	2.36	540.9	470.9	52.67	10.53	9.86	27.69		88.6	26.7
24-2	21-25	7.85	2.48	538.1	471.8	53.21	10.87	9.83	28.01		91.8	26.3
24-3	48-52	7.86	2.43	537.2	466.8	52.82	11.18	9.84	27.48		98.8	25.8
24-4	98-102	7.89	2.36	535.3	467.5	51.33	11.96	9.76	26.91		115.9	25.4
24-5	155-159	7.85	1.97	532.5	466.5	49.61	12.83	9.75	25.50		132.2	24.6

Blue Moon Seamount

Sample ID	depth (cm)	pH	Alk (meq/kg)	Cl (mmol/kg)	Na (mmol/kg)	Mg (mmol/kg)	Ca (mmol/kg)	K (mmol/kg)	S (mmol/kg)	HS- (umol/kg)	Sr (umol/kg)	Li (umol/kg)
GC-25												
25-1	7-10	7.90	2.54	536.9	467.1	52.13	10.51	10.20	27.04		90.8	26.8
25-2	18-21	7.90	2.36	534.1	477.5	51.91	11.11	10.27	27.11		102	26.8
25-3	32-35	7.90	2.12	535.0	457.6	50.61	11.62	10.11	26.81		113	25.4
PC-25												
25-1	14-18	7.90	2.45	535.9	464.3	51.69	10.87	10.11	27.06		97.0	26.5
25-2	29-34	7.91	2.26	535.0	466.1	51.04	11.40	10.02	26.77		104	27.0
25-3	57-61	7.87	1.72	535.0	460.8	48.65	12.16	9.91	26.26		128	26.0
25-4	91-96	8.24	1.39	531.3	457.9	46.27	14.06	9.96	25.81		166	23.0
25-5	125-130	8.03	0.63	528.5	463.9	42.45	17.15	9.81	25.71		217	22.0
25-6	166-170			523.8	459.1	37.33	20.43	9.54	24.45		262	19.8
25-7	191-196	8.15	0.67	522.9	449.6	35.27	22.75	9.45	24.92		291	19.2
25-8	206-212	7.52	0.49	521.9	454.4	34.41	24.05	9.36	25.90		305	19.7

Blue Moon Seamount

Sample ID	Rb umol/ kg	Cs nmol/ kg	Ba nmol/ kg	U nmol/ kg	Mo nmol/ kg
Dive J40					
1-1	1.39	2.7	169	13.77	122
1-2	1.41	2.9	180	13.60	120
1-3	1.35	2.9	181	12.48	116
1-4	1.35	3.3	193	11.14	118
1-5	1.38	3.5	210	10.19	135
1-6	1.41	3.9	210	8.06	129
2-1	1.34	3.0	187	11.38	86
2-2	1.29	3.1	184	10.10	76
2-3	1.14	2.9	187	18.42	1063
2-4	0.98	2.8	167	19.60	373
2-5	0.90	2.5	149	3.14	145
2-6	0.79	2.8	145	0.42	50
2-7	0.72	2.7	158	0.43	30
3-1	1.31	2.9	158	12.69	101
3-2	1.46	3.1	178	14.23	110
3-3	1.34	3.0	162	12.67	91
3-4	1.31	3.1	170	15.94	145
3-5	1.19	2.9	147	39.25	1072
3-6	1.13	2.9	149	36.72	585
6-1	1.68	4.6	234	9.95	123
6-2	1.69	4.5	240	10.22	129
6-3	1.70	4.7	227	9.86	126
6-4	1.72	4.9	231	10.05	127
6-5	1.68	4.7	224	10.50	126
6-6	1.66	4.5	219	10.02	127
6-7	1.73	5.0	225	10.20	131
7-1	1.69	5.1	234	9.97	124
7-2	1.73	5.0	248	10.37	123
7-3	1.89	6.2	236	10.16	122
7-4	1.68	5.1	227	10.54	130
7-5	1.66	4.8	206	11.82	123
7-6	1.67	4.8	209	12.17	128
7-7	1.75	6.0	210	11.30	121

Blue Moon Seamount

Sample ID	B umol/ kg	Si umol/ kg	Rb umol/ kg	Cs nmol/ kg	Ba nmol/ kg	U nmol/ kg	Mo nmol/ kg
GC-25							
25-1	436	409					
25-2	424	197					
25-3	401	186					
PC-25							
25-1	415	186	1.30	2.5	162	12.60	113
25-2	424	480	1.33	2.6	171	11.36	115
25-3	412	140	1.27	2.5	168	7.46	100
25-4	351	350	1.34	3.0	171	26.00	225
25-5	309	35	1.29	3.0	187	0.69	93
25-6	238		1.24	2.9	200	0.36	79
25-7	243	608	1.29	3.2	206	0.38	96
25-8	220	54	1.25	3.0	228	0.50	79
BAC-24							
24-1	419		1.23	2.3	177	10.09	118
24-2	383		1.24	2.3	194	11.36	119
24-3	404		1.28	2.6	170	11.29	118
24-4	362		1.28	3.0	160	9.77	115
24-5	364		1.32	3.5	165	7.74	113

Blue Moon Seamount

Sample ID	V nmol/ kg	Cr nmol/ kg	Co nmol/ kg	Ni nmol/ kg	Cu nmol/ kg	Zn nmol/ kg
Dive J40						
2-1	65.2	8.5	1.37	307	11	4.4
2-2	56.1	3.8	8.81	731	9.5	5.1
2-3	17.9	0.7	78.4	1806	1.3	4.6
2-4	4.0	0.3	0.21	137	0.6	0.5
2-5	68.8	11.6	0.73	27	10	40
2-6	164	32.2	1.56	25	14	41
2-7	1.2	0.4	0.04	2	1.4	1.7
3-1	42.9	15.7	0.59	100	6.9	9.0
3-2	36.5	25.7	1.05	176	4.7	8.3
3-3	38.0	18.0	1.06	294	4.1	9.9
3-4	484	94	51.7	1925	31	111
3-5	536	100	19.1	2402	29	114
3-6	6.0	0.9	13.2	1499	1.0	9.7
PC-25						
25-1	17.9	39.2	2.46	147	2.7	18
25-2	14.7	42.1	4.76	166	5.2	81
25-4	26.8	5.7	34.6	4674	7.7	57
25-7	44.5	8.4	4.34	64	14	187
25-8	10.5	14.2	8.96	88	3.1	23

Blue Moon Seamount

		Dive J40		
nmol/kg		2-1	2-4	2-7
	Y	0.180	0.006	0.004
	Cd	1.887	0.007	0.011
pmol/kg				
	La	23.5	0.9	1.3
	Ce	3.4	2.3	2.1
	Pr	2.93	0.17	0.31
	Nd	13.6	0.6	1.1
	Sm	3.19	1.58	0.27
	Eu	0.714	0.060	0.110
	Gd	4.50	0.22	0.30
	Tb	0.630	0.057	0.048
	Dy	4.93	0.32	0.26
	Ho	1.176	0.061	0.058
	Er	4.31	0.27	0.15
	Tm	0.662	0.036	0.020
	Yb	4.58	0.27	0.17
	Lu	0.836	0.070	0.031

South Chamorro Seamount

Sample ID	depth (cm)	pH	Alk (meq/kg)	Cl (mmol/kg)	Na (mmol/kg)	Mg (mmol/kg)	Ca (mmol/kg)	K (mmol/kg)	S (mmol/kg)	HS- (umol/kg)	Sr (umol/kg)	Li (umol/kg)
Dive J41												
2-1	0-3	8.99	1.34	538.6	468.6	53.19	6.64	10.36	27.00		51.6	19.7
2-2	3-6	8.79	1.46	537.6	478.9	52.55	6.77	10.45	26.88		49.5	14.5
3-1	0-3	8.47	1.92	539.5	479.9	54.80	9.15	10.47	27.91		71.3	24.9
3-2	6-9	8.71	1.47	539.5	478.7	54.19	8.10	10.38	27.73		61.6	24.1
3-3	12-15	7.83	2.14	539.5	474.3	52.97	9.72	10.45	27.60		82.4	27.2
3-4	15-18	7.85	2.41	538.6	477.4	52.48	10.12	10.38	27.91		85.6	28.2
3-5	18-21	7.95	2.57	537.6	481.6	52.60	10.31	10.46	27.69		86.3	27.9
4-1	0-2	8.00	1.81	537.6	474.2	53.67	8.85	10.27	27.72		71.0	26.7
4-2	2-4	8.70	1.31	535.8	479.6	55.12	7.95	10.43	28.07		58.6	25.1
4-3	7-9.5	8.72	1.09	536.7	479.2	55.13	8.14	10.52	27.74		58.1	24.5
4-4	9.5-12	8.46	1.40	537.6	478.6	54.32	8.47	10.50	28.07		65.0	24.8
4-5	12-14.5	8.01	1.77	537.6	476.0	53.39	8.84	10.49	27.74		73.0	25.4
4-6	14.5-17	7.77	2.07	536.7	474.6	52.93	9.59	10.55	28.27		80.2	25.5
4-7	17-18.5	7.80	2.25	537.6	471.0	52.14	9.68	10.49	27.53		82.7	25.0
4-8	20-27	7.83	2.39	536.7	478.0	52.70	10.11	10.67	28.11		85.2	25.9
5-1	0-3	8.18	1.79	539.5	479.3	54.71	9.22	10.47	28.17	0	71.1	27.2
5-2	6-8.5	8.85	1.03	539.5	478.4	54.70	7.97	10.47	28.03	0	57.0	26.2
5-3	8.5-11	8.70	1.32	537.6	479.8	54.08	7.99	10.49	27.53	0	58.9	25.4
5-4	11-13.5	8.79	1.14	537.6	473.1	52.70	6.72	10.41	26.76	0	51.0	23.2
5-5	13.5-16	8.79	1.19	538.6	483.2	52.80	6.68	10.55	26.84	0	48.8	21.7
5-6	16-19	8.64	2.26	538.6	477.9	51.67	7.90	10.51	26.79	0	61.5	19.1
5-7	19-23	8.27	3.28	538.6	483.8	49.42	7.56	10.67	25.51	0	61.3	11.0

South Chamorro Seamount

Sample ID	depth (cm)	pH	Alk (meq/kg)	Cl (mmol/kg)	Na (mmol/kg)	Mg (mmol/kg)	Ca (mmol/kg)	K (mmol/kg)	S (mmol/kg)	HS- (umol/kg)	Sr (umol/kg)	Li (umol/kg)
Dive J41												
6-1	0-3.5	7.76	2.56	552.6	486.2	54.22	10.61	10.40	28.40		89.2	28.0
6-2	3.5-6.5	7.78	2.51	545.1	479.9	53.84	10.68	10.40	28.20		88.6	28.4
6-3	9-11.5	7.83	2.44	541.4	484.9	53.72	10.71	10.41	28.39		87.7	28.5
6-4	1.5-13.3	7.93	2.38	542.3	475.2	53.51	10.00	10.42	27.57		85.5	28.1
6-5	3.3-15.5	7.86	2.33	542.3	490.6	53.99	10.47	10.51	28.42		84.1	29.0
6-6	15.5-18	7.92	2.33	545.6	476.8	53.51	9.76	10.42	27.77		81.3	28.3
7-1	0-3	7.80	2.62	539.5	469.8	53.02	10.67	10.42	28.00		89.8	28.5
7-2	6-9	7.83	2.60	538.1	479.5	52.24	10.45	10.34	27.75		88.2	29.5
7-3	12-15	7.86	2.49	537.2	479.7	53.46	10.45	10.52	28.19		88.1	29.2
7-4	15-18	8.41	1.95	541.8	481.4	54.75	9.17	10.30	28.31		74.7	25.9
7-5	18-21	7.86	2.41	539.5	476.0	53.43	10.50	10.52	28.24		88.5	28.6
7-6	21-14	7.92	2.58	537.6	478.9	53.16	10.38	10.51	28.05		86.7	29.4
7-7	24-27	7.94	2.54	545.1	482.9	54.44	10.34	10.52	28.38		85.1	29.8
PC-26												
26-1	24-27	7.71	2.41	539.0	472.8	52.51	9.98	10.41	28.09		84.8	27.1
26-2	54-57	7.78	2.31	537.6	468.0	52.06	9.71	10.32	27.75		82.2	26.9
26-3	69-72	7.80	2.10	537.6	465.8	51.95	9.61	10.32	27.36		79.0	26.8
26-4	75-77	7.83	2.15	537.2	461.6	51.40	9.14	10.27	26.90		76.6	26.5
26-5	82-85	7.85	2.02	537.6	470.2	52.10	9.38	10.41	27.13		76.7	26.9
26-6	90-94	7.97	2.01	538.6	473.7	51.68	9.26	10.37	27.19		76.1	26.7
MAJORS												
J41 Black		9.82	9.15	538.1						3840	33.4	18.2
J41 White		10.13	24.26	540.4						7740	29.4	22.2

South Chamorro Seamount

Sample ID	B umol / kg	Si umol / kg	Mn umol / kg	Fe umol / kg	Rb umol / kg	Cs nmol / kg	Ba nmol / kg	U nmol / kg	Mo nmol / kg
3-1					1.38	4.3	189	1.81	246
3-2					1.43	8.1	187	0.57	236
3-3					1.36	4.7	165	11.15	131
3-4					1.39	4.2	167	14.75	123
3-5					1.39	4.4	171	25.85	572
4-1					1.36	3.5	138	8.65	168
4-2					1.34	5.2	151	0.44	232
4-3					1.42	9.1	188	0.42	201
4-4					1.47	8.4	187	0.95	181
4-5					1.38	7.5	177	6.43	148
4-6					1.51	7.4	198	10.92	136
4-7					1.48	6.7	199	11.78	112
4-8					1.56	6.2	208	13.49	214
5-1	561	633	0.8	0.9	1.41	3.7	160	9.68	190
5-2	477	39	12.0	0.2	1.39	5.1	156	0.35	196
5-3	474	268	7.8	0.4	1.42	6.2	151	0.49	180
5-4	479	491	12.0	0.6	1.44	6.2	149	0.01	340
5-5	472	10	9.1	0.4	1.47	6.8	184	0.11	241
5-6	487	34	3.5	0.4	1.54	7.7	333	1.51	160
5-7	539	362	0.2	0.4	1.61	9.3	612	6.96	24
PC-26									
26-1					1.43	4.5	193	12.10	120
26-2					1.40	5.7	191	14.32	109
26-3					1.44	6.5	186	13.74	108
26-4					1.37	6.8	172	13.10	101
26-5					1.41	7.4	177	13.80	104
26-6					1.48	8.3	172	15.12	115
MAJORS									
J41									
Black	1367	17	0.0	0.0	2.41	21.4	153	4.32	94
J41									
White	835	23	0.0	0.1	3.63	42.0	544	4.78	70

South Chamorro Seamount

		Dive J41	
	nmol/kg	Black MAJOR	White MAJOR
	V	16.6	16.3
	Cr	1.9	1.0
	Co	0.08	0.11
	Ni	9	4
	Cu	2.4	14
	Zn	3.5	5.9
	Y	0.002	0.003
	Cd	0.042	0.054
	pmol/kg		
	La	0.7	1.1
	Ce	0.5	1.3
	Pr	0.10	0.18
	Nd	0.4	1.0
	Sm	0.57	1.16
	Eu	0.005	0.026
	Gd	0.18	0.28
	Tb	0.021	0.015
	Dy	0.10	0.16
	Ho	0.015	0.023
	Er	0.09	0.06
	Tm	0.011	0.006
	Yb	0.06	0.07
	Lu	0.015	0.016

Sample ID	depth (cm)	pH	Alk (meq/kg)	Cl (mmol/kg)	Na (mmol/kg)	Mg (mmol/kg)	Ca (mmol/kg)	K (mmol/kg)	S (mmol/kg)	HS- (umol/kg)	Sr (umol/kg)	Li (umol/kg)
GC-9 Nip Seamount												
9-1	2-5	8.08	2.31	536.0	464.0	50.97	11.93	9.21	26.40	2	107	26.0
9-2	9-12	8.55	1.62	534.2	459.6	45.55	17.45	9.00	24.00	22	163	25.7
9-3	15-18	9.12	0.72	521.4	413.1	11.93	59.51	6.84	16.99	1	686	23.3
9-4	26-29	10.22	1.63	507.7	373.3	0.42	78.02	4.23	12.81	0	891	21.1
PC-15 Nip Seamount												
15-1	28-30	8.08	2.41	538.5	470.6	49.80	14.10	10.10	26.30	8	137	26.6
15-2	36-39	8.01	2.03	534.7	456.4	44.90	18.20	9.80	23.40	92	190	26.0
15-3	62-65	8.73	1.04	521.6	407.8	9.30	58.60	7.30	12.00	232	705	22.0
15-4	93-96	10.03	1.07	512.2	381.9	0.60	72.90	5.70	8.80	4	888	19.3
15-5	155-158	10.65	2.40	504.7	366.8	0.20	77.30	4.20	7.50	0	900	16.7
15-6	181-184	10.67	2.74	502.8	368.9	0.20	77.40	3.90	7.40	0	900	17.4
15-7	216-219	10.74	3.05	500.9	365.0	0.20	76.80	3.70	6.90	0	900	15.3
15-8	237-240	10.61	3.13	500.9	360.4	0.20	74.80	3.80	7.20	0	914	15.7
GC-15 Nip Seamount												
15-1	20-22	8.07	2.21	537.5	463.4	47.79	15.22	10.07	25.04	20	144	25.7
15-2	33-35	8.91	1.10	518.7	401.9	8.76	59.44	6.84	11.86	1	683	21.0
15-3	46-48	10.03	1.29	510.3	374.2	0.52	73.49	4.92	8.35	4	873	18.9
15-4	~15	7.88	2.32	535.7	464.7	50.87	12.08	10.12	26.23	0	109	26.2
15-5	~25	8.16	2.19	535.7	471.8	48.75	14.51	10.08	25.67	3	135	26.2
15-6	~40	9.56	1.21	513.1	386.0	1.21	72.18	5.62	9.21	0	854	17.9
GC-8 Blip Seamount												
8-2	8-12	7.69	2.30	598.8	530.7	55.87	15.40	11.20	30.76		175	28.3
8-3	13-17	8.03	1.88	543.8	475.3	47.76	16.72	9.79	27.67		209	24.3
8-1	18-22	8.26	1.31	488.0	420.8	20.85	33.17	7.64	23.13		563	14.2

Sample ID	depth (cm)	pH	Alk (meq/kg)	Cl (mmol/kg)	Na (mmol/kg)	Mg (mmol/kg)	Ca (mmol/kg)	K (mmol/kg)	S (mmol/kg)	HS- (umol/kg)	Sr (umol/kg)	Li (umol/kg)
PC-18 Baby Blue Seamount												
18-1	24-26	7.64	2.09	537.9	479.6	52.38	9.63	10.81	27.82	0	82.3	28.2
18-2	36-41	7.76	1.85	536.0	480.1	51.66	9.41	10.69	27.43	0	77.8	28.4
18-3	71-74	8.03	1.48	535.0	485.7	50.83	8.21	10.48	26.45	0	69.6	30.1
18-4	97-103	8.62	1.29	533.2	476.1	49.57	7.76	10.39	25.73	0	62.4	27.7
18-5	111-116	9.01	1.15	533.2	483.7	49.73	7.31	10.53	25.41	0	58.1	28.9
18-6	149-155	8.96	1.02	530.4	480.6	45.32	6.92	10.50	23.69	0	59.7	29.4
18-7	171-177	9.02	1.01	527.5	489.8	39.90	7.18	10.59	22.17	0	60.9	31.5
PC-13 Pacman Seamount Summit												
13-1	23-25	7.61	2.31	537.9	470.3	53.20	10.20	10.50	28.10		86.2	27.7
13-2	40-43	7.65	2.18	536.1	473.9	52.90	9.90	10.50	28.10	0	82.8	28.3
13-3	62-65	7.69	2.02	537.0	472.0	52.50	9.60	10.40	27.70		80.6	28.2
13-4	91-94	7.75	1.92	535.2	474.4	52.30	9.60	10.30	27.90	0	79.0	28.1
13-5	118-122	7.79	1.83	534.2	474.4	52.10	9.40	10.40	27.50	0	76.3	28.6
13-6	157-163	7.83	1.72	534.2	476.0	51.80	9.10	10.40	27.60	0	74.5	29.4
13-7	198-203	7.87	1.64	534.2	477.9	52.10	9.20	10.40	28.00		75.1	29.2
13-8	242-248	8.63	1.15	531.5	474.8	49.30	7.80	10.40	26.10	0	61.9	29.3
13-9	282-288	8.87	0.97	525.0	464.6	44.20	6.90	10.10	24.60	2	56.3	30.3

Sample ID	depth (cm)	pH	Alk (meq/kg)	Cl (mmol/kg)	Na (mmol/kg)	Mg (mmol/kg)	Ca (mmol/kg)	K (mmol/kg)	S (mmol/kg)	HS- (umol/kg)	Sr (umol/kg)	Li (umol/kg)
GC-16 Dip Seamount												
16-1	10-14	7.61	2.46	543.8	469.4	52.91	10.45	9.83	27.50		88.0	26.4
16-2	30-33	7.63	2.51	540.0	470.1	53.42	10.83	9.94	27.50		88.6	26.0
16-3	53-57	7.67	2.48	537.2	471.1	53.74	10.93	9.98	27.72		88.7	25.8
16-4	74-77	7.68	2.50	537.2	474.5	54.08	11.24	10.17	28.11		89.9	25.7
PC-23 Unnamed Seamount												
23-1	171-175	7.66	2.35	535.0	472.2	48.19	12.47	10.30	25.97		95.3	26.1
23-2	128-132	7.68	2.33	534.6	464.1	48.05	12.40	10.32	25.72		95.5	25.9
23-3	89-92	7.67	2.37	536.0	470.1	49.12	12.06	10.31	26.33		92.7	26.2
23-4	72-75	7.67	2.35	537.4	465.6	49.22	11.83	10.34	26.26		92.5	25.9
23-5	38-42	7.70	2.43	536.0	470.0	50.68	11.49	10.14	26.78		90.3	26.5
23-6	14-18	7.70	2.45	536.0	470.3	51.33	10.78	10.05	27.36		88.4	26.6
GC-23 Unnamed Seamount												
23-1	18-21	7.64	2.41	536.0	468.0	52.71	10.68	9.88	27.80		88.3	26.4
23-2	25-31	7.67	2.59	536.0	473.3	52.68	11.02	9.91	27.96		89.7	26.4
23-3	79-82	7.67	2.50	534.1	460.5	50.23	11.14	9.59	26.47		87.9	25.2
23-4	96-100	7.67	2.54	535.0	470.7	52.72	10.93	9.86	28.03		89.0	26.5

Sample ID	B	Si	Mn	Fe	Rb	Cs	Ba	U	Mo	V	Cr	Co	Ni	Cu	Zn	
	umol / kg	umol / kg	umol / kg	umol / kg	umol / kg	nmol / kg	nmol / kg	nmol / kg	nmol / kg	nmol / kg	nmol / kg	nmol / kg	nmol / kg	nmol / kg	nmol / kg	
GC-9 Nip Seamount																
9-1	373	416	2.8	2.2	1.27	1.7	129	25.6	1791							
9-2	344	1131	6.2	1.3	1.35	3.6	149	10.8	962							
9-3	205	1153	2.1	1.5	1.49	20.0	399	0.33	36							
9-4	125	732	1.8	1.4	1.47	43.7	1025	1.42	2362							
PC-15 Nip Seamount																
15-1	412	224	1.9	3.9	1.38	4.3	302	34.6	2771	4.4	1.6	2.25	624	0.5	3.7	
15-2	389	900	0.7	0.9	1.40	5.2	316	36.9	3428	6.2	12.0	0.30	226	0.1	720	
15-3	157	92	1.1	0.5	1.53	22.3	692	0.35	506	0.4	0.7	0.11	103	0.1	2.2	
15-4	84	740	0.9	0.9	1.59	35.4	807	0.27	488	0.9	6.7	0.30	23	1.6	24	
15-5	53	3787	7.5	17.2	1.76	56.0	840	0.33	206	9.1	218	51.9	793	4.2	377	
15-6	45	3490	3.5	4.8	1.74	62.0	838	0.19	199	2.2	1.8	0.26	20	2.6	191	
15-7	44	2847	4.1	4.8	1.78	66.4	807	0.28	198	5.9	1.3	0.17	13	1.7	2.6	
15-8	36	1121	2.2	3.0	1.82	69.2	803	0.12	215	0.8	1.0	0.25	10	2.4	16	
GC-8 Blip Seamount																
8-2	481	825	0.7	0.9	1.37	2.7	185	15.1	116	47.6	8.4	1.22	161	17	21	
8-3	386	1642	2.6	2.8	1.29	3.8	151	12.0	107	16.7	13.3	0.50	230	21	15	
8-1	185	104	0.9	1.1	1.23	6.1	277	2.37	50	40.7	2.2	0.88	62	21	44	
GC-16 Dip Seamount																
16-1	394	228	0.0	0.4	1.31	2.0	204	14.0	129							
16-2	370	1276	1.6	1.5	1.29	1.7	211	13.6	133							
16-3	370	306	0.4	0.3	1.29	1.6	211	13.7	138							
16-4	382	692	1.0	0.7	1.31	1.5	218	13.6	144							

Sample ID	B	Si	Mn	Fe	Rb	Cs	Ba	U	Mo	V	Cr	Co	Ni	Cu	Zn
	umol / kg	umol / kg	umol / kg	umol / kg	umol / kg	nmol / kg	nmol / kg	nmol / kg	nmol / kg	nmol / kg	nmol / kg	nmol / kg	nmol / kg	nmol / kg	nmol / kg
PC-18 Baby Blue Seamount															
18-1					1.53	3.5	216	10.5	127	43.7	3.7	0.26	9	1.4	343
18-2					1.54	4.0	212	8.68	136						
18-3					1.45	3.6	171	6.99	137	9.4	1.5	1.82	133	1.0	6.0
18-4					1.49	6.1	150	3.28	176						
18-5					1.47	6.6	148	1.40	166	0.0	0.4	0.69	101	0.9	0.2
18-6					1.51	7.9	153	0.54	181	1.6	1.3	0.24	69	0.9	1.7
18-7					1.69	10.3	216	1.80	198	5.4	574	9.92	503	32	2.5
PC-13 Pacman Seamount Summit															
13-1	459	2244	2.8	4.3	1.40	2.8	193	11.7	127						
13-2	477	4833	7.0	11.1	1.37	3.3	169	10.4	133						
13-3	446	275	0.6	1.6	1.33	3.4	166	11.2	131						
13-4	458	2953	2.5	3.6	1.29	3.7	154	11.1	131						
13-5	476	2308	1.8	2.4	1.37	4.1	149	10.9	137						
13-6	489	1898	1.5	2.6	1.36	4.5	147	9.04	125						
13-7	512	5084	4.3	8.0	1.38	4.6	144	9.66	124						
13-8	467	1602	3.7	2.1	1.43	7.1	123	2.58	123						
13-9	387	35	2.5	0.5	1.36	9.1	118	0.28	145						

		PC-15 Nip Seamount			PC-18 Baby Blue Seamount	
nmol/kg		15-1	15-3	15-8	18-2	18-7
	Y	0.105	0.001	0.001	0.106	0.001
	Cd	0.021	0.008	0.013	0.46	0.014
pmol/kg						
	La	7.4	0.9	0.4	25.6	0.8
	Ce	10.4	1.4	2.4	25.1	0.3
	Pr	1.60	0.25	0.19	5.06	0.12
	Nd	6.7	0.9	0.6	25.1	0.5
	Sm	1.61	0.11	0.13	5.12	0.07
	Eu	0.56	0.058	0.039	1.33	0.025
	Gd	2.77	0.17	0.19	6.68	0.17
	Tb	0.45	0.019	0.012	0.94	0.009
	Dy	3.59	0.13	0.16	6.11	0.08
	Ho	0.87	0.023	0.023	1.28	0.015
	Er	3.16	0.06	0.04	4.04	0.04
	Tm	0.48	0.005	0.008	0.51	0.011
	Yb	2.84	0.02	0.09	3.79	0.03
	Lu	0.48	0.015	0.014	0.57	0.019